ATMÓSFERA

Revista trimestral publicada por el
Instituto de Ciencias de la Atmósfera y Cambio Climático
de la Universidad Nacional Autónoma de México

Volumen 35
Número 4
1 de octubre de 2022

CONTENTS

MÉXICO 2022

INFORMATION FOR CONTRIBUTORS

ATMOSFERA seeks contributions on theoretical, empirical and applied research in all the areas of atmospheric sciences, with emphasis on meteorology, climatology, aeronomy, physics, chemistry, and aerobiology. Interdisciplinary contributions are also accepted; especially those related with oceanography, hydrology, ecology, forestry, glaciology, agriculture, environmental pollution, and other topics related to economy and society as they are affected by climate variability and change, and atmospheric hazards.

ATMOSFERA publishes articles, short contributions and correspondence in English. The submission of a contribution to be considered an article is assumed to indicate that no similar paper, other than an abstract or preliminary report, has been or will be submitted for publication elsewhere. Short contributions should not exceed 1000 words. Correspondence is intended for discussion of papers published in the journal and should not exceed 250 words.

Manuscripts. Please submit an electronic copy of your final version of the manuscript, preferably prepared with MS Word or compatible software, through the journal's webpage at http://www.revistascca.unam.mx/atm/index.php/atm/about/submissions#onlineSubmissions. It should be formatted with wide margins, double-spacing and all pages numbered. Footnotes to the text should be avoided. When symbols in mathematical work could be in doubt, the authors should submit a list identifying typographically the symbols used. Equations will be numbered in parentheses to the right.

Title, name, address. Provide the title in full and suggest a short title for headers on odd-numbered pages. Author's name, affiliation, e-mail and present postal address will not be included in the document, but they should be captured in the "Submission Metadata" section.

Abstract. All articles shall include an abstract, both in Spanish and in English. Abstracts are not required for short contributions.

Text. The text should be divided into sections, each with a separate heading.

Acknowledgements. Brief.

Appendices. Supplementary materials and lengthy mathematical analyses, whose details are subordinate to the main theme of the paper, should normally appear in an appendix. Each appendix should have a title.

Units, abbreviations and symbols. The International System of Units (m, kg, s, K) should be used. Only standardized terms that have been generally accepted should be used. Unfamiliar abbreviations must be defined when first used. Particular care should be taken to ensure that all symbols are clearly identified. The minus sign should be –.

References. Articles should be fully documented with references in the text and a reference listing ordered alphabetically by author's names at the end of the paper. Digital object identifiers (DOIs) should be provided whenever possible for each reference. Authors are encouraged to adjust to the citation system. Examples:

Articles in journals: Hoerling M.P. and Kumar A., 2002. Atmosphere response patterns associated with tropical forcing. J. Climate 15, 2184-2203.

Chapters in books: Magaña V. and Conde C., 2003. Climate variability and climate change and their impacts on the freshwater resources in the border region: A case study for Sonora, México. In: Climate and water-transboundary challenges in the Americas (Díaz H.F. and Morehouse B.S., Eds.). Kluwer Academic Publishers, Dordrecht, 373-393.

Articles in proceedings: Gallardo L., Córdova A.M., Rojas M., Quintana J., Alcafuz R. and Ramos I., 2004. Stratosphere-troposphere exchange (STE) over Easter Island and Cerro Tololo stations in South America: analysis and simulation of an intensive sounding campaign. 8th International Global Atmospheric Chemistry Conference, Christchurch, New Zealand, September 2004.

Books: Thompson R.D., 1998. *Atmospheric processes and systems.* Routledge, New York, 194 pp.

References cited in the text should indicate, within parenthesis, the last name of each author and the year of publication. If there are more than two authors, the last name of the first author should be followed by et al. When the name forms part of the content of the article, and does not appear solely as a reference, the year of publication is parenthesized. For example:

...a weekly cycle has been observed in surface temperature (Gordon, 1994).

...Gordon (1994) has observed a weekly cycle in surface temperature.

Illustrations and tables. Vector graphics should be supplied in a vector format (eps, ps, ai, etc.) or as pdfs. Photographs should be provided as tiff or jpeg images (with at least 300 dpi); the same applies to line drawings (with at least 1000 dpi). Graphics created in Microsoft Office applications should be supplied in their original format. Figure captions should be self-explanatory and printed on a separate sheet of paper. All figures should be numbered and specifically mentioned in the text by number. Please number all tables with Roman numerals and include a short title.

Proofs. Copies of the proofs will be sent to the author. Revised proofs should be returned to the publisher without delay. The only changes that could be accepted in proofs are on grammar or related to printing errors.

Authors can print copies of their articles from: http://www.revistascca.unam.mx/atm/index.php/atm.

ATMÓSFERA

Revista trimestral publicada por el
Instituto de Ciencias de la Atmósfera y Cambio Climático
de la Universidad Nacional Autónoma de México

MÉXICO 2022

Atmósfera is included in: Web of Science (WoS), SCOPUS, SCISEARCH, Research Alert, GeoBase, Current Contents Connect, and Aquatic Sciences and Fisheries Abstracts (ASFA).

Registrada en el Sistema de Clasificación de Revistas Mexicanas de Investigación Científica y Tecnológica del Consejo Nacional de Ciencia y Tecnología (CONACyT), e indizada en PERIÓDICA.

Manuscripts should be submitted through our website at: https://www.revistascca.unam.mx/atm/.

Subscriptions and all correspondence should be sent to:
Editor of *Atmósfera*, Instituto de Ciencias de la Atmósfera y Cambio Climático, UNAM, Circuito Exterior, Ciudad Universitaria, 04510 Coyoacán, Ciudad de México. Tel.: 52 (55) 5622-4240 Ext. 81888; fax: 52 (55) 5616-0789; e-mail: editorial@atmosfera.unam.mx

Subscription information: Institutional rate: US $90.00 per volume (4 issues); Private rate: US $70.00 per volume (4 issues).

The complete texts of Atmósfera are available in digital format at:
https://www.revistascca.unam.mx/atm/; Redalyc: https://redalyc.org; SciELO: https://www.scielo.org.mx/.

Atmósfera, vol. 35, núm. 3, octubre-diciembre de 2022, es una publicación trimestral editada por la Universidad Nacional Autónoma de México, Ciudad Universitaria, 04510 Coyoacán, Ciudad de México, teléfono (55) 5622-4240, ext.81888, https://www.revistascca.unam.mx/atm/. Editor responsable: Graciela B. Raga. Reserva de derechos al uso exclusivo del título núm. 001559/94 otorgado por el Instituto Nacional del Derecho de Autor. ISSN: 0187-6236. Certificado de licitud de título y contenido 7719 y 5464 otorgados por la Comisión Calificadora de Publicaciones y Revistas Ilustradas de la Secretaría de Gobernación. Las opiniones expresadas por los autores no necesariamente reflejan la postura del editor de la publicación. Se autoriza la reproducción total o parcial de los textos aquí publicados siempre y cuando sea sin fines de lucro y se cite la fuente completa y la dirección electrónica de la publicación.

Printed in Mexico.

Atmósfera 35(4), 611-631 (2022)
https://doi.org/10.20937/ATM.53021

CONTENTS

Changes to tropical eastern North Pacific intraseasonal variability under global warming, implications for tropical cyclogenesis

Hien X. BUI* and Eric D. MALONEY

Department of Atmospheric Science, Colorado State University, Fort Collins, CO, USA.
*Corresponding author; email: hien.bui@colostate.edu

Received: December 15, 2020; accepted: March 3, 2021

RESUMEN

Los cambios en la Oscilación Intraestacional del Pacífico Tropical del Norte (ISO, por sus siglas en inglés) al final del siglo XXI y sus implicaciones para la génesis de los ciclones tropicales (CT) se analizan en el escenario Trayectorias Socioeconómicas Compartidas del conjunto de datos del Proyecto de Intercomparación de Modelos Acoplados fase 6 (CMIP6). Las medias combinadas multimodelo de vientos de nivel bajo y anomalías de precipitación asociadas con el modo dominante intraestacional muestran que la amplitud de la precipitación aumenta mientras que la del viento se debilita en un escenario de calentamiento global, de manera consistente con estudios previos sobre la alberca de agua caliente del Indo-Pacífico. El patrón intraestacional de precipitación y viento del Pacífico nororiental también tiende a desplazarse hacia el suroeste en un clima más cálido, asociado con anomalías positivas de precipitación más débiles cerca de la costa de México y Centroamérica durante la fase de intensificación de la convección y los vientos del oeste. Posteriormente se analizan las implicaciones del modo intraestacional dominante para la formación de CT mediante un índice potencial de formación (GPI, por sus siglas en inglés) de CT empírico. En la simulación histórica, el GPI muestra anomalías positivas en la fase de intensificación convectiva del ISO en la zona del Pacífico nororiental. La modulación del GPI por la ISO se debilita cerca de la costa de México y Centroamérica como resultado del calentamiento, en asociación con el desplazamiento hacia el sur de las anomalías del GPI. Un análisis más a fondo de la contribución de variables individuales que intervienen en el GPI muestra que la humedad relativa y los cambios de vorticidad que se manifiestan en los episodios del ISO debilitan con el calentamiento las anomalías positivas de este índice cerca de las costas mexicanas y favorecen la formación de CT hacia el suroeste. El impacto de los cambios anómalos de la cizalla vertical también favorece la formación lejos de la costa. Estos resultados sugieren una modulación más débil de los CT por el ISO cerca de la costa mexicana en un clima más cálido.

ABSTRACT

Changes to the tropical eastern North Pacific Intraseasonal Oscillation (ISO) at the end of the 21st century and implications for tropical cyclone (TC) genesis are examined in the Shared Socioeconomic Pathways (SSP585) scenario of the Coupled Model Intercomparison Project phase 6 (CMIP6) data set. Multimodel mean composite low-level wind and precipitation anomalies associated with the leading intraseasonal mode indicate that precipitation amplitude increases while wind amplitude weakens under global warming, consistent with previous studies for the Indo-Pacific warm pool. The eastern North Pacific intraseasonal precipitation/wind pattern also tends to shift southwestward in a warmer climate, associated with weaker positive precipitation anomalies near the coast of Mexico and Central America during the enhanced convection/westerly wind phase. Implications for the modulation of TC genesis by the leading intraseasonal mode are then explored using an empirical genesis potential index (GPI). In the historical simulation, GPI shows positive anomalies in the eastern North Pacific in the convectively enhanced phase of the ISO. The ISO's modulation of GPI weakens near the coast of Mexico and Central America with warming, associated with a southward shift of

GPI anomalies. Further examination of the contribution from individual environmental variables that enter the GPI shows that relative humidity and vorticity changes during ISO events weaken positive GPI anomalies near the Mexican coast with warming and make genesis more favorable to the southwest. The impact of vertical shear anomaly changes is also to favor genesis away from the coast. These results suggest a weaker modulation of TCs near the Mexican Coast by the ISO in a warmer climate.

Keywords: ISO, global warming, eastern North Pacific, tropical cyclone.

1. Introduction

The eastern North Pacific (ENP) warm pool is a part of the Western Hemisphere warm pool (Wang and Enfield, 2001), approximately encompassed by the area east of 120º W and west of Mexico and Central America, where the surface temperature is generally above 27 ºC. Although not as large as its Indo-Pacific counterpart, the ENP features similar large-scale atmospheric circulation, tropical convection, and tropical cyclone features and variability to that of the west Pacific warm pool (Misra et al., 2016). Tropical cyclones (TCs) that form in the ENP and their remnants are an important source of precipitation in Mexico and the southwestern United States (Englehart and Douglas, 2001; Ritchie et al., 2011; Domínguez and Magaña, 2018). On the intraseasonal time scale, the Madden Julian Oscillation (MJO; Madden and Julian, 1971, 1972; Maloney and Esbensen, 2003; Neena et al., 2014) modulates convection in this region during boreal summer, with notable northward propagation of convection anomalies (Jiang and Waliser, 2008, 2009; Maloney et al., 2008). Modeling evidence suggests that the ENP can support its own intraseasonal mode of variability (hereafter ENP ISO) in isolation from the Eastern Hemisphere, although variability in this region tends to phase-lock with the MJO (Jiang et al., 2012; Rydbeck et al., 2013). The ENP ISO has been implicated in the modulation of TC genesis and overall TC activity in this region (e.g., Molinari et al., 1997; Maloney and Hartmann, 2000, 2001; Higgins and Shi, 2005; Romero-Vadillo et al., 2007; Camargo et al., 2008; Klotzbach, 2010, 2014; Jiang et al., 2012; Slade and Maloney, 2013).

The MJO affects TC genesis by altering large-scale environmental variables including relative vorticity, humidity, and vertical wind shear, with the relative importance of different variables depending on basin (Camargo et al., 2009; Zhao and Li, 2019). By analyzing a genesis potential index (GPI) using reanalysis data over the global oceans, Camargo et al. (2009) showed that midlevel relative humidity fluctuations make the largest contribution to MJO composite GPI anomalies, followed by contributions from low-level absolute vorticity, with only minor contributions from vertical wind shear and potential intensity. In the ENP region, while midlevel humidity and low-level vorticity are the two most important contributors to ISO composite GPI anomalies (Camargo et al., 2009), the relative importance of each variable depends strongly on location and ISO phase (Jiang et al., 2012). Previous studies have reported that TC development is increased (by up to four times) when lower-tropospheric wind anomalies in the east Pacific associated with the ISO are westerly (when convection is enhanced) vs. easterly (e.g., Maloney and Hartmann, 2000; Aiyyer and Molinari, 2008). Barotropic energy conversions from the mean state to eddies during the convective phase of the MJO have been hypothesized to contribute to the increase of cyclogenesis by strengthening the easterly wave seed disturbances for TCs (Maloney and Hartmann, 2001). Barrett and Leslie (2009) attributed increased TC formation during the ISO's convectively active phase to enhanced upper-tropospheric divergence. Given these impacts of the ISO on TC activity in the current climate, understanding changes of ENP intraseasonal variability under global warming and its influence on TC activity is of interest to people living in this region.

Much recent work has been conducted on MJO changes under global warming (see a review in Maloney et al., 2019). Global climate models generally predict that MJO precipitation amplitude will increase while MJO circulation strength increases at a slower rate or even weakens in the presence of global mean temperature warming (e.g., Takahashi et al., 2011; Arnold et al., 2013, 2015; Chang et al., 2015; Adames et al., 2017a, b; Bui and Maloney, 2018, 2019a, 2020; Rushley et al., 2019, among many others). Differences in the rate of change between MJO precipitation and wind are explained by increased static stability in the tropics under global warming in the presence of weak horizontal temperature gradients (Bui and Maloney, 2019b). In addition, MJO variance is projected to shift further eastward into the central equatorial Pacific in a warmer climate (Bui and Maloney, 2018). Most of the studies above have focused on MJO change in the Eastern Hemisphere, with ISO change in the ENP receiving less emphasis. The fact that the ENP ISO tends to be poorly represented in most global climate models is likely one reason for this lack of emphasis (e.g., Jiang et al., 2013; Lin et al., 2008).

ISO variance and northward propagation in the ENP were underestimated in the previous climate models in phase 3 of the Coupled Model Intercomparison Project (CMIP3; Lin et al., 2008). The fifth phase of CMIP (CMIP5) shows some improvements in the ENP ISO, although only a few models can capture the spatial pattern of the leading mode of intraseasonal variability (Jiang et al., 2013). CMIP6 (Eyring et al., 2016) provides another state-of-the-art multimodel dataset to advance our knowledge of climate variability and climate change. After documenting the ability of CMIP6 models to simulate ENP ISO precipitation and wind variability in current climate, we will examine how the ENP ISO changes at the end of the 21st century in the Shared Socioeconomic Pathways (SSP) with fossil-fueled development combined with 8.5 W m^{-2} forcing scenario (SSP585; O'Neill et al., 2016) in 14 CMIP6 models. We will then use a GPI to infer how the modulation of TC genesis by the ENP ISO may change in a future warmer climate. The effect of anthropogenic forcing on the mean TC activity including its frequency, intensity, and spatial distribution has been extensively studied in recent years (see the review of Knutson et al., 2010, 2020; Murakami et al., 2020), although relatively little work has examined how the intraseasonal modulation of TC activity may change. In particular, we will quantify the contributions from changes in ENP ISO dynamics including wind shear and vorticity anomalies (e.g., Liebmann et al., 1994; Maloney and Hartmann, 2000; Hall et al., 2001) and relative humidity anomalies (e.g., Camargo et al., 2009) to changes in the ENP ISO's modulation of TC genesis in a future warmer climate.

We describe the CMIP6 models, observational datasets, and methodology in section 2. Section 3 examines projected ISO changes in the ENP at the end of the 21st century in the SSP585 scenario, followed by an examination of the impacts on TC genesis in section 4. The main conclusions are summarized in section 5.

2. Data and methodology

2.1 CMIP6 models and observational datasets

The historical and the Shared Socioeconomic Pathways (SSP) with fossil-fueled development combined with 8.5 W m^{-2} forcing scenario (SSP585; O'Neill et al., 2016) experiments from 14 CMIP6 models (Eyring et al., 2016) were used to investigate changes of the ENP ISO and its impacts on TC genesis under anthropogenic warming. The present and future climate were defined using 1986-2005 in the historical run and 2081-2100 in SSP585, respectively. The 14 CMIP6 models examined provide daily mean data that are necessary for ISO-related diagnosis. A brief description and the spatial resolution of the models used are given in Table I.

Among these 14 models, 12 of them will be shown to produce a reasonable simulation of ENP intraseasonal variability in current climate, and only these models are used to examine changes of ENP ISO behavior with warming. These 12 models are indicated in bold in Table I. Due to the availability of variables that are needed to calculate TC potential intensity that goes into the calculation of genesis potential index (GPI), only eight of the 12 chosen models were included in the GPI calculation in section 4. These models are noted with an asterisk in Table I.

ENP ISO convective characteristics in the observed record are assessed using the Integrated Multi-satellitE Retrievals for Global Precipitation Measurement (GPM IMERG) version 6 (Huffman et al., 2018) and interpolated daily with outgoing longwave radiation (OLR) from the National Oceanic and Atmospheric Administration (NOAA) polar-orbiting satellite product (Liebmann and Smith, 1996). Observed ENP ISO wind variability is characterized using 850-hPa zonal wind from the fifth global reanalysis produced by the European Center for Medium-Range Weather Forecasts (ERA5; Hersbach et al., 2020). All of the observational analysis covers the period 2001-2019.

Table I. List of the 14 CMIP6 models used in this study. Models determined to have a good eastern North Pacific ISO in the current climate are noted in bold. Eight models included in the GPI calculation are noted with *.

#	Model	Description	Resolution
1*	**BCC-CSM2-MR**	Beijing Climate Center, China	1.125 × 1.125
2*	**CESM2**	National Center for Atmospheric Research, USA	1.25 × 0.94
3*	**CESM2-WACCM**		
4	**CNRM-CM6-1**	Centre National de Recherches Météorologiques, France	1.4 × 1.4
5	**CNRM-CM6-1-HR**		0.5 × 0.5
6*	**EC-Earth3**	A European Community Earth System Model	0.7 × 0.7
7	**EC-Earth3-Veg**		
8	**GFDL-CM4**	Geophysical Fluid Dynamics Laboratory, USA	2.5 × 2
9*	**MIROC6**	Model for Interdisciplinary Research on Climate, Japan	1.4 × 1.4
10	MPI-ESM1-2-HR	Max Planck Institute Earth System Model, Germany	0.94 × 0.94
11	MPI-ESM1-2-LR		1.875 × 1.875
12*	**MRI-ESM2**	Meteorological Research Institute, Japan	1.125 × 1.125
13*	**NorESM2-LM**	Norwegian Climate Centre, Norway	2.5 × 1.875
14*	**NorESM2-MM**		1.25 × 0.94

Both model output and observational data are converted to a daily mean and have been interpolated to a common grid of 2.5º (longitude) 2º (latitude) before analysis. Only boreal summer (May to October) is examined in this study.

2.2 ENP ISO composite and genesis potential index

To highlight boreal summer intraseasonal variability in the ENP, a local ENP ISO index was generated from the first principal component (PC1) of the leading combined empirical orthogonal function (CEOF; e.g., Wheeler and Hendon, 2004; Lee et al., 2013) of 20-100 day filtered 850-hPa zonal wind and OLR over the ENP domain (0º-30º N, 75º-125º W). Each field was normalized by its domain standard deviation before the CEOF analysis was conducted. The structure of this leading mode is shown in Figure 3, which explains 29.6 and 33.1% of the total variance in observations and historical simulation, respectively. The ENP ISO index created here is similar to that employed by Maloney and Hartmann (2001), except that a CEOF analysis is done rather than EOF analysis using only the 850-hPa zonal wind field. Maloney et al. (2008) and Jiang et al. (2013) similarly produced a local ENP intraseasonal index based on the leading complex EOF of 30-90 day filtered precipitation. In our analysis, days when the PC time series of the leading CEOF is greater than 1σ are used for composite analysis, corresponding to positive precipitation anomalies and anomalous low-level westerly winds. Composites based on negative deviations of the index have a similar pattern, but with opposite sign (see Fig. S1 in the supplementary materials).

We use the TC genesis potential index (GPI) developed by Emanuel and Nolan (2004) and discussed in detail by Camargo et al. (2007) to assess how ENP ISO changes affect TC genesis potential in a warmer climate. Following Camargo et al. (2009), the GPI is calculated as

$$\mathrm{GPI} = \left|10^5 \eta\right|^{3/2} \left(\frac{\mathcal{H}}{50}\right)^3 \left(\frac{\mathrm{PI}}{70}\right)^3 \left(1 + 0.1 V_{\mathrm{shear}}\right)^{-2} \tag{1}$$

where η is the absolute vorticity at 850 hPa (s^{-1}), $\mathcal{H}$ is the relative humidity at 600 hPa (%), PI is the potential intensity ($m\ s^{-1}$), and V_{shear} is the magnitude of the vertical wind shear between 850 and 250 hPa ($m\ s^{-1}$). The potential intensity (PI) is calculated based on Emanuel (1995) as modified by Bister and Emanuel (1998). Since daily values at sufficient vertical resolution are not available for most models to adequately calculate PI, we use monthly mean surface temperature and pressure and vertical profiles of atmospheric temperature and humidity. While this prevents a realistic depiction of intraseasonal PI variations, PI has been shown to only produce minor contribution to intraseasonal TC genesis potential variations in the east Pacific (Camargo et al., 2009). To assess the individual importance of the variables that comprise the GPI for determining the ENP ISO GPI anomalies, the following method is used. First, the GPI is calculated where all three variables other than PI (i.e., η, $\mathcal{H}$, V_{shear}) are allowed to fully vary. Then, we recompute the GPI such that two out of the three variables are allowed to vary, but with the climatological annual cycle of the remaining variable input. This quantity can then be subtracted from the GPI calculated using all variables to assess the importance of the variable of interest. This allows more nonlinearity in the calculation than setting all variables to the climatological mean as done in Camargo et al. (2009). The method therefore provides a better quantitative estimate of the relative importance of the different factors to intraseasonal variability of GPI anomalies.

3. Changes in the ENP ISO

3.1 Changes in summer mean state

We first briefly discuss the multimodel mean oceanic climatological May-October precipitation, 850 hPa zonal wind and OLR distributions over the eastern North Pacific (Fig. 1). Given our emphasis on warm pool intraseasonal variability and TC genesis potential, we only concentrate on oceanic fields in this analysis. Similar plots from satellite and reanalysis fields can be found in Maloney and Esbensen (2007) and Xie et al. (2005), and from CMIP5 models in Jiang et al. (2013). The multimodel mean precipitation in the historical CMIP6 simulation has the main axis of the ITCZ centered at around 9º N (Fig. 1a), coincident with the minimum OLR in the ITCZ region (Fig. 1c), which expands northward toward the coast east of 120º W. We note that the precipitation minimum over the cold waters west of Costa Rica Dome (9º N and 90º W; also see figure 4 in Xie et al., 2005) is still not well-produced in the CMIP6 models analyzed here. The 850 hPa zonal wind is dominated by an easterly component (Fig. 1e), although the flow at the surface is mean westerly near 10º N in the ENP warm pool (not shown here). This basic state flow has implication for air-sea interaction, since a westerly anomaly at the surface would produce enhanced wind speed and surface latent heat flux (Maloney and Esbensen, 2003) that has been argued to be important for the dynamics of ISO in the ENP (e.g., Maloney and Esbensen, 2007; Maloney et al., 2008).

Under global warming, mean precipitation increases over the southern part of the ENP between 5º to 10º N and west of 150º W (Fig. 1b), suggesting a strengthening and southwestward shift of mean precipitation within the ENP intertropical convergence zone (ITCZ). The westward shift may be related to a more frequent occurrence of central Pacific El Niño in a future warmer climate (see Fig. S2 in the supplementary materials for the entire tropical pattern; Yeh et al., 2009). This feature is also clearly apparent in the OLR pattern (Fig. 1d). These projected changes in the mean state convection are also in agreement with previous results from the CMIP3 (Neelin et al., 2006) and CMIP5 (Jiang et al., 2013) datasets, and other models (Maloney et al., 2014). In general, the pattern resembles the "rich-get-richer" pattern of precipitation change found in previous warming studies (e.g., Chou et al., 2009). It is also worth noting that precipitation near the Mexico coast, where most tropical cyclones occur in current climate, tends to slightly decrease, consistent with previous findings of Jiang et al. (2013). Implications for future changes of tropical cyclogenesis in this region will be further discussed below.

3.2 Changes in the ISO amplitude over the ENP

We now analyze precipitation and wind anomalies over the ENP warm pool on intraseasonal timescales. Figure 2 shows the multimodel mean amplitude of intraseasonal variability (calculated as 20-100-day filtered variance fields) from the historical simulation and differences between SSP585 and the historical simulation. In the historical simulation, intraseasonal precipitation generally maximizes in regions of high mean precipitation, although the maximum is slightly shifted toward the coast relative to the mean precipitation pattern (Fig. 2a). The 850 hPa zonal wind variance peak occurs just south of the precipitation variance peak. The ENP ISO OLR variance peak (Fig. 2c) occurs to the west of the ISO precipitation

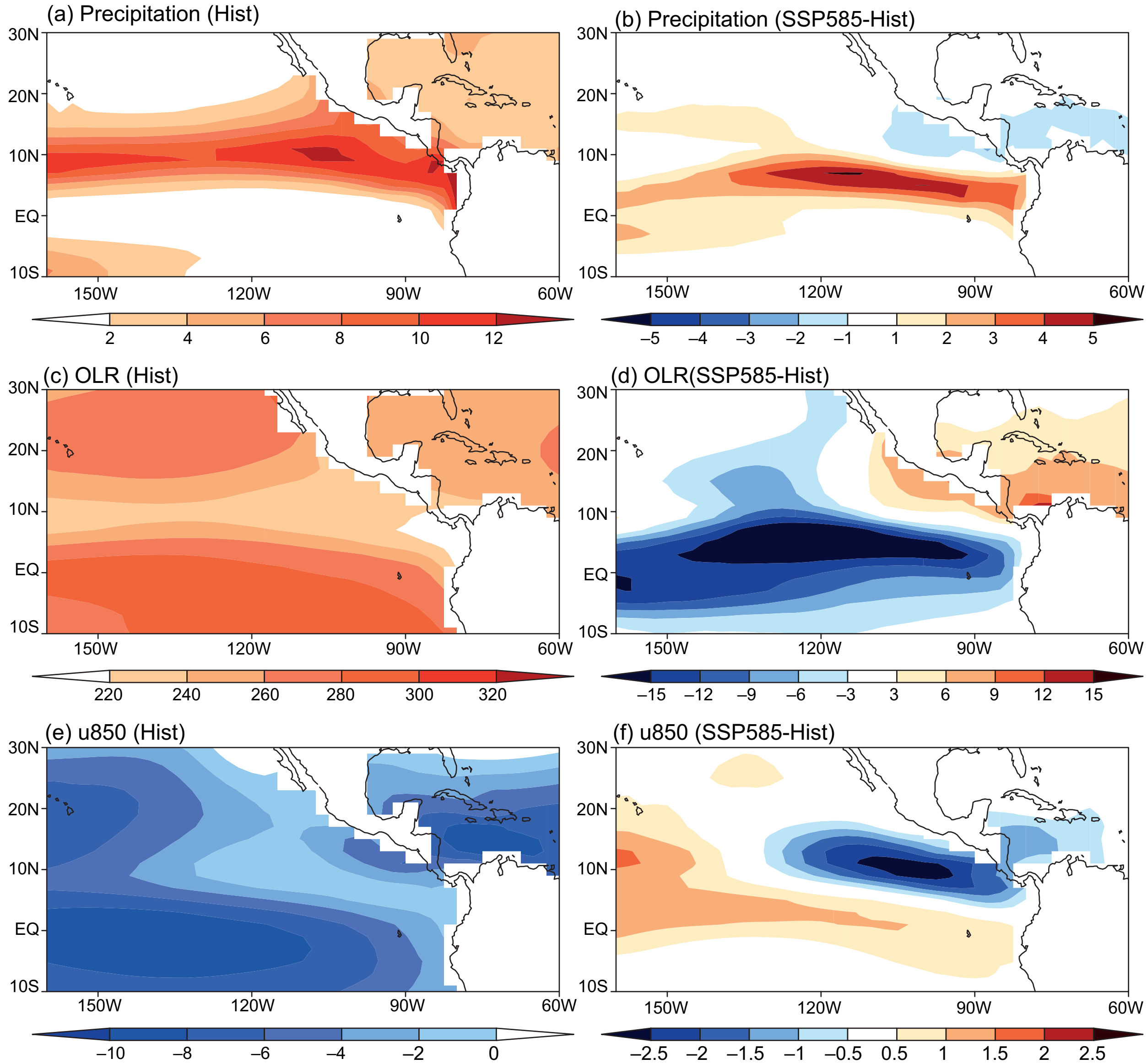

Fig. 1. Multimodel mean (from 14 CMIP6 models) spatial distribution of the boreal summer climatological mean. (a, b) Precipitation (mm day^{-1}), (c, d) outgoing longwave radiation (OLR; W m^{-2}), and (e, f) 850 hPa zonal wind (m s^{-1}) for the historical simulation and differences between SSP585 and historical simulations, respectively. See Figure S2 in the supplementary material for the entire tropical pattern.

and 850 hPa zonal wind variance maxima (Fig. 2e). The multimodel mean intraseasonal variability fields are generally consistent with those in observations (Maloney and Esbensen, 2003) and CMIP5 models (Jiang et al., 2013). Examination of individual models, including the model spread and the magnitude of variability compared to observations, is presented in Figure 4.

Figure 2b, d and f shows the differences in multimodel mean intraseasonal variance between 2081-2100 and 1986-2005. Largely mimicking the mean precipitation changes shown in Figure 1, an increase in precipitation variance occurs between 5º and 10º N, and with a modest decrease in variance near a portion of the ENP Mexican coast. The southwestward shift of ENP ISO precipitation variance is also clearly seen in

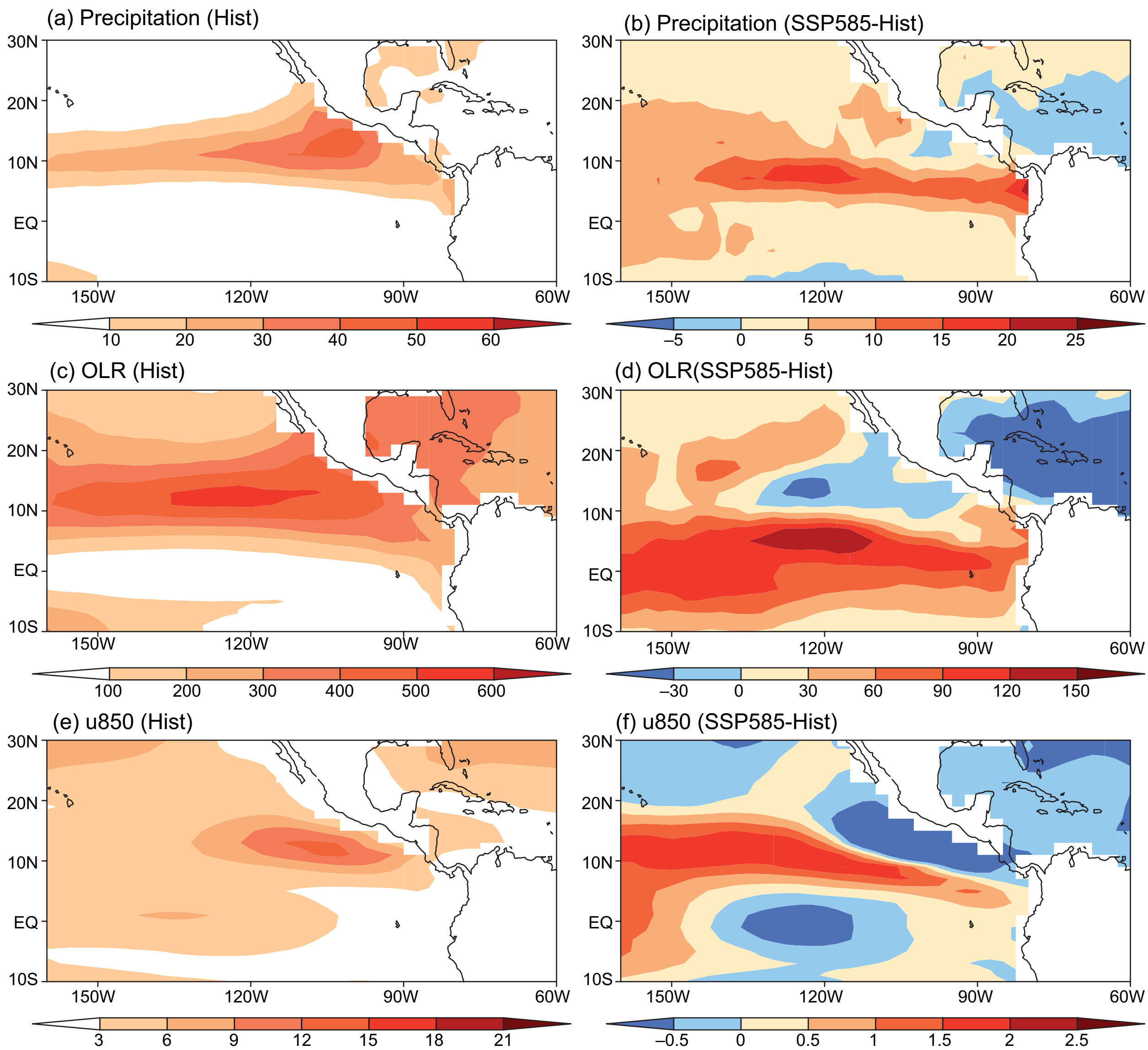

Fig. 2. Multimodel mean (from 14 CMIP6 models) spatial distribution of the boreal summer 20-100 day filtered. (a, b) precipitation (mm^2 day^{-2}), (c, d) outgoing longwave radiation (OLR; W^2 m^{-2}), and (e, f) 850 hPa zonal wind (m^2 s^{-2}) variance for the historical simulation and differences between SSP585 and historical simulations, respectively. See Figure S3 in the supplementary material for the entire tropical pattern.

the OLR (Fig. 2d), where an opposite signed change of OLR variance occurs near the Mexican coast relative to that south of 10º N. A similar shift is also seen in the 850 hPa zonal wind variance field (Fig. 2f). While coastal precipitation variance changes are modest, reductions in the amplitude of wind variability are of greater amplitude. The relative weakening of intraseasonal wind variability relative to precipitation variability is consistent with that shown in previous studies for the MJO, which can be explained by increasing static stability of the tropical troposphere under climate warming (Maloney et al., 2019; see also Fig. S4). Interestingly, similar increases of MJO precipitation variance and weakening of MJO wind variance under global warming also occur over the Indian monsoon/Bay of Bengal region (see Fig. S3 in the supplementary material).

In order to identify the leading intraseasonal modes over the ENP in both observations and CMIP6 simulations, a CEOF analysis is conducted using the 850 hPa zonal wind and OLR. Spatial patterns of the leading CEOF from observations and the multimodel mean of the leading CEOF from individual models are shown in Figure 3 (see Fig. S4 for the pattern of the second CEOF), with the variance explained listed in the caption and on top of each figure. OLR amplitude in CEOF1 peaks between 10º-20º N in observations, with an 850 hPa zonal wind peak on its south flank, is consistent with Maloney and Esbensen (2003, 2005, 2007). The variability in this region also coincides with the ENP hurricane genesis region (see figure 1 in Maloney and Hartmann, 2000). While CMIP6 shows a similar pattern as observed, we note that the historical simulations tend to have higher variance that extends further to the west than observations. The leading EOF in SSP585 becomes slightly more diffuse and the peak amplitudes shift westward (cf. Fig. 3b, c), behavior that is possibly seen better in the difference plot (Fig. 3d, h). The amplitude of zonal wind and OLR in the leading EOF both decrease near the coast in SSP585 relative to the historical simulations. The explained variance of CEOF1 is also decreased in SSP585 relative to the historical period (e.g., 25.6 vs. 33.1%).

Motivated by Jiang et al. (2013), the fidelity in simulating the leading ENP ISO mode by each CMIP6 model is then objectively assessed by calculating the pattern correlation of the simulated CEOF1 against its observed counterpart. Pattern correlations between observed and simulated CEOF1 patterns over the ENP domain are calculated individually for 850 hPa zonal wind and OLR, and then a final pattern correlation score for a particular model is derived by averaging these two correlation coefficients. We also calculate the relative amplitude of models' precipita-

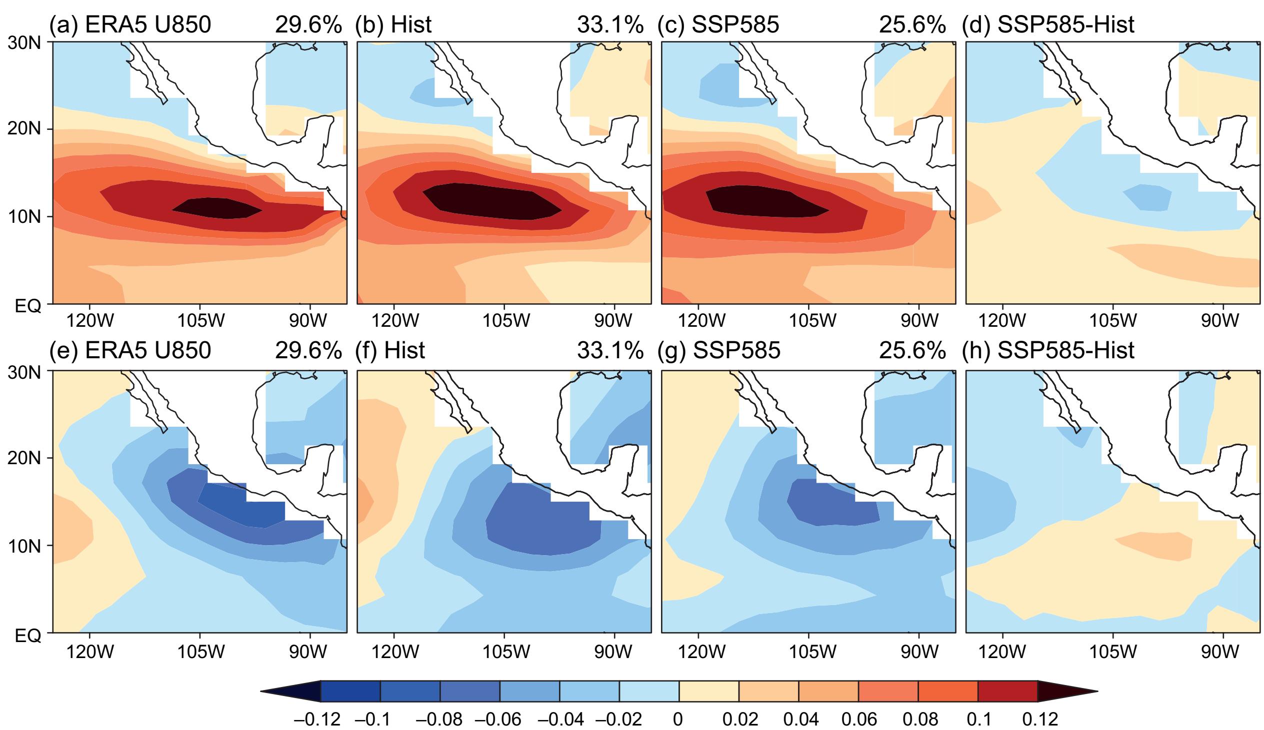

Fig. 3. Spatial distribution of the leading CEOF mode of 850 hPa zonal wind and outgoing longwave radiation (OLR) during boreal summer over the eastern north Pacific for (a, e) observations (explain 29.6% of the total variance), (b, f) mulimodel mean of the CMIP6 historical simulations (33.1% of total variance), (c, g) multimodel mean of the SSP585 simulations (25.6% of total variance), and (d, h) differences between SSP585 and historical simulations. See Figure S4 in the supplementary material for the spatial pattern of the second leading CEOF.

tion and wind to observations by computing the root mean square of the composite precipitation and 850 hPa zonal wind (shown in Fig. 5) over the domain of 10º-20º N, 95º-115º W. As shown in Figure 4, while most of the CMIP6 models produce a reasonable pattern correlation (> 0.8) relative to observations (*x*-axis), biases in the relative amplitude of ISO precipitation and wind (*y*-axis) are apparent, associated with overestimation of the amplitude of the ENP ISO 850 hPa zonal wind and underestimation of the amplitude of precipitation variability. The two models that have relatively low pattern correlations of 0.7 or less, i.e., MPI-ESM-2-HR and MPI-ESM-2-LR, are excluded from further analyses.

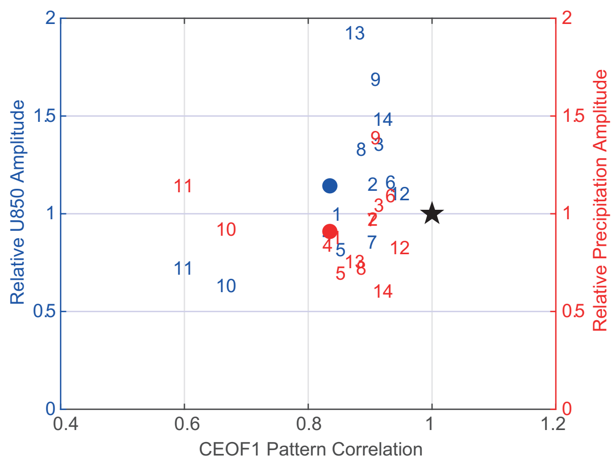

Fig. 4. The *x*-axis shows pattern correlation coefficients of CEOF1 between observations and CMIP6 historical simulations. The *y*-axes show relative composite amplitude of 850 hPa zonal wind (blue, left axis) and precipitation (red, right axis) of the models to observations averaged over the domain of 10º-20º N, 95º-115º W. The black star represents the observations and the circles represent the CMIP6 multimodel mean. The 14 CMIP6 models are indexed according to Table I.

Multimodel mean composite patterns of the remaining CMIP6 models' precipitation, OLR and 850 hPa vector winds anomalies derived using days > 1σ in the time series of CEOF1, with a similar analysis for observations, are shown in Figure 5. Positive deviations of the index correspond to the enhanced intraseasonal convective phase in this region. In general, the CMIP6 multimodel mean shows a similar composite pattern to observations, with maximum precipitation occurring near the coast from 10º-20º N, except with smaller amplitude. As in observations, stronger ISO precipitation tends to be associated with westerly wind and negative OLR anomalies. Under global warming, the maximum precipitation anomaly tends to shift to the west, weakening the positive anomaly near the coastal region (Fig. 5c). Westerly wind anomalies also weaken with warming. The westward shift in the pattern of convection is also clearly seen in the OLR composites (Fig. 5f).

We also examine changes in composite ISO precipitation and wind anomalies for each model averaged over the same domain (10º-20º N, 95º-115º W) as shown in Figure 5. In Figure 6, 10 out of 12 models show a weakening in the 850 hPa zonal wind anomalies in a warmer climate relative to present, with a multimodel mean decrease of about –4.7% K^{-1}. ISO precipitation increase in most of the models (~1.9% K^{-1} in the multimodel mean), associated with the westward shift in the precipitation anomaly pattern. Note that we define the ENP ISO amplitude by computing the root mean square of the composited fields in Figure 5, and all the values have been normalized by the historical simulation and are expressed per unit global mean surface temperature warming. Results are also similar when using the standard deviation calculated from filtered fields to define the amplitude, rather than a composite analysis (not shown). Consistent with our previous studies for the global MJO (Bui and Maloney, 2018, 2019a), while ISO precipitation amplitude increases in most models with warming, wind amplitude increases at a slower rate or decreases with warming. This relationship is expected from an increase in tropical static stability with warming (Fig. S5 in the supplementary material; also see Bui and Maloney, 2019b).

4. Implications for TC genesis

To draw connections between ISO amplitude and structure changes and implications for the modulation of TC genesis in the ENP in a warmer climate, Figure 7 shows a composite for the three most important environmental variables to the intraseasonal modulation of TC genesis according to Camargo et al. (2009): mid-level relative humidity, low-level relative vorticity, and magnitude of vertical wind shear. Figure 7a-c

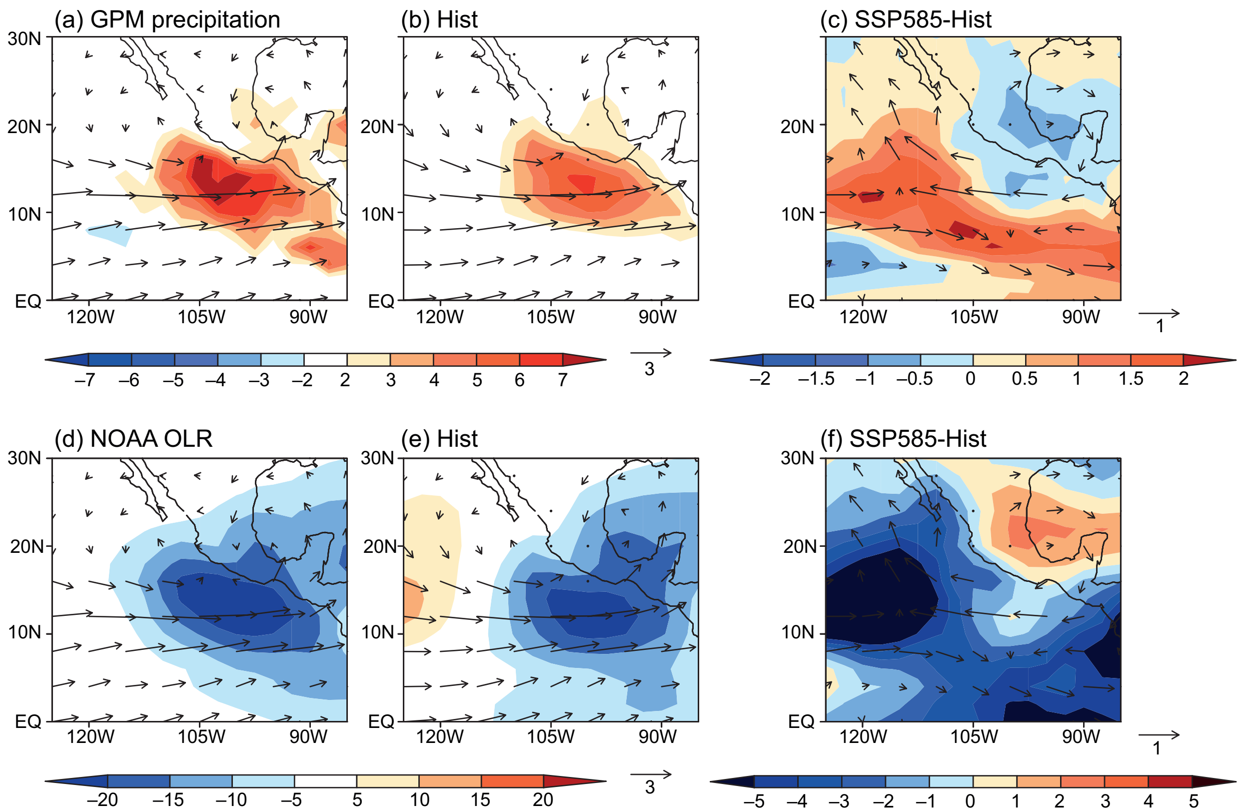

Fig. 5. Boreal summer 20-100 day filtered (a-c) precipitation (shaded, mm day^{-1}), (d-f) OLR (shaded, W m^{-2}) and 850 hPa wind vector (m s^{-1}) composites based on the PC1 timeseries from (a, d) observations, (b, e) historical simulation and (c, f) differences between SSP585 and historical simulations. See Figure S1 in the supplementary material for the composites based on negative deviations of the PC1 timeseries.

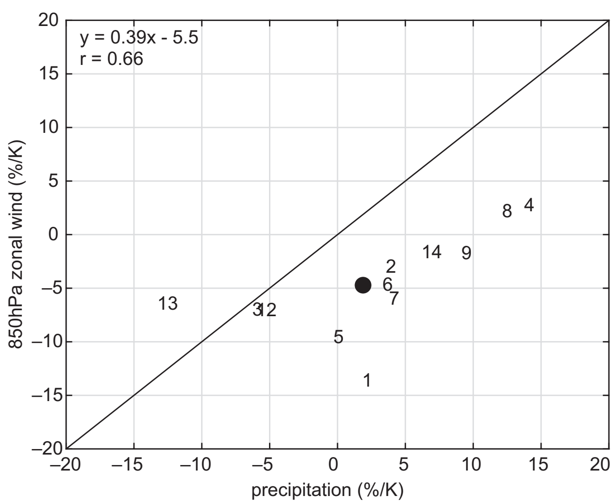

Fig. 6. Scatterplot of ENP ISO 850 hPa zonal wind amplitude (y-axis) and precipitation amplitude (x-axis) changes at the end of 21st century relative to historical simulation from 12 selected CMIP6 models averaged over the domain of 10º-20º N, 95º-115º W. All values have been normalized by the historical simulation and are expressed per unit global mean surface temperature warming (% K^{-1}). The 12 selected CMIP6 models are indexed according to Table I. The black circle represents the multimodel mean.

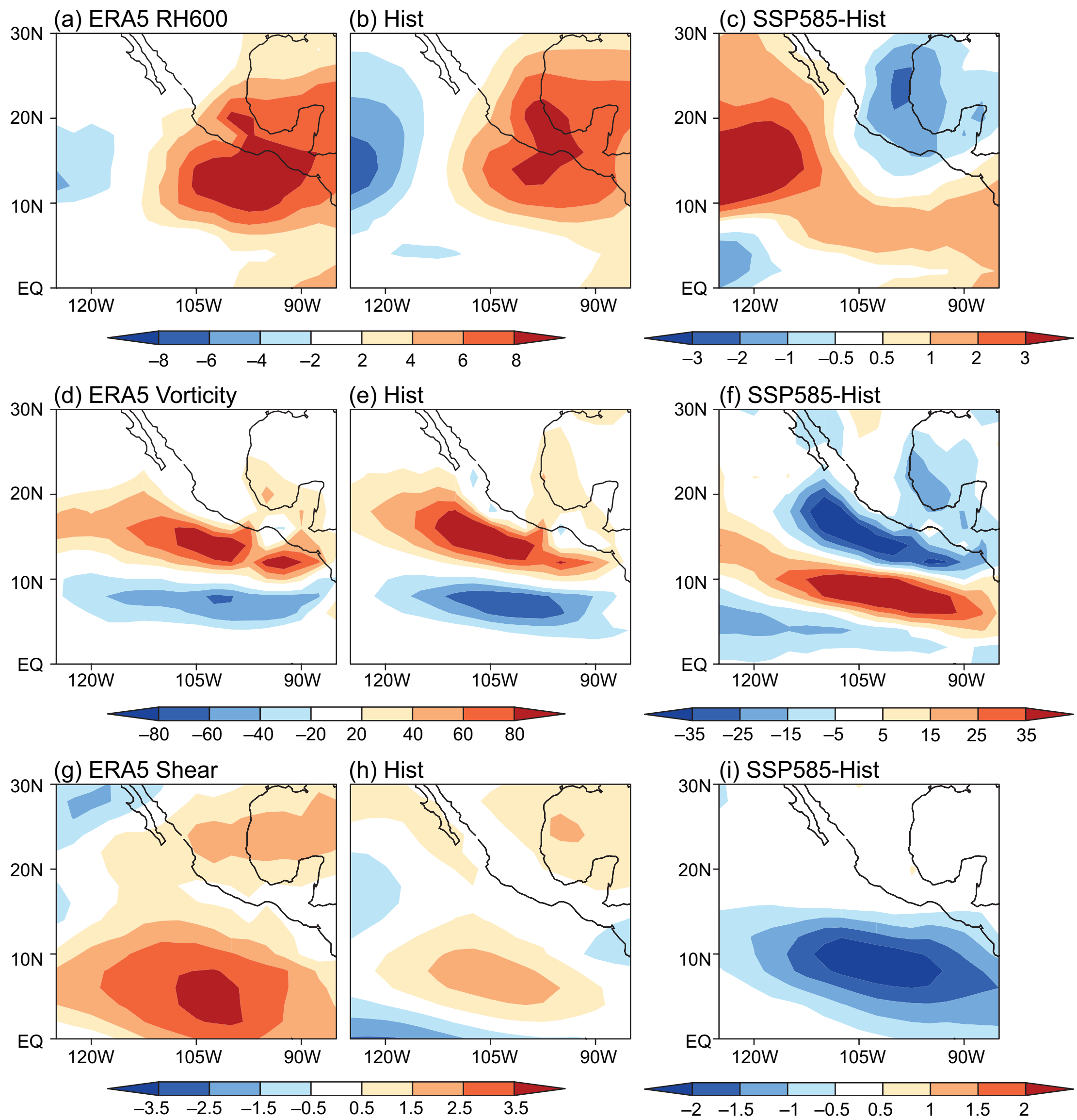

Fig. 7. Similar to Figure 5, but for composite (a-c) 600 hPa relative humidity (%), (d-f) 850 hPa relative vorticity (10^7 s^{-1}) and (g-i) magnitude of vertical wind shear between 250 hPa wind and 850 hPa wind (m s^{-1}) from (a, d, g) observations, (b, e, h) CMIP6 historical simulation multimodel mean and (c, f, i) differences between the SSP585 and historical simulations.

shows the composite pattern of the 600 hPa relative humidity from observational analyses, the historical simulation multimodel mean, and the difference in SSP585 relative to the historical. ERA5 relative humidity anomalies peak within ISO convective areas (cf. Fig. 5). The CMIP6 anomalies tend to slightly underestimate the magnitude of relative humidity anomalies that are also more confined to coastal regions, with a prominent negative anomaly to the west of 120º W that is weaker in observations (Fig. 7b). Under global warming, the relative humidity anomalies become weaker near the coast and shift westward (Fig. 7c), consistent with the pattern of precipitation anomalies.

The 850 hPa relative vorticity field is characterized by cyclonic anomalies north of the axis of strongest wind anomalies, approximately coincident with the area of enhanced precipitation (cf. Figs. 5a and 7d-e). A band of anticyclonic vorticity anomalies occurs to the south of the axis of maximum winds, coincident with the narrow band of suppressed convection (between 8º and 10º N). Under global warming, vorticity anomalies weaken relative to the current climate (Fig. 7f), consistent with the weakening of the ISO circulation with warming. We also examine the change in composite eastern North Pacific vertical wind shear magnitude between 250 and 850 hPa levels (Fig. 7g-i). The anomalous vertical shear patterns are similar between observations and the CMIP6 multimodel mean with low shear anomalies occurring at the same location as cyclonic anomalies (cf. panels [d-e] and [g-h] in Fig. 7) with the maximum wind shear to the south (equator to 10º N). It is worth noting that the smaller magnitude of wind shear in the CMIP6 relative to ERA5 is because the field is averaged across multiple models that have peak variability in slightly different places, thus resulting in smaller multimodel mean composite amplitude. In a warmer climate, the vertical shear near the Mexico coast shows only modest changes in the region of positive vorticity anomalies (cf. panels [f] and [i] in Fig. 7), with greater reductions in anomalies to the south. In other words, both thermodynamic and dynamic changes suggest less favorable conditions during the convectively enhanced ISO phase for TC genesis in the traditional ENP TC genesis region (10º-20º N, 90º-120º W; also see their figure 1 in Maloney and Hartmann, 2000) in a future warmer climate. Individual models (not shown), as might be expected, produce noisier patterns than the multimodel means, as well as different amplitude responses, although the overall conclusions on the sense of the change are consistent with the multimodel mean.

Based on the above and previous results from Camargo et al. (2009) and Jiang et al. (2012), we might expect that GPI anomalies that favor TC genesis in favored eastern North Pacific regions during the convectively active ISO phase will decrease with global warming. This is demonstrated in Figure 8, which shows the ENP ISO composite of GPI from the multimodel mean of eight CMIP6 models during the boreal summer. The multimodel mean does an excellent job capturing observed GPI variability in the TC genesis region near the Mexico coast, where positive genesis potential anomalies occur (Fig. 8a; also see their figure 1 in Maloney and Hartmann, 2000) in the region of positive precipitation anomalies (cf. Fig. 5). In SSP585, the peak of GPI tends to shift southwest, resulting in a reduction in anomalous GPI near the coast (Fig. 8c), consistent with the change in ENP ISO precipitation and wind anomaly patterns shown in Figure 5, and also the variables that go into GPI including relative humidity, vorticity, and shear shown in Figure 7.

To understand the pattern shift of GPI anomalies, we further decompose these and their changes in a warmer climate into the contributions from each environmental variable: relative humidity, absolute vorticity and magnitude of vertical shear (Fig. 9).

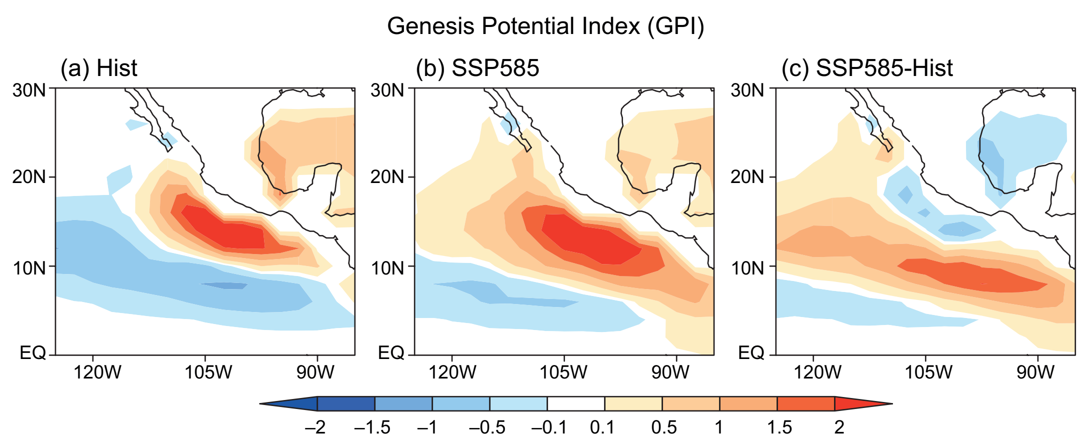

Fig. 8. Boreal summer GPI composite from eight CMIP6 models for (a) historical multimodel mean, (b) SSP585 multimodel mean, and (c) differences between SSP585 and historical.

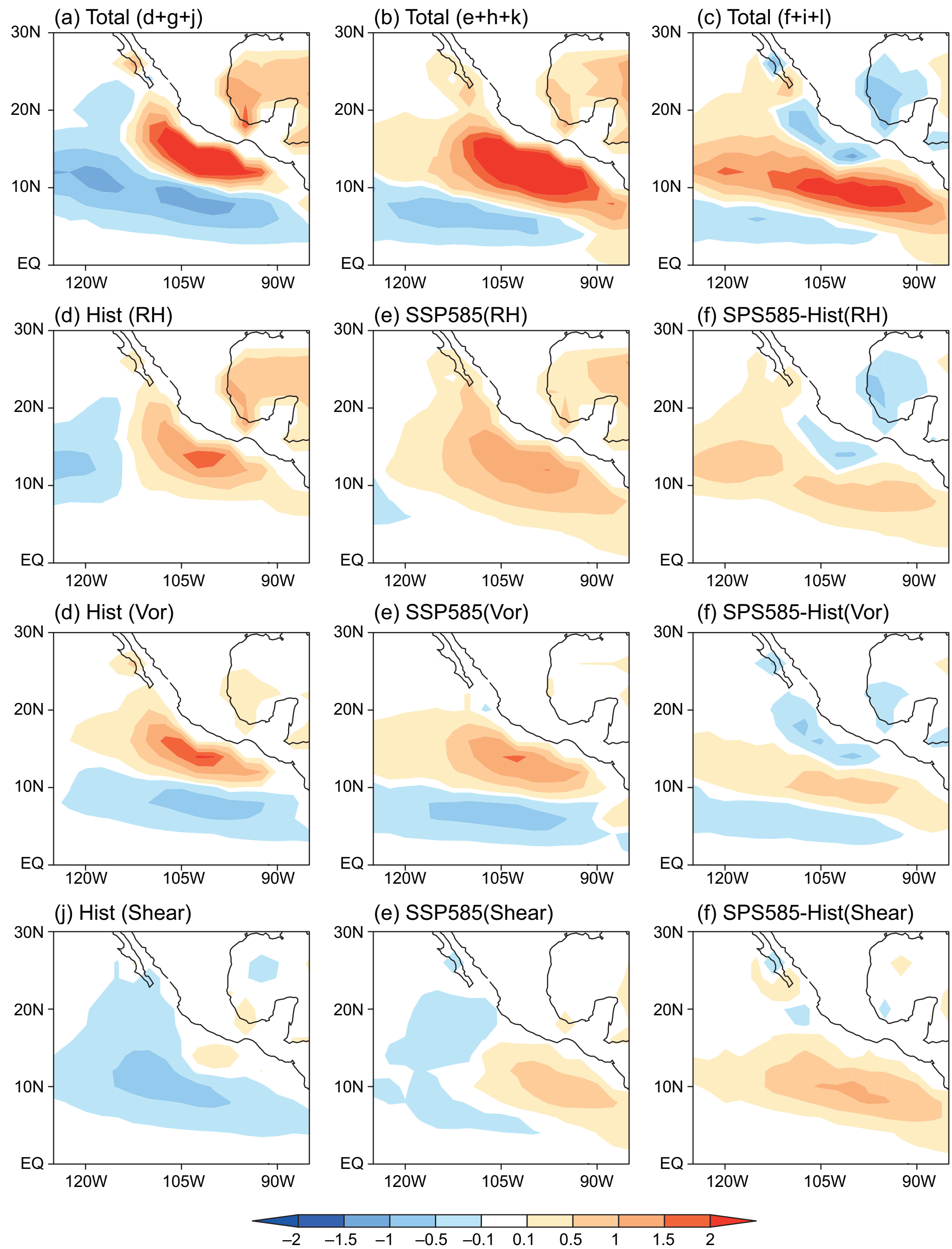

Fig. 9. Same as Figure 8, except for the contributions of the three main environmental variables (d-f) 600 hPa relative humidity, (g-i) 850 hPa absolute vorticity, and (j-l) magnitude of vertical wind shear between 250 hPa and 850 hPa to the GPI anomalies (shown in Fig. 8). The first row shows the result of adding the three components.

As mentioned before, to conduct this calculation we allow two variables to vary while the third one is fixed to the corresponding annual cycle. The result of adding the three contributions calculated this way produces a similar anomaly pattern to the total field shown in Figure 8 (cf. Figs. 9a-c and 8), with a reduction of GPI anomalies near the coast with warming, and strengthening to the southwest. Both relative humidity and vorticity changes with warming are associated to the weakening GPI anomalies near the coast with warming and increase of GPI anomalies to the southwest (Fig. 9), consistent with the respective fields shown in Figure 7. The vorticity changes are also consistent with the reduction of ISO wind amplitude previously discussed. The effect of shear anomalies on GPI has a larger contribution than humidity and vorticity in increasing GPI anomalies away from the coast. The result generally highlights the importance of both dynamical and thermodynamic factors to the reduction of positive GPI anomalies during the enhanced ISO phase near the coastal region under global warming and suggests that the ISO will favor TC genesis over the region away from the coast in a future warmer climate.

5. Conclusions

We have analyzed the historical and SSP585 simulations from 14 CMIP6 models to understand the change of boreal summer intraseasonal variability over the eastern north Pacific (ENP) with climate warming and its influence on tropical cyclone (TC) genesis. We specifically analyzed a genesis potential index (GPI) and its components to understand how individual genesis potential variables influence changes in GPI anomalies during ISO events with climate warming. Our primary conclusions are as follows:

In the ENP under global warming in SSP585, the CMIP6 multimodel mean shows decreases in intraseasonal precipitation and low-level westerly wind anomaly amplitude in regions near the Mexican coast (Figs. 2 and 5), although wind amplitude decreases are stronger (Fig. 6). The stronger decreases in ISO wind amplitude are consistent with those found in previous studies of the MJO in the Indo-Pacific region (Maloney et al., 2019).

The amplitude maximum for ENP intraseasonal precipitation and wind anomalies during enhanced ISO precipitation events also tends to shift southwestward in a warmer climate (Fig. 5c).

Positive ISO precipitation events are associated with weaker intraseasonal GPI anomalies near the Mexican coast with warming, and an enhancement of positive GPI anomalies to the southwest. A decomposition of the GPI anomalies into thermodynamic (i.e., relative humidity) and dynamic (vorticity and vertical shear) components was conducted to assess the importance of these factors for regulating GPI anomaly changes with warming. Relative humidity and vorticity changes during ISO events weaken positive GPI anomalies near the Mexican coast with warming and make genesis more favorable to the southwest. The impact of vertical shear anomaly changes is to favor genesis away from the coast.

The results here suggest that weakening of ENP ISO wind anomalies and a general southwestward shift of the ISO maxima in a future warmer climate would importantly impact TC activity in this region. In particular, TC genesis is projected to be less favored near the coast during ISO events and more favored to the southwest. The current study only focuses on the ISO timescale over the ENP, thus extending this analysis to examine other types of climate variability (such as with the ENSO) would be warranted. Although we found generally consistent results among models in ISO amplitude and pattern changes with warming, projected future changes still vary considerably in their details among the models (e.g., Fig. 6). Therefore, a larger ensemble of climate model simulations would help assess the robustness of our analysis. Recent studies (e.g., Sobel et al., 2019) show that aerosol cooling reduces TC potential intensity more strongly than greenhouse gases warming increase it. A more in-depth study with climate model simulations that can separate external forcing into its various components (e.g., greenhouse gases, aerosols) and natural variability (e.g., decadal variability) would be useful to clarify the impact of each forcing agent on the ISO and the regional TC activity.

Acknowledgments

This work was supported by the Climate and Large-Scale Dynamics Program of the National Science Foundation under grants AGS-1735978 and AGS-1841754.

We thank the World Climate Research Programme (WCRP) Working Group for providing the CMIP6 data, which can be downloaded at https://esgf-node.llnl.gov/search/cmip6/. The ERA5 data and NOAA outgoing longwave radiation data were obtained from the NCAR Research Data Archive (https://doi.org/10.5065/BH6N-5N20) and NOAA Physical Sciences Laboratory (https://psl.noaa.gov/data/gridded/data.interp_OLR.html), respectively. We also thank the NASA Goddard Space Flight Center for providing the global precipitation measurement (GPM) precipitation (https://gpm.nasa.gov/data-access/downloads/gpm). A Python code to calculate the potential intensity is available online (https://emanuel.mit.edu/products).

References

Adames ÁF, Kim D, Sobel AH, Del Genio A, Wu J. 2017a. Changes in the structure and propagation of the MJO with increasing CO2. Journal of Advances in Modeling Earth Systems 9: 1251-1268. https://doi.org/10.1002/2017MS000913

Adames ÁF, Kim D, Sobel AH, Del Genio A, Wu J. 2017b. Characterization of moist processes associated with changes in the propagation of the MJO with increasing CO2. Journal of Advances in Modeling Earth Systems 9: 2946-2967. https://doi.org/10.1002/2017MS001040

Aiyyer A, Molinari J. 2008. MJO and tropical cyclogenesis in the Gulf of Mexico and eastern Pacific: Case study and idealized numerical modeling. Journal of the Atmospheric Sciences 65: 2691-2704. https://doi.org/10.1175/2007JAS2348.1

Arnold NP, Kuang Z, Tziperman E. 2013. Enhanced MJO-like variability at high SST. Journal of Climate 26: 988-1001. https://doi.org/10.1175/JCLI-D-12-00272.1

Arnold NP, Branson M, Kuang Z, Randall DA, Tziperman E. 2015. MJO intensification with warming in the superparameterized CESM. Journal of Climate 28: 2706-2724. https://doi.org/10.1175/JCLI-D-14-00494.1

Barrett BS, Leslie LM. 2009. Links between tropical cyclone activity and Madden-Julian oscillation phase in the north Atlantic and northeast Pacific basins. Monthly Weather Review 137: 727-744. https://doi.org/10.1175/2008MWR2602.1

Bister M, Emanuel KA. 1998. Dissipative heating and hurricane intensity. Meteorology and Atmospheric Physics 65: 233-240. https://doi.org/10.1007/BF01030791

Bui HX, Maloney ED. 2018. Changes in Madden-Julian oscillation precipitation and wind variance under global warming. Geophysical Research Letters 45: 7148-7155. https://doi.org/10.1029/2018GL078504

Bui HX, Maloney ED. 2019a. Mechanisms for global warming impacts on Madden-Julian Oscillation precipitation amplitude. Journal of Climate 32: 6961-6975. https://doi.org/10.1175/JCLI-D-19-0051.1

Bui HX, Maloney ED. 2019b. Transient response of MJO precipitation and circulation to greenhouse gas forcing. Geophysical Research Letters 46: 13546-13555. https://doi.org/10.1029/2019GL085328

Bui HX, Maloney ED. 2020. Changes to the Madden-Julian oscillation in coupled and uncoupled aquaplanet simulations with 4xCO2. Journal of Advances in Modeling Earth Systems 12: e2020MS002179. https://doi.org/10.1029/2020MS002179

Camargo SJ, Emanuel KA, Sobel AH. 2007. Use of a genesis potential index to diagnose ENSO effects on tropical cyclone genesis. Journal of Climate 20: 4819-4834. https://doi.org/10.1175/JCLI4282.1

Camargo SJ, Robertson AW, Barnston AG, Ghil M. 2008. Clustering of eastern north Pacific tropical cyclone tracks: ENSO and MJO effects. Geochemistry Geophysics Geosystems 9: Q06V05. https://doi.org/10.1029/2007GC001861

Camargo SJ, Wheeler MC, Sobel AH. 2009. Diagnosis of the MJO modulation of tropical cyclogenesis using an empirical index. Journal of the Atmospheric Sciences 66: 3061-3074. https://doi.org/10.1175/2009JAS3101.1

Chang CWJ, Tseng WL, Hsu HH, Keenlyside N, Tsuang BJ. 2015. The Madden-Julian oscillation in a warmer world. Geophysical Research Letters 42: 6034-6042. https://doi.org/10.1002/2015GL065095

Chou C, Neelin JD, Chen CA, Tu JY. 2009. Evaluating the "Rich-Get-Richer" mechanism in tropical precipitation change under global warming. Journal of Climate 22: 1982-2005. https://doi.org/10.1175/2008JCLI2471.1

Domínguez C, Magaña V. 2018. The role of tropical cyclones in precipitation over the tropical and subtropical North America. Frontiers in Earth Science 6: 19. https://doi.org/10.3389/feart.2018.00019

Emanuel KA. 1995. Sensitivity of tropical cyclones to surface exchange coefficients and a revised steady-state model incorporating eye dynamics. Journal of the Atmospheric Sciences 52: 3969-3976. https://doi.org/10.1175/1520-0469(1995)052<3969:SOTCTS>2.0.CO;2

Emanuel KA, Nolan DS. 2004. Tropical cyclone activity and global climate. 26th Conference on Hurricanes and Tropical Meteorology, Miami, FL. American Meteorological Society, 240-241.

Englehart PJ, Douglas AV. 2001. The role of eastern North Pacific tropical storms in the rainfall climatology of western Mexico. International Journal of Climatology 21: 1357-1370. https://doi.org/10.1002/joc.637

Eyring V, Bony S, Meehl GA, Senior CA, Stevens B, Stouffer RJ, Taylor KE. 2016. Overview of the coupled model intercomparison project phase 6 (CMIP6) experimental design and organization. Geoscientific Model Development 9: 1937-1958. https://doi.org/10.5194/gmd-9-1937-2016

Hall JD, Matthews AJ, Karoly DJ. 2001. The modulation of tropical cyclone activity in the Australian region by the Madden-Julian oscillation. Monthly Weather Review 129: 2970-2982. https://doi.org/10.1175/1520-0493(2001)129<2970:TMOTCA>2.0.CO;2

Hersbach H, Bell B, Berrisford P, Hirahara S, Horányi A, Muñoz-Sabater J , Nicolas J, Peubey C, Radu R, Schepers D, Simmons A, Soci C, Abdalla S, Abellan X, Balsamo G, Bechtold P, Biavati G, Bidlot J, Bonavita M, De Chiara G, Dahlgren P, Dee D, Diamantakis M, Dragani R, Flemming J, Forbes R, Fuentes M, Geer A, Haimberger L, Healy S, Hogan RJ, Hólm E, Janisková M, Keeley S, Laloyaux P, Lopez P, Lupu C, Radnoti G, de Rosnay P, Rozum I, Vamborg F, Villaume S, Thépaut JN. 2020. The ERA5 global reanalysis. Quarterly Journal of the Royal Meteorological Society 146: 1999-2049. https://doi.org/10.1002/qj.3803

Higgins RW, Shi W. 2005. Relationships between Gulf of California moisture surges and tropical cyclones in the eastern Pacific basin. Journal of Climate 18: 4601-4620. https://doi.org/10.1175/JCLI3551.1

Huffman GJ, Bolvin DT, Braithwaite D, Hsu K, Joyce R, Kidd C, Nelkin EJ, Xie P. 2018. NASA global precipitation measurement (GPM) integrated multi-satellite retrievals for GPM (IMERG). Algorithm theoretical basis document (ATBD), version 4.5, 26 pp.

Jiang X, Waliser DE. 2008. Northward propagation of the subseasonal variability over the eastern Pacific warm pool. Geophysical Research Letters 35: L09814. https://doi.org/10.1029/2008GL033723

Jiang X, Waliser DE. 2009. Two dominant subseasonal variability modes of the eastern Pacific ITCZ. Geophysical Research Letters 36: L04704. https://doi.org/10.1029/2008GL036820

Jiang X, Zhao M, Waliser DE. 2012. Modulation of tropical cyclones over the eastern Pacific by the intraseasonal variability simulated in an AGCM. Journal of Climate 25: 6524-6538. https://doi.org/10.1175/JCLI-D-11-00531.1

Jiang X, Maloney ED, Li JLF, Waliser DE. 2013. Simulations of the eastern north Pacific intraseasonal variability in CMIP5 GCMs. Journal of Climate 26: 3489-3510. https://doi.org/10.1175/JCLI-D-12-00526.1

Klotzbach PJ. 2010. On the Madden-Julian oscillation-Atlantic hurricane relationship. Journal of Climate 23: 282-293. https://doi.org/10.1175/2009JCLI2978.1

Klotzbach PJ. 2014. The Madden-Julian oscillation's impacts on worldwide tropical cyclone activity. Journal of Climate 27: 2317-2330. https://doi.org/10.1175/JCLI-D-13-00483.1

Knutson T, McBride JL, Chan J, Emanuel K, Holland G, Landsea C, Held I, Kossin JP, Srivastava AK, Sugi M. 2010. Tropical cyclones and climate change. Nature Geoscience 3: 157-163. https://doi.org/10.1038/ngeo779

Knutson T, Camargo SJ, Chan J, Emanuel K, Ho C-H, Kossin J, Mohapatra M, Satoh M, Sugi M, Walsh K, Wu L. 2020. Tropical cyclones and climate change assessment: Part II: Projected response to anthropogenic warming. Bulletin of the American Meteorological Society 101: E303-E322. https://doi.org/10.1175/BAMS-D-18-0194.1

Lee JY, Wang B, Wheeler MC, Fu X, Waliser DE, Kang IS. 2013. Real-time multivariate indices for the boreal summer intraseasonal oscillation over the Asian summer monsoon region. Climate Dynamics 40: 493-509. https://doi.org/10.1007/s00382-012-1544-4.

Liebmann B, Hendon HH, Glick JD. 1994. The relationship between tropical cyclones of the western Pacific and Indian Oceans and the Madden-Julian oscillation. Journal of the Meteorological Society of Japan 72: 401-412. https://doi.org/10.2151/jmsj1965.72.3_401

Liebmann B, Smith CA. 1996. Description of a complete (interpolated) outgoing longwave radiation dataset. Bulletin of the American Meteorological Society 77: 1275-1277.

Lin J, Mapes BE, Weickmann KM, Kiladis GN, Schubert SD, Suarez MJ, Bacmeister JT, Lee MI. 2008. North American monsoon and convectively coupled equatorial waves simulated by IPCC AR4 coupled

GCMs. Journal of Climate 21: 2919-2937. https://doi.org/10.1175/2007JCLI1815.1

Madden RA, Julian PR. 1971. Detection of a 40-50-day oscillation in the zonal wind in the tropical Pacific. Journal of the Atmospheric Sciences 28: 702-708. https://doi.org/10.1175/1520-0469(1971)028<0702:-DOADOI>2.0.CO;2

Madden RA, Julian PR. 1972. Description of global-scale circulation cells in the Tropics with a 40-50-day period Journal of the Atmospheric Sciences 29: 1109-1123. https://doi.org/10.1175/1520-0469(1972)029<1109:DOGSCC>2.0.CO;2

Maloney ED, Hartmann DL. 2000. Modulation of hurricane activity in the Gulf of Mexico by the Madden-Julian oscillation. Science 287: 2002-2004. https://doi.org/10.1126/science.287.5460.2002

Maloney ED, Hartmann DL. 2001. The Madden-Julian oscillation, barotropic dynamics, and north Pacific tropical cyclone formation. Part I: Observations. Journal of the Atmospheric Sciences 58: 2545-2558. https://doi.org/10.1175/1520-0469(2001)058<2545:T-MJOBD>2.0.CO;2

Maloney ED, Esbensen SK. 2003. The amplification of east Pacific Madden-Julian oscillation convection and wind anomalies during June-November. Journal of Climate 16: 3482-3497. https://doi.org/10.1175/1520-0442(2003)016<3482:TAOEPM>2.0.CO;2

Maloney ED, Esbensen SK. 2005. A modeling study of summertime east Pacific wind-induced ocean-atmosphere exchange in the intraseasonal oscillation. Journal of Climate 18: 568-584. https://doi.org/10.1175/JCLI-3280.1

Maloney ED, Esbensen SK. 2007. Satellite and buoy observations of boreal summer intraseasonal variability in the tropical northeast Pacific. Monthly Weather Review 135: 3-19. https://doi.org/10.1175/MWR3271.1

Maloney ED, Chelton DB, Esbensen SK. 2008. Subseasonal SST variability in the tropical eastern north Pacific during boreal summer. Journal of Climate 21: 4149-4167. https://doi.org/10.1175/2007JCLI1856.1

Maloney ED, Jiang X, Xie SP, Benedict JJ. 2014. Process-oriented diagnosis of east Pacific warm pool intraseasonal variability. Journal of Climate 27: 6305-6324. https://doi.org/10.1175/JCLI-D-14-00053.1

Maloney ED, Adames ÁF, Bui HX. 2019. Madden-Julian oscillation changes under anthropogenic warming. Nature Climate Change 9: 26-33. https://doi.org/10.1038/s41558-018-0331-6

Misra V, Groenen D, Bhardwaj A, Mishra A. 2016. The warm pool variability of the tropical northeast Pacific. International Journal of Climatology 36: 4625-4637. https://doi.org/10.1002/joc.4658

Molinari J, Knight D, Dickinson M, Vollaro D, Skubis S. 1997. Potential vorticity, easterly waves, and eastern Pacific tropical cyclogenesis. Monthly Weather Review 125: 2699-2708. https://doi.org/10.1175/1520-0493(1997)125<2699:PVEWAE>2.0.CO;2

Murakami H, Delworth TL, Cooke WF, Zhao M, Xiang B, Hsu PC. 2020. Detected climatic change in global distribution of tropical cyclones. Proceedings of the National Academy of Sciences 117: 10706. https://doi.org/10.1073/pnas.1922500117

Neelin JD, Münnich M, Su H, Meyerson JE, Holloway CE. 2006. Tropical drying trends in global warming models and observations. Proceedings of the National Academy of Sciences 103: 6110-6115. https://doi.org/10.1073/pnas.0601798103

Neena JM, Jiang X, Waliser D, Lee JY, Wang B. 2014. Eastern Pacific intraseasonal variability: A predictability perspective. Journal of Climate 27: 8869-8883. https://doi.org/10.1175/JCLI-D-14-00336.1

O'Neill BC, Tebaldi C, van Vuuren DP, Eyring V, Friedlingstein P, Hurtt G, Knutti R, Kriegler E, Lamarque JF, Lowe J, Meehl GA, Moss R, Riahi K, Sanderson BM. 2016. The scenario model intercomparison project (ScenarioMIP) for CMIP6. Geoscientific Model Development 9: 3461-3482. https://doi.org/10.5194/gmd-9-3461-2016

Ritchie EA, Wood KM, Gutzler DS, White SR. 2011. The influence of eastern Pacific tropical cyclone remnants on the southwestern United States. Monthly Weather Review 139: 192-210. https://doi.org/10.1175/2010MWR3389.1

Romero-Vadillo E, Zaytsev O, Morales-Pérez R. 2007. Tropical cyclone statistics in the northeastern Pacific. Atmósfera 20: 197-213.

Rushley SS, Kim D, Adames ÁF. 2019. Changes in the MJO under greenhouse gas-induced warming in CMIP5 models. Journal of Climate 32: 803-821. https://doi.org/10.1175/JCLI-D-18-0437.1

Rydbeck AV, Maloney ED, Xie S, Hafner J, Shaman J. 2013. Remote forcing versus local feedback of east Pacific intraseasonal variability during boreal summer. Journal of Climate 26: 3575-3596. https://doi.org/10.1175/JCLI-D-12-00499.1

Slade SA, Maloney ED. 2013. An intraseasonal prediction model of Atlantic and east Pacific tropical cyclone genesis. Monthly Weather Review 141: 1925-1942. https://doi.org/10.1175/MWR-D-12-00268.1

Sobel AH, Camargo SJ, Previdi M. 2019. Aerosol vs. greenhouse gas effects on tropical cyclone potential intensity and the hydrologic cycle. Journal of Climate 32: 5511-5527. https://doi.org/10.1175/JCLI-D-18-0357.1

Takahashi C, Sato N, Seiki A, Yoneyama K, Shirooka R. 2011. Projected future change of MJO and its extratropical teleconnection in East Asia during the northern winter simulated in IPCC AR4 models. Science Online Letters on the Atmosphere 7: 201-204. https://doi.org/10.2151/sola.2011-051

Wang C, Enfield DB. 2001. The tropical western hemisphere warm pool. Geophysical Research Letters 28: 1635-1638, https://doi.org/10.1029/2000GL011763

Wheeler M, Hendon HH. 2004. An all-season real-time multivariate MJO index: Development of an index for monitoring and prediction. Monthly Weather Review 132: 1917-1932. https://doi.org/10.1175/1520-0493(2004)132<1917:AARMMI>2.0.CO;2

Xie SP, Xu H, Kessler WS, Nonaka M. 2005. Air-sea interaction over the eastern Pacific warm pool: Gap winds, thermocline dome, and atmospheric convection. Journal of Climate 18: 5-20. https://doi.org/10.1175/JCLI-3249.1

Yeh S., Kug JS, Dewitte B, Kwon MH, Kirtman BP, Jin FF. 2009. El Niño in a changing climate. Nature 461: 511-514. https://doi.org/10.1038/nature08316

Zhao C, Li T. 2019. Basin dependence of the MJO modulating tropical cyclone genesis. Climate Dynamics 52: 6081-6096. https://doi.org/10.1007/s00382-018-4502-y

Supplementary Material

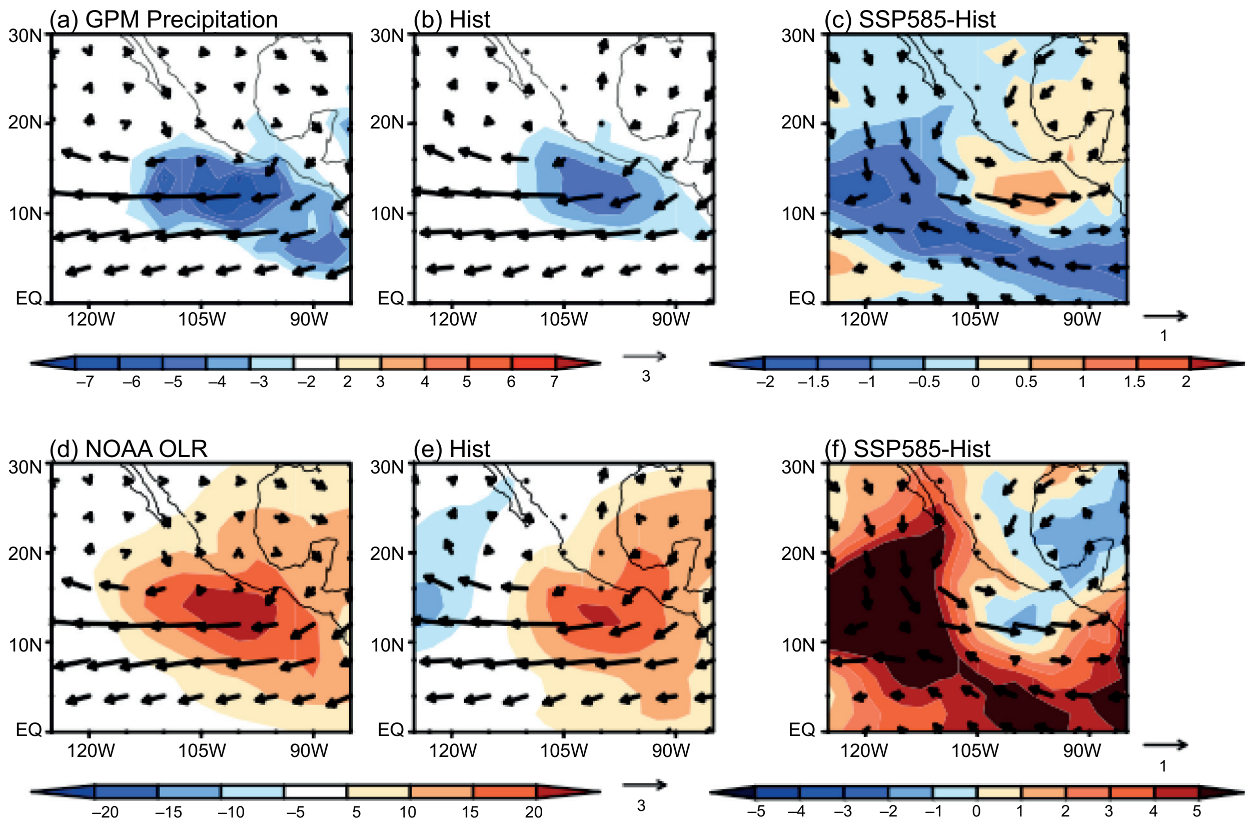

Fig. S1. Similar to Figure 5, but for composite based on negative deviation of the PC1.

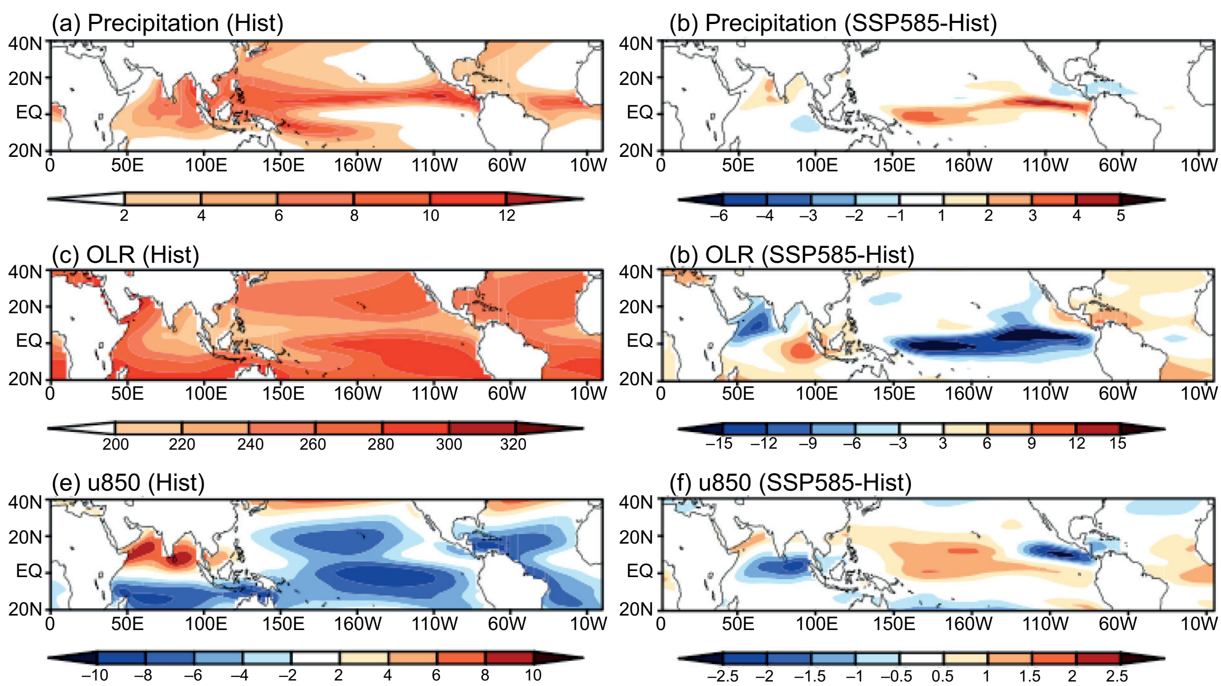

Fig. S2. Same as Figure 1, but for the entire tropics.

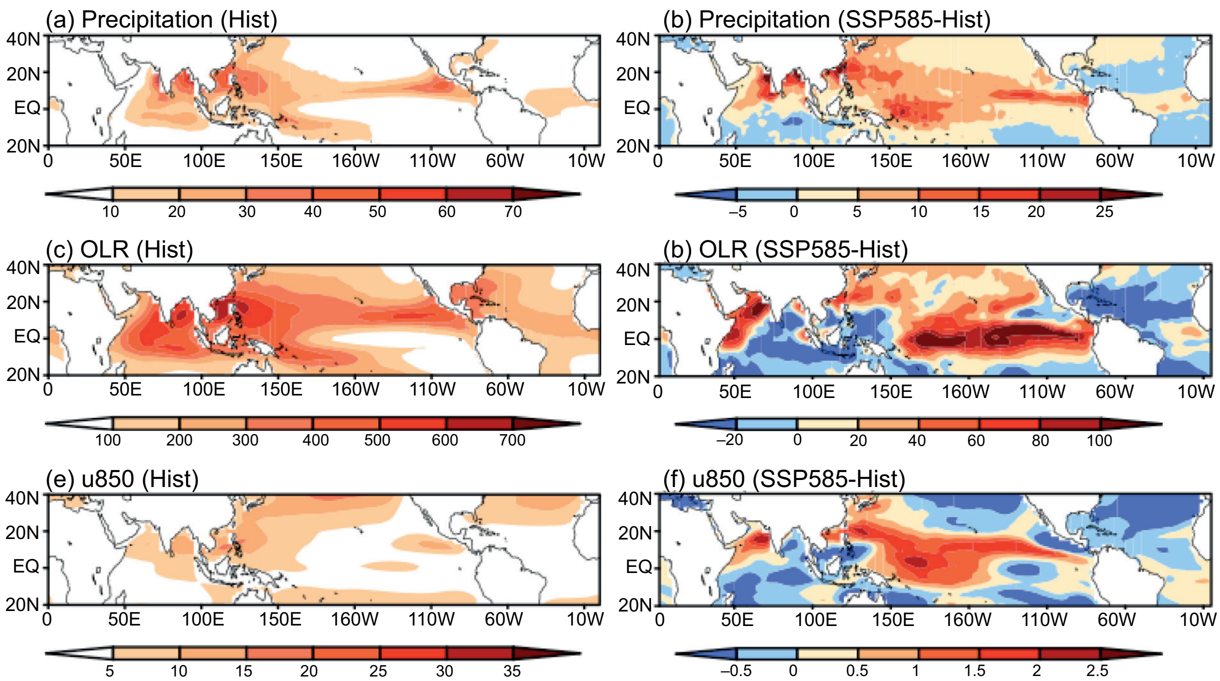

Fig. S3. Same as Figure 2, but for the entire tropics.

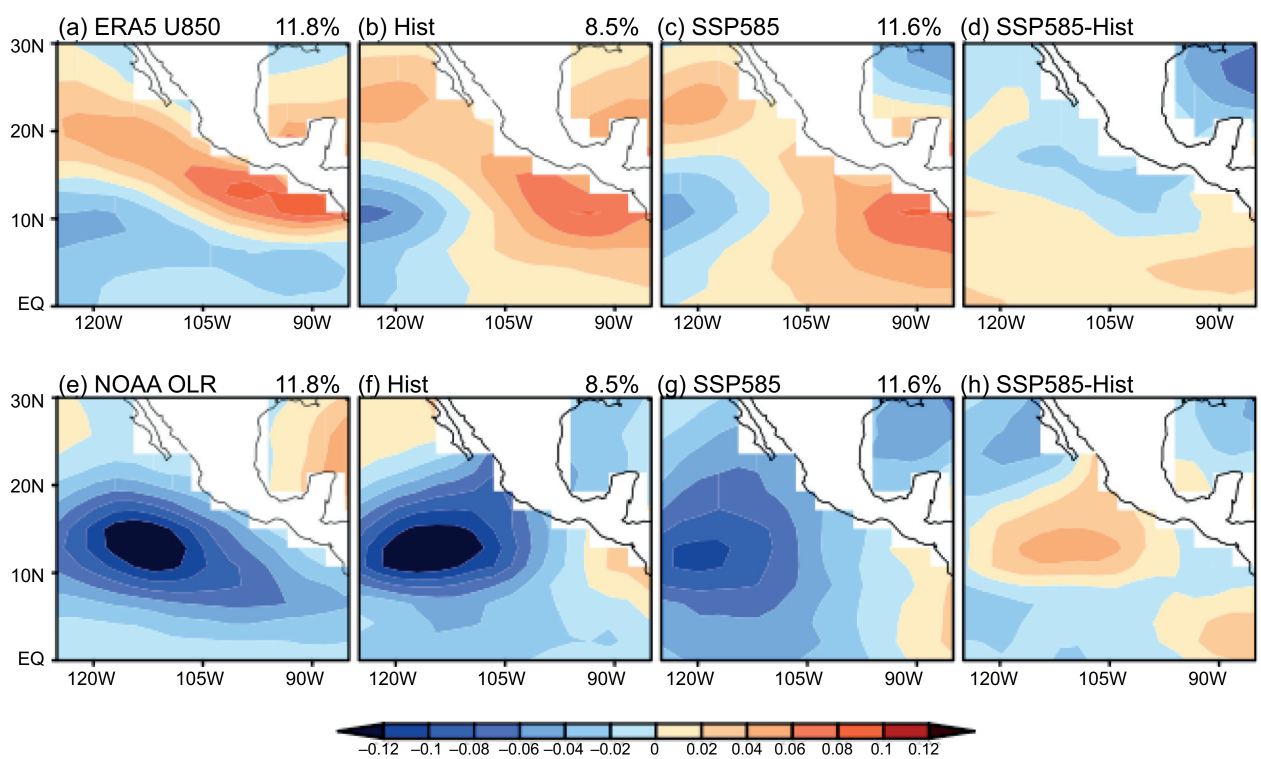

Fig. S4. Same as Figure 3, but for the second CEOF.

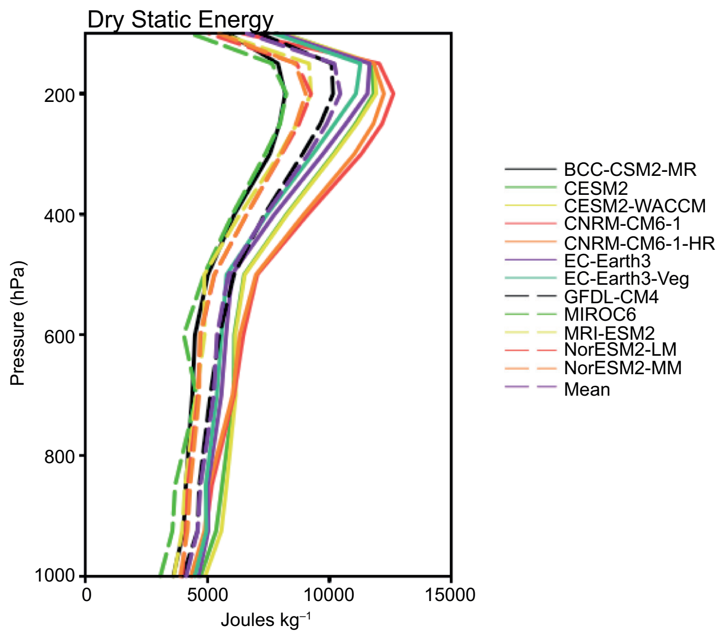

Fig. S5. Changes in vertical structure of May-October mean dry static energy in the SSP585 relative to historical simulations averaged over the eastern North Pacific domain (0-30º N, 85º-125º W). Units are in J kg^{-1}.

Atmósfera 35(4), 633-650 (2022)
https://doi.org/10.20937/ATM.52937

Stratospheric temperature features over Saudi Arabia and their relationship to Atlantic SSTs and surface temperatures in winter

H. M. HASANEAN and Abdulhaleem H. LABBAN*

Department of Meteorology, King Abdulaziz University, P.O. Box 80234, Jeddah, Saudi Arabia.
*Corresponding author; email: alabban@kau.edu.sa

Received: June 30, 2020; accepted: April 13, 2021

RESUMEN

La temperatura estratosférica es un factor climático importante a nivel regional y mundial. Este artículo investiga las tendencias de temperatura en la estratosfera inferior a 50 hPa (T50), la estratosfera media a 30 hPa (T30) y la estratosfera superior a 10 hPa (T10), así como sus impactos en la temperatura superficial en el océano (SST, por sus siglas en inglés) Atlántico y la temperatura superficial del aire (SAT) en Arabia Saudita durante la temporada de invierno de 1979 a 2019. Los resultados muestran un enfriamiento significativo en la tendencia lineal de T50, un enfriamiento progresivo en la tendencia lineal de T30 y un enfriamiento en la tendencia lineal de T10 durante el periodo de estudio en Arabia Saudita. Los resultados también indican una tendencia de enfriamiento no lineal significativa en la temperatura estratosférica de T50 y T30, así como un enfriamiento débil en T10. Existen cambios climáticos abruptos tendientes al aumento de la temperatura para T50 y T30 en 1992, y para T10 en 1983, los cuales pudieran estar relacionados con erupciones volcánicas. Los resultados del estudio también indican que existe una fuerte relación negativa entre T50 y las SST del Atlántico tropical del sur (TSA) con la oscilación atlántica multidecenal (AMO), en tanto que se observa una relación estadísticamente negativa con la AMO. La correlación cruzada entre adelanto y retraso sugiere que las TSM del Atlántico (Atlántico tropical del norte [TNA], TSA y AMO) están vinculadas con temperaturas estratosféricas en tres inviernos adelantados. Como resultado de la teleconexión entre el SAT y la temperatura estratosférica sobre Arabia Saudita, el acoplamiento del SAT y la temperatura estratosférica se produce en invierno, especialmente en las capas baja y media de la estratosfera.

ABSTRACT

Stratospheric temperature is an important climatic factor regionally and globally. This paper investigates temperature trends in the lower stratosphere at 50 hPa (T50), the mid-stratosphere at 30 hPa (T30), and the upper stratosphere at 10 hPa (T10), as well as their impacts on Atlantic Ocean sea surface temperature (SST) and Saudi Arabian surface air temperature (SAT) during the entire winter seasons of 1979-2019. The results show significant cooling for the T50 linear trend, progressive cooling for the T30 linear trend, and cooling for the T10 linear trend during the study period over Saudi Arabia. The results also indicate a significant nonlinear cooling trend for stratospheric temperature at T50 and T30, while a weak cooling at T10 is observed. Abrupt climatic changes towards warmth exist at all three levels of stratospheric temperature, which occur in 1992 for T50 and T30 and in 1983 for T10. These abrupt climate changes may be related to volcanic eruptions.
Our results also indicate that a strong negative relationship exists between T50 and the SST of the tropical South Atlantic (TSA) and the Atlantic Multi-Decadal Oscillation (AMO), while T30 indicates a statistically negative relationship with the AMO. The lead-lag cross-correlation suggests that the SST of the Atlantic Ocean (tropical North Atlantic [TNA], TSA, and AMO) are linked to stratospheric temperatures at three lead winters. As a result of the teleconnection between SAT and stratospheric temperature over Saudi Arabia, the coupling of these two features occurs in winter, especially in the lower to mid-stratosphere layers.

Keywords: Sea surface temperature, Atlantic Ocean, Surface temperature, Saudi Arabia, ArabiaIndices, Teleconnection.

1. Introduction

Stratospheric temperature characteristics are an important component to consider when studying global climate change. The trends of stratospheric temperature can guide the roles of anthropogenic and natural climate change mechanisms. According to the IPCC (2001, 2007), increases (decreases) in tropospheric temperatures and/or decreases (increases) in stratospheric temperatures provide insight into the influences of these mechanisms (Karl et al., 2006; Randel et al., 2009). Based on satellite data from the 1990s, decreases in the mean annual lower and mid-stratospheric temperatures were found by many researchers (Pawson et al., 1998; Randel et al., 2009; Maycock et al., 2018). Knowledge on these changes in stratospheric temperature is vital for estimating trends (Shine et al., 2003) and variations in stratospheric ozone (Ramaswamy et al., 2001; WMO, 2006; Randel et al., 2009). These researchers concluded that among the factors determining the global stratospheric temperature mean, the upper part of the stratosphere and lower area of the mesosphere had a cooling rate of at least 2 ºK/decade between 1980 and 2000. During this time, the lower stratosphere had a cooling rate of approximately half to 1ºK per decade, while that of the mid-stratosphere was approximately 0.5 ºK/decade. Through a model inter-comparison, Shine et al. (2003) attempted to set-up an agreement between the potential reasons for temperature decrease in the layers of the stratosphere. The relationship between observations and model values was not consistently strong in the middle and lower stratosphere, while the model fails to find a significant rate of cooling within the mid-stratosphere and the temperature trends in the lower stratosphere (Aquila et al., 2016). During the same period, the degree of mean stratospheric temperature trends was approximately 0.2 ºK/decade, which is highly correlated to the degree of trends in global mean surface temperature (IPCC, 2007).

Beneath the stratosphere is the troposphere, which interacts with the oceans and is thus directly affected by circumstances at the ocean surface. The stratosphere is linked to surface weather and climate variability. Extreme circulation events in the stratosphere are recognized to exert feedback on the troposphere (Baldwin et al., 2003). Moreover, the stratosphere is influenced by the propagation of waves up from the troposphere (Manzini, 2009). Modeling together with observational studies illustrates that the changes in sea surface temperature (SST) related to El Niño Southern Oscillation (ENSO) influence both tropospheric and stratospheric circulations (Reid et al., 1989; Seager et al., 2003; Manzini, et al., 2006; Xie et al., 2011, 2012; Feng et al., 2013). Domeisen et al. (2019) found that “El Niño leads to a warming of the polar stratosphere in both hemispheres, while the lower tropical stratosphere cools. These signatures are linked by a strengthened stratospheric circulation from the tropics to the polar regions. El Niño also leads to more frequent breakdowns of the stratospheric polar vortex. For La Niña, these effects tend to be opposite, though they are not always robust, suggesting nonlinear or non-stationary effects, long-term variability, and trends in the teleconnections”. Moreover, the Brewer-Dobson circulation strengthened during the positive phase of ENSO through the spread of vertical waves (Sassi et al., 2004; Calvo et al., 2010). Camp and Tung (2007) illustrated that ENSO has an effect on the Northern Hemisphere temperature in the polar stratosphere during winter. However, adjusting stratospheric temperature and circulation due to SST gradient changes remains unknown. Temperatures of the stratosphere are influenced not only by changes in SST but also by changes in ozone and by other greenhouse variations (Santer, 2003; IPCC, 2007). Chen et al. (2010) studied the source regions, spread tracks, and time of air mass movements from the stratosphere to the troposphere in the region of the Asian summer monsoon. Kodera et al. (1990) explained how climatic changes in the troposphere may be affected by the stratospheric procedure.

On global average, since 1979 surface air temperatures (SAT) were warm compared to tropospheric temperatures, and the troposphere was warm compared with the stratosphere (Pielke et al., 1998a, b; Brown et al., 2000; Stendel et al., 2000). Nevertheless, in the tropics and subtropics, warming is highly spatially variable and highly substantial (Christy et al., 2001; Gaffen et al., 2000). According to global observations, SAT has experienced continued warming since the late 1950s, whereas cooling of the stratosphere has been continuing since 1979 (IPCC, 2007). The reason behind this trend is the crucial role of greenhouse gases in cooling the stratosphere and warming the troposphere (Solomon, 1999; Karl et al., 2006; Ramaswamy et al., 2006; IPCC, 2007; Aquila et al., 2016, Maycock et al., 2018). Troposphere-stratosphere unifications characterized by this association occur at all temporal scales, from weekly variability (Kolstad et al., 2010) to long-term climate change (Sigmond et al., 2008; Scaife et al., 2012; Polvani et al., 2011; Karpechko and Manzini, 2012).

Many studies (Cubasch et al., 2001; Rind et al., 2008; Sigmond and Scinocca, 2010; Kidston et al., 2015) illustrate the cooling of the stratosphere and warming of the troposphere due to increased greenhouse gases. SSTs are related to the atmospheric greenhouse gas load. Increasing trends in the tropical SSTs are partly due to rising greenhouse gases. Nevertheless, SST variations can influence the dynamics of the troposphere extending to the stratosphere. Almost every instance of a large-amplitude tropospheric anomaly displays a strong link to the stratosphere, proposing that tropospheric variability would be less without the impact from the stratosphere (Baldwin and Dunkerton, 1999). Regarding the results of these studies, one can credibly hypothesize that SST may influence the activity of the stratospheric wave that drives the residual circulation in the stratosphere. The upper zonal winds of the troposphere increase according to the thermal wind association, and vertically broadcasted waves are deflected more poleward in the stratosphere (Olsen et al., 2007). Therefore, the residual circulation of the stratosphere is strengthened.

Moreover, the study of Olsen et al. (2007) suggests that SSTs significantly influence stratospheric circulation. Omrani et al. (2014) found that warming in the north Atlantic Ocean leads to changes in the extratropical stratosphere in early winter. SSTs have an important role in the atmospheric response in tropical and subtropical regions. Changes in the stratosphere during winter frequently cause significant adjustments in the circulation of the troposphere (Omrani et al., 2014). Additionally, these authors found that the stratosphere is an important element of subtropical atmospheric reactions to variability in the ocean, where it aids in atmospheric processes. These findings suggest that the prediction and simulation of the subtropical climate should improve by using stratosphere-resolving models to provide the best understanding of anthropogenic and natural climate change. Experiments by Omrani et al. (2016) show that north Atlantic Ocean (NAO) variability influences the coupled stratosphere-troposphere system. Kalnay et al. (1996) found that almost all alterations in the NAO were prolonged in the stratosphere and were detected in the stratospheric polar vortex in early winter. Scaife et al. (2005) found that changes in the stratospheric vortex lead to changes in the NAO. The interaction between the troposphere and stratosphere could enhance the NAO in winter and be sensitive to surface forcing. This means that stratospheric variability affects the annular modes and NAO (Black, 2002; Thompson et al., 2002; Kolstad et al., 2010). Atlantic Multi-Decadal Oscillation (AMO) phases (warm/cold) are related to the phases of the NAO (negative/positive) structure in late winter and weaken/strengthen the polar vortex of the stratosphere in early winter (Gastineau and Frankignoul, 2015; Keenlyside et al., 2015).

The current research is important because it is the first in the region to address the characteristics of stratospheric temperatures and their relationships with Atlantic SST and SAT during winter over Saudi Arabia. Section 2 of this paper covers the data and methodology. Changes in stratospheric temperatures in the lower (50 hPa), mid- (30 hPa) and upper stratosphere (10 hPa) are presented in section 3.1. Section 3.2 focuses on the association between SSTs over the Atlantic Ocean and SAT over Saudi Arabia. In section 3.3, teleconnections between the stratosphere and troposphere are examined. Finally, section 4 addresses the conclusions of this study.

2. Data and methodology

2.1 Data

In the current study, monthly of ERA-Interim data (Berrisford et al., 2011) with a resolution of $0.75^o \times 0.75^o$ for the period 1979-2019 for lower stratospheric temperature at 50 hPA (T50), middle stratospheric temperature at 30 hPa (T30), and upper stratospheric temperature at 10 hPa (T10) is used. Similarly, the NCEP/NCAR reanalysis data (Kistler et al., 2001) with a resolution of $2.5^o \times 2.5^o$ (Kalnay et al., 1996) for the period 1979-2019 for 2-m winter SAT (December to February) is used in the current study.

Saudi Arabia covers a wide region (approximately 2 250 000 km^2) located between 15.5º-32.5º N and 32º-55º E (Fig. 1). It is characterized by a complex orography. Almazroui et al. (2012) estimated that the region comprises approximately 80% of the Arabian Peninsula.

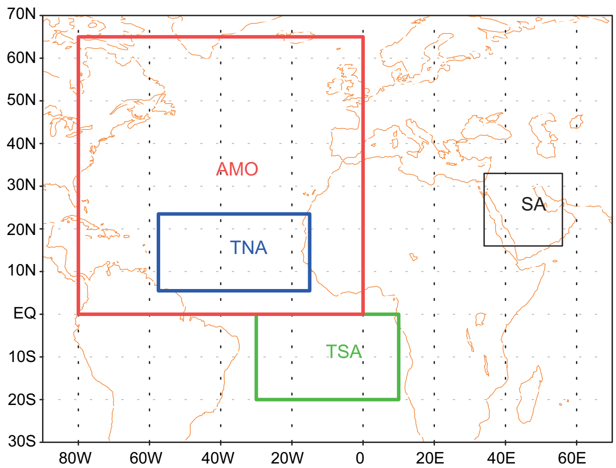

Fig. 1. Locations of Saudi Arabia (SA) and sea surface temperature indices. TNA: tropical northern Atlantic; TSA: tropical southern Atlantic; AMO: Atlantic Multi-decadal Oscillation.

2.2 Atlantic Ocean indices

The tropical northern Atlantic (TNA) and tropical southern Atlantic (TSA) indices were created following Enfield et al. (1999) as anomalies of the average monthly SST between 5.5º-23.5º N, 15º-57.5º W for TNA, and from 0º-20º S, 10º E-30º W for TSA. The northern tropical Atlantic (NTA) SST index time series anomalies were computed as averages over the area between 60º-20º W, 6º-18º N, and 20º-10º W, 6º-10º N. All SST data were obtained from the ERSST V3b dataset. Anomalies were computed and smoothed by a three-month running mean and superimposed onto 20 leading eigenvalue orthogonal functions. The Atlantic meridional mode (AMM) is well defined as the leading mode of non-ENSO coupled atmosphere/ocean fluctuations in the Atlantic Ocean. The principal component analysis finds patterns without reference to prior knowledge about whether the samples come from different treatment groups or have phenotypic differences. The spatial distribution pattern is defined over the area 21º S-32º N, 74º W-15º E. Two-time series of AMM are calculated through SST projection and the wind field at 10 m. Generally, it is more logical to use the SST index for the AMM because it is more representative of the coupled mode. The TNA, TSA, NTA and AMM time series are acquired from NOAA's Earth System Research Laboratory (ESRL). AMO time series are computed from the Kaplan SST dataset, which is an index of the temperature in the north Atlantic basin (0º-65º N, 80º W-0º E). Wintertime series (December to February) were also calculated for all indices.

2.3 Methodology

Weighted areal averages of stratospheric temperatures during winter were calculated over the region of Saudi Arabia. The regression least squares method (Wilks, 2006) was used to estimate the linear trend in stratospheric temperature. In section 3.1 when analyzing trends, the choice of start and end dates of the time series is very important due to trend estimates can change dramatically by including or excluding a few years particularly when computing from relatively short time series (e.g., see Liebmann et al., 2010). So, to minimize period selection biases in warming/cooling anomalies we report, the basis of the 1979-2019 intervals selected to characterize the recent decadal behavior of stratospheric temperature variability. The non-parametric Mann-Kendall statistical test was used for the detection of a nonlinear trend within the T50, T30 and T10 time series and the testing of statistical relevance (Sneyers, 1990; Huth, 1999; Schonwiese and Rapp, 1997). The sequential version of the Mann-Kendall rank statistic method can be used to identify abrupt climatic changes (Mitchel et al., 1966; Sneyers, 1990). Many researchers have found that the mentioned method is suitable for detecting climatic changes in climatological time series (Goossens and Berger, 1986; Sneyers, 1990). The correlation technique is a straightforward procedure compared to other methods (such as principal component analysis) to access teleconnection patterns (Nigam, 2003). Koutroulis et al. (2012) explained that several natural physical systems are usually characterized by lead-lag relationships and play a critical role in correlational studies between time series. Cross-correlation analyses are very useful to investigate the manifestation of elements of large-scale climate variability in regional climate and are therefore applied in the current study to investigate relationships between Saudi Arabian stratospheric and surface temperature changes and indices descriptive of major modes of variability in the Atlantic atmospheric and oceanic environments. The time-frame of the lead-lag analysis in this study is ± 10 yr at a 1-yr temporal resolution.

3. Results and discussion

3.1 Characteristics of the stratospheric temperature

The means and linear trends in the lower, mid- and upper stratospheric temperature time series over Saudi Arabia at 50 hPa (T50), 30 hPa (T30), and 10 hPa (T10) during winter were calculated and plotted for the study period 1979-2019 (Fig. 2). The average (standard deviation) values for T50, T30, and T10 are −65.41 ºC (2.0 ºC), −57.02 ºC (2.3 ºC) and −43.74 ºC (2.54 ºC), respectively, for the entire period of study; however, year-to-year variations in T50, T30 and T10 are not clear. The T50 time series for the period 1979-2019 is highlighted in Figure 2a, accompanied by the findings of the linear trend analysis. A significant decreasing trend ($R^2 = -0.50$) in winter for T50 occurred during the entire period (1979-2019). The analysis of temperatures in the mid-stratosphere (T30, Fig. 2b) and in the upper stratosphere (Fig. 2c) shows an insignificant decreasing linear trend ($R^2 = 0.20$ for T30; $R^2 = 0.05$ for T10). The statistical Mann-Kendall rank test clearly illustrates that the values for the T50, T30 and T10 non-linear trends are equivalent to −0.40 ºC (99% confidence level), −0.32 ºC (95% confidence level) and −0.16 ºC, respectively, over the entire study period. Hasanean (2004) and Hasanean et al. (2019) found similar results for the T50 trend over the Arabian Peninsula in separate studies.

A very strong positive relationship between T50 and T30 ($r = 0.78$) exists at the 99% confidence level. Moreover, the relationship between T50 and T10 is strong ($r = 0.50$, 99% confidence level). Additionally, there is a moderate relationship between T30 and T10 ($r = 0.37$) at the 99% confidence level.

The Mann-Kendall's t-test of abrupt changes for stratospheric temperatures at the lower stratosphere (50 hPa), mid-stratosphere (30 hPa) and upper stratosphere (10 hPa) are shown in Figure 3. A significant abrupt climatic change is evident at all three levels. Lower, mid-, and upper stratospheric temperatures show changes towards warming during the year 1992 for T50 and T30 and during the year 1983 for T10. Our analysis indicates that abrupt changes of stratospheric temperatures during those years may have resulted from the impact of volcanic eruptions. The largest volcanic eruptions occurred in the years of maximum stratospheric temperatures (the El Chichón eruption in 1982, the Colo eruption in 1983, and the Mt. Pinatubo eruption in 1992). These findings are in agreement with works from other researchers (e.g., Angell, 1997; Randel et al., 2009; Zossi and Fernández, 2011). For example, the 1982 El Chichón and the 1992 Mt. Pinatubo eruptions influenced the stratospheric temperature of the Northern Hemisphere (Pawson et al., 1998). The surface temperature showed cooling after the Pinatubo eruption, which caused changes in atmospheric circulation, while at the same time, the temperature in the lower stratosphere warmed (Self et al., 1996). Several past studies (e.g., Labitzke and McCormick, 1992; Young et al., 1994; Soden et al., 2002) illustrate the impacts of volcanic eruptions on temperatures in the lower stratosphere and at Earth's surface. These researchers found that lower stratospheric warming and surface cooling were documented after a volcanic eruption. Aquila et al. (2016) stated that in the lower stratosphere, Mount Pinatubo and the solar cycle caused abrupt steps through the aerosol-associated warming and the volcanically induced ozone depletion. They also stated that in the middle and upper stratosphere, changes in solar irradiance are largely responsible for the step-like behavior of global temperature anomalies, together with volcanically induced ozone depletion and water vapor increases in the post-Pinatubo years.

To better understand the dynamics of changes in stratospheric temperature, the time series of stratospheric temperatures in Saudi Arabia may be compared with time series of stratospheric temperature in the Northern Hemisphere's tropical regions (0º-25º N), subtropical regions (25º-40º N), mid-latitude regions (40º-60º N), and polar regions (60º-90º N). Therefore, the correlation coefficient between the Saudi Arabian temperature time series during winter in the lower (T50), mid- (T30), and upper stratosphere (T10), and the winter stratospheric temperatures in those areas at the same levels were calculated (Table I) in the

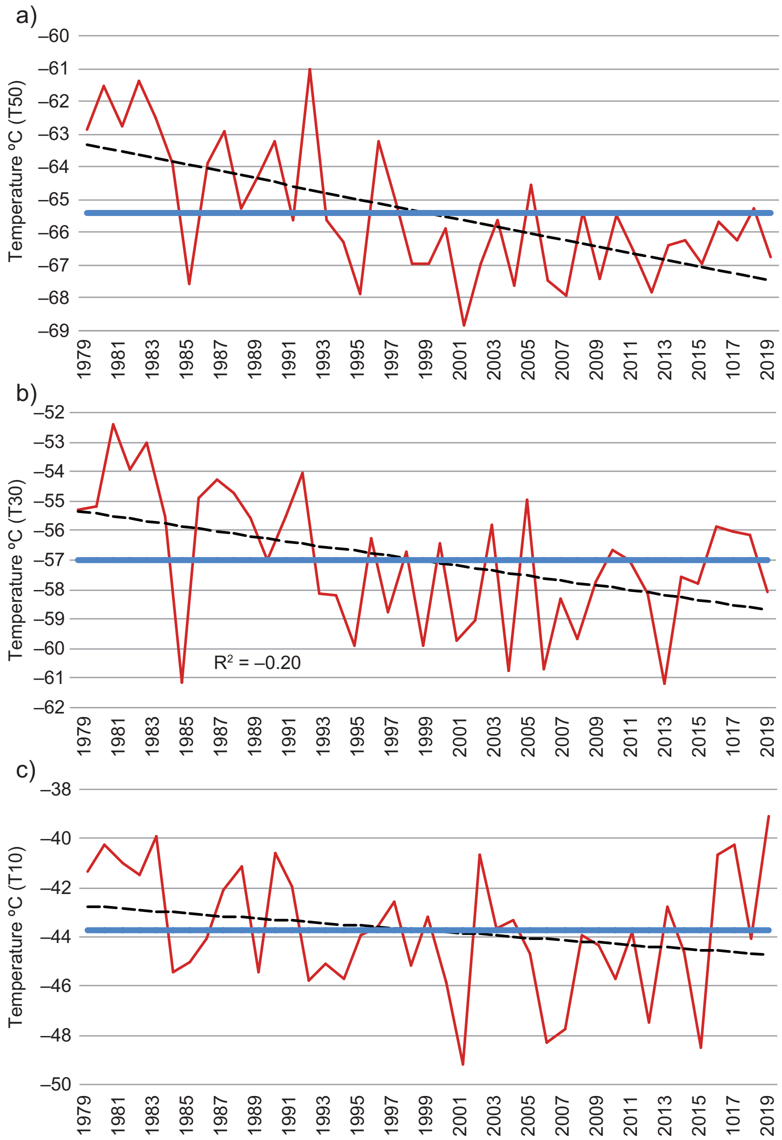

Fig. 2. Time series of stratospheric temperature at: (a) 50 hPa (T50), (b) 30 hPa (T30), (c) 10 hPa (T10) during winter in the period 1979-2019. The blue solid line represents the mean value for the entire period. Trends (black dotted line) are displayed for the entire period.

current study. A strong positive relationship (99% significance level) between the stratospheric winter temperature time series over Saudi Arabia and time series over the Northern Hemisphere (tropical, subtropical, and mid-latitude regions) in lower, middle and upper levels are evident in Table I. However, a weak relationship between the temperature time series in the lower, middle and upper stratosphere over Saudi Arabia and the polar region is observed. Salby and Callaghan (2003) showed the inverse relationship between stratospheric temperatures at high and low latitudes and affirmed that it was accompanied by a similar reversal trend in ozone (WMO, 1999, 2006). Such behavior of the subtropical and mid-latitude lower stratospheric temperature time series is the same as that over the tropics (Randel et al., 2009).

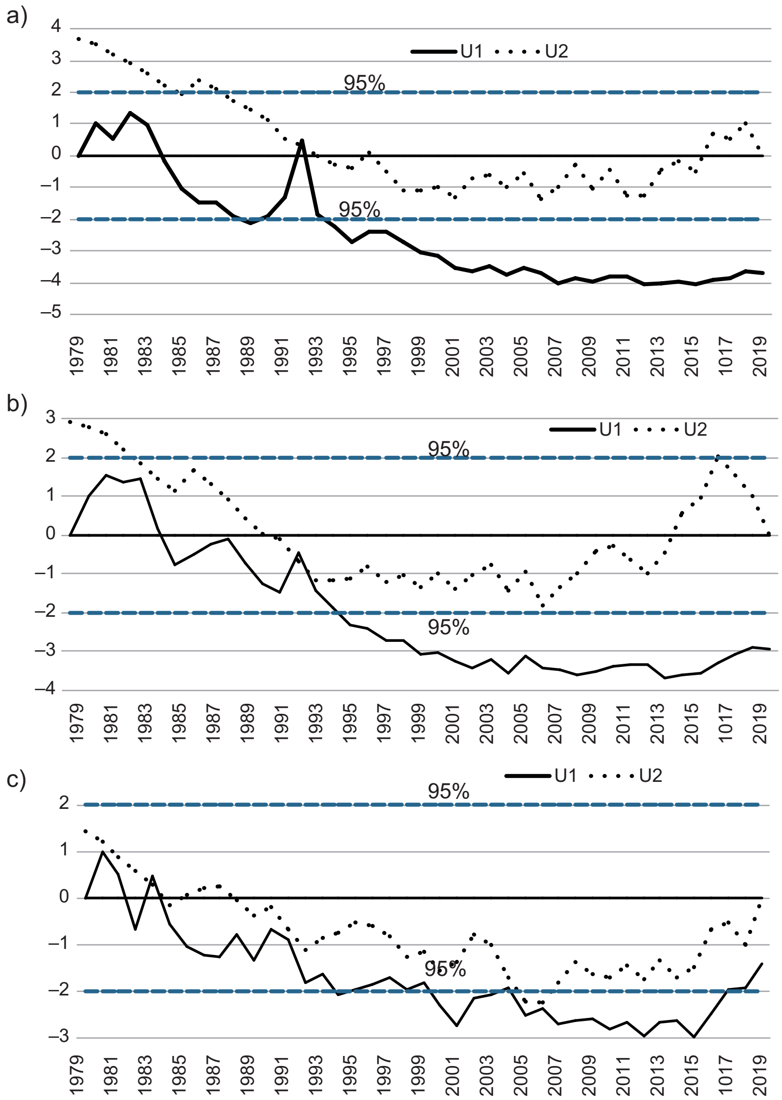

Fig. 3. Abrupt changes in temperature time series for (a) lower stratosphere (T50); (b) mid-stratosphere (T30); and (c) upper stratosphere (T10), as derived from the sequential version of the Mann Kendall test. U1: forward sequential statistic; U2: backward sequential statistic.

3.2 Teleconnection between stratospheric temperature and sea surface temperature

Table II shows the correlation between all SST indices. All SST indices over the Atlantic Ocean are related to each other with the exception of the TSA regarding the TNA, AMO, and AMM. A strong positive association is observed between SST indices over the Atlantic Ocean. Although the areas of TNA and NTA are different, the results of the relationships between each index and other parameters are nearly the same. Additionally, the results of the relationship of NTA and AMM with other parameters are approximately the same. So, it is reasonable to use only the TNA, TSA and AMO indices (Fig. 1).

The relationships between stratospheric temperatures (T50, T30, and T10) and SST indices over the Atlantic Ocean TNA, TSA, and AMO are given in Table III and also shown in Figures 4-6. In general, a negative correlation between the SST over the Atlantic Ocean and stratospheric temperatures

Table I. Correlation coefficient (CC) between stratospheric temperature over Saudi Arabia and over the Northern Hemisphere (tropical [0º-25ºN], subtropical [25ºN-40ºN], mid-latitude [40ºN-60ºN], and Polar [60ºN-90ºN] regions) at T50, T30, and T10 during winter for the entire period (1950-2019.

CC	Northern Hemisphere (0º-90º)	Tropical (0º-25º N)	Subtropical (25º-40º N)	Mid-latitude (40º-60º N)	Polar (60º-90º N)
Saudi Arabia T50	0.84* (T50)	0.79* (T50)	0.92* (T50)	0.75* (T50)	−0.16(T50)
Saudi Arabia T30	0.68* (T30)	0.61* (T30)	0.96* (T30)	0.86* (T30)	−0.13(T30)
Saudi Arabia T10	0.61* (T10)	0.81* (T10)	0.89* (T10)	0.62* (T10)	0.23(T10)

*99% significance level.

Table II. Relationship between sea surface temperatures indices (SSTs) over the Atlantic Ocean.

CC	TNA	TSA	AMO	AMM	NTA
TNA	1				
TSA	0.24	1			
AMO	0.84	0.42	1		
AMM	0.83	−0.12	0.71	1	
NTA	0.99	0.28	0.85	0.82	1

Table III. Correlation coefficient (CC) between stratospheric temperature over Saudi Arabia (T50, T30, and T10) and SSTs indices over the Atlantic Ocean for the entire period (1979-2019).

CC	T50	T30	T10
TNA	−0.17	−0.12	0.08
TSA	−0.36*	−0.10	−0.02
AMO	−0.41**	−0.32*	−0.03

*95% significance level; **99% significance level.

in the three levels (entire period: 1979- 2019) is found. A strong negative relationship (r = −0.41; 99% confidence level) exists between lower stratospheric temperature (T50) and the AMO index for the entire period (Fig. 4c). Moreover, a statistically significant negative relationship (r = −0.36) at the 99% confidence level between T50 and TSA (Fig. 4b) is evident. There is an insignificant negative relationship between T50 and the TNA (r = −0.17; Fig. 4a). Regarding the correlations among mid-stratospheric temperature, T30, and SST indices over the Atlantic Ocean, we found only a significant relationship between T30 and AMO (r = −0.32; 95% confidence level [Fig. 5C]), whereas an insignificant negative relationships between T30 and the TNA and TSA indices (Fig. 5a, b) was present. However, there is no relationship between upper stratospheric temperature (T10), with SSTs of the Atlantic Ocean (TNA, TSA, and AMO [Fig. 6a-c]).

Regarding the results of our lead-lag cross-correlation analysis, a strong negative relationship between SSTs indices at three lead and stratospheric temperatures (Table IV) is present. A strong negative association between the T50 and TSA index at zero lead-lag is present. Additionally, only T30 is related to the TSA SST index at a one winter lead, which reveals a statistically negative relationship (95% confidence level). Moreover, there is a strong negative relationship between T30 and the TNA and AMO index over at least three winters (95% confidence level). There are three lead cross-correlations between the T10 and the SST indices over the Atlantic Ocean. For instance, a good negative association between T10 and the TNA (−0.40), TSA (−0.32), and AMO SST (−0.40) indices at a three winters lead is observed. A strong negative relationship between T50 and each of TNA (−0.63) and AMO SSTs (−0.62) with a 99% confidence level is also present.

From the above results, it is found that over the entire study period, the temperature in the lower, mid- and upper stratosphere is connected at three leads with TNA and AMO SST indices over the Atlantic Ocean. Therefore, the increase in SST over the Atlantic Ocean may lead to a decrease in the stratospheric temperature over Saudi Arabia. In addition, the temperature in the lower and mid-stratosphere is associated with the SSTs of the TSA index at zero lead-lag and one lag respectively.

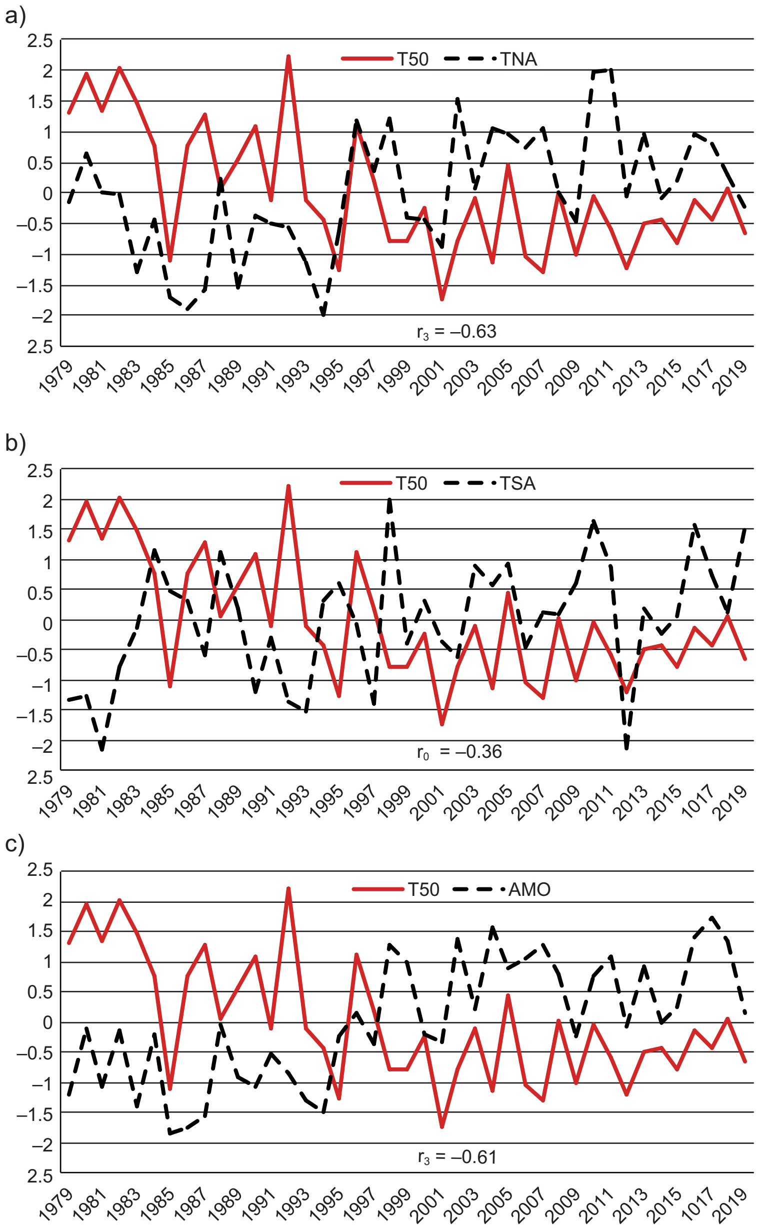

Fig. 4. Time evolution of standardized anomalies of the lower stratospheric temperature at 50 hPa (T50). (a) tropical North Atlantic (TNA), (b) tropical South Atlantic (TSA), and (c) Atlantic Multi-decadal Oscillation (AMO). r_o is a correlation between two patterns at zero lag and $r_{max=3}$ is the maximum correlation at three lead.

3.3 Teleconnection between the surface and stratospheric temperatures

We also examined the teleconnection of Saudi Arabia's winter time T10, T30, and T50 stratospheric temperature and SAT records with the estimation of correlation coefficients (see Fig. 7). Correlation coefficient calculations are performed between the winter SAT and T50, T30, and T10. Negative relationships ($r = -0.32$ and -0.35; 95% confidence level) between the Saudi Arabian winter SAT and the T50 and T30 time series are observed. A weak association between T10 and SAT ($r = -0.10$) over Saudi Arabia is found. The

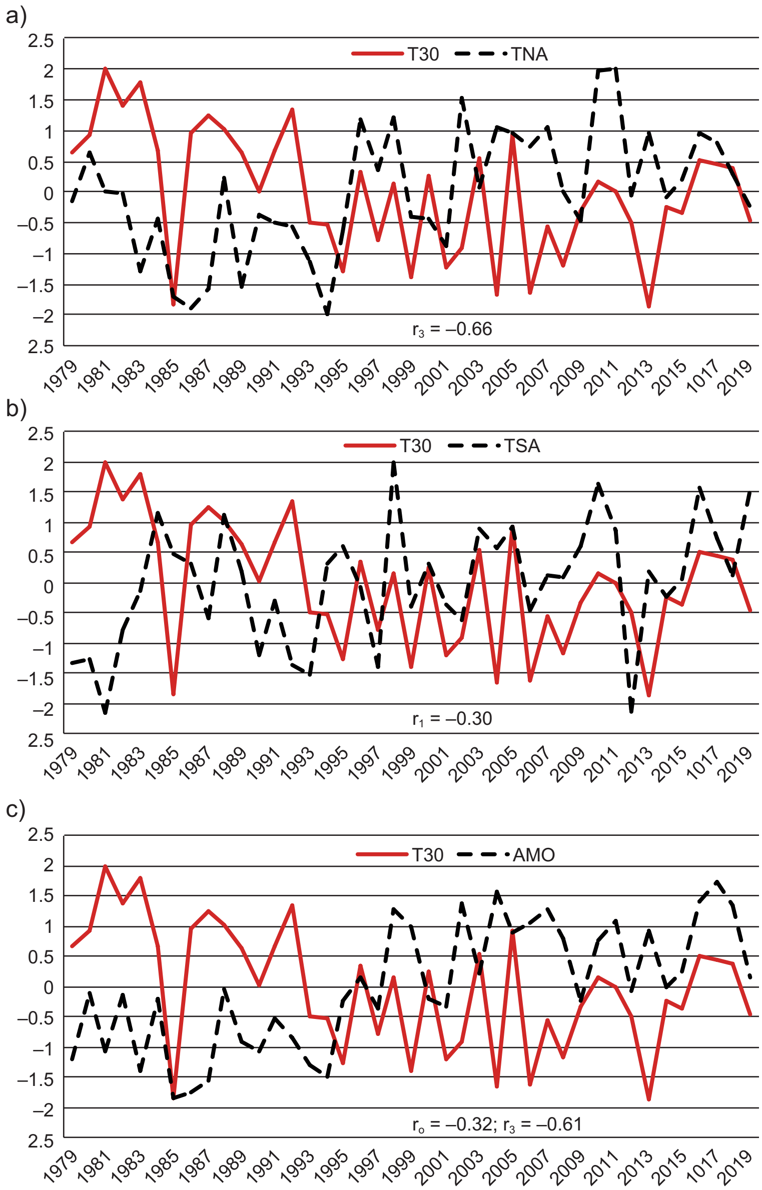

Fig. 5. As Figure 4 but for middle stratospheric temperature at 30 hPa (T30).

maximum correlations of STA with T50 and T30 are found at a zero lag (r = −0.32 and r = −35, respectively; statistically significant at the 99% confidence level). The maximum correlation between the STA and T10 (r = −0.10) is observed with a lead of four seasons. This result proposes that the SAT in the Saudi region is linked to lower and mid-stratospheric temperatures.

Since 1979, the global average temperature at the surface has been warmer than that in the troposphere, while the troposphere is warmer than the stratosphere (Hurrell et al., 2000; Pielke et al., 1998a, b; Stendel et al., 2000). A variety of observations confirm that the rate of SST warming in the tropics since 1979 has been higher than the warming observed in the atmosphere (Gaffen et al., 2000; Christy et al., 2001). According to global observations, the SAT started to warm from the late 1950s, while cooling of the stratosphere has contin-

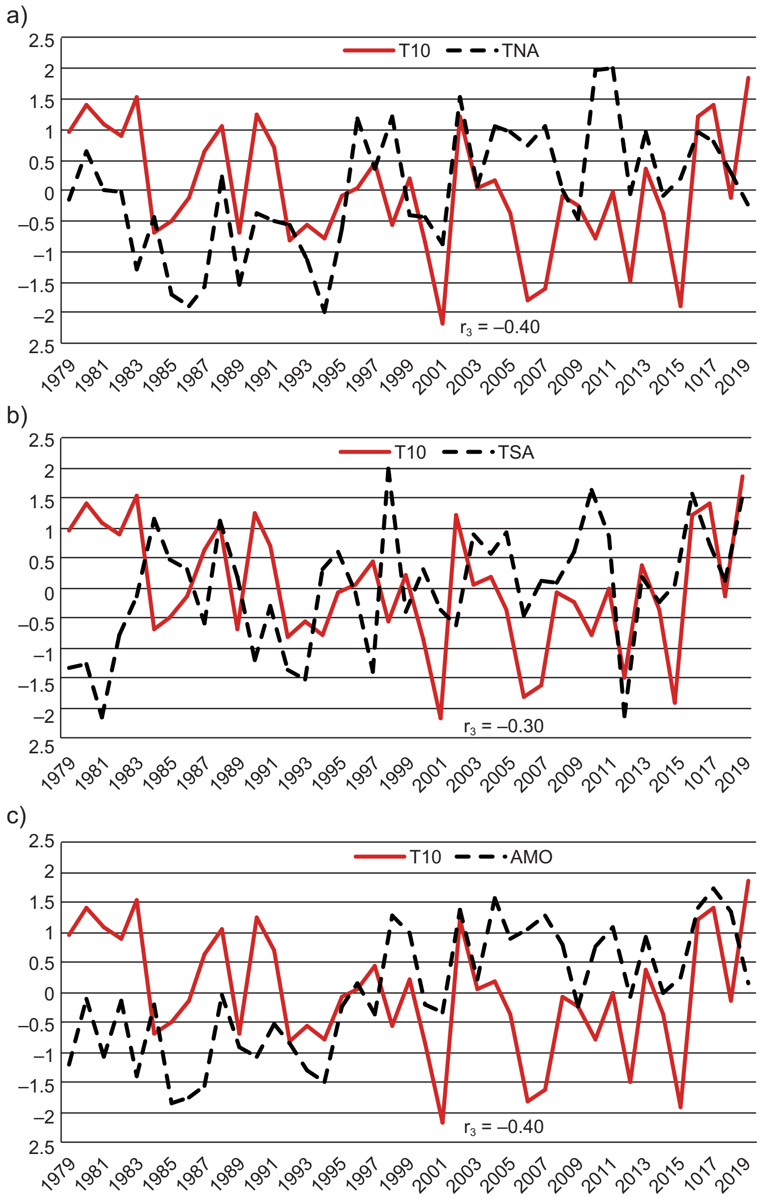

Fig. 6. As Figure 4 but for upper stratospheric temperature at 10 hPa (T10).

Table IV. Maximum lead-lag cross correlation between sea surface temperatures (SSTs) indices over the Atlantic Ocean and stratospheric temperature (ST).

T50-SST	Lag/Lead	Correlation	T30-SST	Lag/Lead	Correlation	T10-SST	Lag/Lead	Correlation
T50-TNA	+3	−0.63	T30-TNA	+3	−0.66	T10-TNA	+3	−0.40
T50-TSA	0	−0.36	T30-TSA	1	−0.30	T10-TSA	+3	−0.30
T50-AMO	+3	−0.62	T30-AMO	+3	−0.61	T10-AMO	+3	−0.40

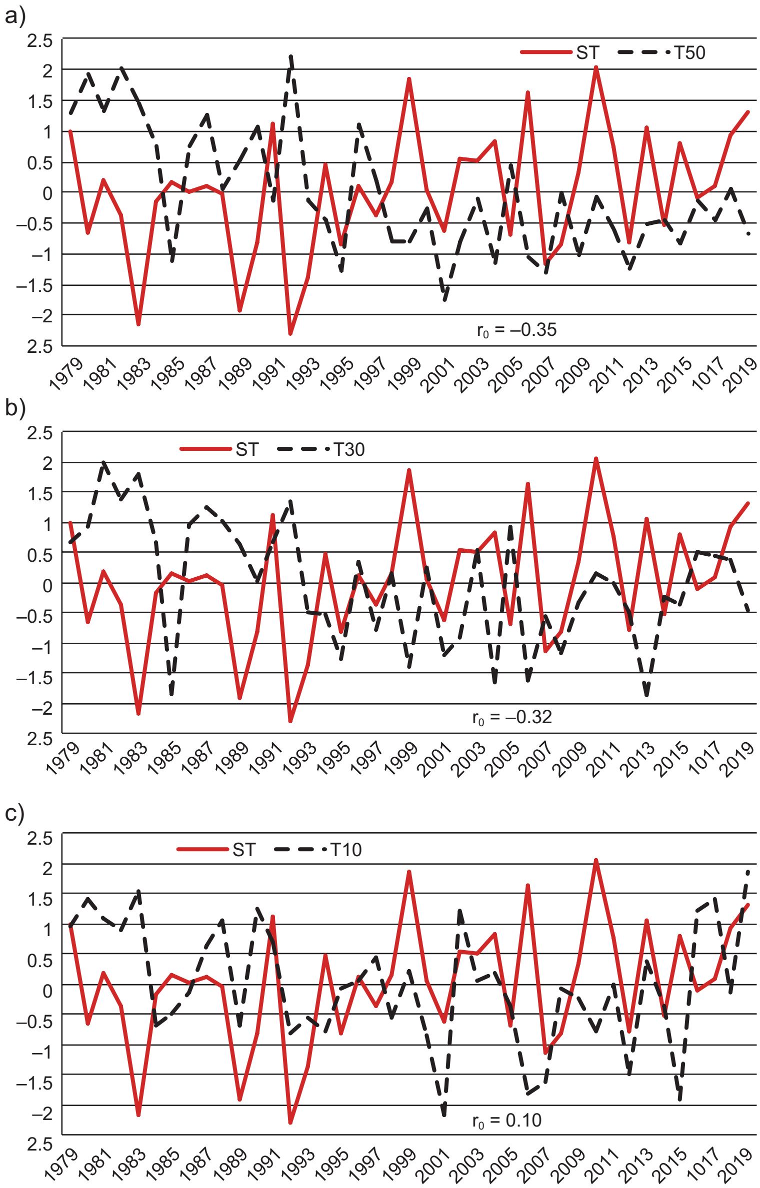

Fig. 7. Relationship between SAT and (a) T50, (b) T30, and (c) T10 over Saudi Arabia in winter during the period 1950-2019.

ued since 1979 (IPCC, 2007). This is attributed to the crucial role of greenhouse gases in cooling the stratosphere and warming the troposphere (Karl et al., 2006; Ramaswamy et al., 2006; IPCC, 2007). A strong positive and negative relationship exists between the SSTs of the equatorial Pacific and the temperature of the lower tropical stratosphere (Reid et al., 1989). Troposphere-stratosphere concurrences characterized by this association exist at all timescales, from weekly variability (Kolstadet al., 2010) to long-term climate change (Sigmond et al., 2008; Scaife et al., 2012; Polvani et al., 2011; Karpechko and Manzini, 2012).

4. Summary and conclusions

Analysis of the stratospheric temperatures in the lower (T50), mid- (T30) and upper (T10) layers provides further insight into the characteristics of stratospheric temperatures. The linear trend of T50 in the winter over Saudi Arabia shows a significant decreasing trend (substantial cooling) for the entire period (1979-2019). Slight cooling in the mid- and upper stratospheric temperature (T30 and T10) is observed for the entire period. Additionally, standard deviation results show a relatively high variability, which means that variability in stratospheric temperatures is greater. Using the Mann-Kendall test, the non-linear trend shows a significant cooling for T50 and T30 but an insignificant cooling for T10. Additionally, from the correlations with stratospheric temperatures in the three layers, a good similarity between T50 and T30 is found, but the similarity is weak when T50 and T30 are compared with T10.

To determine the underlying forces of stratospheric temperature variation, stratospheric temperatures in Saudi Arabia are associated with time series of stratospheric winter temperatures over the Northern Hemisphere (tropical, subtropical, mid-latitude, and polar regions). A strong positive connection between time series of stratospheric winter temperature over Saudi Arabia and the tropical, subtropical, and mid-latitude regions of the Northern Hemisphere were found at the three levels. However, a very weak negative association between stratospheric temperature in wintertime series in the lower, mid-, and upper stratosphere over Saudi Arabia and polar regions was observed. At lower stratospheric temperatures, similar behaviors in tropical, subtropical, and mid-latitude regions are observed (Randel et al., 2009); moreover, the opposite association of stratospheric temperatures between high and low latitudes is found (Salby and Callaghan, 2003; WMO, 1999, 2006).

Regarding teleconnections between SSTs over the Atlantic Ocean (TNA, TSA, and AMO) and stratospheric temperatures over Saudi Arabia, it is concluded that there is an association between them. Generally, a negative correlation between SSTs over the Atlantic Ocean and stratospheric temperatures over Saudi Arabia is found. Notably, a strong negative relationship between SSTs over the TSA and AMO SSTs of the Atlantic Ocean and T50 is observed for the entire study period, while the relationship between TNA and T50 is absent. A statistically negative relationship between the mid-stratospheric temperature T30 and the AMO index exists for the entire period. Moreover, a very weak relationship between T30 and TNA and TSA SSTs indices is observed. In addition, the relationships between T10 and the SSTs of the Atlantic Ocean are absent.

To discover the physical mechanisms that contribute to Saudi Arabian stratospheric temperatures, the lead-lag cross-correlation method was used. Notably, SSTs indices of the Atlantic Ocean are linked with lower, mid- and upper stratospheric temperatures. Moreover, the TSA SST index is linked with the lower stratospheric temperature (T50) at a zero lag and mid-stratosphere (T30) is linked at one lead. Also, T50 and T30 are linked with TNA and AMO SST indices after three winter seasons. Additionally, T10 is linked with SSTs indices of the Atlantic Ocean after three winter seasons.

Two ways to clarify the effects of SSTs on stratospheric temperatures are:

1. SSTs are linked to greenhouse gases that warm the troposphere and cool the stratosphere (e.g, Cubasch et al., 2001; IPCC, 2007; Rind et al., 2008; Sigmond et al., 2008; Omrani et al., 2014).
2. SSTs influence the vertical propagation of tropospheric waves that extend to the stratosphere (Reichler et al., 2012; Hu et al., 2014; Kidston et al., 2015; Zhang et al., 2019). A reverse procedure can occur where air current movement in the stratosphere spreads down to impact the tropospheric circulation.

By inspecting the association between SAT and the stratospheric temperatures at the three levels (lower [T50], middle [T30], and upper [T10]) over Saudi Arabia, a coupling between them in winter is observed. Correlation analysis is used to determine the teleconnection between stratosphere and troposphere. There is good coupling of SAT with T50 and T30, but the coupling is weak between SAT and T10. Stratosphere-troposphere coupling is associated with changes in surface weather and is mainly observed in winter and early spring (Mohanakumar, 2008; Gerber and Polvani, 2009; Domeisen, 2012; Kunz and Greatbatch, 2013).

Acknowledgments
This project received funding from the Deanship of Scientific Research (DSR), King Abdulaziz Uni-

versity, Jeddah, under grant No. D-198-155-1439. The authors give their sincere acknowledgment and gratitude to the DSR for their utmost support, both technically and financially.

References

Aquila V, Swartz WH, Waugh DW, Colarco PR, Pawson S, Polvani LM, Stolarski RS. 2016. Isolating the roles of different forcing agents in global stratospheric temperature changes using model integrations with incrementally added single forcings. Journal of Geophysical Research-Atmospheres 121: 8067-8082. https://doi.org/10.1002/2015JD023841

Almazroui M, Islam M, Athar H, Jones PD, Rahman MA. 2012. Recent climate change in the Arabian Peninsula: Annual rainfall and temperature analysis of Saudi Arabia for 1978-2009. International Journal of Climatology 32: 953-966. https://doi.org/10.1002/joc.3446

Angell JK. 1997. Stratospheric warming due to Agung, El Chichón, and Pinatubo taking into account the quasi-biennial oscillation. Journal of Geophysical Research 102: 9479-9485. https://doi.org/10.1029/96JD03588

Baldwin MP, Dunkerton TJ. 1999. Propagation of the Arctic Oscillation from the stratosphere to the troposphere. Journal of Geophysical Research 104: 30937-30946. https://doi.org/10.1029/1999JD900445

Baldwin MP, Thompson DWJ, Shuckburgh EF, Norton WA, Gillett NP. 2003. Weather from the stratosphere? Science 301: 317-319. https://doi.org/10.1126/science.1085688

Berrisford P, Dee DP, Poli P, Brugge R, Fielding M, Fuentes M, Kållberg PW, Kobayashi S, Uppala S, Simmons, A. 2011. The ERA-Interim archive Version 2.0. Report of ECMWF. Shinfield Park, Reading, UK. Available at: https://www.ecmwf.int/node/8174

Black RX. 2002. Stratospheric forcing of surface climate in the Arctic oscillation. Journal of Climate 15: 268-277. https://doi.org/10.1175/1520-0442(2002)015<0268:S-FOSCI>2.0.CO;2

Brown SJ, Parker DE, Folland CK, Macadam I. 2000. Decadal variability in the lower-tropospheric lapse rate. Geophysical Research Letters 27: 997-1000. https://doi.org/10.1029/1999GL011174

Calvo N, García RR, Randel WJ, Marsh DR. 2010. Dynamical mechanism for the increase in tropical upwelling in the lowermost tropical stratosphere during warm ENSO events. Journal of Atmospheric Science 67: 2331-2340. https://doi.org/10.1175/2010JAS3433.1

Camp CD, Tung K-K. 2007. The influence of the solar cycle and QBO on the late-winter stratosphere polar vortex. Journal of Atmospheric Science 64: 1267-1283. https://doi.org/10.1175/JAS3883.1

Chen B, Xu X, Bian J. 2010. Sources, pathways and timescales for the troposphere to stratosphere transport over Asian Monsoon regions in boreal summer. Chinese Journal of Atmospheric Sciences 34: 495-505. https://doi.org/10.3878/j.issn.1006-9895.2010.03.03.

Christy JR, Parker DE, Brown SJ, Macadam I, Stendel M, Norris WB. 2001. Differential trends in tropical sea surface and atmospheric temperatures. Geophysical Research Letters 28: 183-186. https://doi.org/10.1029/2000GL011167

Cubasch U, Meehl GA, Boer G J, Stouffer RJ, Dix M, Noda A, Senior CA, Raper S, Yap KS. 2001. Projections of future climate change. In: Climate Change 2001: The Scientific Basis: Contribution of Working Group I to the Third Assessment Report of the Intergovernmental Panel on Climate Change (Houghton JT, Ding Y, Griggs DJ, Noguer M, van der Linden PJ, Dai X, Maskell K, Johnson CA, Eds.). Cambridge University Press, Cambridge, United Kingdom and New York, NY, USA, 525-582

Domeisen DI. 2012. Stratosphere-troposphere interaction during stratospheric sudden warming events. Department of Earth, Atmospheric, and Planetary Sciences, . http://hdl.handle.net/1721.1/78368

Domeisen DI, Garfinkel CI, Butler AH. 2019. The tele-connection of El Niño Southern Oscillation to the stratosphere. Reviews of Geophysics 57: 5-47. https://doi.org/10.1029/2018RG000596

Enfield DB, Mestas-Núñez AM, Mayer DA, Cid-Serrano L. 1999. How ubiquitous is the dipole relationship in tropical Atlantic sea surface temperatures? Journal of Geophysical Research: Oceans 104: 7841-7848. https://doi.org/10.1029/1998JC900109

Feng J, Li JP, Xie F. 2013. Long-term variation of the principal mode of boreal spring Hadley circulation linked to SST over the Indo-Pacific warm pool. Journal of Climate 26: 532-544. https://doi.org/10.1175/JCLI-D-12-00066.1

Gaffen DJ, Santer BD, Boyle JS, Christy JR, Graham NE, Ross RJ. 2000. Multidecadal changes in the vertical structure of the tropical troposphere. Science 287: 1242-1245. https://doi.org/10.1126/science.287.5456.1242

Gastineau G, Frankignoul C. 2015. Influence of the North Atlantic SST variability on the atmospheric circulation during the twentieth century. Journal of Climate 28: 1396-1416. https://doi.org/10.1175/JCLI-D-14-00424.1

Gerber EP, Polvani LM. 2009. Stratosphere-troposphere coupling in a relatively simple AGCM: The importance of stratospheric variability. Journal of Climate 22: 1920-1933. https://doi.org/10.1175/2008JCLI2548.1

Goossens C, Berger A. 1986. Annual and seasonal climatic variations over the northern hemisphere and Europe during the last century. Annales Geophysicae 4: 385-400. http://hdl.handle.net/2078.1/66385

Hasanean HM. 2004. Variability of the North Atlantic subtropical high and associations with tropical sea surface temperature. International Journal of Climatology 24: 945-957. https://doi.org/10.1002/joc.1042

Hasanean HM, Abdulhaleem H. Labban. 2019. Study of the lower stratospheric temperature over the Arabian Peninsula. Climate 7: (54). https://doi.org/10.3390/cli7040054

Hurrell JW, Brown SJ, Trenberth KE, Christy JR. 2000. Comparison of tropospheric temperatures from radiosondes and satellites: 1979-1998. Bulletin of the American Meteorological Society 81: 2165-2177. https://doi.org/10.3103/S1068373917020030

Hu D, Tian W, Xie F, Shu J, Dhomse S. 2014. Effects of meridional sea surface temperature changes on stratospheric temperature and circulation. Advance of Atmospheric Science 31: 888-900. https://doi.org/10.1007/s00376-013-3152-6

Huth R. 1999. Testing of trends in data unevenly distributed in time. Theoretical of Applied Climatology 64:151-162. https://doi.org/10.1007/s007040050119

IPCC. 2001. Climate Change 2001: The Scientific Basis. Contribution of Working Group I to the Third Assessment Report of the Intergovernmental Panel on Climate Change (Houghton JT, Ding Y, Griggs DJ, Noguer M, van der Linden PJ, Dai X, Maskell K, Johnson CA, Eds.). Cambridge University Press, Cambridge, United Kingdom and New York, NY, USA, 881pp.

IPCC. 2007. Climate Change 2007: The Physical Science Basis. Contribution of Working Group I to the Fourth Assessment Report of the Intergovernmental Panel on Climate Change (Solomon S, Qin D, Manning M, Chen Z, Marquis M, Averyt KB, Tignor M, Miller HL, Eds.). Cambridge University Press, Cambridge, United Kingdom and New York, NY, USA, 996 pp.

Kalnay E, Kanamitsu M, Kistler R, Collins W, Deaven D, Gandin L, Iredell M, Saha S, White G, Woollen J, Zhu Y, Chelliah M, Ebisuzaki W, Higgins W, Janowiak J, Mo KC, Ropelewski C, Wang J, Leetmaa A, Reynolds R, Roy J, Dennis J. 1966. The NCEP/NCAR 40-year reanalysis project. Bulletin of the American Meteorological Society 77: 437-471. https://doi.org/10.1175/1520-0477(1996)077<0437:TNYRP>2.0.CO;2

Karl TR, Hassol SJ, Miller CD, Murray WL, Eds. 2006. Temperature trends in the lower atmosphere: Steps for understanding and reconciling differences. A report by the Climate Change Science Program and the Subcommittee on Global Change Research, Washington, DC, 164 pp.

Karpechko AY, Manzini E. 2012. Stratospheric influence on tropospheric climate change in the Northern Hemisphere. Journal of Geophysical Research 117: D05133. https://doi.org/10.1029/2011JD017036

Keenlyside NS, Bader J, Mecking J, Omrani NO, Latif M, Zhang R, Msadek R. 2015. North Atlantic multi-decadal variability—Mechanisms and predictability. In: Climate change: Multidecadal and beyond (Chang P, Ghill M, Latif M, Wallace JM, Eds.). World Scientific, 141-157.

Kidston J, Scaife AA, Hardiman SC, Mitchell DM, Butchart N, Baldwin MP, Gray LJ. 2015. Stratospheric influence on tropospheric jet streams, storm tracks and surface weather. Nature Geoscience 8: 433-440. https://doi.org/10.1038/ngeo2424

Kistler R, Kalnay E, Collins W, Saha S, White G, Woollen J, Chelliah M, Ebisuzaki W, Kanamitsu M, Kousky V, van den Dool H, Jenne R, Fiorino M. 2001. The NCEP-NCAR 50-year reanalysis: Monthly means CD-ROM and documentation. Bulletin of the American Meteorological Society 82: 247-268. https://doi.org/10.1175/1520-0477(2001)082<0247:TNNYRM>2.3.CO;2

Kodera K, Yamazaki K, Chiba M, and Shibata K. 1990. Downward propagation of upper stratospheric mean zonal wind perturbation to the troposphere. Journal of the Meteorological Society of Japan 9: 1263-1266. https://doi.org/10.1029/GL017i009p01263

Kolstad EW, Breiteig T, Scaife AA. 2010. The association between stratospheric weak polar vortex events and cold air outbreaks in the Northern Hemisphere. Quarterly Journal of the Royal Meteorological Society 136: 886-893. https://doi.org/10.1002/qj.620

Koutroulis AG, Grillakis M, Tsanis IK, Kotroni V, Lagouvardos K. 2012. Lightning activity, rainfall and flash flooding—Occasional or interrelated events? A case study in the island of Crete. Natural Hazards and Earth System Science 12: 881-889. https://doi.org/10.5194/nhess-12-881-2012

Kunz T, Greatbatch RJ. 2013. On the Northern Annular Mode surface signal associated with stratospheric variability. Journal of Atmospheric Science 70: 2103-2118. https://doi.org/10.1175/JAS-D-12-0158.1

Labitzke K, McCormick MP. 1992. Stratospheric temperature increases due to Pinatubo aerosols. Geophysical Research Letters 19: 207-210. https://doi.org/10.1029/91GL02940

Liebmann B, Dole R, Jones C, Bladé I, Allured D. 2010. Influence of choice of time period on global surface temperature trend estimates. Bulletin of the American Meteorological Society 91: 1485-1492. https://doi.org/10.1175/2010BAMS3030.1

Manzini E, Giorgetta MA, Esch M, Kornblueh L, Roeckner E. 2006. The influence of sea surface temperatures on the Northern winter stratosphere: ensemble simulations with the MAECHAM5 model. Journal of Climate 19: 3863-3881. https://doi.org/10.1175/JCLI3826.1

Manzini E. 2009. Atmospheric science ENSO and the stratosphere. Nature Geoscience 2: 749-750. https://doi.org/10.1038/ngeo677

Maycock AC, Randel WJ, Steiner AK, Karpechko AY, Christy J, Saunders R, Thompson DW, Zou CZ, Chrysanthou A, Luke AN, Akiyoshi H. 2018. Revisiting the mystery of recent stratospheric temperature trends. Geophysical Research Letters 45: 9919-9933. https://doi.org/10.1029/2018GL078035

Mitchell JM, Dzerdzeevskii B, Flohn H, Hofmery WL. 1966. Climatic change: Report of a working group of the Commission for Climatology. Technical Note 79. World Meteorological Organization, Geneva, 79 pp.

Mohanakumar K. 2008. Stratosphere troposphere interactions: An introduction. Springer, 416 pp.Nigam S. 2003. Teleconnections. In: Encyclopedia of atmospheric science, vol. 3. 2nd ed. Academic Press, Elsevier Science, 90-109.

Olsen MA, Schoeberl MR, Nielsen JE. 2007. Response of stratospheric circulation and stratosphere-troposphere exchange to changing sea surface temperatures. Journal of Geophysical Research 112. https://doi.org/10.1029/2006JD008012

Omrani NE, Keenlyside NS, Bader J, Manzini E. 2014. Stratosphere key for wintertime atmospheric response to warm Atlantic decadal conditions. Climate Dynamics 42: 649-663. https://doi.org/10.1007/s00382-013-1860-3

Omrani NE, Bader J, Keenlyside NS, Manzini E. 2016. Troposphere-stratosphere response to large scale North Atlantic Ocean variability in an atmosphere/ocean coupled model. Climate Dynamics 46:1397-1415. https://doi.org/10.1007/s00382-015-2654-6

Pawson S, Labitzke K, Leder S. 1998. Stepwise changes in stratospheric temperature. Geophysical Research Letters 25: 2157-2160. https://doi.org/10.1029/98GL51534

Pielke RA, Eastman J, Chase TN, Knaff J, Kittel TGF. 1998a. Errata to 1973-1996 trends in depth-averaged tropospheric temperature. Journal of Geophysical Research 103: 16927-16933. https://doi.org/10.1029/1998JD200023

Pielke RA, Eastman J, Chase TN, Knaff J, Kittel TGF. 1998b. 1973-1996 trends in depth-averaged tropospheric temperature. Journal of Geophysical Research 103: 28909-28912. https://doi.org/10.1029/98JD01645

Polvani LM, Waugh DW, Correa GJP, So S-W. 2011. Stratospheric ozone depletion: The main driver of twentieth-century atmospheric circulation changes in the southern hemisphere. Journal of Climate 24: 795-812. https://doi.org/10.1175/2010JCLI3772.1

Ramaswamy VML, Chanin J, Angell J, Barnett D, Gaffen M, Gelman P, Keckhut,Y, Koshelkov K, Labitzke JJR, Lin A, O'Neill J, Nash W, Randel R, Rood K, Shiotani M, Swinbank R. 2001. Stratospheric temperature trends: Observations and model simulations. Reviews of Geophysics 39: 71-122. https://doi.org/10.1029/1999RG000065

Ramaswamy V, Schwarzkopf MD, Randel WJ, Santer BD, Soden BJ, Stenchikov GL. 2006. Anthropogenic and natural influences in the evolution of lower stratospheric cooling. Science 311: 1138-1141. https://doi.org/10.1126/science.1122587

Randel WJ, SK, Austin J, Barnett J, Claud C, Gillett NP, Keckhut P, Langematz U, Lin R, Long C, Mears C, Miller A, Nash J, Seidel DJ, Thompson DWJ, Wu F, Yoden S. 2009. An update of observed stratospheric temperature trends. Journal of Geophysical Research 114. https://doi.org/10.1029/2008JD010421

Reichler T, Kim J, Manzini E, Kröger J. 2012. A stratospheric connection to Atlantic climate variability. Nature Geoscience 5: 783-787. https://doi.org/10.1038/ngeo1586.

Reid GC, Gage KS, McAfee JR. 1989. The thermal response of the tropical atmosphere to variations in equatorial Pacific sea surface temperature. Journal of Geophysical Research 94: 14705-14716. https://doi.org/10.1029/JD094iD12p14705

Rind D, Lean J, Lerner J, Lonergan P, Lebois-Sitier A. 2008. Exploring the stratospheric/tropospheric response to solar forcing. Journal of Geophysical Research 113. https://doi.org/10.1029/2008JD010114

Salby ML, Callaghan PF. 2003. Systematic changes of stratospheric temperature: Relationship between the tropics and extratropics. Journal of Geophysical Research 108. https://doi.org/10.1029/2001JD-002034Santer BD. 2003. Contributions of anthropogenic and natural forcing to recent tropopause height changes. Science 301: 479-483. https://doi.org/10.1126/science.1084123

Sassi F, Kinnison D, Boville BA, Garcia RR, Roble R. 2004. Effect of El Niño-Southern Oscillation on the dynamical, thermal, and chemical structure of the middle atmosphere. Journal of Geophysical Research 109. https://doi.org/10.1029/2003JD004434

Scaife AA, Knight J, Vallis GK, Folland CK. 2005. A stratospheric influence on the winter NAO and North Atlantic surface climate. Geophysical Research Letters 32: 1-5. https://doi.org/10.1029/2005GL023226

Scaife AA, Spangehi T, Cubasch U, Langematz U, Akiyoshi H, Bekki S, Butchart N, Chipperfield MP, Gettelman A, Hardiman SC, Michou M, Rozanov E, Shepherd TG. 2012. Climate change projections and stratosphere-troposphere interaction. Climate Dynamics 38: 2089-2097. https://doi.org/10.1007/s00382-011-1080-7

Schonwiese CD, Rapp J. 1997. Climate trend Atlas of Europe based on observations 1891-1990. Kluwer Dordrecht, The Netherlands.

Seager R, Harnik N, Kushnir Y, Robinson W, Miller J. 2003. Mechanisms of hemispherically symmetric climate variability. Journal of Climate 16: 2960-2978. https://doi.org/10.1175/1520-0442(2003)016<2960:MOHSCV>2.0.CO;2

Self S, Zhao J, Holasek RE, Torres RC, King AJ. 1998. The atmospheric impact of the 1991 Mount Pinatubo eruption. In: Fire and mud: Eruptions and lahars of Mount Pinatubo (Newhall GC, Punongbayan RS, Eds.). Philippine Institute of Volcanology and Seismology/University of Washington Press, Quezon City/Seattle and London, 1089-1115.Shine KP, Bourqui MS, PM de F Forster, Hare SHE, Langematz U, Braesicke P, Grewe V, Ponater M, Schnadt C, Smith CA, Haigh JD, Austin J, Butchart N, Shindell DT, Randel WJ, Nagashima T, Portmann RW, Solomon S, Seidel DJ, Lanzante J, Klein S, Ramaswamy V, Schwarzkopf MD. 2003. A comparison of model-simulated trends in stratospheric temperatures. Quarterly Journal of the Royal Meteorological Society 129: 1565-1588. https://doi.org/10.1256/qj.02.186

Sigmond M, Scinocca JF, Kushner PJ. 2008. Impact of the stratosphere on tropospheric climate change. Geophysical Research Letters 35. https://doi.org/10.1029/2008GL033573

Sigmond M, Scinocca JF. 2010. The influence of the basic state on the northern hemisphere circulation response to climate change. Journal of Climate 23: 1434-1446. https://doi.org/10.1175/2009JCLI3167.1

Sneyers R. 1990. On the statistical analysis of series of observations. Technical note 143. World Meteorological Organization, Geneva, 192 pp.

Soden BJ, Wetherald R, Stenchikov GL, Robock A. 2002. Global cooling after the eruption of Mount Pinatubo: A test of climate feedback by water vapor. Science 296: 727-730. https://doi:10.1126/science.296.5568.727

Solomon S. 1999. Stratospheric ozone depletion: A review of concepts and history. Reviews of Geophysics 37: 275-316. https://doi.org/10.1029/1999RG900008

Stendel M, Christy JR, Bengtsson L. 2000. Assessing levels of uncertainty in recent temperature time series. Climate Dynamics 16: 587-601. https://doi.org/10.1007/s003820000064

Thompson DWJ, Baldwin MP, Wallace JM. 2002. Stratospheric connection to Northern Hemisphere wintertime weather: Implications for prediction. Journal of Climate 15: 1421-1428. https://doi.org/10.1175/1520-0442(2002)015<1421:SCTNHW>2.0.CO;2

Wilks DS. 2006. Statistical methods in the atmospheric Sciences. Academic Press, New York.

WMO 1999. Scientific assessment of ozone depletion: 1998. Global Ozone Research and Monitoring Project report No. 44. World Meteorological Organization, Geneva, 558 pp.

WMO. 2006. Scientific assessment of ozone depletion: 2006. Global Ozone Research and Monitoring Project report No. 50. World Meteorological Organization, Geneva, 560 pp.

Xie F, Tian W, Austin J, Li J, Tian H, Shu J, Chen C. 2011. The effect of ENSO activity on lower stratospheric water vapor. Atmospheric Chemistry and Physics Discussions 11: 4141-4166. https://doi.org/10.5194/acpd-11-4141-2011Xie F, Li J, Tian W, Feng J, Huo Y. 2012. Signals of El Niñno Modoki in the tropical tropopause layer and stratosphere. Atmospheric Chemistry and Physics Discussions 12: 5259-5273. https://doi.org/10.5194/acp-12-5259-2012

Young RE, Houben H, Toon OB. 1994. Radiatively forced dispersion of the Mt. Pinatubo volcanic cloud and induced temperature perturbations in the stratosphere during the first few months following the eruption. Geophysical Research Letters 21: 369-372. https://doi.org/10.1029/93GL03302

Zhang R, Sutton R, Danabasoglu G, Kwon YO, Marsh R, Yeager SG, Amrhein DE, Little CM. 2019. A review of the role of the Atlantic Meridional Overturning Circulation in Atlantic Multidecadal Variability and associated climate impacts. Reviews of Geophysics 57: 316-375. https://doi.org/10.1029/2019RG000644

Zossi de Artigas M, Fernández de Campra P. 2011. Stratospheric temperature trends between 10 and 70 hPa during the period 1948-2009. The Open Atmospheric Science Journal 5: 16-22. https://doi.org/10.2174/1874282301105010016

Atmósfera 35(4), 651-672 (2022)
https://doi.org/10.20937/ATM.52977

CONTENTS

Evaluation of the WRF-ARW model during an extreme rainfall event: Subtropical storm Guará

Yasmin Kaore LAGO KITAGAWA[1,4], Erick Giovani SPERANDIO NASCIMENTO[2], Noéle Bissoli PERINI DE SOUZA[1], Pedro JUNIOR ZUCATELLI[1], Prashant KUMAR[4], Taciana Toledo DE ALMEIDA ALBUQUERQUE[1,3], Marcelo ROMEIRO DE MORAES[5] and Davidson MARTINS MOREIRA[1,2]*

[1]*Universidade Federal do Espírito Santo (UFES), Vitória, Espírito Santo, Brazil.*
[2]*Centro Integrado de Manufatura e Tecnologia (SENAI CIMATEC), Salvador, Bahia, Brazil.*
[3]*Universidade Federal de Minas Gerais (UFMG), Belo Horizonte, Minas Gerais, Brazil.*
[4]*Global Centre for Clean Air Research (GCARE), Department of Civil and Environmental Engineering, Faculty of Engineering and Physical Sciences, University of Surrey, Guildford GU2 7XH, United Kingdom.*
[5]*Universidade Federal do Pampa (UNIPAMPA), Bagé, Rio Grande do Sul, Brazil.*
*Corresponding author; email: davidson.moreira@fieb.org.br

Received: September 11, 2020; accepted: March 24, 2021

RESUMEN

El presente estudio simula un evento inusual de lluvia extrema ocurrido en la ciudad de Salvador, Bahía, Brasil, el 9 de diciembre de 2017, que se denominó tormenta subtropical Guará y tuvo una precipitación de aproximadamente 24 mm en menos de 1 h. Se realizaron simulaciones numéricas utilizando el modelo Weather Research and Forecasting (WRF) en tres dominios con resoluciones horizontales de 9, 3 y 1 km. Se evaluaron diferentes combinaciones de siete esquemas de microfísica, tres cumulus y tres capas límites planetarias en función de su capacidad para simular la precipitación horaria durante este evento de lluvia. Los índices estadísticos (MB = –0.69; RMSE = 4.11; MAGE = 1.74; r = 0.55; IOA = 0.66, y FAC2 = 0.58) y los gráficos de series temporales mostraron que las configuraciones más adecuadas para este evento meteorológico fueron las de Mellor-Yamada-Janjić, Grell-Freitas y Lin para los esquemas de capa límite planetaria, cumulus y microfísica, respectivamente. Los resultados se compararon con los datos medidos en las estaciones meteorológicas ubicadas en la ciudad de Salvador. El modelo WRF simuló bien la llegada y ocurrencia de este evento climático extremo en una región tropical y costera, considerando que la región ya tiene características convectivas intensas y está constantemente influenciada por brisas marinas, las cuales podrían interferir con los resultados del modelo y comprometer el desempeño de las simulaciones.

ABSTRACT

This study simulates an unusual extreme rainfall event that occurred in Salvador city, Bahia, Brazil, on December 9, 2017, which was named subtropical storm Guará and had precipitation of approximately 24 mm within less than 1 h. Numerical simulations were conducted using the Weather Research and Forecasting (WRF) model over three domains with horizontal resolutions of 9, 3, and 1 km. Different combinations of seven microphysics, three cumulus, and three planetary boundary layer schemes were evaluated based on their ability to simulate the hourly precipitation during this rainfall event. Statistical indices (MB = –0.69; RMSE = 4.11; MAGE = 1.74; r = 0.55; IOA = 0.66; FAC2 = 0.58) and time series plots showed that the most suitable configurations for this weather event were the Mellor-Yamada-Janjić, Grell-Freitas, and Lin formulations for the planetary boundary layer, cumulus, and microphysics schemes, respectively. The results were compared with the data measured at meteorological stations located in Salvador city. The WRF model simulated well the arrival and occurrence of this extreme weather event in a tropical and coastal region, considering that the region already has intense convective characteristics and is constantly influenced by sea breezes, which could interfere in the model results and compromise the performance of the simulations.

Keywords: atmospheric modeling, WRF model, extreme rainfall, northeastern Brazil, physical parameterization.

1. Introduction

Northeastern Brazil experiences a semiarid climatic regime, and over 80% of the area often decrees a state of public emergency due to extreme drought. However, most of the population lives along the coast, where the rainfall regime can occur intensely or depend on several ocean-atmosphere processes, or a combination of these factors (Kouadio et al., 2012). The occurrence of heavy rain and storms in the region typically causes flash floods, power outages, damage to road structures, and material and human losses; therefore, these extreme weather events are highly disruptive to the urban system and pose a major challenge to the government and society.

Some adaptive measures have been implemented to prevent and mitigate these weather conditions, and convection-permitting models (CPM) have been appropriate to characterize extreme rainfall events. Forecasting centers have successfully improved the precision in representing this severe weather environment using CPM, however, computational costs to implement these models are higher compared to numerical weather prediction (NWP) models that use parameterization schemes to represent convection (Clark et al., 2016; Chan et al., 2018; Woodhams et al., 2018). Even though, accurately representing any extreme weather event with realistic temporal and spatial distribution remains a challenge in NWP studies, particularly over coastal and tropical areas with intense convective characteristics that can change rapidly due to the influences of land-sea breezes and mesoscale systems (Hariprasad et al., 2014; Salvador et al., 2016; Surussavadee, 2017). The Center for Weather Forecasts and Climate Studies of the Brazilian National Institute for Space Research (CPTEC/INPE) provides information regarding weather conditions by employing a modeling domain that covers South America (Chou et al., 2005, 2014; Solman et al., 2013). However, global and hemispheric models cannot represent the local to regional characteristics of the spatiotemporal variability of precipitation; therefore, regional models are preferable for properly representing physical processes. As such, local information could be more valuable to local urban planners for managing more efficient solutions. Doppler Weather Radar (DWR) data are a vital source of information for studying the characteristics of mesoscale systems (Gao et al., 1999; Kim and Lee, 2006, but the lack of adequate observational data has prompted numerous researchers to apply mesoscale numerical models for identifying the mesoscale features and studying the evolution and propagation of extreme rainfall. Furthermore, the present heavy precipitation prediction capabilities are limited due to the uncertainties in the initial state, coarse resolution, and physics parameterization techniques of the model (Bei and Zhang, 2007; Hally et al., 2014).

The mesoscale numerical Weather Research and Forecasting (WRF) model, which is an advanced atmospheric model, allows users to select physics and dynamics settings that can be more suitable for a given region, and has gained wider popularity due to its various applications that aid the performance of numerical experiments, allowing a better understanding of the atmospheric dynamics of some episodes or phenomena such as precipitation, heat and cold events, pollution, wind cycles, and severe storms. However, some physical processes cannot be described by traditional fluid mechanics equations; therefore, several researchers have undertaken the development of a parameterization that can effectively describe the spatial and temporal evolutions of these processes (Chen et al., 1996; Koren et al., 1999; Chen and Dudhia, 2001; Salvador et al., 2016). It is widely agreed that the best model configuration will depend on the studied area and time of the year, and relevant research has been mainly conducted in tropical and mid-high latitudes (Jiménez et al., 2006; Balzarini et al., 2014; Carvalho et al., 2014; Ekström, 2015; Banks et al., 2016; Sharma et al., 2016; Avolio et al., 2017; Powers et al., 2017; Imran et al., 2018; Lian et al., 2018; Tymvios et al., 2018), with few studies conducted in tropical and coastal regions or lower latitudes (Hariprasad et al., 2014; Boadh et al., 2016; Gunwani and Mohan, 2017; Penchah et al., 2017).

Salvador city, the capital of the state of Bahia, Brazil, experiences the highest number of natural disasters associated with intense rain on the coast of the northeast region of the country, and rainfall is mostly concentrated between April and July (Rao et al., 1993). The occurrence of intense rain is very rare outside this period. However, the Guará cyclone/subtropical storm occurred on December 9, 2017, originating from a strong decrease in atmospheric pressure between the coast of southern Bahia and northern Espírito Santo state. The cyclone caused strong winds that devastated several areas of the city, and waves of up to 5 m, according to the Brazilian Navy. Therefore, to analyze this event in the metropolitan region of Salvador (MRS), 63 runs using different combinations of seven microphysics (MP), three cumulus (CU), and three planetary boundary layer (PBL) schemes with a very fine resolution (1 km) were conducted to elucidate the most suitable physical parameterization scheme for this extreme rainfall event over an urban-coastal area. This extreme rainfall event was selected since it can be difficult for the model to depict such abrupt changes in atmospheric behavior (Surussavadee, 2017). Therefore, this case study was conducted to evaluate parameterizations in a coastal region during extreme rainfall by comparing the modeled results with data obtained at meteorological stations. Few studies have evaluated the parameterizations used in the WRF model under extreme rainfall conditions over coastal regions, even though the coastal zone of Brazil extends for over 8500 km.

The remainder of this paper is organized as follows. Section 2 presents the methodology, with a description of the meteorological event, WRF physical parameterization schemes, and statistical indices used in the evaluation of the model performance. Section 3 presents and compares the numerical results to experimental data. Finally, the conclusions are presented in section 4.

2. Methodology

2.1 Description of the observed meteorological event

The MRS, which is an urban-industrial and coastal area formed by 13 cities with a total population of over four million inhabitants, was affected by a subtropical storm, Guará, on December 9, 2017. During this event, 23.6 mm of precipitation were measured within 1 h (between 17:00 and 18:00 LT) at the Brazilian National Institute of Meteorology (INMET) meteorological station located in Salvador (Fig. 1), the largest city and capital of Bahia state. The hottest day of 2017 was also recorded on the same day (34.9 ºC) at INMET and International Airport stations. The high temperatures associated with humidity originating from the Amazon region and ocean intensified the cloudiness, and heavy rain with lightning struck the region. According to the Brazilian Navy Hydrography Center, a frontal system moved from the Atlantic Ocean (east) to the MRS (west), with a minimum atmospheric pressure of 998 hPa and wind speed of 74 km h^{-1} (~ 20 m s^{-1}), which caused strong wind fields and rainfall over the MRS. The South Atlantic Convergence Zone (SACZ) exerts its greatest influence over Brazil during the end of spring and summer, and can extend from the Amazon basin to the subtropical Atlantic Ocean, provoking rainfall over the north, central-west, and southeast regions (Carvalho et al., 2004). During the analyzed episode, the synoptic weather charts indicated the presence of SACZ over 15 consecutive days, and mainly acted over the midwest-southeast and northeast Brazil, where the presence of the SACZ is considered anomalous.

2.2 WRF physical parameterization schemes and modeling setup

Moisture, heat, and momentum exchange within the planetary boundary layer through mixing associated with turbulent eddies that influence the evolution of lower-tropospheric thermodynamic and kinematic structures. However, such eddies operate on spatiotemporal scales that cannot be explicitly represented on the grid scales and time steps employed in most NWP models. Therefore, their effects are expressed through mathematical equations, which are also called physical parameterization schemes (Stensrud, 2007). The conventional parameterizations in the WRF model include the longwave and shortwave

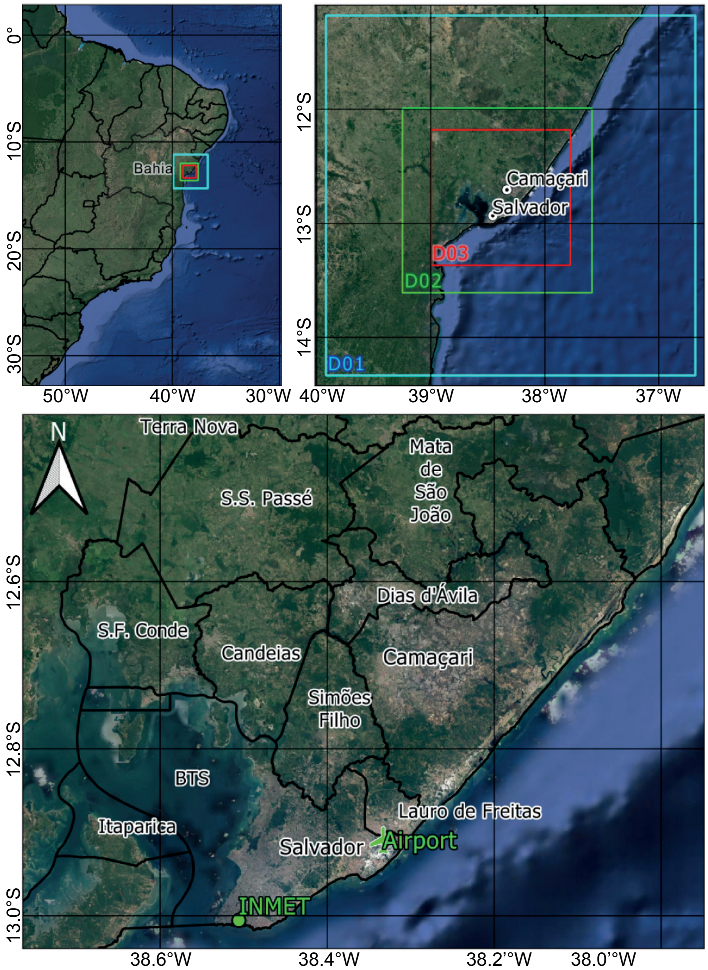

Fig. 1. Location of Bahia State in Brazil (upper left) and the domains used in the simulations (upper right). Meteorological stations in Salvador City (green dots) and the major cities of the MRS. BTS means Bay of All Saints, which is the second largest coastal bay in Brazil.

radiation, PBL, surface layer (SL), cumulus (CU), and microphysics (MP) schemes.

The MP parameterization scheme controls the various types of precipitation processes and humidity by modifying the air temperature based on the interaction between clouds and radiation, and the absorption and latent heat release due to the phase changes of water. The impact of MP schemes on the subtropical storm Guará was examined using seven MP options in the WRF model: Kessler, Lin, WRF single-moment 3 (WSM3), WRF single-moment 5 (WSM5), WRF single-moment 6 (WSM6), Eta and Goddard schemes. They are categorized as bulk schemes, and usually represent the size distributions of particles, referred as hydrometeors species, through gamma distribution functions that use the mixing ratio and/or the number concentration (Li et al., 2008; Comin et al., 2018; Lee and Baik, 2018). Thus, one of the major differences between the MP schemes is related to the number of hydrometeors considered as prognostic variable, namely: water vapor (*v*), cloud droplets (*c*), rainwater (*r*), cloud ice (*i*), snow (*s*), and graupel (*g*). Kessler is a simple warm cloud scheme that considers *v*, *c*, and *r* classes. The others are mixed-phase schemes that evolved from Kessler and are considered more sophisticated because more numbers of hydrometeors are used (Skamarock et al., 2008). However, sophisticated schemes are not synonym of meaningful improvements, that is why it is recommended to perform an evaluation to establish the cost benefit of longer simulations and computational expense due to the use of more sophisticated schemes (Jeworrek et al., 2019).

The CU schemes are responsible for the sub-grid effects of convective and/or shallow clouds as a consequence of larger-scale processes. Thus, these schemes are responsible for the distribution of moisture and heat that influence clouds formation and precipitation prediction. Theoretically, CU schemes are not activated for fine grid sizes, because it is assumed that regional models are able to resolve organized convection. Thus, in the present work, Kain-Fritsch (KF), Betts-Miller-Janjić (BMJ) and Grell-Freitas (GF) schemes were only activated on the coarsest grid (D01) and switched off on the finer grids (D02 and D03). KF and GF are mass flux parameterizations, from which the former has been widely used by operational applications (Zheng et al., 2016). It is based on the early version of KF, that used a relatively simple cloud model (Skamarock et al., 2008). The latter is based on the Grell-Devenyi scheme, and was formulated to be used in high resolution mesoscale models. It was developed through experiments over South America, using the Brazilian version of the Regional Atmospheric Modeling system (BRAMS) (Grell and Freitas, 2014), which could be more realistic for our study. BMJ scheme is an adjustment type scheme that uses reference profiles from a field campaign at the tropical Atlantic Ocean from Africa to South America in 1974, to adjust vertical profile of temperature and humidity (Janjić, 2000).

The PBL parameterization schemes represent the vertical sub-grid scale fluxes, known as eddies, due to turbulence that can be generated by buoyancy or shear throughout the entire grid column, and not just in the boundary layer. The treatment of the moisture, heat, and momentum exchange processes in the PBL by the WRF considers the order of turbulence closure and whether the employed mixing approach is local or non-local. Among the three PBL schemes evaluated in this study, the Yonsei University (YSU) is a first-order non-local scheme that uses information of multiple vertical levels to determine a variable at a given point. The non-local vertical fluxes are reached by adding a non-local gradient adjustment term to the local gradient for any prognostic variables (Hong et al., 2006). The non-local approach has been suggested to be better because they would be able to account the amount of turbulence generated by large vortices, as opposed to the local closure schemes, which only use the variables of vertical levels that are directly adjacent to the given point. To overcome this deficiency, higher orders of treatments have been developed (Mellor and Yamada, 1982), such as the Mellor-Yamada-Janjić (MYJ) scheme, which is one-and-a-half order local closure. The Asymmetric Convective Model 2 (ACM2) considers both approaches depending on the stability conditions, which hypothetical would be an ideal scheme (Kolling et al., 2013). Like YSU, ACM2 has an eddy diffusion component in addition to the explicit nonlocal transport. The SL schemes calculate the friction velocities and exchange coefficients used in the calculation of surface heat and moisture fluxes by the land surface models and surface stress in the PBL schemes. As some PBL schemes are tied to a unique SL scheme, three SL schemes were used in the simulations: Eta to MYJ, MM5 to YSU, and PX to ACM2 (Skamarock et al., 2008).

As the simulations were conducted for an extreme rainfall event, this work considered combinations of different PBL, CU, and MP schemes. The selection of the MP scheme influences the spatial pattern of rainfall, while the selection of the PBL and CU parameterization schemes influences the magnitude of rainfall in the WRF model during extreme rainfall events (Chawla et al., 2018; Singh et al., 2018, Song and Sohn, 2018). The non-local PBL closure schemes simulate heavy rainfall events more correctly close to the sea, while other configurations more accurately predict rainfall in mountainous terrains (Avolio and Federico, 2018). Although no scheme uniformly represents well all atmospheric conditions (Shin et al., 2012), the most suitable physical parameterization ensemble that represents the atmosphere dynamics over a region must be elucidated. Therefore, 63 simulations using different combinations of MP, CU, and PBL schemes were evaluated based on their ability to simulate hourly precipitation during the extreme rainfall event. The physical parameterization schemes were selected based on whether they directly influenced the representation of precipitation production by the model. As no previous studies had assessed the MRS using the WRF model, the most common parameterization schemes found in literature were tested. Furthermore, the study was conducted using version 3.9 of the WRF model with the Advanced Research WRF (ARW) dynamical solver. The meteorological data were obtained from NCEP Final Analysis (FNL) with a grid resolution of 0.25 × 0.25º every 6 h (NCEP, 2015). The MODIS land-use dataset was used, which is the default land-use dataset of the WRF. The simulations were set to run from December 5 to 10, 2017. The model was run with three nested domains and grid resolutions of 9 km (D01), 3 km (D02), and 1 km (D03; see Fig. 1). The domain of interest (D03) had a horizontal resolution of 1 km and 23 vertical levels with the model top set to 50 hPa. An overview of the physical and spatial configuration of WRF is shown in Table I. The references of each option available in the WRF model can be found in its manual and in Skamarock et al. (2008).

2.3 Evaluation of the model performance

The model performance was evaluated by comparing the hourly observed and modeled data. The latter was extracted from the grid point nearest to the latitude and longitude of the ground weather stations in D03, whose locations are displayed in Fig. 1. These were INMET (13.01 ºS, 38.52 ºW, 51.41 m above the ground) and the Airport (12.91 ºS, 38.33 ºW, 19.51 m above the ground). The former is represented by

Table I. Details of the physical parameterization schemes and spatial configuration adopted in the WRF simulations.

Domain	D01	D02	D03
Horizontal resolution	9 km	3 km	1 km
Domain cell numbers	39 × 39 × 23	60 × 60 × 23	132 × 132 × 23
Domain size	11.18º-14.33º S 36.66º-39.92º W 359 × 359 km	11.99º-13.61º S 37.58º-39.25º W 180 × 180 km	12.18º-13.37º S 37.78º-39.00º W 132 × 132 km
Longwave radiation	Dudhia scheme (option 1)		
Shortwave radiation	Rapid Radiative Transfer Model (option 1)		
Land surface scheme	Noah land-surface model (option 1)		
Microphysics (MP)	Kessler (option 1) Lin (option 2) WRF single-moment 3 (WSM3) (option 3) WRF single-moment 5 (WSM5) (option 4) WRF single-moment 6 (WSM6) (option 6) Eta scheme (option 4) Goddard (option 7)		
Cumulus (CU)	Kain-Fritsch (KF) (option 1) Betts-Miller-Janjić (BMJ) (option 2) Grell-Freitas (GF) (option 3)		
Planetary boundary layer (PBL)	Mellor-Yamada-Janjić (MYJ) (option 2) Yonsei University (YSU) (option 1) Asymmetric Convective Model 2 (ACM2) (option 7)		
Surface layer (SL)	Eta similarity (option 2) MM5 (option 1) Pleim-Xiu (PX) (option 7)		

the following observed meteorological parameters: wind speed at 10 m (WS10), wind direction at 10 m (WD10), temperature at 2 m (T2), relative humidity at 2 m (RH2), and precipitation (RAIN).

The following statistical indices recommended by Zhang et al. (2012) and Emery et al. (2001) were computed: mean bias (MB), standard deviation of the modeled data (SD), root-mean-square-error (RMSE), mean absolute gross error (MAGE), correlation coefficient (R), index of agreement (IOA), and the fraction of predictions within a factor of two observations (FAC2). The MB, RMSE, and MAGE are indices related to the errors and deviations of the model. Therefore, high-quality simulations have values closer to zero. R, IOA, and FAC2 are indices of association and agreement between modeled and observed data, with zero indicating an absence of correlation and values closer to 1 indicating a strong correlation. As wind direction is a circular variable, the errors should be calculated considering the shortest angular distance between the modeled and observed data (Jiménez and Dudhia, 2013). Therefore, for wind direction, if the observed or modeled value was greater than 180º, 360 was subtracted.

The indices are presented as Taylor diagrams (Taylor, 2001) and soccer plots in the following section. The different markers and colors represented the 63 simulations. The numbers in the Taylor diagrams represent the combination of the PBL and CU schemes, while the colors represent the different MP schemes, with 01, 02, 03, 04, 05, 06, 07, 08, and 09 indicating MYJ-KF, MYJ-BMJ, MYJ-GF, YSU-KF, YSU-BMJ, YSU-GF, ACM2-KF, ACM2-BMJ, and ACM2-GF, respectively. In addition, the best configuration is identified through a scoring procedure, following Somos-Valenzuela and Manquehual-Cheuque (2020). The configuration with the best score receives a value of 1, adding a unit to the next, while the worst score receives a value of 63. This procedure is repeated for each station and parameter. Finally, the score is summed, and the configuration with the lowest value is the one with the best performance for the variable.

3. Numerical results

The results of the simulations conducted with the WRF model during the passing subtropical storm Guará are presented to elucidate whether the mesoscale model could capture this extreme rainfall event. The performance of the parameterization schemes considering wind speed, wind direction, temperature, relative humidity, and rainfall is first presented, followed by the spatial distribution of the wind fields and precipitation.

3.1 Parameterization schemes performance

3.1.1 Wind speed results

Figure 2 shows the comparison soccer plot for the RMSE and MB statistical metrics of WS10 from the INMET and Airport meteorological stations.

The very low wind speed values registered at the INMET ground station were due to the presence of vegetation and hills surrounding the station. Over built areas, the presence of obstructions slows down the wind speed, and besides the WRF model was formulated for mesoscale systems. To have a better agreement with observed wind speed over built areas, it is suggested to turn on the urban physics schemes that use lower values for land surface parameters (Martilli et al., 2002; Sarmiento et al., 2017). Therefore, by comparing the WRF results with the INMET data (Fig. 2a), the statistical error indices (RMSE and MB) did not agree well, and all runs were overestimated.

Figure 3 shows the WS10 comparison Taylor diagram for the SD (blue line) and R (black line) statistical metrics. The highest positive correlation (R = 0.68) was obtained for the MYJ-KF-Eta configuration (ID 01, pink marker), while the most negative correlation (R = –0.73) was obtained for the MYJ-BMJ-WSM6 ensemble (ID 02, purple marker) for the INMET station. The IOA and FAC2 did not exceed 0.60 and 0.50 for any simulation, as suggested by Emery et al. (2001) and Hanna and Chang (2012), respectively, as these are conservative benchmarks that consider analyses over simple terrains and rural areas.

The best statistical indices for WS10 were related to the Airport station, where the different combination schemes exhibited similar deviations. However, the simulations using the ACM2-PBL scheme (regardless of the type of CU parameterization used) exhibited the smallest deviations for both stations (Fig. 2).

The Taylor diagram (in Fig. 3b) indicates there were significant differences between the results. The simulations using the MYJ-PBL scheme with KF

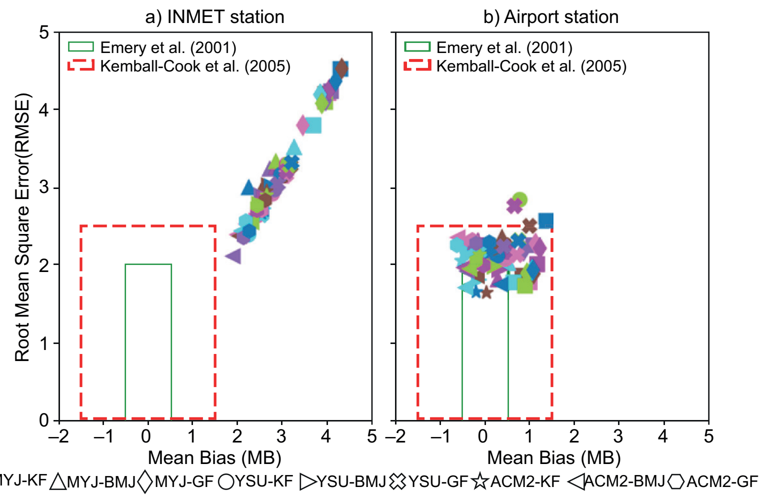

Fig. 2. Comparison soccer plot for the statistical metrics of RMSE and MB for WS10. The green line represents the statistical benchmarks suggested by Emery et al. (2001) for WS10 over simple terrains (MB ≤ ±0.5 m s^{-1} and RMSE ≤ 2 m s^{-1}), while the red line represents the statistical benchmarks suggested by Kemball-Cook et al. (2005) over complex terrains (MB ≤ ± 1.5 m s^{-1} and RMSE ≤ 2.5 m s^{-1}).

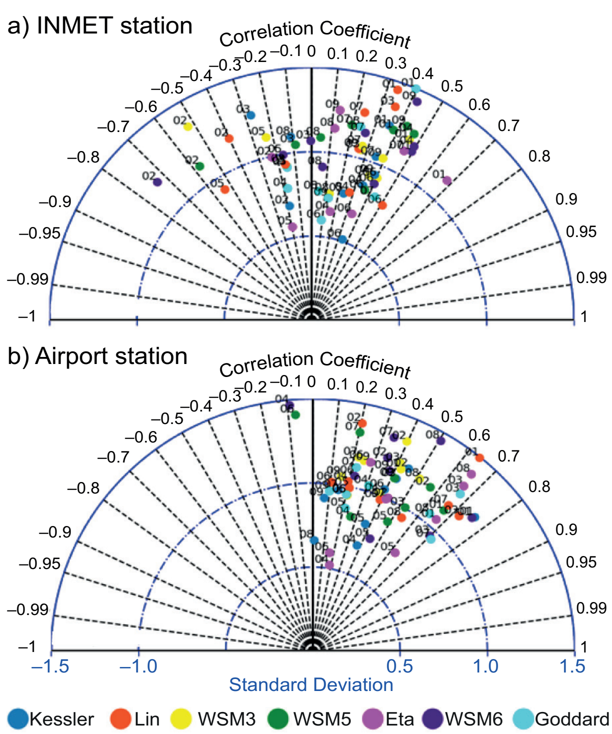

Fig. 3. WS10 comparison Taylor diagram for the SD (blue line) and R (black line) statistical metrics. (a) INMET and (b) Airport stations. The numbers 01, 02, 03, 04, 05, 06, 07, 08, and 09 indicate MYJ-KF, MYJ-BMJ, MYJ-GF, YSU-KF, YSU-BMJ, YSU-GF, ACM2-KF, ACM2-BMJ, and ACM2-GF, respectively

(ID 01) and GD (ID 03) had the highest R values for WS10, with the best scores achieved by the MYJ-KF-Kessler (R = 0.76, IOA = 0.74, FAC2 = 0.75), MYJ-KF-WSM6 (R = 0.75, IOA = 0.75, FAC2 = 0.83) and MYJ-GF-Lin (R = 0.72, IOA = 0.72, FAC2 = 0.71) configurations. Additionally, all simulations using the YSU-PBL scheme, and most simulations with ACM2-PBL scheme did not achieve an IOA value of over 0.60, regardless of the CU and MP schemes.

3.1.2 Wind direction results

Figure 4 shows a comparison soccer plot for the MAGE and MB statistical metrics at the INMET and Airport meteorological stations for WD10. The observed WD10 values were more similar between both stations, with most winds originating from the north, northeast, and northwest directions. According to the WRF results, the majority of simulated wind direction had a positive bias (clockwise) during the period, with a mean error varying between 0º and 20º. The lowest deviations were obtained for the MYJ-GF-Lin configuration for INMET station (brown diamond in Fig. 4a), and MYJ-GF (diamond markers in Fig. 4b), regardless of the MP parameterization used for the Airport station. Emery et al. (2001) indicate that the MB and MAGE of WD10 should be less than ± 10º and 30º, respectively, while Kemball-Cook et

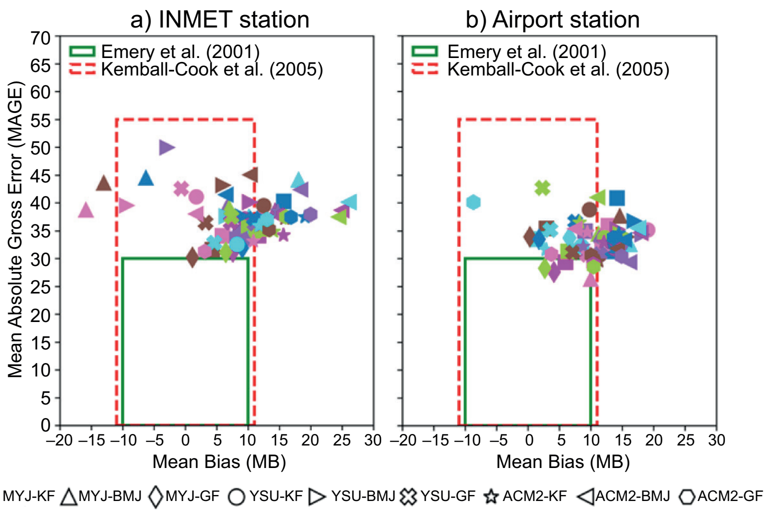

Fig. 4. WD10 comparison soccer plot for the MAGE and MB statistical metrics. The green line represents the statistical benchmarks suggested by Emery et al. (2001) for WD10 over simple terrain (MB ≤ ±10º and MAGE ≤ 30º), and the red line represents the statistical benchmarks suggested by Kemball-Cook et al. (2005) over complex terrain (MAGE ≤ 55º).

al. (2005) stated that MAGE should be below 55º over complex terrains.

The largest amount of FAC2 values greater than 0.5 for INMET station were achieved for the simulations using the GF-CU scheme, even though a single configuration was emphasized for the Airport station. The highest IOA values were associated with MYJ-KF-Lin (IOA = 0.67) for the INMET station, and YSU-GF-Kessler (IOA = 0.70) for the Airport station.

Figure 5 shows the WD10 comparison Taylor diagram for the SD (blue line) and R (black line) statistical metrics at the INMET and Airport meteorological stations.

The R-values were very low as the analysis of this parameter is critical due to the sudden change in wind direction. The highest correlation values were achieved for the MYJ-KF-Lin (ID 01, orange marker; R = 0.48) and ACM2-BMJ-WSM3 (ID 08, yellow marker; R = 0.60) configurations for the INMET (Fig. 5a) and Airport (Fig. 5b) stations, respectively. Both configurations also exhibited reasonable agreement indices (MYJ-KF-Lin: IOA = 0.67, FAC2 = 0.46; ACM2-BMJ-WSM3: IOA = 0.63, FAC2 = 0.42).

3.1.3 Temperature and relative humidity

Figure 6 shows an hourly comparison of T2 between observed and modeled data at the INMET station on

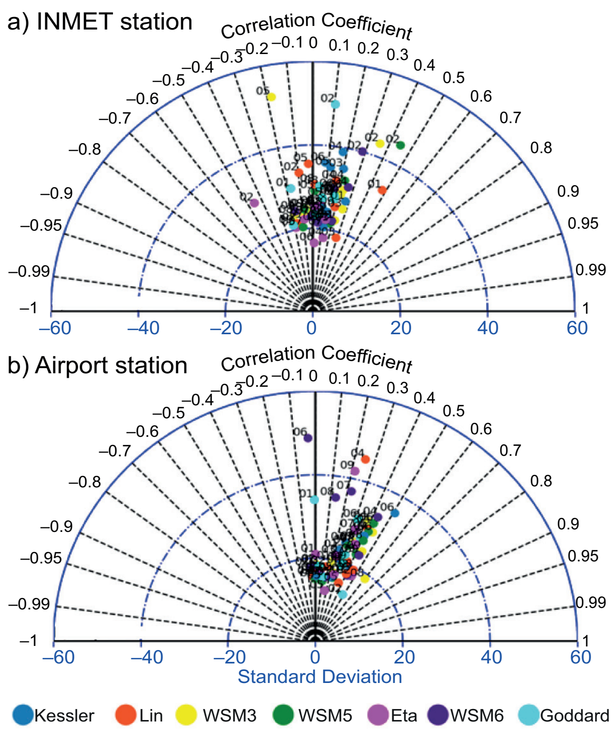

Fig. 5. WD10 comparison Taylor diagram for the SD (blue line) and R (black line) statistical metrics. (a) INMET and (b) Airport stations. The numbers 01, 02, 03, 04, 05, 06, 07, 08, and 09 represent MYJ-KF, MYJ-BMJ, MYJ-GF, YSU-KF, YSU-BMJ, YSU-GF, ACM2-KF, ACM2-BMJ, and ACM2-GF, respectively.

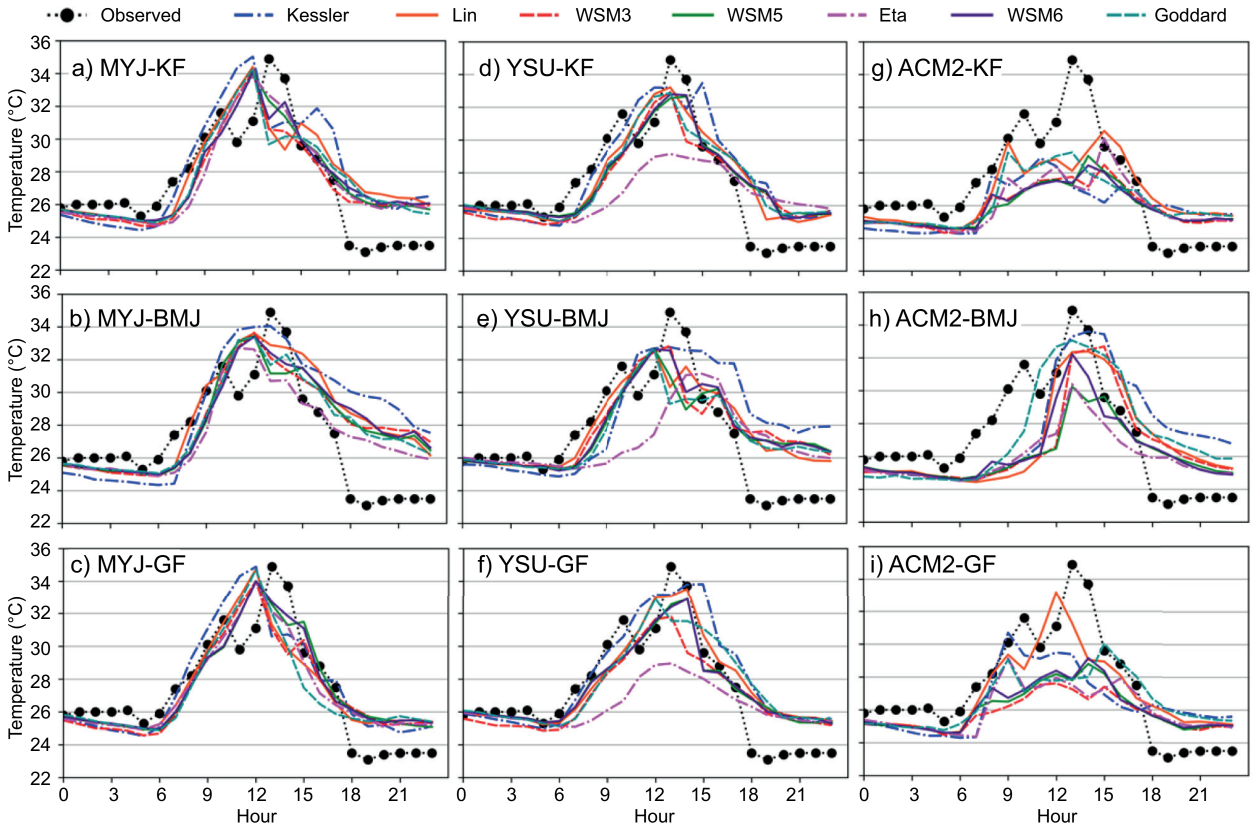

Fig. 6. Time-series of T2 from the INMET data (observed) and numerical simulations of Subtropical Storm Guará over MRS on December 9, 2017, with different MP, PBL, and CU schemes

December 9, 2017, which was the hottest day in 2017 registered in the region, with a thermal amplitude of 11.8 ºC. This great variation could be challenging for the model to emulate, even though most of the simulations could depict this oscillation (Fig. 6).

Statistical indices showed that the mean errors were acceptable, with most of the simulations meeting the criteria suggested by Emery et al. (2001), which are more conservative than those suggested by Kemball-Cook et al. (2005). Additionally, IOA and FAC2 values of ≥ 0.80 and ≥ 0.50 are also recommended, respectively, which were met by most simulations, excluding the BMJ CU and ACM2 PBL schemes. The combination of both schemes (ACM2 + BMJ) achieved the worst R and IOA values for T2. The results of T2 were very uniform for MYJ-PBL and YSU-PBL (except using Eta-MP), which also produced the smallest deviations and highest agreement index values, together with the GF-CU scheme.

Figure 7 shows the T2 comparison Taylor diagram for the SD (blue line) and R (black line) statistical metrics at the INMET and Airport meteorological stations.

The highest correlation values were achieved by the YSU-GF-WSM5 (R = 0.92, IOA = 0.93, FAC2 = 1.00) and MYJ-GF-WSM6 (R = 0.91, IOA = 0.95, FAC2 = 1.00) for the INMET and Airport stations (ID 06-03, purple and green markers in Figs 7a-b). Therefore, the GF-CU scheme with the MP-WSM series is a suitable combination of physical parameterization schemes in the WRF model for studies that mainly aim to evaluate temperature, such as those assessing the urban heat island effects.

Figure 8 shows the RH2 comparison soccer plot and Taylor diagram for the MAGE, MB, SD, and R statistical metrics at the INMET meteorological station.

RH2 data were only available at the INMET station, where the relative humidity varied between 47 and 93%, with an average of 75%. None of the

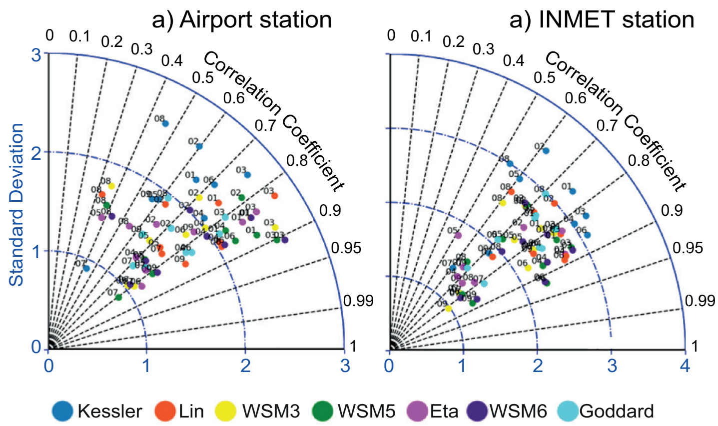

Fig. 7. T2 comparison Taylor diagram for the SD (blue line) and R (black line) statistical metrics. (a) INMET and (b) Airport stations. The numbers 01, 02, 03, 04, 05, 06, 07, 08, and 09 represent MYJ-KF, MYJ-BMJ, MYJ-GF, YSU-KF, YSU-BMJ, YSU-GF, ACM2-KF, ACM2-BMJ, and ACM2-GF, respectively.

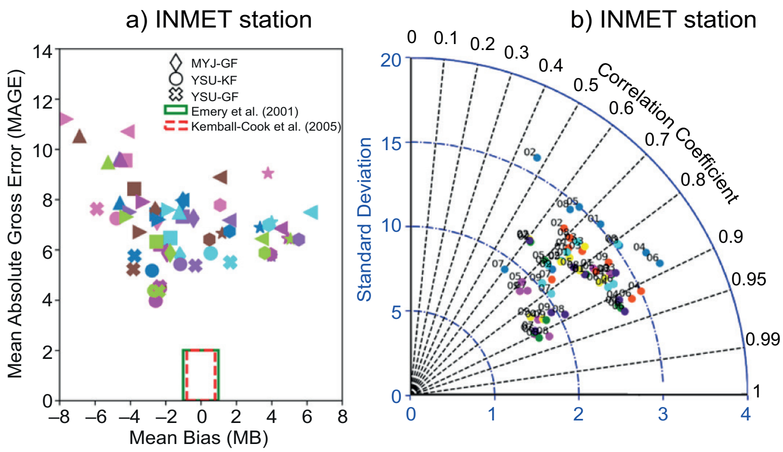

Fig. 8. RH2 comparison soccer plot (a) and Taylor diagram (b) for the MAGE, MB, SD, and R statistical metrics at the INMET station. The green line represents the statistical benchmarks suggested by Emery et al. (2001) for RH2 over simple terrain (MB $\leq \pm 1$ g kg^{-1} and MAGE ≤ 2 g kg^{-1}), and the red line represents the statistical benchmarks suggested by Kemball-Cook et al. (2005) over complex terrain (MB $\leq \pm$ 0.80 g kg^{-1} and MAGE ≤ 2 g kg^{-1}).

simulations met the error benchmarks recommended by Emery et al. (2001) and Kemball-Cook et al. (2005) (Fig. 8a). In contrast, all simulations met FAC2 $\geq$ 0.50 and IOA $\geq$ 0.60. The lowest deviations were achieved by the simulations that used the YSU-PBL scheme with the KF and GF-CU schemes (ID 04-06 with orange [Lin], green [WSM5], and purple [WSM6] markers in Fig. 8b). Therefore, despite the moderate deviations, the values of the agreement indices were high, with the best score achieved by YSU-GF-WSM6 (R = 0.93, IOA = 0.96, FAC2 = 1.00) due to the good results achieved for T2.

Table II shows the configuration of PBL, MP, and CU schemes that were highlighted considering

Table II. Physical parameterization schemes highlighted for each parameter and station using the WRF model.

Parameter	INMET station	Airport station
WS10	ACM2-GF-WSM3	MYJ-KF-WSM6
WD10	MYJ-KF-Lin	MYJ-GF-Goddard
T2	YSU-KF-WSM6	YSU-BMJ-WSM6
RH2	MYJ-GF-Eta	-

the statistical indices for WS10, WD10, T2 and RH2 and each station. The scoring procedure was used for the selection of each configuration. The MYJ-PBL and GF-CU schemes could be reasonable for evaluations related to wind direction and relative humidity, whereas the YSU- PBL and WSM6-MP schemes for temperature.

3.1.4 Rainfall results

In the WRF model, rainfall is based on two variables: RAINC and RAINNC, which are the rainfall produced by cumulus parameterization and grid-scale processes, respectively. Therefore, the total rainfall would be the sum of the variables RAINC and RAINNC. However, as the cumulus parameterization was switched off under D02 and D03, the sole contributor to the total rainfall under these domains was the variable RAINNC. Additionally, the hourly precipitation has to be subtracted from the previous hour because both are cumulative variables.

Figure 9 shows the time-series of RAIN from INMET data (observed) and numerical simulations of subtropical storm Guará over MRS on December 9, 2017 with different MP, PBL, and CU schemes using data from D03 (the domain of interest). The

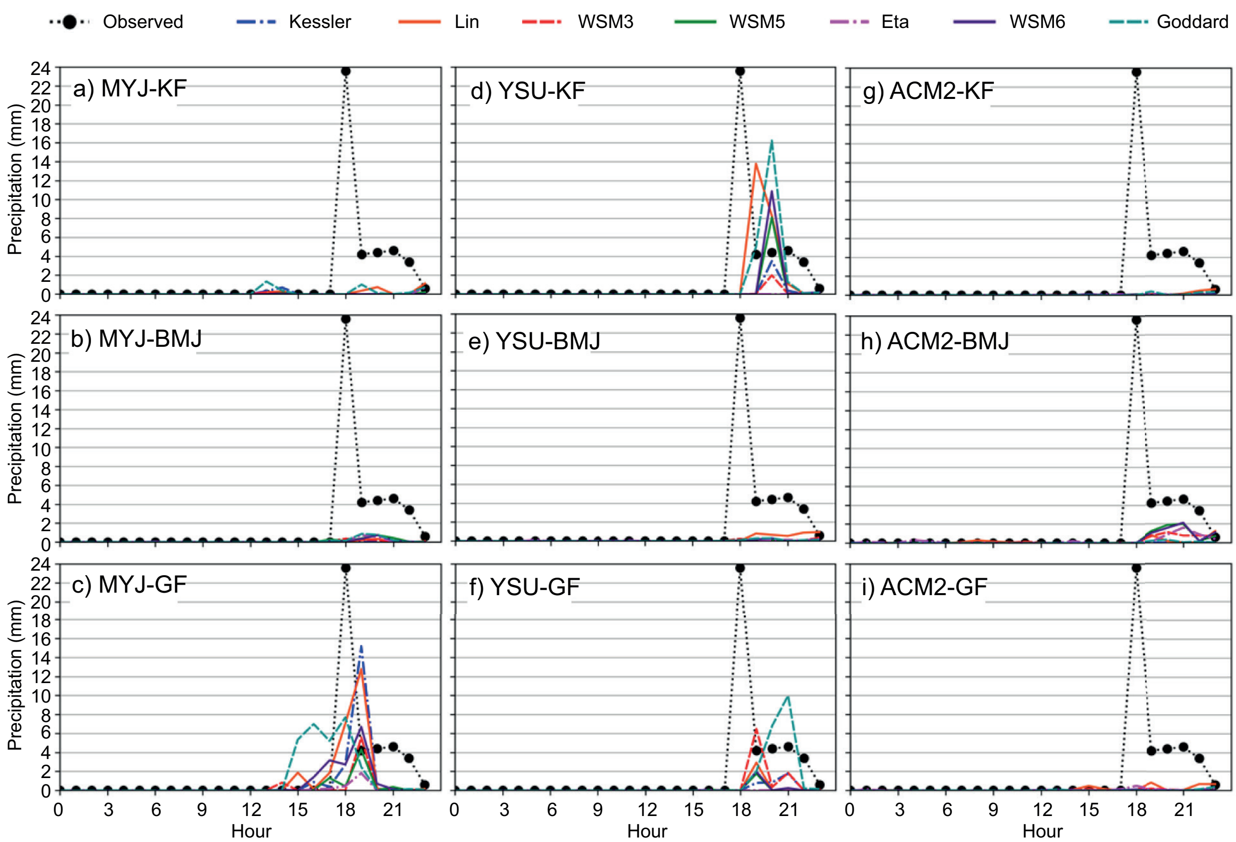

Fig. 9. Time-series of RAIN from the INMET data (observed) and numerical simulations of subtropical storm Guará over MRS on December 9, 2017, with different MP, PBL, and CU schemes.

rain gauge at INMET station registered 23.6 mm of rainfall within 1 h (between 17:00-18:00 LT), and accumulated daily precipitation of 40.80 mm.

The MYJ-GF, YSU-KF, and YSU-GF schemes (depending on the MP scheme adopted) were able to simulate the precipitation peaks with time lags and quantitative errors (Fig. 9c, d, f).

The MYJ-GF-Goddard, with a value of 7.7 mm, and MYJ-GF-Lin, with a value of 7.1 mm, produced reasonable rainfall values at the same time as the storm. However, the MYJ-GF-Goddard configuration reported the occurrence of rainfall 3 h before the event. The other MYJ-GF ensembles (Fig. 9c) depicted the storm with a time lag of 1 h, and their results decreased in the following order MYJ-GF-Kessler (15.2 mm) and MYJ-GF-Lin (12.8 mm), followed by WSM6 (6.7 mm), WSM3 (5.6 mm), WSM5 (4.3 mm), Goddard (2.5 mm) and Eta (1.8 mm).

The YSU-KF case (Fig. 9d) also achieved reasonable results. However, the occurrence of rainfall was simulated to occur an hour after the event. The MP-Lin produced a rainfall value of 13.8 m, and Goddard produced a value of 5 mm at 19 h. YSU-KF-Goddard (16.2 mm), WSM6 (10.9 mm), Lin (8.3 mm), WSM5 (8.1 mm), Kessler (3.5 mm), and WS3 (2 mm) also simulated precipitation values, but with a time lag of 2 h. The MP-Eta configuration did not produce any rainfall. The WSM5 and WSM6 exhibited similar behavior, except for WSM3. The YSU-GF ensembles (Fig. 9f) also exhibited some peaks in the time-series plots; however, the rainfall values were smaller than the results obtained using YSU-KF.

Although all simulations underestimated the observed precipitation value, the smallest errors were achieved by the MYJ-GF and YSU-KF schemes. By analyzing the agreement indices, low IOA values were achieved, with the MYJ-GF-Lin ensemble achieving the highest IOA value of 0.66 (R = 0.55). However, some combinations, such as MYJ-BMJ-WSM3 (R = 0.87) and ACM2-GF-WSM6 (R = 0.84), achieved higher R-values than MYJ-GF-Lin. This was because the simulated precipitation value was zero, which agreed with most of the daily observed data but is not representative, thereby demonstrating the importance of not only considering the statistical metric values but also the time-series assessment.

The GF-CU scheme also showed the best agreement with observations in terms of shape and intensity of the precipitation for finer resolutions in the study of Jeworrek et al. (2019). These authors related it to the maximum threshold of 0.9 for the convective coverage of a grid cell that prevents the scheme from turning itself off entirely. Despite the cumulus parameterization being switched off in D03, its activity can affect the rainfall patterns at a finer resolution (Kwon and Hong, 2017). The BMJ-CU scheme did not depict the occurrence of this subtropical storm (also seen through spatial plots [not shown]). The inability to produce any significant convective precipitation by the BMJ-CU scheme could be caused by the adjustment processes through the reference profiles, that would depend on available moisture in the form of precipitation. The effectiveness of this scheme is limited in regions with little moisture, less rainy or semiarid zones (Gilliland and Rowe, 2007; Sikder and Hossain, 2016). MYJ-KF schemes also presented poor results, according to Jeworrek et al. (2019). The KF-CU scheme had a weaker precipitation feature and was delayed in time.

The WRF results also showed that PBL schemes played a role in the precipitation production because PBL-ACM2 (Fig. 9g-i) also did not depict the occurrence of the rainfall, regardless of the MP and CU schemes used. Various previous studies already pointed out that non-local schemes (e.g., YSU and ACM2) portray phenomena that occur into the PBL more accurately than local schemes (e.g., MYJ and BouLac) because they take into account the effect of larger turbulent eddies (Xie et al., 2012; Cohen et al., 2015). However, it is worth to mention that these studies were not carried out in the same climatological conditions as in our study, where the PBL scheme that presented the best agreement with hourly rainfall (and also with wind direction and relative humidity) was MYJ. This agrees with findings by Madala et al. (2016), who showed that the thermo-dynamical parameters of local-TKE closures were better simulated than non-local closures during thunderstorms over an Indian region. The authors informed that the generation of instability in the model due to the convective process is highly influenced by turbulence diffusions that are efficiently represented by the TKE local closures, leading to a realistic representation of the development of instability of pre-storm atmospheres, and a better simulation of various thunderstorm environments. Similar results can be seen in Wang et al. (2014), who found that local schemes had better agreement with observations than non-local schemes during the East Asian summer monsoon.

Further examination was conducted based on the accumulated daily precipitation, as this work aimed to elucidate the most suitable physical parameterization scheme for characterizing an extreme rainfall event over the urban-coastal area of MRS. Therefore, Figure 10 compares the accumulated daily precipitation of configurations simulated only by MYJ-GF and YSU-KF with all MP schemes. Since none of the other simulations produced any significant precipitation, the results from these simulations will not be discussed further. The analysis reveals that both schemes with MP-Goddard and MP-Lin produced the closest values to the daily observed data, especially MYJ-GF-Goddard (28.07 mm day^{-1}) and MYJ-GF-Lin (24.17 mm day^{-1}).

The best agreement of the MYJ-GF-Goddard configuration to the accumulated daily precipitation is related to the fact that this scheme simulated an anticipated rainfall, which occurs from !4:00 LT, which it is not realistic, since the subtropical storm reached Salvador city at 17:00 LT. Meanwhile, the configuration using YSU-KF was 1-h delayed (Figure 11). Thus, it can be noted that PBL-MYJ, CU-GF and MP-Lin configurations exhibited the most suitable agreement with the observed precipitation data.

3.2 Spatial distribution of wind fields and precipitation

For the WRF model sensitivity analyses, spatial plots of rainfall with wind fields at 10 m were produced to analyze the capture and displacement of subtropical storm Guará over the region. Figure 12 presents the spatial plots of hourly precipitation with wind fields

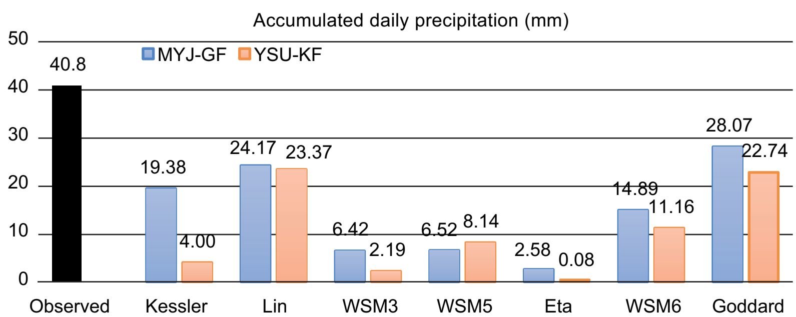

Fig. 10. Comparison of the daily accumulated precipitation on December 9, 2017, at INMET station for MYJ-GF and YSU-KF with all MP schemes.

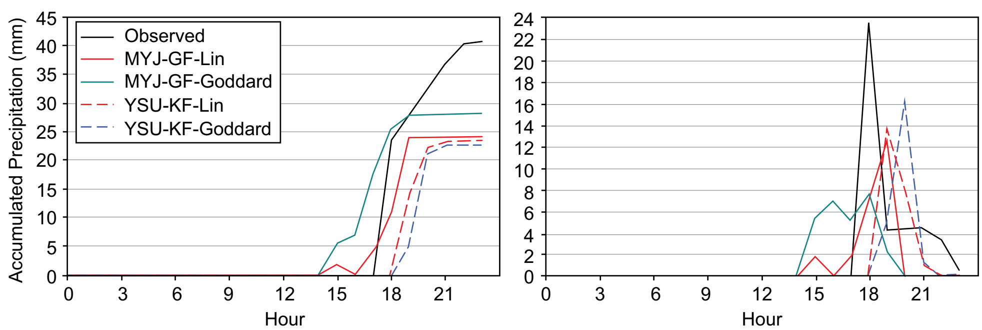

Fig. 11. Comparison of the accumulated (left) and hourly (right) precipitation simulated by the PBL-MYJ and YSU, CU-GF and KF, and MP-Lin and Goddard configurations to observed rainfall on December 9, 2017 at INMET station.

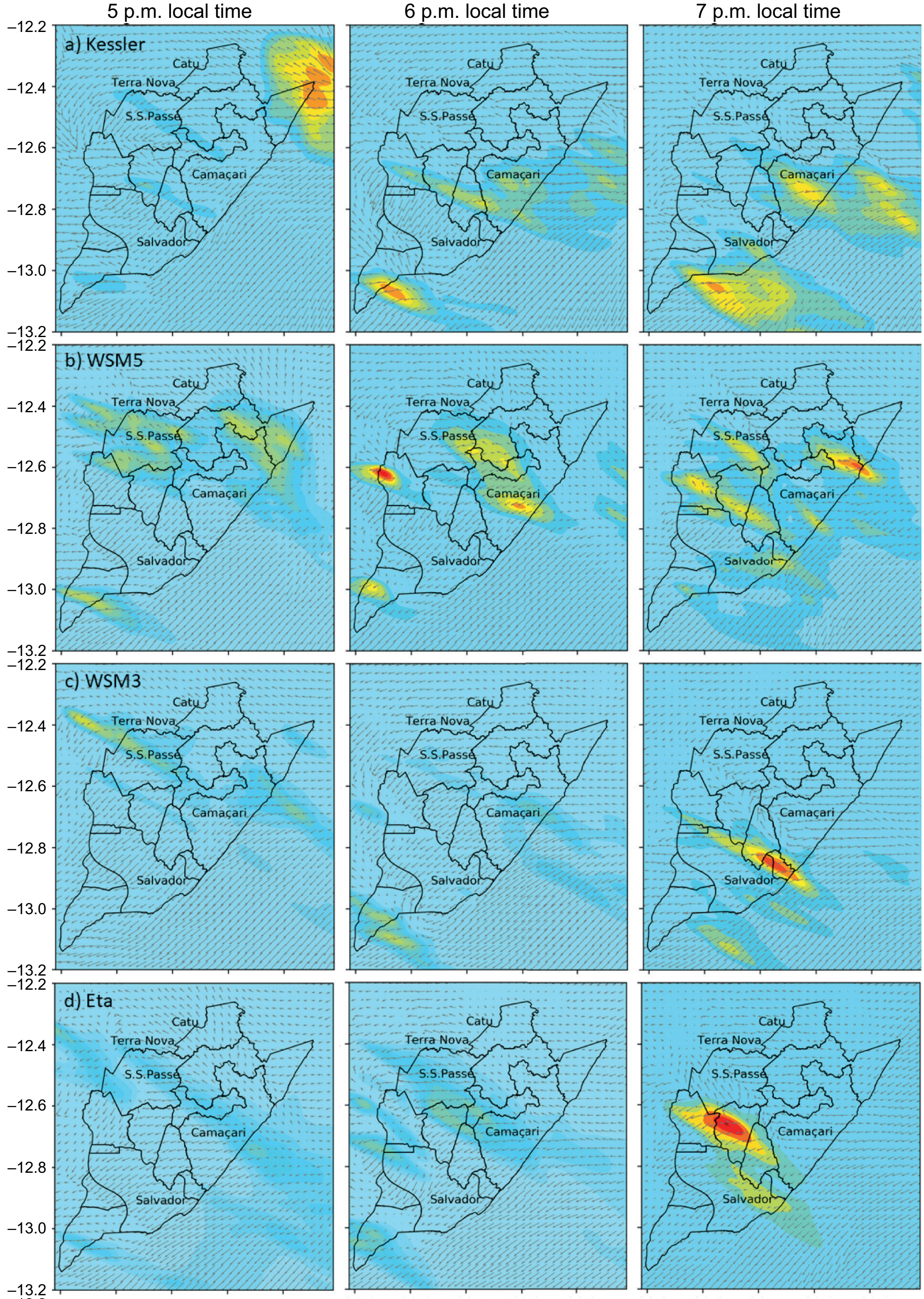

Fig. 12. Spatial distribution of the hourly modeled precipitation with wind fields at 10 m at D03 at 17:00 (left), 18:00 (center) and 19:00 (right) LT for all runs using MYJ-PBL and GF-CU with different MP schemes.

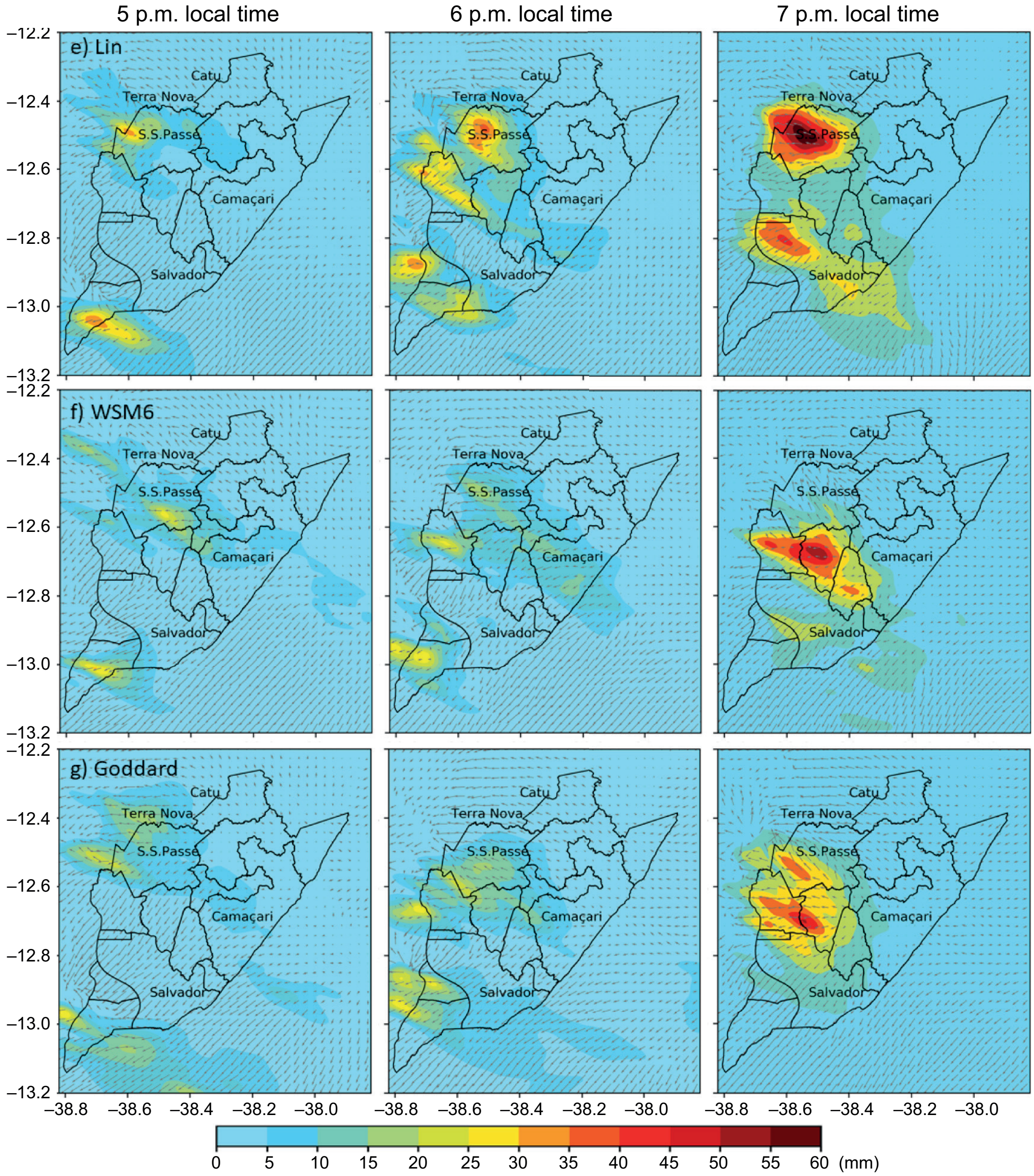

Fig. 12. Spatial distribution of the hourly modeled precipitation with wind fields at 10 m at D03 at 17:00 (left), 18:00 (center) and 19:00 (right) LT for all runs using MYJ-PBL and GF-CU with different MP schemes.

at 10 m between 20:00 and 22:00 UTC (17:00 and 19:00 LT, respectively) at D03 using MYJ-PBL and GF-CU schemes. The choice to show the spatial plots of all runs is to investigate the effect of MP schemes, and also to eliminate the spatial component as the precipitation previous results were compared to a single rain gauge for the entire region. The others were not included as the WRF model presented almost no rain or differences between scenarios.

It is simple to distinguish the most suitable MP schemes by visual comparison for this event. The arrival of the subtropical storm was reasonably depicted by Lin, WSM6 and Goddard MP schemes (Fig. 12e-g), which reproduced the evolution of this subtropical storm throughout the hours, with Lin simulation yielding the highest total precipitation rates. Kessler and WSM5 had similar results and emulated the arrival of the event with weak magnitude and patterns precipitation (Fig. 12a, b), despite Kessler is the least complex scheme used. Meanwhile, WSM3 and Eta (Fig. 12c, d) awerend delayed and presented much weaker precipitation fields, therefore they were not suitable for this event. Similar results were found in Sun et al. (2019), who conducted experiments of a typhoon case in South China.

The six-class schemes (Lin, WSM6 and Goddard), which are more complex MP schemes when compared to the other schemes used in the present study, had better performance for this severe event over a Brazilian urban-coastal area. Sikder and Hossain (2016) noted the need to use more complex MP schemes for high rainfall events at high resolution grids since CU schemes are not explicitly employed. Additionally, the inclusion of graupel, which is the hydrometeor class that differs from the others, produced a more realistic precipitation in the region in size and intensity. In Lin and Goddard schemes, graupel is assumed to have a constant bulk density of 400 kg m^{-3}, whereas for WSM6 of 500 kg m^{-3}. However, they also differ in other parameters of the gamma distribution function (Adams-Selin et al., 2013; Han et al., 2013). This analysis revealed that again the most suitable configuration for this weather event was MYJ, GF, and Lin for PBL, CU and MP schemes, respectively, since these schemes appeared to have the most suitable location, shape and intensity of the precipitation.

Figure 13 displays the spatial distribution at 19:00 LT using the MYJ-GF-Lin configuration, and the hourly average contribution of MP and CU schemes to the precipitation of each domain.

The coarsest domain (D01; Fig. 13a) yielded the lowest rainfall rates, while at a finer resolution (D02 and D03), where the CU scheme was not activated, precipitation was directly produced by the MP schemes. This agrees with Jeworrek et al. (2019), who observed that MP schemes had more impact on precipitation production in mesoscale convective cases. This happens because grid-scale rainfall has to increase its processes to compensate the non-activation of CU parameterization in the finer grids (Sharma and Huang, 2012), thus sub-grid scale motions become

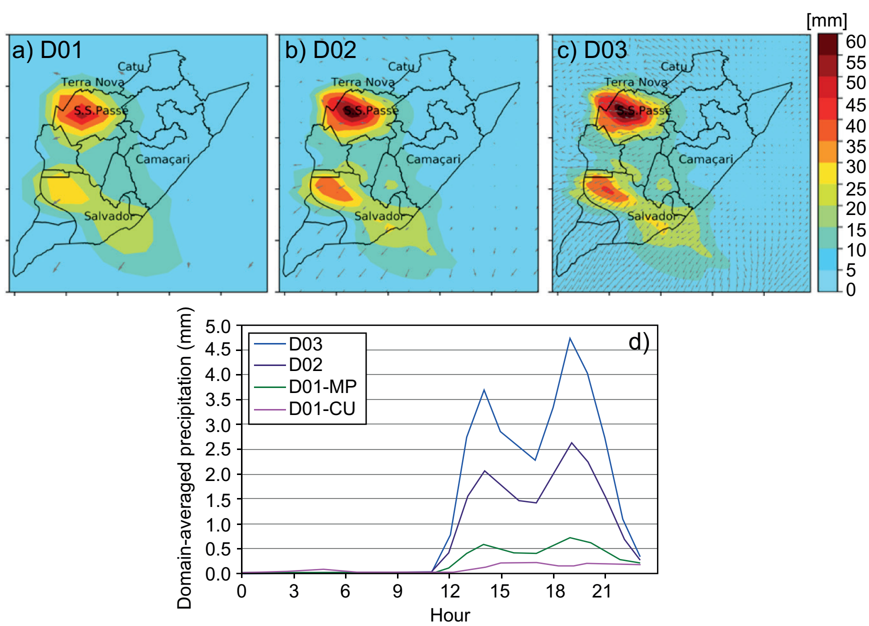

Fig. 13. Average contribution of MP and CU schemes to the precipitation of each domain using PBL-MYJ, CU-GF, and MP-Lin configuration. Spatial plots are depicted at 19:00 LT.

better resolved and dominate the total transport and precipitation (Fowler et al., 2016).

As the peak rainfall was registered in the region between 17:00-18:00 LT, rainfall modeled across the entire domain started to be predicted 5 h before the actual peak, with the highest modeled values occurring at 19:00 LT (Fig. 13d). The highest modeled rainfall rates were concentrated over the São Sebastião do Passé (see S.S.Passé in the spatial distribution of Fig.13c) county. Terra Nova and Salvador municipalities, especially over the BTS, also were affected by the subtropical storm Guará. Additionally, over the surrounding areas, where there are large areas of vegetation and water bodies, the wind fields were smaller and divergent. The wind fields agreed with the observed wind roses, which indicates that most of the winds originated from the north, north-northeast, and northeast areas and blew toward the southwest and south-southwest.

The wind rose diagrams (not shown) show that frequency distribution of the observed wind originated from the 25% north, 25% north-northeast, and 33.3% northeast at the INMET station. Meanwhile, the modeled data exhibited a frequency distribution of 20.8, 45.8, and 29.6%. The observed frequency distribution at the Airport station was 33.3% north, 16.7% north-northeast, and 16.7% northeast, while that of the modeled data was 25, 41.7, and 33.3%, respectively. Therefore, the WRF results could depict the same wind sectors with variations in the percentage of frequency distribution and wind magnitudes.

4. Conclusions

Abrupt changes in the atmosphere over coastal-tropical sites are one of the most challenging aspects of atmospheric modeling, particularly for precipitation. Results indicate that the WRF model performed well in the simulation of an extreme rainfall event, i.e., the Guará subtropical storm. Although several studies have already been conducted on this subject in other regions, the best model configuration will depend on the area under analysis. This constitutes the first study evaluating physical parameterization schemes over the MRS in Brazil, using the WRF model.

Several configurations combining different PBL, CU, and MP schemes were tested in our study. Although the results are based on a single case study, significant differences could be seen on the hourly variation of meteorological parameters. The PBL-MYJ, CU-GF, and MP-Lin schemes were selected to generate the spatial and temporal distribution plots, and the wind roses, as this combination agreed with the main variable best. The precipitation production was majorly influenced by the microphysics scheme when compared to the cumulus scheme in D01. The model represented well the arrival and occurrence of this extreme weather event in a tropical and coastal region, considering that the region already had intense convective characteristics and was constantly influenced by sea breezes, which could interfere in the model results and compromise the performance of the simulations. The WRF model could represent phenomena that occur in the PBL reasonably well, justifying its application at an urban scale. Over the past 15 years, the MRS region has experienced industrialization and urbanization, which may have caused the weather station to become poorly located. Furthermore, one rain gauge was available for the entire region to compare with the WRF data, indicating that the model validation could be better conducted with more observational data, which is a limitation of the study. The results demonstrate that schemes must be thoroughly validated using additional experimental observations, such as Light Detection and Ranging and Sonic Detection and Ranging measurements. In addition, future work should include the analyses of more cases, and also other environmental conditions to reach definitive conclusions in the use of the selected schemes.

Acknowledgments

The authors thank the Programa Institucional de Internacionalização da Coordenação de Aperfeiçoamento de Pessoal de Nível Superior (CAPES-PrInt) for granting the Ph.D. scholarship to the first author, the Global Centre for Clean Air Research (GCARE) at the University of Surrey, the Supercomputing Center for Industrial Innovation (CIMATEC), the FAPESB, and the NQualiAr of UFES.

References

Adams-Selin RD, van den Heever SC, Johnson RH. 2013. Sensitivity of bow-echo simulation to microphysical parameterizations. Weather and Forecasting 28:1188–1209. https://doi.org/10.1175/WAF-D-12-00108.1

Avolio E, Federico S, Miglietta MM, Lo Feudo T, Calidonna CR, Sempreviva AM. 2017. Sensitivity analysis of WRF model PBL schemes in simulating boundary-layer variables in southern Italy: An experimental campaign. Atmospheric Research 192: 58-71. https://doi.org/10.1016/j.atmosres.2017.04.003

Avolio E, Federico S. 2018. WRF simulations for a heavy rainfall event in southern Italy: Verification and sensitivity tests. Atmospheric Research 209: 14-35. https://doi.org/10.1016/j.atmosres.2017.04.003

Balzarini A, Angelini F, Ferrero L, Moscatelli M, Perrone MG, Pirovano G, Riva GM, Sangiorgi G, Toppetti AM, Gobbi GP, Bolzacchini E. 2014. Sensitivity analysis of PBL schemes by comparing WRF model and experimental data. Geoscientific Model Development 7: 61336171. https://doi.org/10.5194/gmdd-7-6133-2014

Banks RF, Tiana-Alsina J, Baldasano JM, Rocadenbosch F, Papayannis A, Solomos S, Tzanis CG. 2016. Sensitivity of boundary layer variables to PBL schemes in the WRF model based on surface meteorological observations, lidar, and radiosondes during the HygrA-CD campaign. Atmospheric Research 176-177: 185-201. https://doi.org/10.1016/j.atmosres.2016.02.024

Bei N, Zhang F. 2007. Impacts of initial condition errors on mesoscale predictability of heavy precipitation along the Meiyu front of China. Quarterly Journal of the Royal Meteorological Society 133: 83-99. https://doi.org/10.1002/qj.20

Boadh R, Satyanarayana ANV, Rama Krishna TVBPS, Madala S. 2016. Sensitivity of PBL schemes of the WRF-ARW model in simulating the boundary layer flow parameters for their application to air pollution dispersion modeling over a tropical station. Atmósfera 29: 61-81. https://doi.org/10.20937/ATM.2016.29.01.05

Carvalho D, Rocha A, Gómez-Gesteira M, Silva Santos C. 2014. WRF wind simulation and wind energy production estimates forced by different reanalyses: Comparison with observed data for Portugal. Applied Energy 117: 116-126. https://doi.org/10.1016/j.apenergy.2013.12.001

Carvalho LMV, Jones C, Liebmann B. 2004. The South Atlantic Convergence Zone: Persistence, intensity, form, extreme precipitation and relationships with intraseasonal activity. Journal of Climate 17: 88-108. https://doi.org/10.1175/1520-0442(2004)017<0088:T-SACZI>2.0.CO;2

Chan SC, Kendon EJ, Roberts N, Blenkinsop S, Fowler HJ. 2018. Large-scale predictors for extreme hourly precipitation events in convection-permitting climate simulations. Journal of Climate 31: 2115-2131. https://doi.org/10.1175/JCLI-D-17-0404.1

Chawla I, Osuri KK, Mujumdar PP, Niyogi D. 2018. Assessment of the Weather Research and Forecasting (WRF) model for simulation of extreme rainfall events in the upper Ganga Basin. Hydrology and Earth System Sciences 22: 1095-1117. https://doi.org/10.5194/hess-22-1095-2018

Chen F, Mitchell K, Schaake J, Xue Y, Pan H, Koren V, Duan Y, Ek M, Betts A. 1996. Modeling of land-surface evaporation by four schemes and comparison with FIFE observations. Journal of Geophysical Research 101: 7251-7268. https://doi.org/10.1029/95JD02165

Chen F, Dudhia J. 2001. Coupling an Advanced Land Surface-Hydrology Model with the Penn State-NCAR MM5 modeling system. Part I: Model implementation and sensitivity. Monthly Weather Review 129: 569-585. https://doi.org/10.1175/1520-0493(2001)129<0569:-CAALSH>2.0.CO;2

Chou SC, Bustamante JF, Gomes JL. 2005. Evaluation of Eta Model seasonal precipitation forecasts over South America. Nonlinear Processes in Geophysics 12, 537-555. https://doi.org/10.5194/npg-12-537-2005

Chou S, Lyra A, Mourão C, Dereczynski C, Pilotto I, Gomes J, Bustamante J, Tavares P, Silva A, Rodrigues D, Campos D, Chagas D, Sueiro G, Siqueira G, Nobre P, Marengo J. 2014. Evaluation of the Eta simulations nested in three global climate models. American Journal of Climate Change 3: 438-454. https://doi.org/10.4236/ajcc.2014.35039

Clark P, Roberts N, Lean H, Ballard SP, Charlton-Perez C. 2016. Convection-permitting models: A step-change in rainfall forecasting. Meteorological Applications 23: 165-181. https://doi.org/10.1002/met.1538

Cohen AE, Cavallo SM, Coniglio MC, Brooks HE. 2015. A review of planetary boundary layer parameterization schemes and their sensitivity in simulating southeastern U.S. cold season severe weather environments. Weather and Forecasting 30: 591-612. https://doi.org/10.1175/WAF-D-14-00105.1

Comin AC, Schumacher V, Justino F, Fernández A. 2018. Impact of different microphysical parameterizations on extreme snowfall events in the Southern Andes.

Weather and Climate Extremes 21: 65-75. https://doi.org/10.1016/j.wace.2018.07.001

Ekström M. 2015. Metrics to identify meaningful downscaling skill in WRF simulations of intense rainfall events. Environmental Modelling & Software 76: 54-68. https://doi.org/10.1016/j.envsoft.2016.01.012

Emery C, Tai E, Yarwood G. 2001. Enhanced meteorological modeling and performance evaluation for two Texas ozone episodes. ENVIRON International Corporation, Rowland Way, Novato, CA. Available at: https://www.tceq.texas.gov/assets/public/implementation/air/am/contracts/reports/mm/EnhancedMetModelingAndPerformanceEvaluation.pdf

Fowler LD, Skamarock WC, Grell GA, Freitas SR, Duda MG. 2016. Analyzing the Grell-Freitas convection scheme from hydrostatic to non-hydrostatic scales within a global model. Monthly Weather Review 144: 2285-2306. https://doi.org/10.1175/MWR-D-15-0311.1

Gao J, Xue M, Shapiro A, Droegemeier KK. 1999. A variation method for the analysis of three-dimensional wind fields from two Doppler radars. Monthly Weather Review 127: 2128-2142. https://doi.org/10.1175/1520-0493(1999)127<2128:AVMFTA>2.0.CO;2

Gilliland EK, Rowe CM. 2007. A comparison of cumulus parameterization schemes in the WRF model. In: Proceedings of the 21st AMS Conference on Hydrology, San Antonio, TX, USA. Available at: https://ams.confex.com/ams/pdfpapers/120591.pdf.

Grell GA, Freitas SR. 2014. A scale and aerosol aware stochastic convective parameterization for weather and air quality modeling. Atmospheric Chemistry and Physics 14: 5233-5250. https://doi.org/10.5194/acp-14-5233-2014

Gunwani P, Mohan M. 2017. Sensitivity of WRF model estimates to various PBL parameterizations in different climatic zones over India. Atmospheric Research 194: 43-65. https://doi.org/10.1016/j.atmosres.2017.04.026

Hally A, Richard E, Fresnay S, Lambert D. 2014. Ensemble simulations with perturbed physical parametrizations: Pre-HyMeX case studies. Quarterly Journal of the Royal Meteorological Society 140: 1900-1916. https://doi.org/10.1002/qj.2257

Han M, Braun SA, Matsui T, Williams CR. 2013. Evaluation of cloud microphysics schemes in simulations of a winter storm using radar and radiometer measurements. Journal of Geophysical Research: Atmospheres 118: 1401-1419. https://doi.org/10.1002/jgrd.50115

Hanna S, Chang J. 2012. Acceptance criteria for urban dispersion model evaluation. Meteorology and Atmospheric Physics 116: 133-146. https://doi.org/10.1007/s00703-011-0177-1

Hariprasad KBRR, Srinivas CV, Singh BA, Rao VBS, Baskaran R, Venkatraman B. 2014. Numerical simulation and intercomparison of boundary layer structure with different PBL schemes in WRF using experimental observations at a tropical site. Atmospheric Research 145-146: 27-44. https://doi.org/10.1016/j.atmosres.2014.03.023

Hong S-Y, Noh Y, Dudhia J. 2006. A new vertical diffusion package with an explicit treatment of entrainment processes. Monthly Weather Review 134: 2318-2341. https://doi.org/10.1175/MWR3199.1

Imran HM, Kala J, Ng AWM, Muthukumaran S. 2018. An evaluation of the performance of a WRF multi-physics ensemble for heatwave events over the city of Melbourne in the southeast Australia. Climate Dynamics 50: 2553-2586. https://doi.org/10.1007/s00382-017-3758-y

janjic zi. 2000. comments on development and evaluation of a convection scheme for use in climate models. Journal of the Atmospheric Sciences 57: 3686. https://doi.org/10.1175/1520-0469(2000)057<3686:CODAEO>2.0.CO;2

Jeworrek J, West G, Stull R. 2019. Evaluation of cumulus and microphysics parameterizations in WRF across the convective gray zone. Weather and Forecasting 34: 1097-1115. https://doi.org/10.1175/WAF-D-18-0178.1

Jiménez P, Jorba O, Parra R, Baldasano JM. 2006. Evaluation of MM5-EMICAT2000-CMAQ performance and sensitivity in complex terrain: High-resolution application to the northeastern Iberian Peninsula. Atmospheric Environment 40: 5056-5072. https://doi.org/10.1016/j.atmosenv.2005.12.060

Jiménez PA, Dudhia J. 2013. On the ability of the WRF model to reproduce the surface wind direction over complex terrain. Journal of Applied Meteorology and Climatology 52: 1610-1617.

Kemball-Cook S, Jia Y, Emery C, Morris R. 2005. Alaska MM5 modeling for the 2002 annual period to support visibility modeling, prepared for Western Regional Air Partnership (WRAP). Environ International Corporation, Novato, CA. Available at: https://views.cira.colostate.edu/docs/iwdw/modeling/wrap/2002/met/Alaska_MM5_DraftReport_Sept05.pdf

Kim HW, Lee DK. 2006. An observational study of mesoscale convective systems with heavy rainfall over the Korean Peninsula. Weather Forecasting 21: 125-148. https://doi.org/10.1175/WAF912.1

Kolling JS, Pleim JE, Jeffries HE, Vizuete W. 2013. A multisensor evaluation of the Asymmetric Convective Model, Version 2, in Southeast Texas. Journal of the Air & Waste Management Association 63: 41-53. https://doi.org/10.1080/10962247.2012.732019

Koren V, Schaake J, Mitchell K, Duan QY, Chen F. 1999. A parameterization of snowpack and frozen ground intended for NCEP weather and climate models. Journal of Geophysical Research 104: 19569-19585. https://doi.org/10.1029/1999JD900232

Kouadio YK, Servain J, MacHado LAT, Lentini C.A.D. 2012. Heavy rainfall episodes in the eastern northeast brazil linked to large-scale ocean-atmosphere conditions in the tropical Atlantic. Advances in Meteorology 2012: 369567. https://doi.org/10.1155/2012/369567

Kwon, YC, Hong S-Y. 2017. A mass-flux cumulus parameterization scheme across gray-zone resolutions. Monthly Weather Review 145: 583-598. https://doi.org/10.1175/MWR-D-16-0034.1

Lee H, Baik J-J. 2018. A comparative study of bin and bulk cloud microphysics schemes in simulating a heavy precipitation case. Atmosphere 9: 475. https://doi.org/10.3390/atmos9120475

Li G, Wang Y, Zhang R. 2008. Implementation of a two-moment bulk microphysics scheme to the WRF model to investigate aerosol-cloud interaction. Journal of Geophysical Research: Atmospheres 113: D15211. https://doi.org/10.1029/2007JD009361

Lian J, Wu L, Bréon FM, Broquet G, Vautard R, Zaccheo TS, Dobler J, Ciais P. 2018. Evaluation of the WRF-UCM mesoscale model and ECMWF global operational forecasts over the Paris region in the prospect of tracer atmospheric transport modeling. Elementa: Science of the Anthropocene 6: 64. https://doi.org/10.1525/elementa.319

Madala S, Satyanarayana ANV, Srinivas CV, Tyagi B. 2016. Performance Evaluation of PBL schemes of ARW model in simulating thermo-dynamical structure of pre-monsoon convective episodes over Kharagpur using STORM data sets. Pure and Applied Geophysics 173: 1803-1827. https://doi.org/10.1007/s00024-015-1210-y

Martilli A, Clappier A, Rotach MW. 2002. An urban surface exchange parameterisation for mesoscale models. Boundary-Layer Meteorology 104: 261-304. https://doi.org/10.1023/A:1016099921195

Mellor GL, Yamada T. 1982. Development of a turbulence closure model for geophysical fluid problems. Reviews of Geophysics 20(4): 851-875. https://doi.org/10.1029/RG020i004p00851

NCEP. 2015. Updated daily GDAS/FNL 0.25 degree global tropospheric analyses and forecast grids. Research data archive at the National Center for Atmospheric Research, Computational and Information Systems Laboratory. National Centers for Environmental Prediction/National Weather Service/National Oceanic and Atmospheric Administration/U.S. Department of Commerce. https://doi.org/10.5065/d65q4t4z

Penchah MM, Malakooti H, Satkin M. 2017. Evaluation of planetary boundary layer simulations for wind resource study in east of Iran. Renewable Energy 111: 1-10. https://doi.org/10.1016/j.renene.2017.03.040

Powers JG, Klem PJB, Skamarock WC, Davis CA, Dudhia J, Gill DO. 2017. The Weather Research and Forecasting model: Overview, system efforts, and future directions. Bulletin of the American Meteorological Society 98: 1717-1737. https://doi.org/10.1175/BAMS-D-15-00308.1

Rao VB, Lima MC, Franchito SH. 1993. Seasonal and interanual variations of rainfall over eastern northeast Brazil. Journal of Climate 6: 1754-1763. https://doi.org/10.1175/1520-0442(1993)006<1754:-SAIVOR>2.0.CO;2

Salvador N, Reis NC, Santos JM, Albuquerque TTA, Loriato AG, Delbarre H, Augustin P, Sokolov A, Moreira DM. 2016. Evaluation of Weather Research and Forecasting model parameterizations under sea-breeze conditions in a North Sea coastal environment. Journal of Meteorological Research 30: 998-1018. https://doi.org/10.1007/s13351-016-6019-9

Sarmiento DP, Davis KJ, Deng A, Lauvaux T, Brewer A, Hardesty M. 2017. A comprehensive assessment of land surface-atmosphere interactions in a WRF/Urban modeling system for Indianapolis, IN. Elementa: Science of the Anthropocene 5: 1-22. https://doi.org/10.1525/elementa.132

Sharma A, Huang H-P. 2012. Regional climate simulation for Arizona: Impact of resolution on precipitation. Advances in Meteorology 2012: 505726. https://doi.org/10.1155/2012/505726

Sharma A, Fernando HJS, Hamlet AF, Hellmann JJ, Barlage M, Chen F. 2016. Urban meteorological modeling using WRF: A sensitivity study. International Journal of Climatology 37: 1885-1900. https://doi.org/10.1002/joc.4819

Sikder S, Hossain F. 2016. Assessment of the Weather Research and Forecasting model generalized parameterization schemes for advancement of precipitation forecasting in monsoon-driven river basins. Journal of Advances in Modeling Earth Systems 8: 1210-1228. https://doi.org/10.1002/2016MS000678

Shin HH, Hong S-Y, Dudhia J. 2012. Impacts of the lowest model level height on the performance of planetary boundary layer parameterizations. Monthly Weather Review 140: 664-682. https://doi.org/10.1175/MWR-D-11-00027.1

Singh KS, Bonthu S, Purvaja R, Robin RS, Kannan BAM, Ramesh R. 2018. Prediction of heavy rainfall over Chennai Metropolitan City, Tamil Nadu, India: Impact of microphysical parameterization schemes. Atmospheric Research 202: 219-234. https://doi.org/10.1016/j.atmosres.2017.11.028

Skamarock WC, Klemp JB, Dudhia J, Gill DO, Barker DM, Duda MG, Huang X, Wang W, Powers JG. 2008. A Description of the Advanced Research WRF Version 3 (No. NCAR/TN-475+STR). University Corporation for Atmospheric Research. https://doi.org/10.5065/D68S4MVH

Solman SA, Sanchez E, Samuelsson P, da Rocha RP, Li L, Marengo J, Pessacg NL, Remedio ARC, Chou SC, Berbery H, Le Treut H, de Castro M, Jacob D. 2013. Evaluation of an ensemble of regional climate model simulations over South America driven by the ERA-Interim reanalysis: Model performance and uncertainties. Climate Dynamics 41: 1139-1157. https://doi.org/10.1007/s00382-013-1667-2

Somos-Valenzuela M, Manquehual-Cheuque F. 2020. Evaluating multiple WRF configurations and forcing over the Northern Patagonian Icecap (NPI) and Baker River Basin. Atmosphere 11: 1-19. https://doi.org/10.3390/atmos11080815

Song H-J, Sohn B-J. 2018. An evaluation of WRF microphysics schemes for simulating the warm-type heavy rain over the Korean Peninsula. Asia-Pacific Journal of Atmospheric Sciences 54: 225-236. https://doi.org/10.1007/s13143-018-0006-2

Stensrud DJ. 2007. Why study parameterization schemes? In: Parameterization schemes: Keys to understanding numerical weather prediction models. 1st ed. Cambridge University Press, Cambridge, United Kingdom.

Sun J, He H, Hu X, Wang D, Gao C, Song J. 2019. Numerical simulations of typhoon Hagupit (2008) using WRF. Weather Forecast 34: 999-1015. https://doi.org/10.1175/WAF-D-18-0150.1

Surussavadee C. 2017. Evaluation of WRF near-surface wind simulations in tropics employing different planetary boundary layer schemes. In: 8th International Renewable Energy Congress (IREC), Amman, Jordan. https://doi.org/10.1109/IREC.2017.7926005

Taylor KE. 2001. Summarizing multiple aspects of model performance in a single diagram. Journal of Geophysical Research: Atmospheres 106: 7183-7192. https://doi.org/10.1029/2000JD900719

Tymvios F, Charalambous D, Michaelides S, Lelieveld J. 2018. Intercomparison of boundary layer parameterizations for summer conditions in the eastern Mediterranean island of Cyprus using the WRF-ARW model. Atmospheric Research 208: 45-59. https://doi.org/10.1016/j.atmosres.2017.09.011

Xie B, Fung JCH, Chan A, Lau A. 2012. Evaluation of nonlocal and local planetary boundary layer schemes in the WRF model. Journal of Geophysical Research: Atmospheres 117: 1-26. https://doi.org/10.1029/2011JD017080

Wang Z, Duan A, Wu G. 2014. Impacts of boundary layer parameterization schemes and air-sea coupling on WRF simulation of the East Asian summer monsoon. Science China Earth Sciences 57: 1480-1493. https://doi.org/10.1007/s11430-013-4801-4

Woodhams BJ, Birch CE, Marsham JH, Bain CL, Roberts NM, Boyd DFA. 2018. What is the added value of a convection-permitting model for forecasting extreme rainfall over tropical East Africa? Monthly Weather Review 146: 2757-2780. https://doi.org/10.1175/MWR-D-17-0396.1

Zhang Y, Bocquet M, Mallet V, Seigneur C, Baklanov A. 2012. Real-time air quality forecasting. Part I: History, techniques, and current status. Atmospheric Environment 60: 632-655. https://doi.org/10.1016/j.atmosenv.2012.06.031

Zheng Y, Alapaty K, Herwehe JA, Genio AD, Niyogi D. 2016. Improving high-resolution weather forecasts using the Weather Research and Forecasting (WRF) model with upgraded Kain-Fritsch cumulus scheme. Monthly Weather Review 144: 833-860. https://doi.org/10.1175/MWR-D-15-0005.1

Atmósfera 35(4), 673-685 (2022)
https://doi.org/10.20937/ATM.52960

CONTENTS

Friction velocity estimation using a 2D sonic anemometer in coastal zones

Bernardo FIGUEROA-ESPINOZA[1,3]*, Zulia SÁNCHEZ-MEJÍA[2,3], Jorge Maximiliano UUH-SONDA[1,3], Paulo SALLES[1,3], Luis MÉNDEZ-BARROSO[2,3] and Hugo Alberto GUTIÉRREZ-JURADO[4]

[1] *Laboratorio de Ingeniería y Procesos Costeros, Instituto de Ingeniería, Universidad Nacional Autónoma de México, Puerto de abrigo S/N, 97355, Sisal, Yucatán, México.*

[2] *Departamento de Ciencias del Agua y Medioambiente, Instituto Tecnológico de Sonora, 5 de Febrero 818 sur, Col Centro, 85000 Ciudad Obregón, Sonora, México.*

[3] *Laboratorio Nacional de Resiliencia Costera (LANRESC), UNAM-CONACYT (www.lanresc.mx).*

[4] *Department of Earth, Environmental and Resource Sciences, The University of Texas at El Paso, 500 W. University Ave., Geological Sciences Bldg., Room 227-A, El Paso, TX 79968, USA.*

*Corresponding author; email: bfigueroae@yahoo.com

Received: August 11, 2020; accepted: March 17, 2021

RESUMEN

La velocidad de fricción (u_*) es un parámetro importante usado en el estudio de flujos geofísicos y de ingeniería. El uso cada vez más frecuente de anemómetros sónicos 2D en estaciones meteorológicas modernas hace que la estimación de u_* a partir de las componentes horizontales de la velocidad sea una posibilidad muy deseable. La presencia de diferentes regímenes de viento (como brisas marinas en zonas costeras) hace que los parámetros turbulentos dependan de la dirección de viento y de la estabilidad atmosférica. Esto hace la estimación de u_* a partir de mediciones 2D muy difícil de obtener. En este trabajo se propone una expresión simple (para u_*) y se valida usando datos provenientes de seis experimentos de campo independientes localizados en zonas costeras. Los resultados muestran que es posible estimar la velocidad de fricción a partir de mediciones 2D (componentes de la velocidad horizontal) usando la intensidad de turbulencia como un proxy de u_*, reduciendo sustancialmente la sensibilidad del estimado a la dirección de viento y estabilidad atmosférica, con bajo error medio cuadrático ($0.06 < \text{RMSE} < 0.097$) y alto coeficiente de correlación ($0.77 < r^2 < 0.95$).

ABSTRACT

Friction velocity (u_*) is an important velocity scale used in the study of engineering and geophysical flows. The widespread use of 2D sonic anemometers in modern meteorological stations makes the estimation of u_* from just the horizontal components of the velocity a very attractive possibility. The presence of different wind regimes (such as sea breezes in or near coastal zones) causes the turbulent parameters to be dependent on the wind direction. Additionally, u_* depends on atmospheric stability, whch makes the estimation of u_* from 2D measurements very difficult. A simple expression is proposed, and then tested with data from six independent experiments located in coastal zones. The results show that it is possible to estimate friction velocity from 2D measurements using the turbulence intensity as a proxy for u_*, reducing substantially the sensitivity to the wind direction or atmospheric stability, with small root mean squared errors ($0.06 < \text{RMSE} < 0.097$) and high correlation coefficients ($0.77 < r^2 < 0.95$).

Keywords: friction velocity, Eddy Covariance, Monin-Obukhov Similarity Theory, Sonic Anemometry, 2D anemometer, Coastal Zone.

1. Introduction

Friction velocity is one of the most important scaling parameters in atmospheric sciences and oceanography (Garrat, 1977; Stapleton and Huntley, 1995). Most processes and relationships in the low atmosphere involve the friction velocity, such as turbulent exchange of mass and energy at the surface and relationships based on the Monin-Obukhov Similarity Theory (Monin and Obukhov, 1954; Wyngaard et al., 1977) and on the surface renewal theory (Brutsaert, 1982; Stull, 1988; Castellví, 2018; Castellví et al., 2020). The friction velocity, u*, is defined as (Stull, 1988):

$$u_* = \left(\overline{u'w'}^2 + \overline{v'w'}^2 \right)^{1/4} \tag{1}$$

where *u, v,* and *w* are the *x, y,* and *z* components of the velocity vector; *u', v' and w'* are the velocity fluctuations with respect to the mean velocity components *U*, *V,* and *W* (i.e., *u' = u – U*). The overbar refers to time averaging. There are many different definitions of the friction or shear velocity (Weber, 1999) and the selection depends primarily on the particular application. Eq. (1) is related to the length of the Reynolds Stress vector when *u* is aligned with the mean velocity, hence this definition is independent of the chosen frame of reference and will be used in this report.

There are a variety of techniques to estimate u_* (Champagne et al., 1977; Nieuwstadt, 1978; Durand et al., 1991; Bauer et al., 1992; Inoue et al., 2011; Newman and Klein, 2014). For instance, the eddy covariance (EC) method uses high frequency direct measurement of velocity fluctuations in the surface layer to obtain the friction velocity from Eq. (1) (Burba, 2013). The measurement can be made using hot wire, sonic or other type of anemometer, as long as (a) the three components of the velocity are measured, and (b) the acquisition frequency is large enough to capture the rapid turbulent fluctuations; note that the averaging period must not be too long in order to avoid contamination from slow non-turbulent signals or trends (usually between 30 and 60 min).

Sonic anemometers are convenient because they do not have moving parts (the measurement is based on the speed of sound). Two dimensional (2D) sonic anemometers are much more robust and affordable than triaxial sonic anemometers. Unfortunately, 2D sonic anemometers cannot be used to directly determine the friction velocity (Eq. 1) because the vertical wind component is not measured; however, an estimate of friction velocity could be obtained from the logarithmic wind profile (Echols and Wagner 1972; Bauer et al., 1992; Bergeron and Abrahams, 1992; Sozzi et al., 1998), but this method requires deployment of 2D anemometers at several heights. In this investigation, a method to estimate friction velocity from a single 2D anemometer is proposed and tested against field measurements.

2. Method

On the basis that the turbulent standard deviation of the horizontal wind speed does not follow similarity and it is well correlated with the friction velocity and the horizontal mean wind speed (Dyer, 1974; Panofsky et al., 1977; Sorbjan, 1987; Stull, 1988; Graefe, 2004; Banerjee et al., 2015), here a semi-empirical relationship is proposed to estimate the friction velocity using a 2D sonic anemometer capable to record (in a half-hourly basis) accurate values of the turbulent standard deviation of the horizontal wind speed and the mean wind speed as follows:

$$\sqrt{\frac{u_{*2D}}{U}} = aI^b \tag{2}$$

$$I = \frac{2\overline{u'^2}}{U^2} \tag{3}$$

where *a* and *b* are coefficients that must be calibrated against the friction velocity determined using a triaxial sonic anemometer. Once *a* and *b* are known, the friction velocity from 2D measurements (u_{*2D}) can be estimated from Eqs. (2) and (3). Here the velocity vector was rotated in the mean wind direction (i.e., the cross-wind component), thus *I* is related to the turbulent intensity (Stapleton and Huntley, 1995; Pope et al., 2006; Yahaya and Frangi, 2009). Notice that Eq. (2) can be interpreted as a relationship between a drag coefficient and the turbulence intensity (it can be rewritten as $C_D \sim I^{4b}$), with the inconvenience that the measurements can be done at different heights above ground (see Table I), so it would not be a "standard" drag coefficient, but a local one (Mahrt et al., 2001).

Table I. Characteristics of the experimental sites.

	Sisal meteorological mast (S1)	El Palmar (S2)	Estero el Soldado (S3)	Navopatia (S4)	Cape Tribulation (S5)	Gingin (S6)
Latitude (˚)	21.1647	21.0293	27.95	26.3999	–16.1032	–31.3763
Longitude (˚)	–89.9533	–90.0637	–110.97	–109.2397	145.4469	115.7138
Type of terrain	Complex, no orography. 100 m from the coastline. Barrier island close to a town	Homogeneous. Tropical dry seasonal forest	Open water, coastal lagoon. Type: Arheic	Flat, homogeneous mangrove close to an estuarine lagoon	Tropical rainforest	Coastal plain woodland on SW Australia
Time-series dates	2010/Jul/29-2012/May/23	2018/Mar/15-2019/Aug/21	2019/Jan/01-2019/Dec/31	2018/Jan/01-2018/Dec/31	2011/Jan/01-2011/Dec/31	2019/Jan/01-2019/Dec/31
Canopy height (m)	Variable	11	0.1	5.0	23	6.8
Roughness length *z*0 (m)	Direction-dependent (1^{-6} to $1.5^{-2} \times 10^{-2}$)	0.15	0.015	0.50	0.1 to 1	0.5
Mean wind speed (m s^{-1})	5.77	3.2	2.5	2.42	1.5	3
Dominant wind direction	ESE	ESE	WSW	WSE	SE	SSW and SE
Sensor height to the ground (m)	12.5	21.8	1.8	6.5	45	45
Data set size (number of records)	12 777	16 813	5962	13 253	16 849	14 819

3. Materials and field data

The proposed semi-empirical relationship (Eqs. 2 and 3) was calibrated at six sites with contrasting wind regimes. Table I shows the site locations and experiment characteristics (such as height above ground of the instruments, canopy height, measurement dates, number of records and mean wind speed). Figure 1 shows the map location (upper panel) and the wind roses for each location (lower panel). Note that a different color scale is used in S1 (wind rose) due to its high wind speed average. The site names (and acronyms in parenthesis) are also shown. They are grouped according to their geographical situation in: (1) Gulf of Mexico data sets, (2) Gulf of California data sets, and (3) Australia data sets.

EC experiments must be carefully assessed with statistical data quality tests (Foken and Wichura, 1996; Aubinet et al., 1999). Although most experiments carry out similar pre-processing (peak removal, detrending, gap filling), data quality control is always site-specific. There exist many quality control methods and indexes. Either method can be used with similar results, and stationarity tests are common due to its ease of implementation and interpretation. The method used for each experiment can be consulted in the next section (and references therein). This is important in this context because one cannot use the vertical component of the wind when using a 2D anemometer. However, one can construct stationarity or ogive tests with the horizontal components using the same principles (with the obvious exception of turbulence tests).

All bad data were previously eliminated by the site-specific quality control schemes. We had access to post-processed data using the EC technique (additionally we had raw data from S1 and S2). All sites used a half-hour averaging period. Another aspect of data processing that has to be brought to mind is wind velocity rotation; the post-processed data was already doubly (or triply) rotated, and a 2D measurement can only be rotated in one axis. This subject will be discussed in the last section, where a comparison with single vs. double (and triple) rotation is carried out to assess this issue quantitatively.

3.1 Gulf of Mexico datasets

The first and second experiments are Sisal (S1) and El Palmar (S2), respectively. They are shown in Figure 1a, both located at the NW of the Yucatan Peninsula in Mexico. S1 is situated at the beach (100 m to the shoreline), to the west end of the town of Sisal; a 50-m height mast equipped with five sonic anemometers at 3, 6, 12.5, 25 and 51 m from the ground was used to acquire wind data between August 2010 and September 2013. Two anemometers (12.5 and 51 m) were 3D (Thies 3.383x) and the rest were 2D (Thies 4.382x). This site is characterized by a bimodal wind speed U regime due to sea breeze (Figueroa-Espinoza et al., 2014). Dominant winds are ESE (seaward) and the average wind speed is 5.77 m s^{-1} at z = 12.5 m. Even though the terrain is flat, it is non-homogeneous because of the internal boundary layers caused by roughness effects on winds coming from different directions (Figueroa-Espinoza and Salles, 2014; Figueroa-Espinoza et al., 2014). Data pre-conditioning included a triple rotation for 3D anemometers, and single rotation for 2D (Wilczak et al., 2001). Data from a 3D anemometer at height z = 12.5 will be used unless specified otherwise. The second site is located 14 km south (inland) of Sisal, in a state reserve called El Palmar (S2 in what follows), a tropical-dry seasonal forest (Fig. 1c; see also Uuh-Sonda et al., 2018, 2021) in flat and homogeneous terrain whose average canopy height ranges from 8 to 12 m. In this site an EC tower is equipped with a WindMaster 3D anemometer at height z = 21.8 m. Data was post-treated with the EC technique, following Aubinet et al. (1999). A double rotation of the velocity vector was applied for all sites that adhere to this methodology (i.e., S2, S3 and S4) (Delgado et al. 2018; Balbuena et al., 2019; Uuh-Sonda et al., 2021). Prevailing wind directions are EES (Fig. 1d) and, despite being in the range of sea breeze influence (Taylor-Espinosa, 2009; Garza-Pérez and Ize-Lema, 2017), Uat S2 (~3.2 m s^{-1}) < Uat S1 (5.8 m s^{-1}). S1 data is freely available to the public (Figueroa-Espinoza and Salles, 2020), as well as S2 (Uuh-Sonda et al., 2020).

3.2 Gulf of California datasets

The two coastal sites from the Gulf of California used for this study were (Fig. 1a): Estero el Soldado (S3) and Navopatia (S4). S3 is located in a tidal coastal lagoon in the central region of the Gulf of California (Fig. 1e; Benítez-Valenzuela and Sánchez-Mejía, 2020). S3 has EC instruments including a WindMaster 2329-701-01 3D sonic anemometer

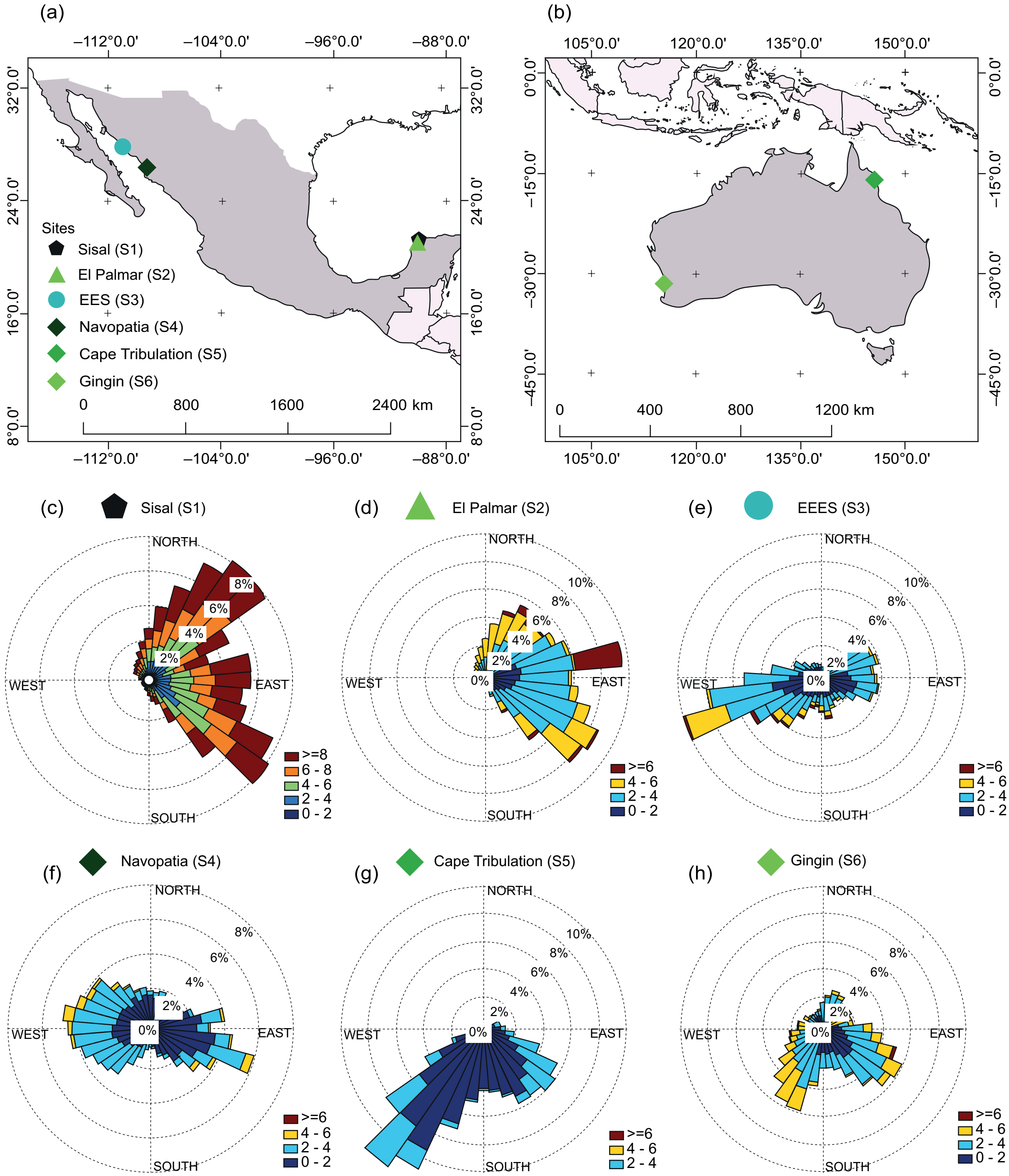

Fig. 1. (a) Location of sites S1, S2, S3, and S4 in Mexico. In the Gulf of California, the site Estero el Soldado (EES, S3-triangle) and Navopatia (S4, dark diamond). To the SE, on the Yucatan Peninsula, El Palmar (S2, green triangle) and Sisal (S1, pentagon). (b) Location of sites S5 and S6 in Australia. In north Queensland, Cape Tribulation (S5, dark green diamond). To the SW, in Western Australia, represented by a green diamond, Gingin (S6). The lower panel shows the wind roses (wind speed in m s^{-1}) for the six experimental sites, together with their respective notation.

deployed on a small floating platform (2 × 2 m) located at the inlet of the lagoon at 1.8 masl (Barreras-Apodaca and Sánchez-Mejía, 2018). Prevailing winds at S3 are WSW (landward; Fig. 1S3), with U = 2.5 m s^{-1}. EC data for S3 is available at the public repository described in Benítez-Valenzuela et al. (2020). S4 is located within an estuarine system along the northern Mexican Pacific coast (Fig. 1a). It has an EC tower with instruments, including a Windmaster Pro 3D sonic anemometer, sitting 1.5 m above a homogeneous mangrove forest surface (5 m mean canopy height) and has two dominant upwind directions (WSW and SE, Fig. 1f). EC raw data, including 10 Hz U and wind direction for both S3 and S4 was processed using EddyPro software v. 7.0.4 (LI-COR Biosciences, USA). EC data for S4 is available to the public as well (Granados-Martínez et al., 2019).

3.3 Australian datasets

The two coastal sites from the Australian continent included in this study (Fig. 1b) are: (1) the Cape Tribulation flux station (S5) in north Queensland, and (2) the Gingin flux station (S6) in Western Australia. Data from S5 and S6 was graciously provided by Liddell (2013) and Silberstein (2015), respectively, through the Australian Flux Network (OzFlux), where it can be freely accessed. S5 is located within the Daintree Rainforest Observatory between the Coral Sea to the east and a section of the Great Dividing Mountain Range to the west. S5 instruments are mounted on a crane tower at 45 m from the ground in lowland tropical rainforest (25 m average canopy height). Prevailing wind directions in S5 are SE and U is 1.5 m s^{-1} (Fig. 1g). S6 is located on the Swan Coastal Plain (~70 km north of Perth) where a flux station equipped with EC and micrometeorological instruments were mounted on a 14 m tall mast inside a native *Banksia* woodland with an irregular canopy (6.8 m average tree height [Silberstein, 2020]). S6 has SW dominant wind directions and U reaching 3 m s^{-1} (Fig. 1h). At both S5 and S6 sites, 10 Hz wind data is measured with CSAT 3D (Campbell Scientific, Logan, UT, USA) sonic anemometers and processed using PyFLUXPro for data quality control and flux processing (Isaac et al., 2017). For S5, additional processing to the wind data (double rotation) was implemented before the covariance calculation.

4. Wind regimes

Figure 2a-f shows the relationship between friction velocity u_* and the mean horizontal wind speed (2D) U for all the experimental sites (S1 to S6). Instead of using point clouds, we decided to plot a 2D probability histogram (PDF) based on a set of (forty) data bins, so a color scale can tell the regions with more frequency of occurrence.

From Figure 2 it can be inferred that for Sl, S3 and S4 (and probably S5) there are two wind regimes due to the sea breeze (direction-dependence). For Sl, two straight lines fit data coming from the sea (small slope) and from land (this is very clear in Sl). One possibility to estimate the friction velocity would be to perform a linear fit in terms of the streamwise mean wind speed U for each regime, as suggested by Weber (1999), using the corresponding range of directions to identify the different wind regimes when necessary. This procedure works very well, with the inconvenience of having different fit constants for each location and regime (one for winds coming from land and other set of constants for winds coming from the sea, for example). The corresponding values for the linear fit parameters of this exercise for Sl are shown in Table II. Even if the wind coming from the sea may present different behavior depending on the sea state (Charnock, 1955; Wu, 1980; Yahaya and Frangi, 2009), the fit is excellent ($r^2 > 0.79$); however, other locations not so close to the coast would be influenced by the terrain between the coast and the measurement site. Even in Sl the distinction between wind from the sea and from land is not sharp for wind directions aligned (±10º) with the shoreline. The data encompasses all atmospheric stabilities, however this calibration would have to be done separately for every location using the wind direction (and a 3D anemometer, for at least one year). Note also that for some sites, such as for S3 and S5, the spread of the data makes very difficult to set a clear-cut criterion for the regime identification, so the method would not be applicable. A method that is insensitive to these wind regimes would be very desirable. The use of the variance instead of the wind speed is intended to achieve regime (and stability) insensitivity, as discussed in the next sections.

5. Results

All experimental data sets include the velocity variance and mean wind speed U. Thus, I can be calculated

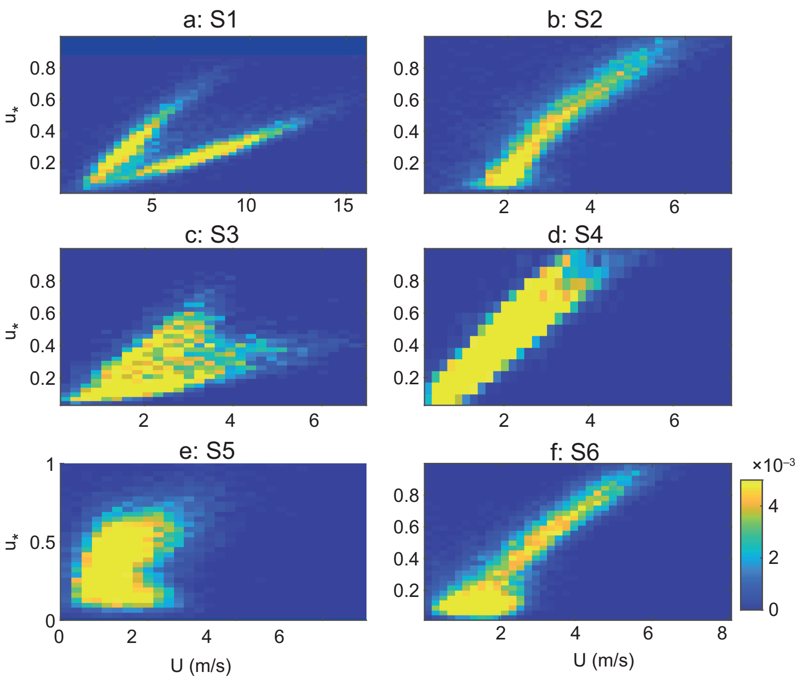

Fig. 2. 2D probability histogram of friction velocity u_* as a function of mean wind speed U (in m s^{-1}) for the six sites.

Table II. Linear fit parameters for site S1 (Sisal), based on u^* vs. U ($u^*2D = p_1U + p_2$) for winds from land and sea (wind speed in m s^{-1}).

Parameter	Sea	Land
p_1	0.03633	0.1018
p_2 (m s^{-1})	–0.0112	–0.0718
r^2	0.7963	0.8614
RMSE	0.0494	0.0659

from Eq. (3) using measured data, and u_{*2D} can be obtained from Eq. (2). Using this simple expression, the best fit parameters (in the least squares sense, comparing to the actual u_* from EC calculations) correspond to a = 0.5646 with a 95% confidence interval (CI) in the range (0.5641, 0.5652), and b = 0.2565 with a 95% C.I. in the range (0.2558, 0.2572). These parameters are dimensionless.

A comparison of the (3D) u_* and u_{*2D} is shown in Figure 3, again as a 2D probability histogram, for all experimental sites. Titles (a:S1, b:S2 and so on) are indicated on top of each panel. White labels inside each sub-plot indicate goodness of fit parameters (RMSE and r^2). A color scale is shown to the right of Figure 3f and is the same for all sub-plots. Note that the correlation coefficient ranges from r^2 = 0.77 (S5) with RMSE of 0.09 m s^{-1} to r^2 = 0.95 (S4) with RMSE of 0.06 m s^{-1} (see also Table III). It is clear that the method based on the turbulent intensity (Eqs. [2] and [3]) succeeded in collapsing the points to a single 1:1 linear relationship for all cases, in spite of the different wind regimes present in S1, S3 and S4 and S5 as well as the atmospheric stability variability. The horizontal variance, as well as I resulted rather insensitive to atmospheric stability (Stull, 1988; Weber, 1999). This was verified using the experimental data and Eq. (2), whose fitting parameters a and b were tabulated on Table IV for different Pasquill-Gifford stability classes (Hall et al., 2000). Both parameters did not vary more than 10% from the values reported in the Method section.

Table III lists the fit coefficients and goodness of fit of the data in Figure 3 (u_* as a function of u_{*2D}). The method works best at S2 and S4, as expected, since these sites do not have dissimilar wind regimes and the terrain and canopy are homogeneous. Interestingly, for S3 the goodness of fit is similar to that of S1.

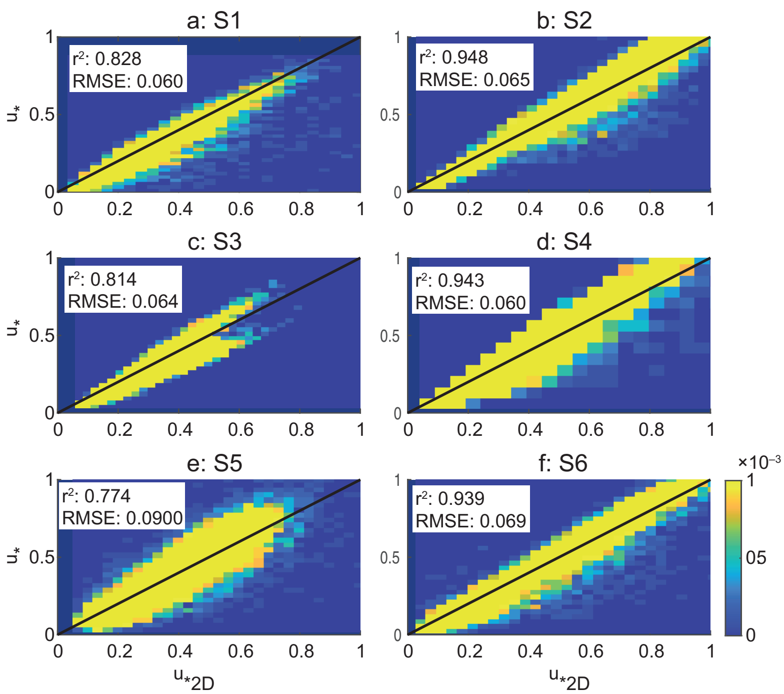

Fig. 3. 2D probability histograms of u_* as a function of u_{*2D} obtained from Eqs. (2) and (3). Hot colors indicate more frequent data (color bar at the lower right). Goodness of fit parameters are also shown in the white label inside each sub-plot (the thick black line is the 1:1 relationship).

Table III. Fit parameters and goodness of fit for Figure 4a-c (u^* vs. u^*2D). Figures in parentheses are the 95% confidence intervals.

Parameter	S1	S2	S3	S4	S5	S6
p_1	0.8267 (0.819, 0.8345)	0.9527 (0.9487, 0.9567)	0.9757 (0.9649, 0.9865)	1.184 (1.179, 1.189)	0.7956 (0.7884, 0.8028)	0.9291 (0.9246, 0.9336)
p_2 (m s^{-1})	0.04947 (0.04692, 0.05203)	0.00936 (0.007061, 0.01166)	–0.03518 (–0.03913, –0.03124)	p_2 = –0.05259 (–0.05496, –0.05021)	0.03299 (0.02938, 0.0366)	–0.008407 (–0.01076, –0.006052)
r^2	0.7738	0.9288	0.8401	0.9429	0.7344	0.9176
RMSE	0.06564	0.07568	0.05911	0.05978	0.0974	0.0800

6. Triple and double rotation vs. single rotation

The purpose of this section is to acknowledge the difference between performing double (or triple) rotation (3D case) and a single rotation (the only possible rotation in a 2D anemometer). The data from most experiments was already averaged using a 3D rotation scheme. To be more precise, S1 used triple rotation and all other sites used double rotation. Nevertheless, for S1 we actually had 2D anemometers mounted on the mast (at a height of 6 and 25 m), so the estimation can be compared with the 3D case (single rotation vs. triple rotation). Moreover,

Table IV. Fit parameters *a* and *b*, and goodness of fit (Eq. [2]) for different Pasquill-Gifford stability classes (Hall et al., 2000).

Stability class	L	a	b	R^2
A	–2	0.528	0.245	0.860
B	–10	0.598	0.282	0.897
C	–100	0.528	0.245	0.860
D	∞	0.587	0.266	0.840
E	100	0.549	0.251	0838
F	20	0.534	0.255	0.825
G	5	0.542	0.280	0.793

for S5 and S6 we had the full covariance matrix and the rotation angles, so we were able to get a "single rotation covariance matrix" and then calculate u_{*2D} as one would do with a 2D anemometer.

The result of this comparison is shown in Figure 4, where this strictly 2D friction velocity u_{*2D} is compared with the 3D u_* for sites S1 (a), S5 (b) and S6 (c). The goodness of fit (shown inside each sub-figure) can be compared with those of Figure 3: for S1, RMSE increased from 0.066 to 0.067, while r^2 decreased from 0.828 to 0.763. S5 and S6 also show a slight modification of goodness of fit, as expected, although r^2 improved for S5. If the measurements are carried out on a flat terrain, such as in most coastal zones, and the instruments are well aligned (a bubble level is sufficient to minimize corrections in the vertical), the method can be applied.

Finally, note that for heterogeneous surfaces and contrasting orography, the planar fit method (Wilczak et al., 2001) is recommended. None of the experimental sites present orography (coastal sites) and only S5 presents a relatively tall canopy (~20 m, see Table I), so a double rotation would be sufficient for calculating fluxes.

7. Conclusions

A simple power law was proposed to estimate the dimensionless friction velocity $u_* U^{-1}$ using only 2D data (horizontal velocity components) from wind measurements at high acquisition rates (of 10 Hz, in this case). This method of estimation was put to test using experimental data coming from six independent experiments carried out in coastal zones of both northern and southern hemispheres (see Table I). Note that at least three of the sites (S1, S3 and S4)

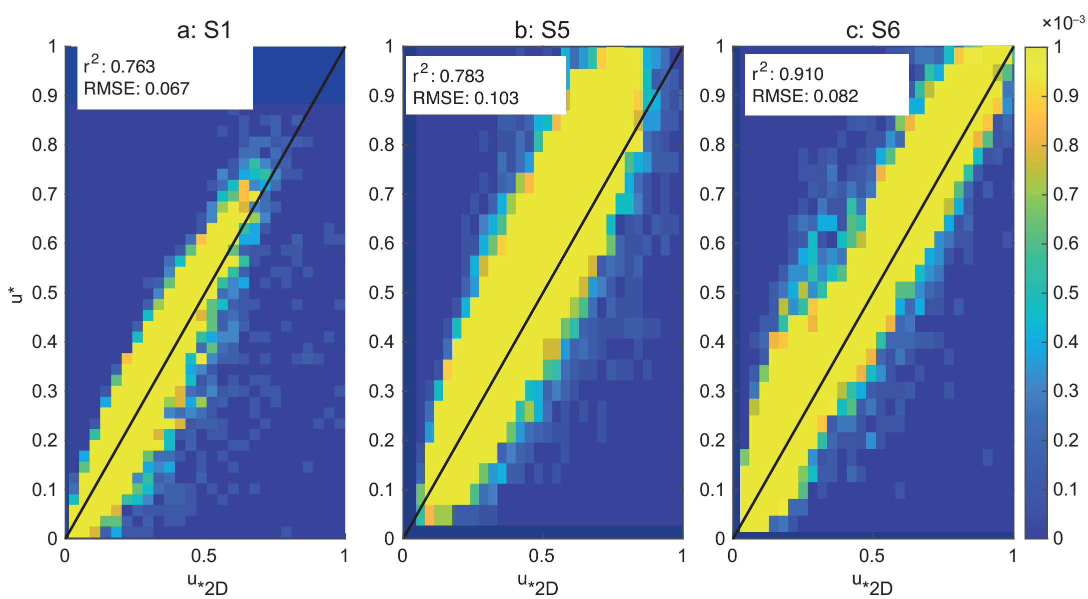

Fig. 4. PDF of actual (3D) friction velocity u_* vs. estimated friction velocity u_{*2D}, obtained from 2D velocity components with single rotation, for the sites (a) S1, (b) S5 and (c) S6. Goodness of fit statistics are shown inside the white labels (the thick black line is the 1:1 relationship).

show two wind regimes due to sea breeze influence, making the estimation a challenging task.

The results show a very good agreement between the 2D estimate of the friction velocity u_{*2D} and u_* (from the 3D EC methodology). The goodness of fit, with $r^2 > 0.77$ in all cases, proves that the methodology can be used at least in flat terrain (homogeneous or complex canopy) like that of coastal zones far from the influence of significant orographic features.

Given the affordability and wide use of 2D anemometers in modern meteorological stations, this study suggests that more estimations of u_* could be carried out by research groups and specialists of different disciplines, particularly in developing countries where 3D anemometry is precluded by the high cost of 3D sonic instruments. Moreover, some sites are located only meters from the shoreline, so the method may also be valid to estimate u_* above the sea surface (or other bodies of water). More research should be carried out in different experimental conditions. In particular, it would be interesting to test (and adapt) the method in complex orography, urban zones and tall and heterogeneous canopies.

Acknowledgments

The authors respectfully acknowledge the support of Laboratorio Nacional de Resiliencia Costera (LANRESC LN271544), as well as Consejo Nacional de Ciencia y Tecnología (CONACYT) research grant CONACYT-CFE 89073, CATEDRAS-CONACYT 1146 and CONACYT-SEMARNAT 278608. The technical support of M.Sc. Mariana Gómez-Nicolás, M.Eng. Juan A. Gómez Liera, Dr. José López González, Engr. Gonzalo U. Martín Ruiz, Engr. Lidia I. Benítez Valenzuela, M.Sc. Karol Granados-Martínez and M.Sc. Christian Anibal Silva Ontiveros is also greatly appreciated. We also thank the Comisión de Ecología y Desarrollo Sustentable del Estado de Sonora (CEDES) for granting the research permit to work at the natural protected area Estero el Soldado, and all the park rangers and students. Special thanks to Dr. Alec Torres for the interesting discussions and the motivation to explore the subject of turbulence and friction velocity estimates. We acknowledge Richard Silberstein and Mike Liddell for generously giving us access to the Gingin and Cape Tribulation datasets. This work used EC data collected by the TERN-OzFlux facility. OzFlux would like to acknowledge the financial support of the Australian Federal Government via the National Collaborative Research Infrastructure Scheme and the Education Investment Fund.

References

Aubinet M, Grelle A, Ibrom A, Rannik Ü, Moncrieff J, Foken T, Kowalski AS, Martin PH, Berbigier P, Bernhofer Ch, Clement R, Elbers J, Granier A, Grünwald T, Morgenstern K, Pilegaard K, Rebmann C, Snijders W, Valentini R, Vesala T. 1999. Estimates of the annual net carbon and water exchange of forests: The EUROFLUX methodology. Advances in Ecological Research 30: 113-175. https://doi.org/10.1016/S0065-2504(08)60018-5

Balbuena JD, Yépez EA, Pellat FP, Pérez GÁ, Gutiérrez CA, Barrientos MSA, Arredondo T, Niño FA, Bullock SH, Castellanos AE, Cueva A, Figueroa-Espinoza BF, Payán JG, Castillo EGD, Sosa EG, Escobar AG, Hinojo CH, Tha PUK, Celaya CL, Delgado YM, Oechel W, Ruiz ERP, Avendaño MQ, Zazueta CAR, Rodríguez JC, Robles NER, Terrazas TT, Diéguez ET, Uuh-Sonda J, Terminel MLV, Vargas R, Puga MGV, Verduzco VS, Vivoni ER, Watts, CJ. 2019. Base de datos de flujos verticales de dióxido de carbono en ecosistemas terrestres y costeros en México. Elementos para Políticas Públicas 2: 93-108.

Banerjee T, Katul GG, Salesky ST, Chamecki M. 2015. Revisiting the formulations for the longitudinal velocity variance in the unstable atmospheric surface layer. Quarterly Journal of the Royal Meteorological Society 141: 1699-1711. https://doi.org/10.1002/qj.2472

Barreras-Apodaca A., Sánchez-Mejía ZM. 2018. Eddy covariance observations of semiarid seagrasses from the Gulf of California. In: Proceedings of the AGU Fall Meeting, Washington DC, 10-14.

Bauer BO, Sherman D J, Wolcott JF. 1992. Sources of uncertainty in shear stress and roughness length estimates derived from velocity profiles. The Professional Geographer 44: 453-464. https://doi.org/10.1111/j.0033-0124.1992.00453.x

Benítez-Valenzuela LI, Sánchez-Mejía ZM. 2020. Observations of turbulent heat fluxes variability in a semiarid coastal lagoon (Gulf of California). Atmosphere 11: 626. https://doi.org/10.3390/atmos11060626

Benítez-Valenzuela LI, Sánchez-Mejía ZM, Silva-Ontiveros CA, Barreras-Apodaca A. 2020. Turbulent fluxes and tide measurements from a coastal lagoon in the Gulf of California. PANGAEA. https://doi.org/10.1594/PANGAEA.918686

Bergeron NE, Abrahams AD. 1992. Estimating shear velocity and roughness length from velocity profiles. Water Resources Research 28: 2155-2158. https://doi.org/10.1029/92WR00897

Brutsaert W. 1982. Mean profiles and similarity in a stationary and horizontally-uniform ABL. In: Evaporation into the atmosphere: Theory, history, and applications. Springer, Dordrecht, 57-112.

Burba G. 2013. Eddy covariance method for scientific, industrial, agricultural and regulatory applications: A field book on measuring ecosystem gas exchange and areal emission rates. LI-COR Biosciences.

Castellví F. 2018. An advanced method based on surface renewal theory to estimate the friction velocity and the surface heat flux. Water Resources Research 54: 10-134. https://doi.org/10.1029/2018WR022808

Castellví F, Medina ET, Cavero Campo J. 2020. Surface eddy fluxes and friction velocity estimates taking measurements at the canopy top. Agricultural Water Management 241: 106358. https://doi.org/10.1016/j.agwat.2020.106358

Champagne FH, Friehe CA, LaRue JC, Wynagaard JC. 1977. Flux measurements, flux estimation techniques, and fine-scale turbulence measurements in the unstable surface layer over land. Journal of Atmospheric Sciences 34: 515-530. https://doi.org/10.1175/1520-0469(1977)034%3C0515:FMFETA%3E2.0.CO;2

Charnock H. 1955. Wind stress on a water surface. Quarterly Journal of the Royal Meteorological Society 81: 639-640. https://doi.org/10.1002/qj.49708135027

Delgado-Balbuena J, Yépez EA, Paz-Pellat F, Ángeles-Pérez G, Aguirre-Gutiérrez C, Arredondo T, Alvarado-Barrientos MS, et al. 2018. Base de datos de flujos verticales de dioxido de carbono en ecosistemas terrestres y costeros en México. Elementos para Políticas Públicas 2: 93-108.

Durand P, De Sa L, Druilhet A, Said F. 1991. Use of the inertial dissipation method for calculating turbulent fluxes from low-level airborne measurements. Journal of Atmospheric and Oceanic Technology 8: 78-84. https://doi.org/10.1175/1520-0426(1991)008%3C0078:UOTIDM%3E2.0.CO;2

Dyer A. 1974. A review of flux-profile relationships. Boundary-Layer Meteorology 7: 363-372. https://doi.org/10.1007/BF00240838

Echols WT, Wagner NK. 1972. Surface roughness and internal boundary layer near a coastline. Journal of Applied Meteorology 11: 658-662. https://doi.org/10.1175/1520-0450(1972)011%3C0658:SRAIBL%3E2.0.CO;2

Figueroa-Espinoza B, Salles P, Zavala-Hidalgo J. 2014. On the wind power potential in the northwest of the Yucatan Peninsula in Mexico. Atmósfera 27: 77-89.

Figueroa-Espinoza B, Salles P. 2014. Local Monin-Obukhov similarity in heterogeneous terrain. Atmospheric Science Letters 15: 299-306. https://doi.org/10.1002/asl2.503

Figueroa-Espinoza B, Salles P. 2020. Wind velocity vertical profile in a 50 m wind mast at Sisal, Yucatán, Mexico [data set]. Zenodo. http://doi.org/10.5281/zenodo.3923126

Foken Th, Wichura B. 1996. Tools for quality assessment of surface-based flux measurements, Agricultural and Forest Meteorology 78: 83-105. https://doi.org/10.1016/0168-1923(95)02248-1

Garratt JR. 1977. Review of drag coefficients over oceans and continents. Monthly Weather Review 105: 915-929. https://doi.org/10.1175/1520-0493(1977)105%3C0915:RODCOO%3E2.0.CO;2

Garza-Pérez JR, Ize-Lema IAR. 2017. Caracterización multidisciplinaria de la zona costera de Sisal, Yucatán. Laboratorio Nacional de Resiliencia Costera, Yucatan, Mexico. Available at: http://www.sisal.unam.mx/labeco/LAB_ECOLOGIA/Produccion_academica_de_Xavier_files/ZONA%20COSTERA%20SISAL.pdf (accessed on May 3, 2020).

Graefe J. 2004. Roughness layer corrections with emphasis on SVAT model applications. Agricultural and Forest Meteorology 124: 237-251. https://doi.org/10.1016/j.agrformet.2004.01.003

Granados-Martínez KP, Méndez-Barroso LA, Rivas Marquez JA 2019. Navopatía flux station eddy covariance (EC) data (2017-2019). PANGAEA. https://doi.org/10.1594/PANGAEA.905663

Hall DJ, Spanton AM, Dunkerley F, Bennett M, Griffiths RF. 2000. An Inter-comparison of the AERMOD, ADMS and ISC dispersion models for regulatory applications. R&D Technical Report P362. Environment Agency, Bristol, UK, 80 pp.

Inoue T, Glud RN, Stahl H, Hume A. 2011. Comparison of three different methods for assessing in situ friction velocity: A case study from Loch Etive, Scotland. Limnology and Oceanography: Methods 9: 275-287. https://doi.org/10.4319/lom.2011.9.275

Isaac P, Cleverly J, McHugh I, Van Gorsel E, Ewenz C, Beringer J. 2017. OzFlux data: Network integration from collection to curation. Biogeosciences 14: 29032928. https://doi.org/10.5194/bg-14-2903-2017

Liddell M. 2013. Cape Tribulation OzFlux tower site. Data from the Cape Tribulation site, Far North Queensland. OzFlux. Australian and New Zealand Flux Research and Monitoring. hdl: 102.100.100/14242

Mahrt L, Vickers D, Sun J, Jensen NO, Jørgensen H, Pardyjak E, Fernando H. 2001. Determination of the surface drag coefficient. Boundary-Layer Meteorology 99: 249-276. https://doi.org/10.1023/A:1018915228170

Monin AS, Obukhov AM. 1954. Basic laws of turbulent mixing in the surface layer of the atmosphere. Tr. Akad. Nauk. SSSR Geophiz. Inst. 24: 163-187.

Newman JF, Klein PM. 2014. The impacts of atmospheric stability on the accuracy of wind speed extrapolation methods. Resources 3: 81-105. https://doi.org/10.3390/resources3010081

Nieuwstadt F. 1978. The computation of the friction velocity u* and the temperature scale T* from temperature and wind velocity profiles by least-square methods. Boundary-Layer Meteorology 14: 235-246. https://doi.org/10.1007/BF00122621

Panofsky H, Tennekes H, Lenschow D, Wyngaard J. 1977. The characteristics of turbulent velocity components in the surface layer under convective conditions. Boundary-Layer Meteorology 11: 355-361. https://doi.org/10.1007/BF02186086

Pope ND, Widdows J, Brinsley MD. 2006. Estimation of bed shear stress using the turbulent kinetic energy approach—A comparison of annular flume and field data. Continental Shelf Research 26: 959-970. https://doi.org/10.1016/j.csr.2006.02.010

Stull RB. 1988. An introduction to boundary layer meteorology. Kluwer Academic Publishers, The Netherlands.

Silberstein R. 2015 Gingin OzFlux: Australian and New Zealand Flux Research and Monitoring. hdl: 102.100.100/22677. Available at: http://data.ozflux.org.au/portal/home.jspx (accessed on June 4, 2020).

Silberstein R. 2020. Personal communication.

Sorbjan Z. 1987. An examination of local similarity theory in the stably stratified boundary layer. Boundary-Layer Meteorology 38: 63-71. https://doi.org/10.1007/BF00121555

Sozzi R, Favaron M, Georgiadis T. 1998. Method for estimation of surface roughness and similarity function of the wind speed vertical profile. Journal of Applied Meteorology 37: 461-469. https://doi.org/10.1175/1520-0450(1998)037<0461:MFEOSR>2.0.CO;2

Stapleton KR, Huntley DA. 1995. Seabed stress determinations using the inertial dissipation method and the turbulent kinetic energy method. Earth Surface Processes and Landforms 20: 807-815. https://doi.org/10.1002/esp.3290200906

Taylor-Espinosa N. 2009. Análisis y visualización de la componente diurna de los vientos en el sur del Golfo de México. B.Sc. thesis. Facultad de Ciencias, UNAM, Mexico. Available at: http://132.248.9.195/ptd2009/marzo/0640679/Index.html

Uuh-Sonda JM, Gutiérrez-Jurado HA, Figueroa-Espinoza B, Méndez-Barroso LA. 2018. On the ecohydrology of the Yucatan Peninsula: Evapotranspiration and carbon intake dynamics across an eco-climatic gradient. Hydrological Processes 32: 2806-2828. https://doi.org/10.1002/hyp.13230

Uuh-Sonda JM, Figueroa-Espinoza B, Gómez-Nicolás MP, Gómez-Liera J. 2020. Wind observations in a 22 m tower at El Palmar state reserve, Yucatan, Mexico [data set]. Zenodo. https://doi.org/10.5281/zenodo.3975261

Uuh-Sonda JM, Figueroa-Espinoza B, Gutiérrez-Jurado HA, Méndez-Barroso LA. 2021. Ecosystem productivity and evapotranspiration dynamics of a seasonally dry tropical forest of the Yucatan Peninsula. Journal of Geophysical Research. Under review.

Weber RO. 1999. Remarks on the definition and estimation of friction velocity. Boundary-Layer Meteorology 93: 197-209. https://doi.org/10.1023/A:1002043826623

Wilczak JM, Oncley SP, Stage SA. 2001. Sonic anemometer tilt correction algorithms. Boundary-Layer Meteorology 99: 127-150. https://doi.org/10.1023/A:1018966204465

Wu J. 1980. Wind-stress coefficients over sea surface near neutral conditions—A revisit. Journal of Physical Oceanography 10: 727-740. https://doi.org/10.1175/1520-0485(1980)010<0727:WSCOSS>2.0.CO;2

Wyngaard JC, Coté OR, Izumi Y. 1971. Local free convection, similarity, and the budgets of shear stress and heat flux. Journal of the Atmospheric Sciences 28: 1171-1182. https://doi.org/10.1175/1520-0469(1971)028<1171:LFCSAT>2.0.CO;2

Yahaya S, Frangi JP. 2009. Profile of the horizontal wind variance near the ground in near neutral flow–K-theory and the transport of the turbulent kinetic energy. Annales Geophysicae 27: 1843-1859. https://doi.org/10.5194/angeo-27-1843-2009

Atmósfera 35(4), 687-699 (2022)
https://doi.org/10.20937/ATM.52982

CONTENTS

Application of a ground-based microwave radiometer in aviation weather forecasting in Indian Air Force

Savitesh MISHRA[1], Shreya PANDIT[1]*, Ashish MITTAL[1] and Velampudi Sudarshan SRINIVAS[2]

[1]*Air Force Centre for Numerical Weather Prediction, New Delhi 110003, India.*
[2]*Directorate of Meteorology, Indian Air Force, New Delhi 110003, India.*
*Corresponding author; email: varsha.23@gov.in

Received: September 28, 2020; accepted: March 24, 2021

RESUMEN

El pronóstico específico en tiempo e intensidad, a muy corto plazo o inmediato, es el mayor reto al que se enfrenta un meteorólogo aeronáutico. El radiómetro de microondas terrestre (MWR, por sus siglas en inglés) se ha utilizado para realizar predicciones inmediatas de la actividad convectiva y se determinó que existe una buena comparación entre los parámetros termodinámicos derivados del MWR y las observaciones de radiosondas GPS, lo que indica que las observaciones realizadas con el MWR se pueden utilizar para desarrollar técnicas de predicción inmediata de condiciones convectivas severas. En este estudio se busca resaltar la eficacia de MWR en tormentas eléctricas y niebla de pronóstico inmediato. En primer lugar, las observaciones del MWR ubicadas en Palam, Nueva Delhi, India, se han comparado con los datos de la radiosonda más cercana para determinar la variación en los perfiles respectivos. Se encontraron grandes diferencias en la humedad relativa (RH), mientras que las temperaturas del MWR se encontraron cercanas a la temperatura de radiosonda observada hasta 3.5 km. Posteriormente, los gráficos de dispersión y el coeficiente de correlación de los índices/parámetros termodinámicos indicaron que la mayoría de los parámetros no están correlacionados o tienen una correlación moderada sólo para los perfiles a las 12:00 UTC. La técnica superepoch de composición rezagada para varios índices/parámetros termodinámicos para obtener una imagen combinada de todos los casos de tormenta y niebla densa en la serie de tiempo no pudo determinar ningún patrón para predecir tormentas y niebla densa con un tiempo de espera de 2-4 h. Se analizó el perfil del MWR para un caso de ocurrencia de tormenta. No se observó una variación significativa en la mayoría de los índices (calculados a partir de los parámetros observados con el MWR) antes de que ocurriera la tormenta. La HR a nivel de congelación y entre 950 y 700 hPa fueron los únicos parámetros que aumentaron 4 h antes de la ocurrencia.

ABSTRACT

Time and intensity-specific very short-term forecasting or nowcasting is the biggest challenge faced by an aviation meteorologist. Ground-based microwave radiometer (MWR) has been used for nowcasting convective activity and it was established that there is a good comparison between thermodynamic parameters derived from MWR and GPS radiosonde observations, indicating that MWR observations can be used to develop techniques for nowcasting severe convective activity. In this study, efforts have been made to bring out the efficacy of MWR in nowcasting thunderstorms and fog. Firstly, the observations of MWR located at Palam, New Delhi, India have been compared with the nearest radiosonde data to ascertain the variation in respective profiles. Large differences were found in relative humidity (RH), whereas temperatures from MWR were found to be close to radiosonde observed temperature up to 3.5 km. Subsequently, the scatter plots and correlation coefficients of thermodynamic indices/parameters indicated that most of the parameters are either not correlated or have moderate correlation only for 12:00 UTC profiles. The superepoch technique of lagged composite for various thermodynamic indices/parameters to obtain a combined picture of all the thunderstorm and dense fog cases on the time series could not determine any pattern to predict thunderstorm and dense fog with lead time of 2-4 hours. MWR profile for a case of occurrence of thunderstorm was analyzed. No significant variation was observed in most of the indices (as calculated from MWR observed parameters) prior to the occurrence of thunderstorm. RH at freezing level and between 950 and 700 hPa levels were the only parameters, which increased four hours prior to the occurrence.

Keywords: radiosonde, microwave radiometer, nowcasting, superepoch analysis.

1. Introduction

1.1 Radiosonde and need of real time profiling

Information about the vertical atmospheric profile plays an important role in weather prediction. Radiosondes have been some of the most reliable means of retrieving these profiles. It is common practice to examine the temperature and humidity profiles measured by radiosonde and its derived thermodynamic indices/parameters in nowcasting convective weather events. Meteorologists have estimated the wind gust based on temperature, humidity and wind measurements (Lee, 2007). However, radiosonde profiles are discrete in nature and are available twice a day in general. On the other hand, weather instances are due to continuous changes in the atmosphere and these changes are more dynamic in pre-monsoon season, especially in tropical region. This necessitates the use of an equipment capable of continuous profiling to support nowcasting. MWR provides vertical profile of the atmosphere high temporal resolution. The ground-based microwave radiometer (MWR) is a passive sensor that provides continuous atmospheric profile from surface to 10 km. It measures the radiation intensity at different frequencies in the microwave spectrum, which are dominated by the absorption/emission of atmospheric water vapor, cloud liquid water and oxygen (Rose et al., 2003).

1.2 Earlier studies using MWR

As per Leena et al. (2015), analysis of MWR-measured temperature (specific humidity) has a warm (wet) bias below 3 km and cold (dry) bias above that altitude. However, correlation of stability indices estimated from radiometers and radiosondes showed fairly good correlation, with a correlation coefficient greater than 0.5 with 95% significance. Madineni et al. (2013) studied MWR profile over Indian region and depicted that MWR observations show warm (cold) bias in the temperature, except at 0.5 km, when compared to radiosonde observations below (above) 3-4 km, assuming latter as a standard technique. In case of water vapor, MWR observations show wet (dry) bias below (above) 2-3 km depending on the time. Venkat et al. (2013) reported warm (cold) bias in temperature below (above) a 3-4 km height when compared with radiosonde measurements. They also noticed a wet (dry) bias in specific humidity for 6-8 g kg^{-1} below (above) 2-3 km. Chan (2009) brought out that MWR does not cater for the scattering effects of rain in the given frequency and hence it must be used with caution during the actual occurrence of precipitation.

1.3 MWR in the Indian Air Force

The Indian Air Force (IAF) is in possession of 21 MWRs evenly distributed across the country. These are MP-3000A series passive radiometers, which provide continuous thermodynamic profile of the planetary boundary layer (PBL) and above up to 10 km. The equipment measures brightness temperature in both water vapor and oxygen bands and produces atmospheric sounding similar to that of radiosonde every minute. The system scans 21 K-band frequencies (22-30 GHz) and 14 V-band frequencies (50-59 GHz), which are dominated by absorption of water vapor and oxygen molecules, respectively. Retrievals are broadly classified into two domains, i.e., zenith and off-zenith (20º) to mitigate heavy precipitation. The intensities thus received are converted to temperature and moisture profiles by applying the Radiative Transfer Equation (RTE), historical soundings of nearby station and artificial neural network.

1.4 Nowcasting with MWR

In the field of aviation, thunderstorms and dense fog are considered as most dangerous aviation weather hazards. Historically, very short-range forecasting of convective weather incidents were based on the extrapolation of radar reflectivity echo. However, the accuracy of these predictions decreases very rapidly in first 30 min because of short life span of convective cells. For forecasts periods beyond

20 min, techniques for predicting the initiation, growth and dissipation of convective storms are essential (Hering et al., 2004). Similarly, significant changes occurring within the PBL are most important to be trapped to predict the occurrence or dissipation of dense fog. MWR has the advantage of continuous monitoring of atmosphere and can play an important role in nowcasting these events. A comprehensive study by Chan (2009) discussed the importance of MWR profile in nowcasting of intense convective weather over Hong Kong. Later (Chan, 2009), he elaborated the importance of MWR derived indices and their usage in nowcasting by correlating derived variables with the lightning activity. Madhulatha et al. (2013) presented the superepoch analysis to bring out the changes in various thermodynamics indices in pre-convective environment.

1.5 Thermodynamic indices of MWR and radiosonde
Thermodynamic indices are considered as predictors for forecasting aviation weather hazards. The thresholds values of indices calculated from radiosonde observations may not be the same as calculated with the MWR profiles, as both equipments have different working principles. MWR data is to be validated against the nearest radiosonde profile to understand the degree of variation. This paper presents validation of profiles of the MWR installed at Palam, New Delhi, India, vis-à-vis the nearest radiosonde station of India Meteorological Department (IMD) at Safdarjung, New Delhi. Efforts have also been made to study the correlation between the various thermodynamic indices generated by MWR and radiosonde data sets. These indices have been studied further on the temporal scale to bring out the usage of MWR in nowcasting thunderstorm and fog events over Delhi.

2. Instrumentation and methodology

2.1 Instrumentation over the area of experimentation

2.1.1 Palam radiometer
The radiometer installed at Palam (28.5º N, 77.1º E, 237 masl), Delhi measures radiation intensity at water vapor (22-30 GHz) and oxygen channel (50-59 GHz) to obtain the temperature and humidity profile. MWR generates profiles every 2 min with 50 m vertical resolution up to 0.5 km, 100 m resolution from 0.5 to 2 km and 250 m resolution from 2 to 10 km. A total of three retrievals are available for a given time period, i.e., one zenith and two off-zeniths on either side at a 20º angle. An average of all the three profiles for each time frame is also made available to the users. However, for the present study only the zenith scan has been utilized. Retrieval of temperature and humidity profiles from radiation intensity is done by applying RTE and artificial neural networks to historical sounding data. The accuracy of temperature and RH sensor of MP-3000A series radiometer is claimed to be 0.5 ºK and 2%, respectively, which is at par with radiosonde observations.

2.1.2 India Meteorological Department radiosonde
Radiosonde data of the nearest India IMD observation station, Safdarjung (28.5º N, 77.2º E, 216 masl, Delhi, is used as the base profile to carry out the comparative study. The observations are available twice (00:00 and 12:00 UTC) daily. Both the profiles have been studied separately in this paper for eight cases of thunderstorm and three cases of dense fog events over Delhi. Occurrence, cessation and variation in the intensity of weather events were studied through half hourly aerodrome routine meteorological reports (METAR). Convective events were further substantiated by a Lightning Detection System (LDS) of IAF, a Doppler Weather Radar (DWR) at the Indira Gandhi International Airport (IGI), Delhi and INSAT-3D IR1 images of the relevant time period. Various cases of the significant weather events considered in the present study are shown in Table I.

Table I. Cases of occurrence of thunderstorms and fog.

No.	Type of event	Date
1	Thunderstorm	07 May 2018
2	Thunderstorm	27 Jun 2018
3	Thunderstorm	22 Jul 2018
4	Thunderstorm	26 Jul 2018
5	Thunderstorm	06 Sep 2018
6	Thunderstorm	08 Sep 2018
7	Thunderstorm	22 Jan 2019
8	Thunderstorm	07 Feb 2019
9	Fog	01 Jan 2018
10	Fog	06 Jan 2018
11	Fog	29 Jan 2018

2.2 Methodology

In the first part of this study, validation of MWR data is undertaken with the nearest radiosonde profile. Thereafter, a total of nine parameters were studied to bring out the correlation between both the derived profiles: K-Index (KI, in ºC); Total Totals Index (TTI, in ºC); Vertical Total Totals Index (VTT, in ºC); Cross Total Totals Index (CTT, in ºC); MEAN_RH (950-700 hPa, in %); RH at freezing level (FL, in %); TEMP_DIFF (950-700 hPa, in ºC); TEMP_DIFF (700-400 hPa, in ºC), and TEMP_DIFF (400-300 hPa, in ºC). P value for each set of indices has been calculated using t-test to bring out the probability of variation between datasets.

KI is a measure of thunderstorm potential based on the vertical temperature lapse rate, and the amount and vertical extent of low-level moisture in the atmosphere, calculated as KI = T(850 hPa) + Td(850 hPa) – T(500 hPa) – DD(700 hPa) × VTT, represents static stability or the lapse rate between 850 and 500 hPa, calculated as VTT = T(850 hPa) – T(500 hPa). Whereas CTT includes the 850 hPa dewpoint and is represented as CT =Td(850 hPa) – T(500 hPa). The Total Totals Index consists of two components, vertical totals (VTT) and cross totals (CTT). As a result, TTI accounts for both static stability and 850 mb moisture but would be unrepresentative in situations where the low-level moisture resides below the 850 mb level. TTI can be calculated as TTI = VTT + CTT. Mean RH between 950-700 hPa and at freezing level (RH_FL), along-with temperature differences at three distinct levels, was calculated to derive the moisture availability and lapse rate in the atmosphere. Last part of the study deals with plotting and studying the temporal variation of stability indices in pre-convective environment. The superepoch analysis is carried out with the aim to comment upon the utility of these indices in nowcasting thunderstorm and dense fog events over Delhi.

3. Results and discussion

3.1 Validation of MWR profile using radiosonde data

3.1.1 Comparison of 00:00 and 12:00 UTC profiles

Temperature and RH profiles of MWR and nearest radiosonde (Safdarjung, Delhi) observations have been compared for all the 11 cases. Mean profiles of the MWR zenith scan for 00:00 and 12:00 UTC and radiosonde are shown in Figures 1 and 2, respectively, where the Y-axis depicts altitude of the comparison in

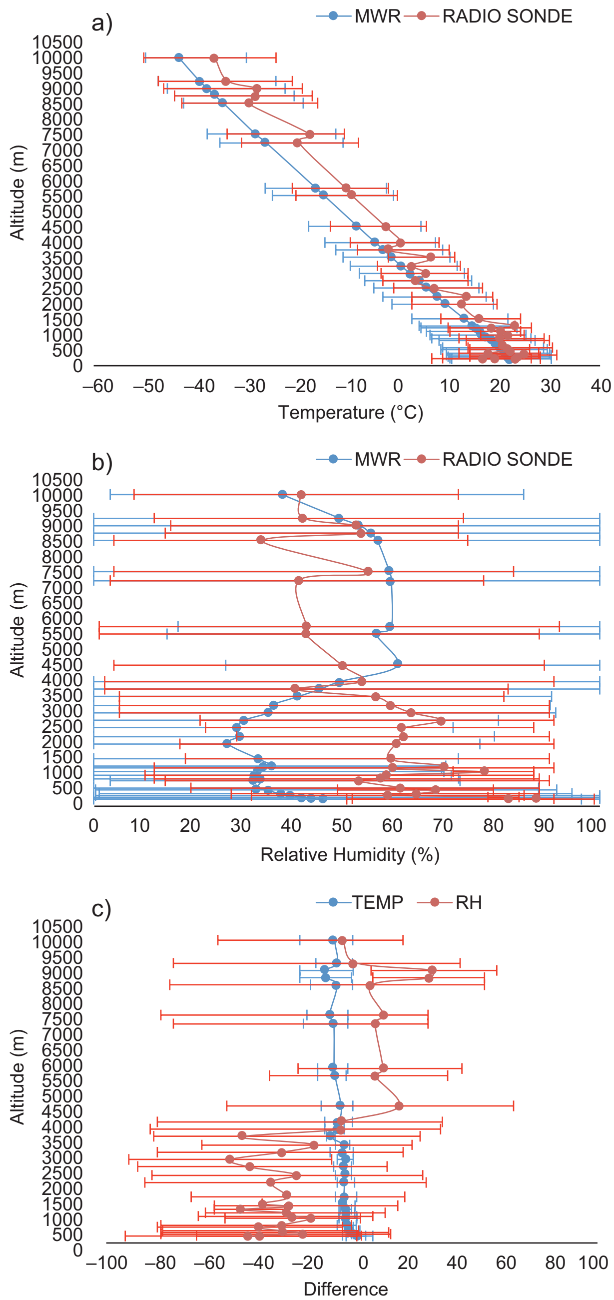

Fig. 1. 00:00 UTC composite profiles along with standard deviation observed for all cases under study. (a) Temperature). (b) Relative humidity (%). (c) Differences between radiosonde and MWR temperatures (blue line) and relative humidity (red line).

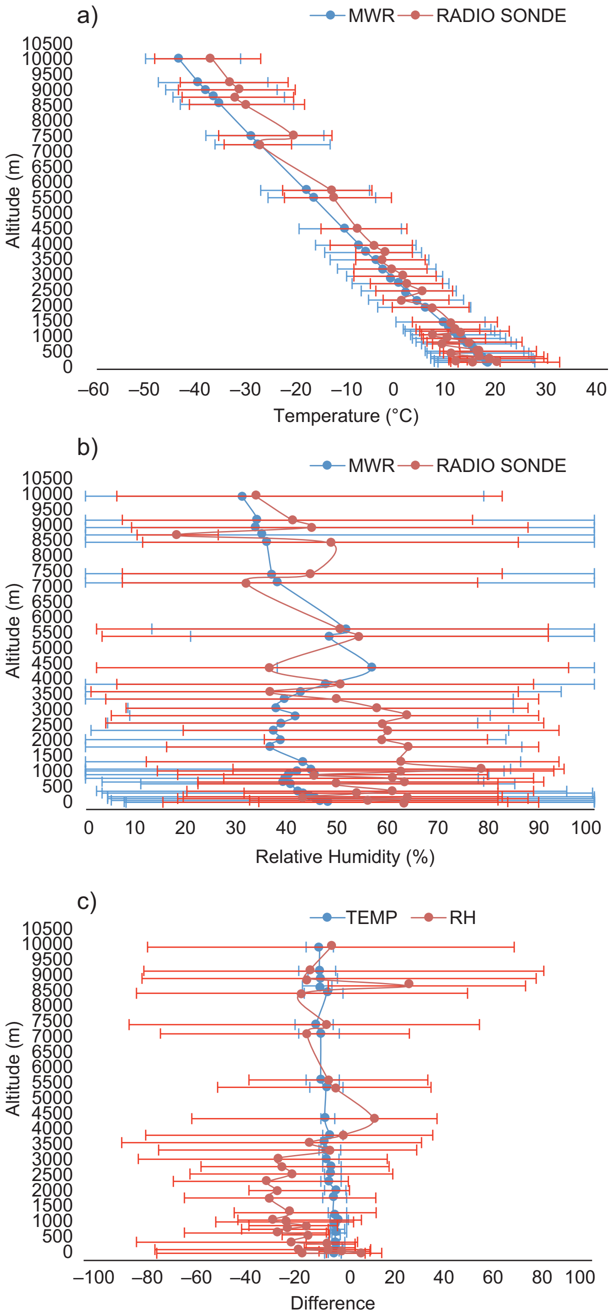

Fig. 2. 12:00 UTC composite profiles along with standard deviation observed for all cases under study. (a) Temperature. (b) Relative humidity (%). (c) Differences between radiosonde and MWR temperatures (blue line) and relative humidity (red line).

meters above mean sea level. Temperature profiles for both 00:00 and 12:00 UTC represent the close match up to 3.5 km (Figs. 1a and 2a). However, temperature has a variation of 1-2 ºC (RS-based temperatures are higher as compared to MWR) at middle and upper levels as shown in the difference profile of Figures 1c and 2c. MWR profiles show a cold bias above 3.5 km and the trend remains the same with variations in quantity at various levels. Contrast in the RH profile was found to be large at different levels for both 00.00 and 12:00 UTC (Figs. 1b and 2b). Deviation is even larger at lower levels, i.e., below 3.5 km. Figures 1c and 2c depict the difference plot of RH. It clearly shows the presence of a dry bias in the range of 30-50% up to 3.5 km, and thereafter a wet bias of 20-30% at higher levels. The variations in RH were found to be higher (about 10-15%) for the morning profiles.

3.1.2 Variations in MWR-radiosonde profiles

Chan and Hon (2011) established that the measurement principle of the two instruments is different (volume integral above a fixed location on the ground for radiometer vs. point measurement of a drifting balloon for radiosonde), hence there are biases and spreads of the data, but the trend was found to be identical. However, the present case study reflects that only the temperature trend of both profiles matches, whereas the RH profile has variations, primarily up to 3.5 km.

3.2 Correlation between MWR and radiosonde based indices

Correlation and p-value (using a t-test) between MWR and RS-based indices were calculated separately for 00:00 and 12:00 UTC profiles (Table II). A total of nine indices/parameters of zenith scan of MWR and nearest RS station have been studied. The results showed that none of these indices are correlated for the 00:00 UTC profile. However, moderate correlation in KI, VTT, TTI, MEAN_RH (950-700 hPa) and TEMP_DIFF (950-700 hPa) were observed for the 12:00 UTC profile. The scattered plots of one of the least (KI for 00:00 UTC) and best (TEMP_DIFF between 950 and 700 hPa for 12:00 UTC) correlated indices are depicted in Figure 3, which the high variation of parameters derived form MWR and radiosonde profiles are confirmed. The best-fit line along with the equation are shown over the plots; however, it cannot be used for forecasting purposes.

Table II. Correlation between MWR- and radiosonde-based indices at 00:00 and 12:00 UTC.

No.	Indices	Correlation values (R)/p-value (00:00 UTC)	Correlation values (R)/p-value (12:00 UTC)
1	KI	0.09/0.79	0.49/0.12
2	CTT	0.09/0.79	0.25/0.45
3	VTT	0.16/0.63	0.49/0.12
4	TTI	0.16/0.63	0.36/0.27
5	MEAN_RH (950-700 hPa)	0.16/0.63	0.49/0.12
6	RH_FL	0.04/0.90	0.16/0.63
7	TEMP_DIFF (950-700 hPa)	0.04/0.90	0.81/0.002
8	TEMP_DIFF (700-400 hPa)	0.09/0.79	0.16/0.63
9	TEMP_DIFF (400-300 hPa)	0.16/0.63	0.16/0.63

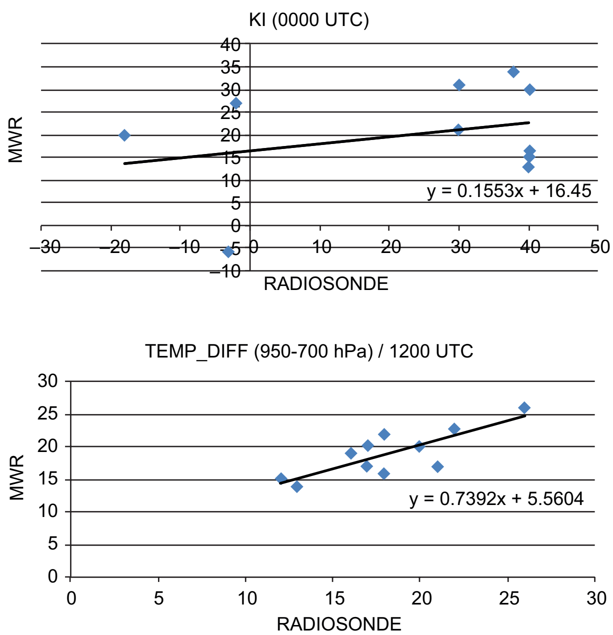

Fig. 3. Scatter plot of MWR-radiosonde indices generated with 00:00 and 12:00 UTC profiles. (a) KI (in ºC) at 00:00 UTC with one of the lower correlations (0.09). (b) Temperature differences between 950 and 700 hPa (in ºC) at 12:00 UTC with best correlation (0.81).

3.3 Case study of thunderstorm over Delhi on February 17, 2009

3.3.1 Cases under study

A total of eight thunderstorm cases over Delhi have been studied**.** An elaborated analysis of a thunderstorm event occurred on February 7, 2019 has been covered in this section.

3.3.2 Weather sequence

Cyclonic storms associated with the mid latitude Subtropical Westerly Jet (SWJ), referred to as Western Disturbances (WDs) play a critical role in the meteorology of the Indian subcontinent. WDs embedded in the southward propagating SWJ produce extreme precipitation over northern India and are further enhanced over the Himalayas due to orographic land-atmosphere interactions (Dimri et al., 2015). A similar type of extra-tropical system moved across the northern region on February 7, 2019. INSAT-3D (IR1) satellite images of that day from 10:30 to 13:30 UTC (Fig. 4) depict the presence of multi-layered clouding embedded with intense convection in isolation over Delhi and adjoining area. METAR reports of IGI airporta in Delhi reveal the commencement of thunderstorm activity with effect from 11:30 UTC.

3.3.3 Movement of convective cells

The MWR location is approximately 10 km (aerial) southwest of the IGI airport, Delhi. The Max (z) product of DWR, installed at the airport, is shown in Figure 5. It clearly indicates the presence of a convective cell southwest of the MWR station at 10:32 UTC with vertical extent up to 6 km. This cell can be seen overhead at 11:02 UTC with a new one developing in southwest direction at a distance of 20 km. A second convective cell reached overhead by 12:32 UTC. Reflectivity on both occasions was > 57.0 dBZ, which substantiates the presence of intense convection.

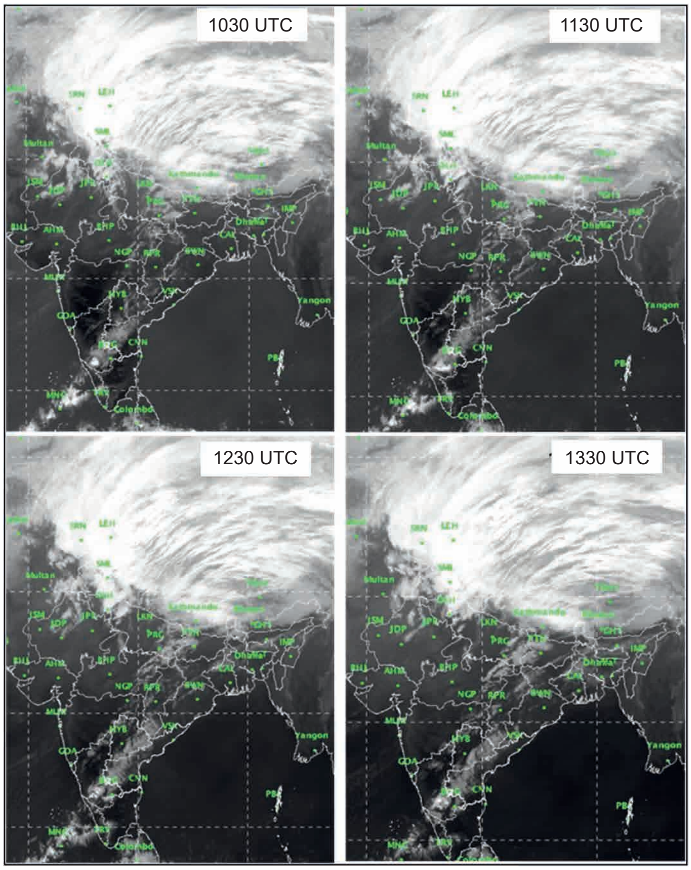

Fig. 4. INSAT-3D (IR1) images of February 7, 2019 from 10:32 to 13:02 UTC.

3.3.4 MWR profile of the episode

Pre- and post-convective environment of February 7, 2019 was also studied in the light of MWR based profile. Timeline of temperature, RH and vapor density variations are depicted in Figure 6, where it is clearly shown that vertical temperatures were insensitive to the pre-convective environment and sharp changes could only be seen during the actual occurrence of the weather event (11:30 UTC). High RH% (> 90%) was seen at lower levels (up to 1.5 km) at 09:00 UTC and the same reduced thereafter until the time of occurrence. RH was seen increasing gradually from 09:00 UTC onwards between 3 and 6 km. However, the quantity reduced significantly to 70% just prior to the occurrence. Absolutely saturated atmosphere is depicted during the time of occurrence of both the spells. A gradual increase of vapor density was also observed prior to the occurrence, wherein the values reached from 1 to 7 g m^{-3} in between 2 and 3 km levels. At lower levels the gradient was higher, with an increase of approximately 8.0 units. Maximum contours in the values coincide with the time of occurrence. Vapor density is the only parameter showing significant changes in pre-convective environment. The rise in this feature is indicative of the increase in saturated water content at different levels of the atmosphere which contributed to the convective build-up.

3.3.5 Lightning counts and MWR indices

The case was further analyzed by calculating and studying the variation of MWR-based indices. For that purpose, pre- and post-convective hourly values of the various indices/parameters have been plotted against the total number of lightning flashes sensed by the IAF LDS within 50 km of the MWR location. Figure 7 shows the variation in different indices with respect to number of lightning flashes on the

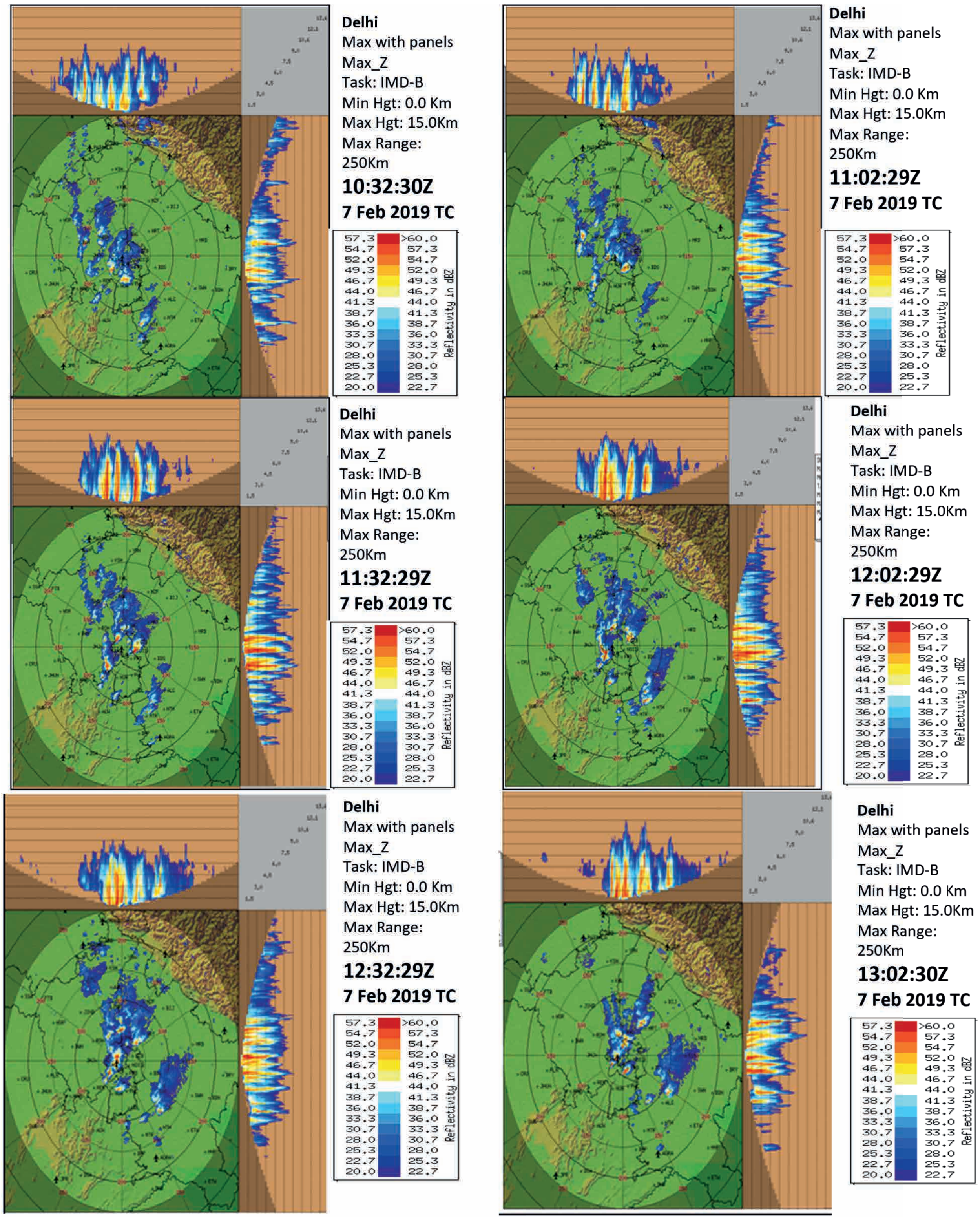

Fig. 5. DWR Max (z) products of Delhi Indira Gandhi International Airport of February 7, 2019 from 10:32 to 13:02 UTC.

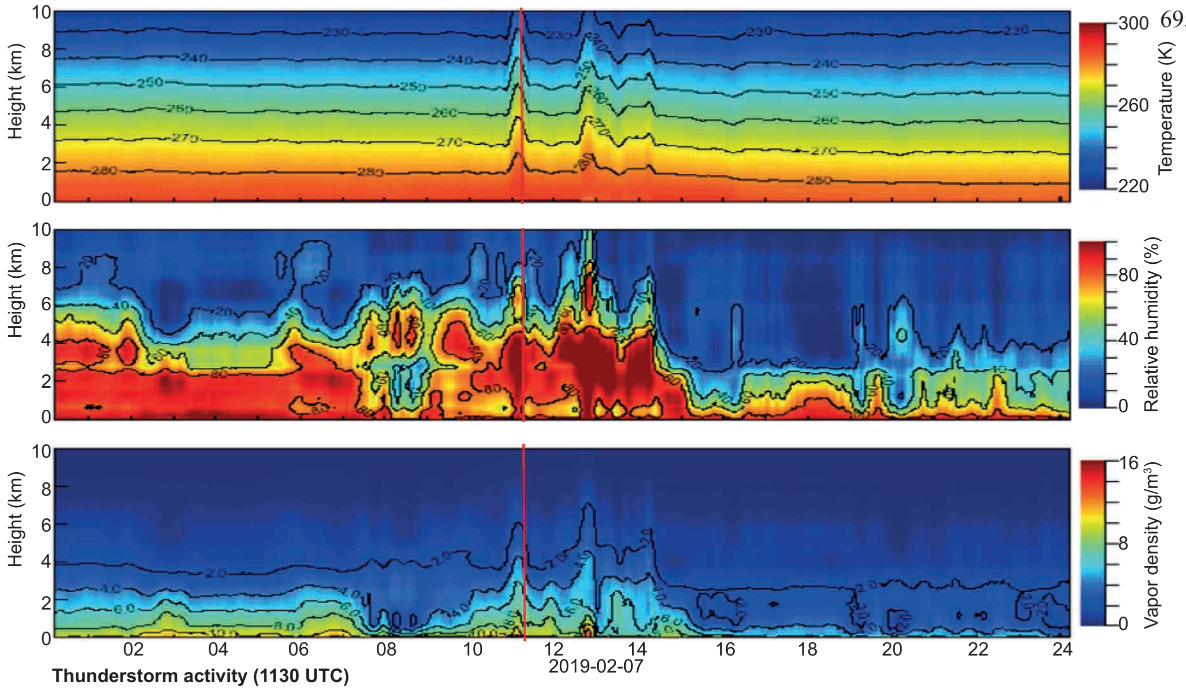

Fig. 6. MWR-generated profile for February 7, 2019 displaying variations in temperature, relative humidity and vapor density regarding the genesis of thunderstorm.

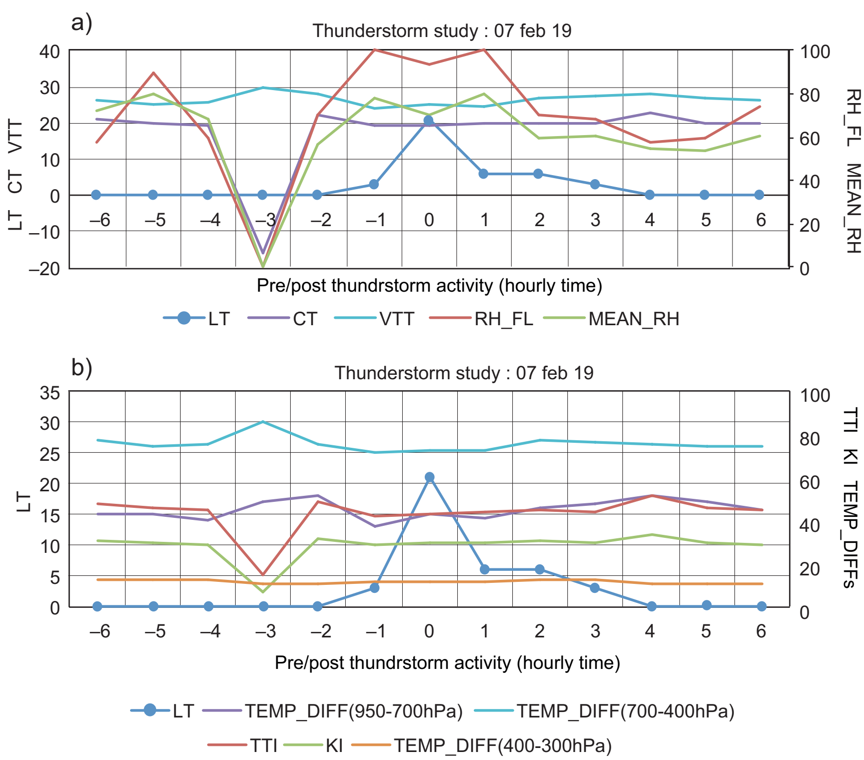

Figure 7. Time series plot of various indices and parameters generated through the MWR profile on February 7, 2019 vs. the count of lightning. X-axis shows the ±6 h of post/pre convective phase where x = 0 depicts the time of maximum thunderstorm activity. (a) The left Y axis denotes the variation of CT, VT and lightning count and the right Y-axis denotes the variation of RH at freezing level (RH_FL), mean relative humidity. (b) The left Y-axis denotes the variation of lightning count and the right Y-axis denotes variations of TTI, KI and temperature differences at various levels (TEMP_DIFFs).

day of occurrence. Left Y-axis depicts the number of lightning flashes, CT and VTT and right Y-axis depicts the variation of RH, TTI, KI and temperature differences for various levels. X-axis represents the timeline where “0” is the time of occurrence (11:30 UTC) and “±” values depict pre- and post-convective hours, respectively. Analysis portrays the significant increase in RH% at freezing level and between 950-700 hPa, wherein the values reach to 98% as compared to nil, recorded 3 h prior to occurrence. Decreasing trend in the CT, VTT (Fig. 7a), TTI and KI (Fig. 7b) indices were noticed prior to the time of occurrence of thunderstorm. Feeble fall (~ 3 ºC) in the temperature difference of 950 and 700 hPa (Fig. 7b) level was recorded 1 h prior to the occurrence of thunderstorm. Temperature variations in middle (700-400 hPa) and upper (400-300 hPa) levels were found to be insignificant (Fig. 7b).

3.4 Superepoch analysis

3.4.1 Time lag analysis

Madhulatha et al. (2013) suggested the superepoch analysis technique to obtain a composite picture of all thunderstorm events vis-à-vis the variation of different indices/parameters on the time series. To examine the temporal variations of various thermal indices lagged composite of all the nine parameters are calculated and depicted in Figure 8. The thunderstorm time of occurrence is considered as lag 0 and lag –6 corresponds to the environment 6 h before the thunderstorm. Similarly, lag +6 denotes the environment 6 h after the occurrence of the thunderstorm. In the current depiction, storm occurrence in considered as zero.

3.4.2 Amalgamated depiction of thunderstorm cases

For this technique, nine parameters were calculated for all the eight thunderstorm cases. Pre- and post-

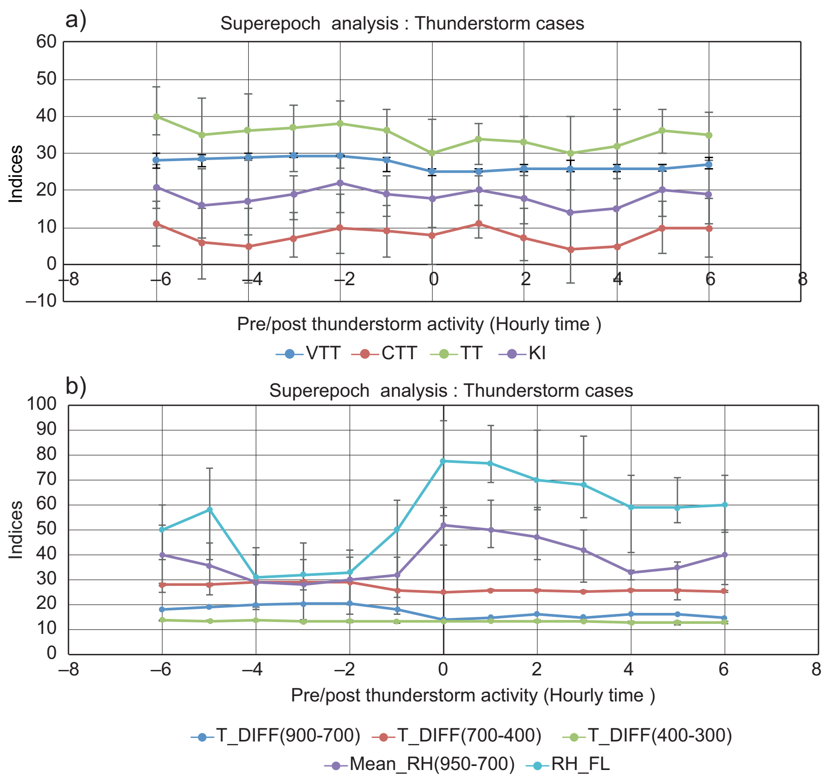

Fig. 8. Superepoch analysis of nine indices/parameters for eight thunderstorm cases, where x = 0 depicts the time of maximum thunderstorm activity. (a) VTT, CTT, TT, and KI. (b) T_DIFF (900-700 hPa), T_DIFF (700-400 hPa), T_DIFF (400-300 hPa), MEAN_RH (950-700 hPa), and RH_FL.

environment conditions were superimposed to give a composite picture of each case and thereafter all the cases were merged to present an average variation in the indices/parameters. The average variation is depicted in bold lines in Figure 8, whereas the vertical bars showcase the range of deviation.

3.4.3 Thunderstorm nowcasting

Rajeevan et al. (2012) mention that the variation of composite time series of thermodynamical parameters can explain the prerequisites necessary for the genesis of thunderstorm activity. A similar concept has been implemented in the superepoch analysis, where the MWR based indices/parameters are studied to enable the nowcasting of thunderstorm events. VTT remained almost constant with a value of 28 ºC (Fig. 8a) prior to the thunderstorm occurrence. The CTT, TT and KI indices (Fig. 8a) showed sinusoidal patterns with a marginal fall prior to the occurrence. During the time of occurrence, KI was about 20 ºC, which is very low as compared to 42 ºC as observed by Madhulatha et al. (2013). A lapse rate in the 900-700 and 700-400 hPa (Fig. 8b) layers was of 1 and 3 ºC, respectively. However, a feeble variation of 0.1 ºC was seen in the lapse rate of 400-300 hPa (Fig. 8b). The other two parameters that displayed gradual variation four hours prior to the occurrence were mean RH between 950 and 700 hPa (Fig. 8b) and RH at freezing level (Fig. 8b). The rise in RH at freezing level was close to 36% whereas that of mean RH between 950 and 700 hPa was almost 20%.

3.4.4 Superepoch analysis of fog events

Superepoch analysis was also applied to three cases of dense fog over Delhi, where the visibility dropped to zero in the morning hours (Fig. 9). However, the studied parameters were related to moisture and temperature variations at the lower levels (between 200 and 500 m) only. A marginal rise of the order of 0.25 ºC in the lapse rate between 500 and 200 m was noticed prior to the occurrence of fog. Total vapor pressure in the similar levels was almost constant with a value of 40 g m^{-3}. Nil variation was noticed in total liquid water with values close to 0.3 g m^{-3}. A gradual increase in mean RH was recorded at the lower levels with a variation of approximately 22%.

4. Inferences and conclusion

The main objective of this study was to analyze the use of a ground based MWR for aviation weather forecasting in the IAF. For this purpose, data of the MWR were first validated using an RS for the similar time period. The results showed that the MWR and RS temperature profiles had minimal variations below 3.5 km for both 00:00 and 12:00 UTC. However, a moderate deviation was noted at mid and higher levels.

The variation in RH profile was noticed with a dry bias at lower levels and a wet bias at middle and higher levels. It was even larger at 00:00 UTC, which means that MWR-generated profiles (especially at 00:00 UTC) are significantly different from RS profiles. Also, a weak correlation and a high p-value between most of the datasets shows a large variation in derived parameters of the MWR and RS profiles.

Hence, the threshold values of indices or parameters developed with the studies of radiometer data cannot be explicitly implemented for forecasting through MWR profiles. Real time inputs received from MWRs should not be used isolated. These

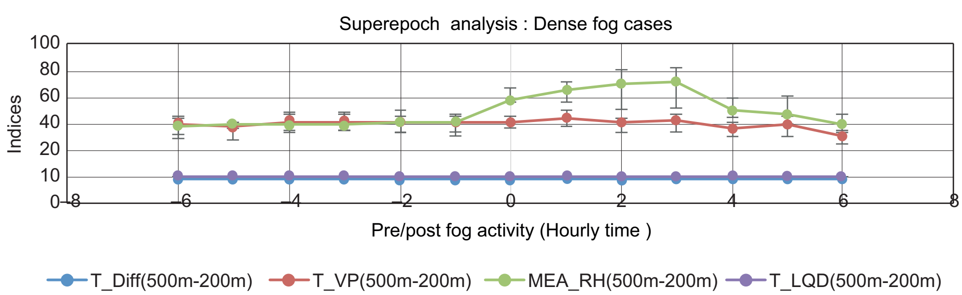

Fig. 9. Superepoch analysis of four parameters for three dense fog cases, where x = 0 depicts the time of maximum intensity of fog.

indices need to be correlated with local forecasting suggestions and thereafter be utilized for nowcasting purposes. These huge variations may be attributable to the neural network technique and the quality of historical data used to generate the MWR profile from raw data of brightness and temperature. After the neural upgrade of MWR, the profile sensitivity needs to be established vs. thunderstorm and fog events. Refinements of the threshold values of thermodynamic indices for MWR-based prediction may also be carried out on large historical datasets.

Similarly, correlation between different indices generated through MWR and RS profiles were calculated. The results showed that parameters of 00:00 UTC have no correlation. However, a total of five parameters showed moderate correlation for 12:00 UTC profiles, which shows that RH% variation has a profound impact on most of the indices and they cannot be implemented for nowcasting purpose in isolation.

As per Madhulatha et al. (2013), the superepoch analysis suggested that many thermodynamic parameters, lower-level RH, stability index at different levels, and lapse rate of equivalent potential temperature exhibited useful signals at least 3 h before the storm occurrence. Their analysis showed sharp changes in the thermodynamic parameters associated with storms. There are appreciable differences in the variations between thunderstorm and non-thunderstorm cases. However, in the present superepoch analysis most of the parameters under study remain insensitive prior to the occurrence of a severe weather phenomenon. At the same time, standard errors were huge. Parameters like total liquid, temperature difference, and total vapor density at 500-200 m gave no indication of dense fog events. Steep variation in the MWR profiles for similar weather makes it difficult for the forecaster to select any reliable nowcasting indices to predict thunderstorm and dense fog events.

Atmospheric instabilities, mainly convection, depend on temperature distribution and moisture availability (Leena, 2015), which are measured at very high resolution using MWR. However, based on the present study it can be inferred that MWR can only be utilized as an observation tool. Due to its inherent sources of error, MWR profiles cannot be exploited for the nowcasting purpose. There could be multiple reasons for this outcome of the study, being the most noticeable the difference between MWR and RS techniques for retrieval/observation of parameters. However, the results may vary if a greater number of cases are studied, a better neural network is treated and also the off-zenith profiles of MWR are considered for different geographical locations of the country.

Acknowledgments

The authors are extremely grateful to Air Vice Marshal Dr. Sanjay Tyagi, Assistant Chief of Air Staff (Meteorology), Indian Air Force, for providing data, professional guidance and motivation during the study period. The authors sincerely thank Air Commodore (Meteorology) Dr. JK Sahu for the encouragement and support for improving the manuscript. The authors are also thankful to Director General, Indian Meteorological Department (IMD) for providing radiosonde data. The authors acknowledge the maintenance services provided by Radiometrics Corporation.

Data availability

Due to the sensitive nature of the data used in this study, authors are not able to share the research data.

References

Chan PW. 2009. Performance and application of a multi-wavelength, ground-based microwave radiometer in intense convective weather. Meteorologische Zeitschrift 18: 253-265. https://doi.org/10.1127/0941-2948/2009/0375

Chan PW, Hon KK. 2011. Application of ground-based, multichannel microwave radiometer in the nowcasting of intense convective weather through instability indices of the atmosphere. Meteorologische Zeitschrift 20: 431-440. https://doi.org/10.1127/0941-2948/2011/0276

Dimri AP, Niyogi D, Barros AP, Ridley J, Mohanty UC, Yasunari T, Sikka DR. 2015. Western disturbances: A review. Reviews of Geophysics 53: 225-246. https://doi.org/10.1002/2014RG000460

Hering AM, Morel C, Galli G, Sénési S, Ambrosetti P, Boscacci M. 2004. Nowcasting thunderstorms in the alpine region using radar based adaptive thresholding scheme. In: 3rd European Conference on Radar in Meteorology and Hydrology (ERAD), Visby, Sweden, September 6-10. Available at: http://www.copernicus.org/erad/2004/online/ERAD04_P_206.pdf (accessed on April 10, 2021).

Lee OSM. 2007. Forecast of strong gust associated with thunderstorms based on data from radiosonde ascents and automatic weather stations. In: 21st Guangdong-Hong Kong-Macao Technical Seminar on Meteorological Science and Technology, Hong Kong.

Leena PP, Dani KK, Nath A, Sanap SD, Pandithurai G, Anil Kumar V. 2015. Validation of ground-based microwave radiometer data and its application in verifying atmospheric stability over Mahbubnagar during 2011 monsoon and post-monsoon seasons. International Journal of Remote Sensing 36: 2920-2933. http://doi.org/10.1080/01431161.2015.1051632

Madhulatha A, Rajeevan M, Madineni VR, Bhate J, Naidu CV. 2013. Nowcasting severe convective activity over southeast India using ground-based microwave radiometer observations. JGR Atmospheres 118: 1-13. https://doi.org/10.1029/2012JD018174

Rajeevan M, Madhulatha A, Rajasekhar M, Bhate J, Kesarkar A, Apparao BV. 2012. Development of a perfect prognosis probabilistic model for prediction of lightning over south-east India. Journal of Earth System Science 121: 355-371. https://doi.org/10.1007/s12040-012-0173-y

Rose T, Crewell S, Löhnert U, Simmer C. 2005. A network suitable microwave radiometer for operational monitoring of the cloudy atmosphere. Atmospheric Research 75: 183-200. https://doi.org/10.1016/j.atmosres.2004.12.005

Venkat Ratnam M, Durga Santhi Y, Rajeevan M, Vijaya Bhaskara Rao S. 2013. Diurnal variability of stability indices observed using radiosonde observations over a tropical station: Comparison with microwave radiometer measurements. Atmospheric Research 124: 21-33. https://doi.org/10.1016/j.atmosres.2012.12.007

Atmósfera 35(4), 701-717 (2022)
https://doi.org/10.20937/ATM.52985

Spatial and temporal changes of land uses and its relationship with surface temperature in western Iran

Noredin ROSTAMI[1]* and Hassan FATHIZAD[2]

[1]*Department of Rangeland and Watershed Management, Faculty of Agriculture, Ilam University, Ilam, Iran.*
[2]*Department of arid and desert regions management, School of Natural Resources and Desert Studies, Yazd University, Yazd, Iran.*
*Corresponding author; email: n.rostami@ilam.ac.ir

Received: October 1, 2020; accepted: March 22, 2021

RESUMEN

Se utiliza un algoritmo de ventana dividida en la cuenca de la presa de Ilam para determinar la relación entre la temperatura de la superficie terrestre (LST, por sus siglas en inglés) y los tipos de uso de suelo. Se utilizan imágenes satelitales Landsat del sensor TM para 1990, 1995, 2000, 2005 y 2010 y Landsat 8 (sensor OLI) para 2015 y 2018. Después de las correcciones geométricas y radiométricas de las imágenes satelitales, los mapas de uso del suelo se extraen mediante el método de lógica difusa ARTMAP. Una evaluación de precisión mostró que el valor más alto del coeficiente kappa fue de 94% con una precisión total de 0.95 para 2015, y que su valor más bajo fue de 87% con una precisión total de 0.9 para 1990. Los valores altos de estos coeficientes indican una precisión aceptable en el uso de datos de teledetección Landsat para el uso del suelo. Los cambios más importantes en el uso del suelo están relacionados con bosques densos y bosques dispersos, con una disminución de 20.07 y 17.04%, respectivamente. Los valores mínimos de LST en 1990, 2010 y 2018 en bosques densos son de 21.27, 30.55 y 33.82 ºC, respectivamente. Los valores máximos de LST para el uso de tierras forestales dispersas en 1990 y 2010 es 52.48 y 56.09 ºC, respectivamente, y de 56.10 ºC para el uso de tierras forestales densas en 2018. Como resultado, el LST promedio en tierras agrícolas fue más bajo que en bosques dispersos y pastizales, lo cual se debe principalmente al alto contenido de humedad y a la mayor tasa de evapotranspiración. Las variaciones de uso del suelo/cobertura del suelo (LULC) de 1990 a 2018 muestran que en todos los usos del suelo se ha experimentado un aumento de la LST.

ABSTRACT

A split-window algorithm has been used in the Ilam dam watershed to determine the relationship between land surface temperature (LST) and types of land use. Landsat satellite images of the TM sensor for 1990, 1995, 2000, 2005 and 2010 and Landsat 8 (OLI Sensor) for 2015 and 2018 are used. After geometric and radiometric corrections of satellite images, land use maps are extracted by using the fuzzy ARTMAP method. An accuracy assessment showed that the highest value of the kappa coefficient was 94% with a total accuracy of 0.95 for 2015, and the lowest kappa coefficient value was 87% with a total accuracy of 0.9 for 1990. The high values of these coefficients indicate the acceptable accuracy of using Landsat's remote sensing data for land use detection. The most important land use change is related to dense forest and sparse forest land uses, with decreases of 20.07 and 17.04%, respectively. The minimum LST measures in 1990, 2010, and 2018 in dense forest are 21.27, 30.55 and 33.82 ºC, respectively. The maximum LSTs for the sparse forest land use in 1990 and 2010 are 52.48 and 56.09, and 56.10 ºC for the dense forest land use in 2018. As a result, the average LST in agricultural lands was lower than in sparse forest and rangeland;, which is mainly due to the high moisture content and the greater evapotranspiration rate. Land use/land cover variations from 1990 to 2018 show that all land uses have experienced an increase in LST.

Key words: Landsat satellite, split-window algorithm, fuzzy ARTMAP, kappa coefficient, Ilam dam watershed.

1. Introduction

Land use and land cover change (LUCC) are among the major driving forces of regional and global climate change (Feddema et al., 2005). However, climatic effects of deforestation and agricultural development vary from one region to another, and studies clearly show that land use changes and land cover play an important biophysical and biochemical role in climate systems at local, regional, and even continental scales (Brovkin et al., 2013; Luyssaert et al., 2014; Mahmood et al., 2014). These also depend on seasonality and land-atmosphere interaction (Halder et al., 2016). Contemporaneous social and economic developments have intensified the impact of human activities on land surface temperature (LST). Urban development, due to the reduction in vegetation cover (Feng et al., 2012) and the increase in impervious materials such as concrete and asphalt (Connors et al., 2013; Hasanlou and Mostofi, 2015; Pal and Ziaul, 2017; Ziaul and Pal, 2018a), increases LST (Amiri et al., 2009). Other factors such as radiation conditions, heat conduction in the upper layer of the Earth's surface, elevation from the surface of the Earth, relief, cloudiness, oceanic flows, and horizontal and vertical air flow are also important to determine LST. Therefore, intensity of land use can reflect the intensity of human activities, providing a basis to assess the relationship between land use change and environmental modifications.

LST is a major parameter in assessing the exchange of surface material, energy balance, and physical and chemical processes, and is now widely used in soil, hydrology, biology, and geochemistry studies (Tomlinson et al., 2011; Hao et al., 2016). Also, LST is an important factor in global studies, and heat stress is considered as a sign of climate change (Srivastava et al., 2009). Because of reflection from surface and roughness of different types of land uses, land use/land cover (LULC) changes are the main causes of LST variations (Hou et al., 2010). The soil LST is sensitive to vegetation cover and soil moisture, so it can be used to track land cover changes and land use, contributing to a better understanding of the desertification phenomena.

Fuzzy ARTMAP is an artificial neural network based on the adaptive resonance theory. The networks which work based on the adaptive resonance theory with supervised learning are known as ARTMAP (Carpenter et al., 1991). Each ARTMAP system consists of two modules (ARTa, ARTb) that create stable recognition classes in response to arbitrary sequences of input patterns. These two modules are connected to each other through an interface module called Fast Appearance-Based Mapping (Fab). The split-window algorithm requires only three parameters (emissivity, atmospheric emission, and average effective air temperature) to calculate LST. This algorithm was developed in 2001 to calculate the surface temperature by using the Landsat 5 Thematic Mapper (TM) sensor. With slight changes in the coefficients of the equations, it was then calibrated for other sensors (Rozenstein et al., 2014). This algorithm is based on mathematical analysis, and calculates LST by using ground data, a thermal infrared sensor (TIRS), land surface emissivity (LSE), and fractional vegetation cover (FVC), obtained from an operational land imager (OLI) (Latif, 2014).

LSTs can be estimated from infrared radiation, which is emitted from the surface, by the Stefan-Boltzmann inverse equation (Reutter et al., 1994). On the other hand, the Normalized Difference Vegetation Index (NDVI) is a good indicator of long-term changes in land cover and its status (Baihua and Isabela, 2015). It should be noted that an increase in temperature might raise the density of vegetation in areas with enough water resources (Xu et al., 2011). It has been demonstrated that there is a logical connection between NDVI and LST (Kustas et al., 2003; Weng et al., 2004; Agam et al., 2007; Inamdar et al., 2008; Wei et al., 2015). While temperature data, recorded by synoptic stations, are not useful for obtaining a good and wide spatial resolution, remote sensing (RS) images are a good source of information for the preparation of thermal maps, which is due to their extensive and continuous coverage, and timeliness (and the ability to obtain information in the reflection and thermal fields of electromagnetic waves) (Jiménez-Muñoz and Sobrino, 2010).

Due to the spatial correlation between data, conventional statistical methods are not suitable to analyze environmental data (Ripley, 1977). In this regard, various studies have been conducted to measure LST using RS technology (Herb et al., 2008; Feizizadeh et al., 2012. Qian et al., 2015; Isaya and Avdan, 2016; Fathizad et al., 2017; Deng et al., 2018;

Li and Jiang, 2018; Ziaul and Pal, 2018 a, b; Tariq and Shu, 2020; Tariq et al., 2020).

Over the past decades, droughts, increased human intervention in soil and natural resources, degradation, rapid population growth, and increasing need for food and new energy resources have caused overexploitation of natural resources in Iran. Undoubtedly, the land use in the Ilam dam watershed has undergone some changes and can be a threat for the residents of the region. So, this study investigates the relationship between land use changes and LST over 28 years (1990-2018) using Landsat satellite imagery, and identifies land uses with the highest surface temperature in the study region. Due to the limited access to ground-based data, the satellite imagery has been used to study the temperature patterns.

2. Materials and methods

2.1. Materials

2.1.1 Study area

This research was conducted in the Ilam dam watershed in Iran (Fig. 1), with a total area of 47 652 ha, located at 46º 16’ 50’’-46º 38’ 56’’ E, 33º 23’ 24’’-33º 38’ 58’’ N, and 936-2584 masl. Figure 1 shows the location of the study area.

The study area forms a part of the folded Zagros zone. Zagros Mountains are a complex chain of ridges and mountains in SW Iran, extending NW-SE from the border areas of eastern Turkey and northern Iraq to the Strait of Hormuz. The Zagros range is about 1600 and 240 km long and wide, respectively. This mountain forms the extreme western boundary of the Iranian plateau and its foothills extend into adjacent countries. It divides the region between Iran’s dry inland plateau to the east and the fertile plains of Mesopotamia and the Persian Gulf lowlands to the west.

The main kind of vegetation in the Zagros forest habitat is oak trees. At altitudes above the forest border (about 2300 masl) there are dense grasslands and shrubs. In the west of Iran, especially in the Zagros region, oak is the most important and abundant tree species. The Zagros Mountains are the largest and most important habitat of various oak species in Iran, and therefore this region is of special importance.

2.1.2 Remote sensing data

In this research, Landsat Thematic Mapper (TM) imagery for 1990, 1995, 2000, 2005 and 2010 (pass/row: 167/37) with six spectral lines with a resolution of 30 m, and Landsat 8 (Operational Land Imager [OLI] Sensor) for 2015 and 2018 (pass/row: 167/37)

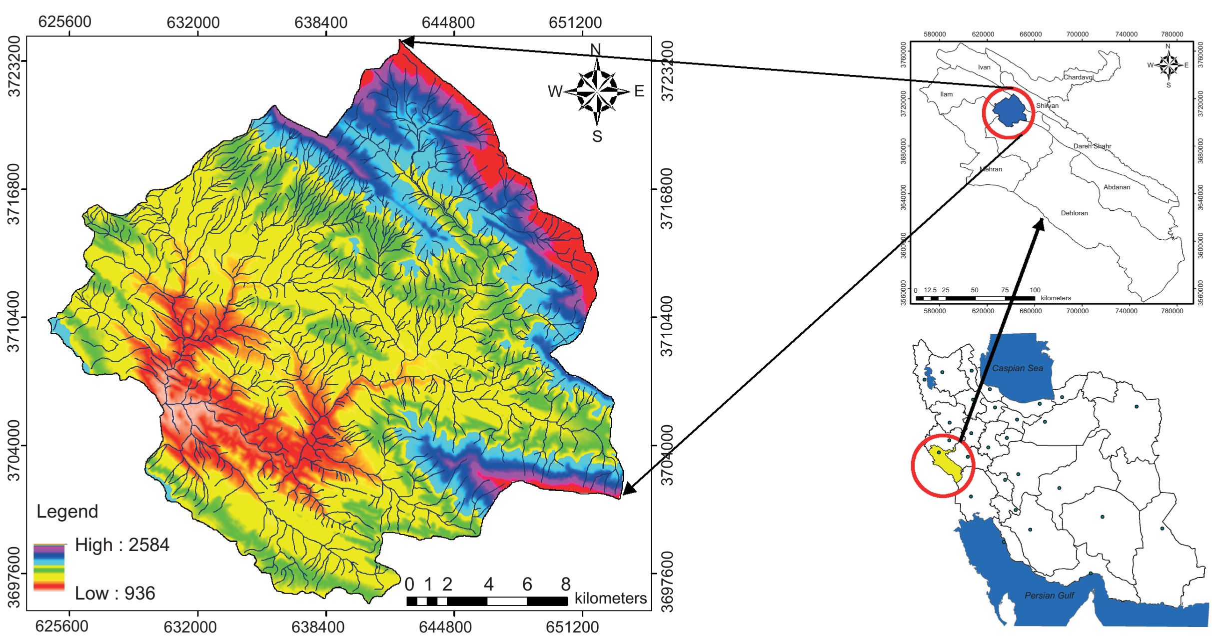

Fig. 1. Location of the study area in Iran and Ilam province.

bands 1 to 7 with a resolution of 30 m, band 8 with a resolution of 15 m and bands 9, 10 and 11 with a 30 m resolution were (Table I). Landsat images, published by the United States Geological Survey (USGS), were retrieved from the Earth Explorer website (http://earthexplorer.usgs.gov).

2.1.3 Software packages

ENVI 4.8, ArcGIS10.3 and Excel have been used in this study. The pre-processing works, including geometric and radiometric corrections, and post-processing tasks such as land use classification and LST layers have been extracted with the ENVI 4.8 software. ArcGIS 10.3 is used to provide the output of the maps and Excel is used to perform the statistical analysis.

2.2 Methodology

2.2.1 Pre-processing of images

The initial raw images of satellite data have incorrect geometry for reasons such as Earth orbits and changes in satellite elevation, in which case these images are not matched with the other satellite data. So, 35 ground control points from topographic maps were gathered for processing and interpreting multi-temporal satellite data. Further, the geometry of images was corrected in the ENVI 4.8 software environment by using the Global Positioning System (GPS).

Radiometric correction is necessary in remote sensing. Removing the undesirable effects of atmosphere is more important when the goal is comparing multi-temporal images (Chavez, 1988). In the present study, the Chavez method, which diminishes the value of dark object subtraction, is used for radiometric correction, and the value of dark object subtraction in the image is reduced to make the classification process highly accurate. For geometrical correction, topographic maps with a scale of 1.55000, prepared by the national *geographical organization* of Iran, were used. Images used in this research have been corrected by using ground control points and re-sampling equations. So, 45 ground control points with suitable distribution were used at the intersection of roads, waterways, etc., leading to a more accurate mathematical model. The average error obtained for the image sensor used was equal to 0.54 pixels, which is acceptable.

There are two types of radiometric corrections, absolute radiometric correction and relative radiometric correction. The absolute radiometric correction method requires data of atmospheric properties and sensor calibration. This type of correction is often very difficult, especially for older data (Du et al., 2002). In contrast, relative radiometric corrections are done with the aim of reducing the expected atmospheric variables, etc., between multi-time images. The *dark-object subtraction technique* is a simple relative radiometric correction method widely used in many cases (Chavez and MacKinnon, 1994). For radiometric correction, digital values are converted into spectral radiance in the first step by using the calibration coefficients of the sensor and the following equation:

Table I. Applied Landsat satellite imagery.

Sensor	Data	Pass/row	Resolution (m)	Number of bands
MSS	1985. 07. 22	167/37	60	4
TM	1990. 08. 29	167/37	30	7
	1995. 08. 19	167/37	30	7
	2000. 08. 16	167/37	30	7
	2005. 10. 1	167/37	30	7
	2010. 07. 11	167/37	30	7
OLI	2015. 08. 26	167/37	30	11
	2018. 08. 18	167/37	30	11

MSS: Multispectral Scanner System; TM: Thematic Mapper; OLI: Operational Land Imager.

$$L = gain \times DN + offset \quad (1)$$

where L is the spectral radiance (Wem^{-2} Ster^{-1} μm^{-1}), DN the digital value of the pixel (0 to 255), and *gain* and *offset* are the calibration coefficients of the sensor. In the next step, according to Eq. (2), the amount of spectral radiance is converted into spectral reflectance (Richards, 2013; Lillesand et al., 2015):

$$p = \frac{\pi L d^2}{ESUN.COS(SZ)} \quad (2)$$

where p is the spectral reflectance without units, from 0 to 1; L is the spectral radiance in the sensor; d^2 is the square of the distance between the Earth and the Sun based on astronomical units; $ESUN$ is the height of the Sun, and SZ is the angle of the Sun when radiating while recording a satellite image.

By converting spectral radiance values to spectral reflectance, the effects of changes in the Sun light, season, latitude, and weather conditions on the images are eliminated. The outcome is relatively standard and can be used to directly compare the reflections of phenomena between different images and an image at different times. In this study, the method of reducing the darkness of the phenomenon, which is implemented in ENVI software, has been used for radiometric correction. This process is to reduce the effects of atmospheric diffusion on the image.

2.2.2 Post-processing of images

After geometric and radiometric corrections of the satellite image and cutting it in the study area, the land use map was extracted by using the fuzzy ARTMAP supervised classification method to six land use types of fair rangeland (26-50% of climax condition), poor rangeland (0-25% of climax condition), dense forest (canopy cover less than 25%), sparse forest (canopy cover more than 25%), agricultural land, and a water body. The main advantage of the fuzzy ARTMAP is that it requires lower training data for accuracy analysis compared with other methods. In addition, this method does not depend on the statistical distribution of data and does not require specific statistical variables. In order to verify the accuracy of the classification, a comparison was made with existing land use maps and field observations. In this way, the reference map or reality map from all parts of the study area was prepared by using other methods. A random sampling method was used to assess the accuracy of the obtained maps. Samples were recorded by using a GPS method in a number of polygons, by using a land use map and local views from the study area. In order to classify and separate the land uses of previous years from each other, the vegetation map of Ilam province (developed by the Forest, Range and Watersheds Management Organization of Iran [FRWO]) was used together with aerial photographs (1:20000) prepared by the National Cartographic Center of Iran (NCC).

Also, a split-window algorithm, which removes atmospheric effects, was developed and applied to estimate the emissivity and LST. In fact, LST is obtained by using the corrected thermal radiance. To calculate the corrected thermal radiance, it is necessary to determine the emissivity in the thermal bond.

2.2.3 Fuzzy ARTMAP classification method

The fuzzy ARTMAP method is a remote sensing classification based on neural network analysis and the Adaptive Resonance Theory (ART). The fuzzy ARTMAP supervised classification method consists of four layers: input layer (F_1), category layer (F_2), field layer, and output layer. The input layer represents the imported images, so there are some neurons to measure each criterion. The input layer for the infinity of the criterion is as follows:

$$I = \left(a, a^c\right) = \left(a_1, a_2 \ldots a_{n,} 1 - a_1,\ 1 - a_2 \ldots 1 - a_n\right) \quad (3)$$

In this method, the number of F_2 layer neurons is automatically determined. The field layer and output layer are constructed with the ARTb model. Each of these two layers has m neurons. There is a one-to-one connection between these two layers.

2.2.4. Split-window algorithm for LST calculation

With this algorithm, LST is obtained by using corrected thermal radiance (Waters et al., 2002). To calculate the corrected thermal radiance, it is necessary to calculate the emissivity in the thermal bond. In fact, every land-related phenomenon is characterized by a specific emissivity, which was indicated by Snyder (1998). After detecting the minimum and maximum values, the NDVI is obtained; therefore, the average of soil and vegetation emissivity and the distribution of other areas can be calculated from Eq. (4).

$$\varepsilon = \varepsilon v \times Pv + \varepsilon s \times (1 - Pv) + d\varepsilon \quad (4)$$

Where εv and εs are the emissivity of areas with complete vegetation and areas with dry soil, respectively, and $d\varepsilon$ is the effect of surface distribution, which is calculated by using Eq. (5).

$$d\varepsilon = (1 - \varepsilon s)(1 - F)\varepsilon v \quad (5)$$

Where F is the form factor and its mean value is equal to 0.55, and Pv is the vegetation percentage, which is calculated by Eq. (6).

$$Pv = \left(\frac{NDVI_{\max} - NDVI}{NDVI_{\max} - NDVI_{\min}} \right)^{a} \quad (6)$$

2.2.5. NDVI index

This index is one of the most practical indicators for vegetation studies. It has a simple computational process and has the best dynamic power compared to other indicators. This index is more sensitive to vegetation changes and less susceptible to atmospheric and soil effects, except in cases where vegetation is low. The NDVI index is derived from Eq. (7).

$$NDVI = \frac{NIR - RED}{NIR + RED} \quad (7)$$

where *NIR* is the reflection in the near infrared band and *RED* is the reflection in the red band. From a theoretical point of view, the value of this index is in the range of ±1. The values of this indicator for dense vegetation cover tend to be +1. Clouds, snow and water are identified with negative values. Rocks and bare lands, with similar spectral responses in two bands, are seen at values close to zero. In this index, the common soil is equal to 1. Density of vegetation is determined by the distance between the indices of one pixel higher than the soil value (Allison, 1989).

2.2.6. Correction of LST

In this method, LST is obtained in ºK by using Eq. (8) (Artis and Carnahan, 1982).

$$LST = \frac{T_B}{1 + \left(\lambda \times {}^{T_B}\!/_{\rho} \right) Ln\varepsilon} \quad (8)$$

Where LST is land surface temperature in ºK, λ is the wavelength of the desired band (11.5 μm) (Weng et al., 2004), ρ is the Boltzmann constant (Eq. 9), h is the Planck's constant (6.626×10^{-34}), c is the speed of light (2.998×10^{8} m s^{-1}), and T_B is the brightness temperature in ºK obtained from Eq. (10).

$$\rho = \frac{h \times c}{1.438 \times 10^{-2} mk} \quad (9)$$

$$T_B = \frac{K_2}{\ln\left(\frac{K_1}{L\lambda} + 1 \right)} \quad (10)$$

K_1 and K_2 are correction coefficients with values of 666.09 and 1287.71, respectively (for Landsat images).

In ENVI, after obtaining the temperature of the black body and multiplying it by the coefficients of any phenomenon (emissivity), temperature can be calculated in ºC or ºK. It is also possible to calculate LST by using ENVI. Finally, the statistical parameters of each land use and LST for the years 1985, 1990, 1995, 2000, 2005, 2010, 2015 and 2018 are plotted on ArcGIS.

The final part of this procedure is the accuracy evaluation of the results. So, by using the ground control points, the correctness of calculations is evaluated by using the error matrix and statistical parameters of the total accuracy, kappa coefficient, and user's and producer's accuracy (Lu et al., 2004).

2.2.7. Accuracy assessment

Estimating accuracy is very important to understand the results and make decisions. The most common parameters for estimating accuracy are the overall accuracy, producer's accuracy, user's accuracy, and kappa coefficient (Lu et al., 2004). From a probability theory point of view, overall accuracy (Eq. 11) cannot be a good criterion for evaluating classification results; randomness may play a significant role in this index.

$$OA = \frac{1}{N} \sum P_{ii} \quad (11)$$

where *OA* is the overall accuracy, *n* is the number of experimental pixels, and P_{ii} are the elements of the original diameter of the error matrix.

Due to the problems of overall accuracy, the kappa coefficient is often used in executive tasks where the comparison of classification accuracy is considered (Mesgari, 2002).

$$Kappa = \frac{p_o - p_c}{1 - p_c} \times 100 \tag{12}$$

where P_o stands for correctly observed and P_c for expected agreement.

The producer's accuracy is the probability that a pixel in the classification image will be placed on the ground in the same class, and the user's accuracy is the probability that a specific class will be placed on the ground in the same class on the classified image (Eqs. 13 and 14)

$$UA = \frac{ta}{n_1} \times 100 \tag{13}$$

$$PA = \frac{ta}{ga} \times 100 \tag{14}$$

where *PA* is the percentage accuracy of *a* class for producer's accuracy, *ta* is the number of correct pixels classified as class *a*, *ga* is the number of class *a* pixels in ground reality, *UA* is the percentage accuracy of *a* class for user's accuracy, and n_1 is the number of pixels in class *a* as a result of classification.

By cutting the classified maps with the ground reality map obtained from the field survey, an error matrix was formed to evaluate the accuracy of the classified maps, and based on that, the overall accuracy and the kappa coefficient were calculated.

3. Results

3.1. Land use map

In this research, a neural network fuzzy ARTMAP algorithm was used to determine and plot land use maps for 1990, 1995, 2000, 2005, 2010, 2015 and 2018 by using Landsat satellite images. Classes of Landsat images in the study area included rangeland, poor rangeland, dense forest, sparse forest, agricultural, and water body land use types. The land use map of the study area for 1990, 1995, 2000, 2005, 2010, 2015 and 2018 is shown in Figure 2.

The results of the accuracy evaluation of the classified images are given in Table II, in which total, producer's and user's accuracy, as well as

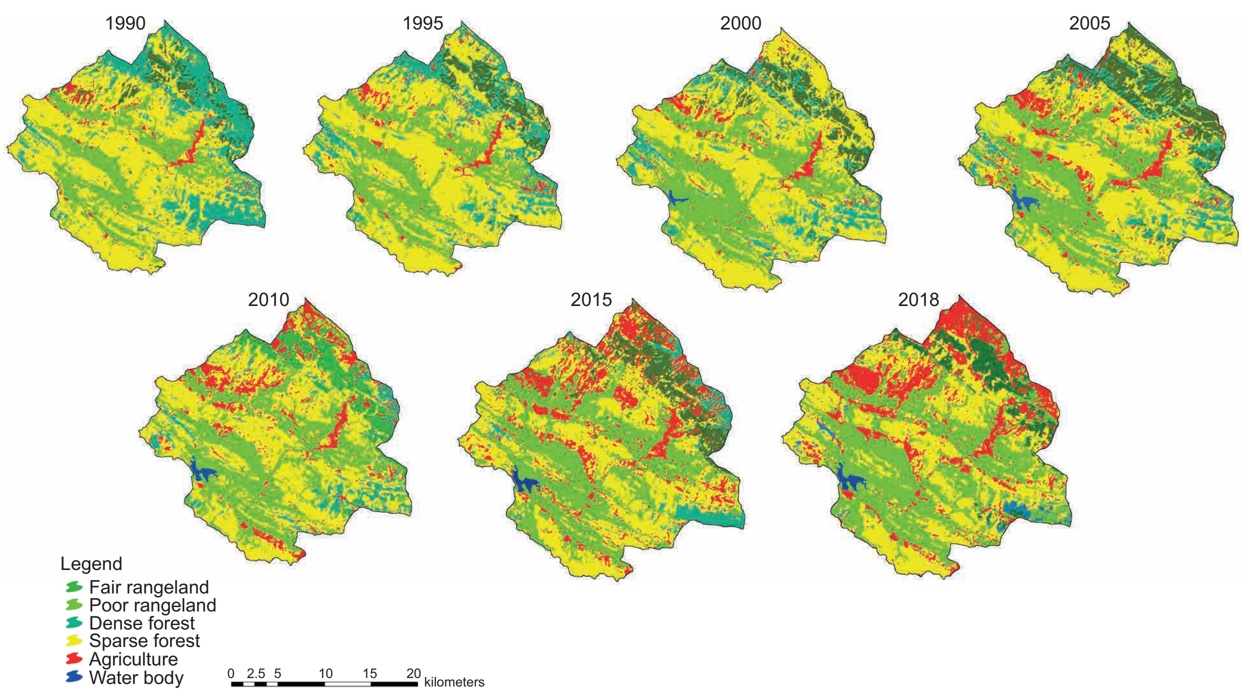

Fig. 2. Land use map of the study area based on the neural network fuzzy ARTMAP classification method for the years 1990, 1995, 2000, 2005, 2010, 2015 and 2018.

Table II: Results of accuracy evaluation of the classified land use images for the period 1985 to 2018.

Year/class	User's accuracy						
	1990	1995	2000	2005	2010	2015	2018
Fair rangeland	0.67	0.73	0.78	0.75	0.74	0.81	0.85
Poor rangeland	0.95	0.95	0.95	0.94	0.94	0.99	0.97
Dense forest	0.8	0.94	0.96	0.92	0.88	0.95	1
Sparse forest	0.84	0.91	0.91	0.88	0.86	0.94	0.83
Agricultural	0.94	0.95	0.88	0.91	0.90	0.94	0.93
Water body	—	—	0.99	0.99	0.99	1	1
Total accuracy (%)	0.90	0.94	0.92	0.92	0.91	0.95	0.93
Year/class	**Producer's accuracy**						
	1990	1995	2000	2005	2010	2015	2018
Fair rangeland	0.81	0.99	0.93	0.96	0.94	0.98	0.99
Poor rangeland	0.96	0.93	0.96	0.94	0.94	0.97	0.94
Dense forest	0.85	0.88	0.88	0.85	0.84	0.93	0.69
Sparse forest	0.80	0.92	0.86	0.89	0.85	0.90	0.96
Agricultural	0.89	0.91	0.88	0.89	0.88	0.95	0.94
Water body	—	—	0.92	0.96	0.95	0.98	0.93
Kappa coefficient (%)	0.87	0.92	0.90	0.90	0.89	0.94	0.91

kappa coefficient, are also reported. High values of these coefficients indicate the acceptable accuracy for the land use identification by using RS data of Landsat images. It is observed that the classification accuracy for all the mentioned years is above 85%, which is an appropriate precision for classification of land uses.

3.2. Land use changes

Results about changes in land use types of the study area during the investigated time periods are shown in Figure 3. They show that during the 28-year period (1990-2018), the area of agricultural land use has increased by 8650.6 ha (18.155%), highlighting an rise in population as well as in human pressure in the studied area. The most important land use change is related to dense and sparse forest land uses, with a decrease of 9867.14 and 8125.11 ha (20.07 and 17.04%), respectively. The study area has been conserved by governmental organizations in recent years. However, a decline in the extent of forest land use in the region is still seen. In a study that examined oak decline in the province of Ilam, results indicated a kind of ailment called charcoal

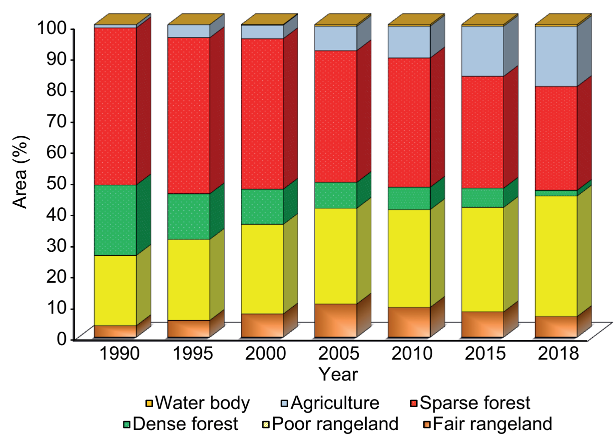

Fig. 3. Area of land use classes (1990-2018).

disease (*Biscogniauxia mediterranea*) and borer beetles, which cause trees to die and fall. This disease has developed in recent years due to climatic conditions including rainfall reduction, drought and moisture stress which provide a suitable field for disease outbreaks (Mirabolfathi, 2013). Indeed, the rising demand for wood, timber, shelter and agricultural products has led to the destruction of natural land cover, especially forests that are becoming agricultural land at an alarming rate. The pressure from population growth has also led to uncontrolled alterations in exploitation, especially forestry in a wide area of the region. Hence, erosion and destruction of land are two of the most important current problems of this region. Negative effects of land use change in the study area include declining soil fertility, reduced vegetation and animal diversity, flood events, and increased landslide risk. The area of fair and poor rangeland land use types has increased by 1399.77 and 7652.16 ha (2.93 and 16.05%), which is due to the change of forest land to rangeland. Water bodies were not included in land use categories in 1985 and they were added in 2000. This land use is related to the Ilam dam, constructed in 2000 to supply drinking water.

3.3. LST maps

According to LST maps (Fig. 4), the central and northwestern parts of the study area have a higher temperature because of agricultural activities, dense forest, and poor rangeland land use. LST maps (Fig. 4) show minimum LSTs of 21.27, 20.88, 25.37, 13.34, 28.85, 26.95 and 30.71 ºC and maximum of 54.18, 50.65, 52.85, 46.16, 57.51, 52.04 and 56.10 ºC for 1990, 1995, 2000, 2005, 2010, 2015 and 2018, respectively. In this study, the lowest temperature was due to dense forest land use in 1990, when the study area had a cool median temperature. However, overtime increases in the LST indicate climate change effects in the region, which could have devastating outcomes in the future. The maximum temperature drop of 2005 was caused by increased rainfall (above 600 mm) in the region, which led to an increase in vegetation cover in the study area.

3.4. Relationship between NDVI, LULC and LST

The LST is affected by different surface conditions, such that areas with vegetation accumulation tend to have lower LST than vegetation-free areas. By absorbing sunlight and transpiration of water through its leaves, vegetation creates a natural air-conditioning system. Changes from forest to rangeland and rainfed farming land uses reduce the vegetation cover, remove the cooling system of natural surfaces and increase LST. Figure 5 shows the NDVI and LST differences between 1990 and 2018 in the study area. As it is obvious, wherever the vegetation has increased, LST has decreased and vice versa.

The results of the survey on average LST of the land uses in the study area for different years are

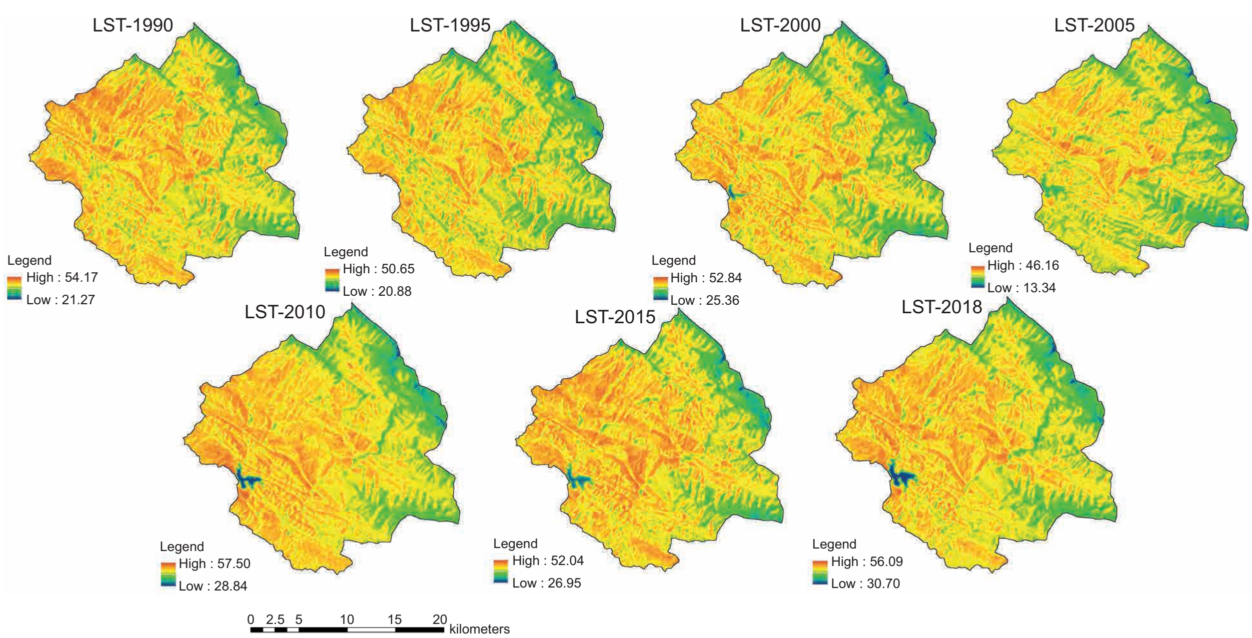

Fig. 4. LST maps obtained with the split-window algorithm (in ºC).

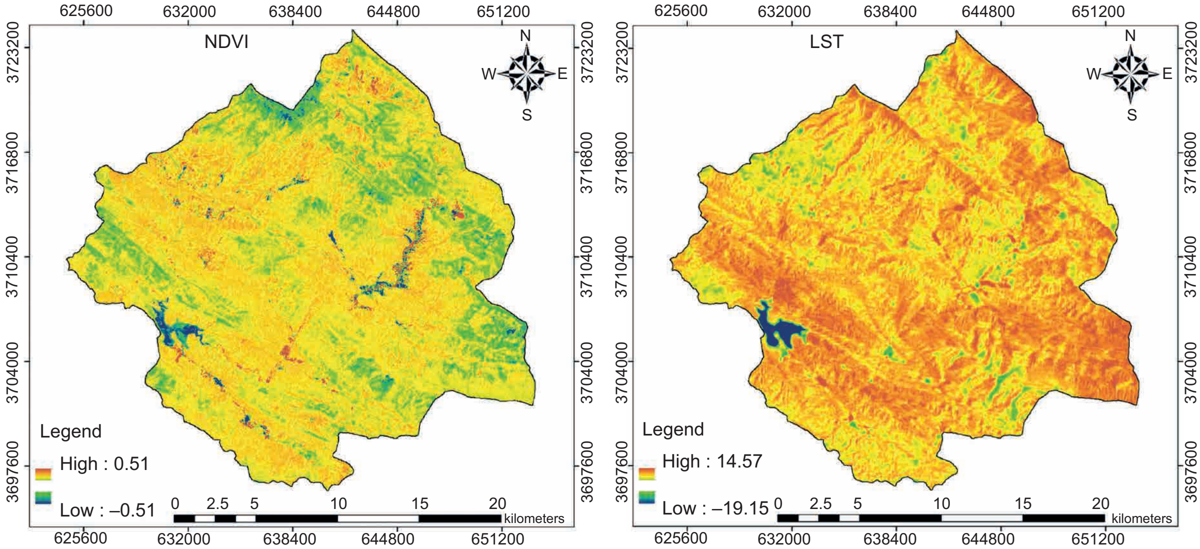

Fig. 5. Role of NDVI and LST (in ºC) differences between 1990 and 2018 in the study area.

shown in Table III. According to this table, the minimum temperature in 1990, 2010, and 2018 in dense forest was 3.5, 7.3 and 7.9 ºC, respectively, while the maximum surface temperature for sparse forest in 1990 and 2010 was 9.5, 11.8 ºC, and 10.9 ºC for dense forest in 2018. During most of the studied period, agricultural land had a lower average temperature than sparse forest and rangeland, which is mainly due to the high moisture content in agricultural land and the greater degree of evapotranspiration. Water bodies have the lowest average temperature due to the high-water heat capacity. Changes between 1990 and 2018 show that all land use types were subject to an increase in average temperature, which can be attributed to the increasing trend in temperature in the study area.

In order to study the effect of land use changes on surface temperature, an LST map for different time periods between 1990 and 2018 was prepared and compared to the land use change map for the same time period (Fig. 6). The results show that there was an increase in average LST in areas where land use change increased, indicating an intensification in heat-producing human-based activities, such as conversion of forest land use to agricultural use.

3.5. The nature of LST changes and land use

The crosstab method was used to investigate the land use and LST changes. In this method, classes of two classified maps are compared one by one. As a result, it is possible to determine the changes occurring in each class relative to the other. Figure 9 shows the crossed classified land use maps for 1990 and 2018, which exhibit the 1990 LULC variations compared to 2018. The difference in LST maps between 1990 and 2018 was used to examine LST changes (Fig. 5). The amount of various land use changes and the LST changes are shown in Figure 7 and Table IV. As Table IV shows, average temperature for all land use changes was positive and increasing, with the exception of dense forest, sparse forest and agricultural land, where LST dropped to –12.4 ºC.

3.6. Relationship between LST and NDVI index

For better analysis of the relationship between LST and Land use, the correlation coefficients between LST and the NDVI index were calculated in 2018, based on randomized control points from each land use (Fig. 8). The highest correlation coefficient was obtained in dense forest and sparse forest land uses at 0.833 and 0.814, respectively. The lowest correlation coefficient (0.288) was related to water body land use, which confirms the lack of vegetation cover in this site compared to other land uses. Comparing the LST values of 2018 (Table III) and their correlation with the NDVI index (Fig. 8), it can be stated that in each land use where the average temperature is higher, the dependence between LST

Table III: Temperature variations in different land uses (1990-2018).

Class	1990				1995			
	Min.	Max.	Mean	Std.	Min.	Max.	Mean	Std.
Fair rangeland	33.17	51.11	42.93	3.34	27.99	43.09	35.65	2.70
Poor rangeland	28.80	54.18	44.02	3.10	22.70	50.65	40.68	2.97
Dense forest	21.27	51.46	38.25	4.15	20.88	46.54	35.61	4.29
Sparse forest	33.17	52.48	43.89	2.86	22.70	48.42	39.72	3.20
Agriculture	32.00	52.48	42.91	5.42	27.99	49.54	39.36	4.62
Water body	—	—	—	—	—	—	—	—
Class	**2000**				**2005**			
	Min.	Max.	Mean	Std.	Min.	Max.	Mean	Std.
Fair rangeland	30.13	49.17	39.73	3.22	20.88	40.75	30.75	3.26
Poor rangeland	30.13	52.85	43.92	2.56	13.34	46.16	34.41	3.97
Dense forest	30.98	50.65	41.30	3.20	18.11	37.97	28.57	3.22
Sparse forest	25.37	51.02	42.01	3.81	19.51	42.71	32.72	3.75
Agriculture	31.40	50.28	42.92	3.65	22.25	44.25	35.52	3.80
Water body	27.55	40.36	32.09	3.00	23.15	31.40	24.85	1.76
Class	**2010**				**2015**			
	Min.	Max.	Mean	Std.	Min.	Max.	Mean	Std.
Fair rangeland	35.95	49.91	43.49	2.39	33.66	49.56	41.54	2.72
Poor rangeland	29.28	57.15	48.13	3.39	28.66	52.04	44.11	2.71
Dense forest	30.55	57.51	44.39	4.60	26.95	50.23	37.31	4.25
Sparse forest	32.24	56.09	48.20	3.17	31.46	51.39	43.85	2.85
Agriculture	32.24	57.15	46.17	4.60	29.24	51.41	43.92	3.70
Water body	28.85	45.02	33.20	3.53	29.65	43.28	32.09	2.42
Class	**2018**							
	Min.	Max.	Mean	Std.				
Fair rangeland	34.83	51.12	43.20	2.77				
Poor rangeland	30.71	54.92	46.90	3.26				
Dense forest	33.82	56.10	44.75	4.43				
Sparse forest	37.71	54.57	47.87	2.25				
Agriculture	33.22	55.20	46.86	4.08				
Water body	31.17	45.71	33.60	2.49				

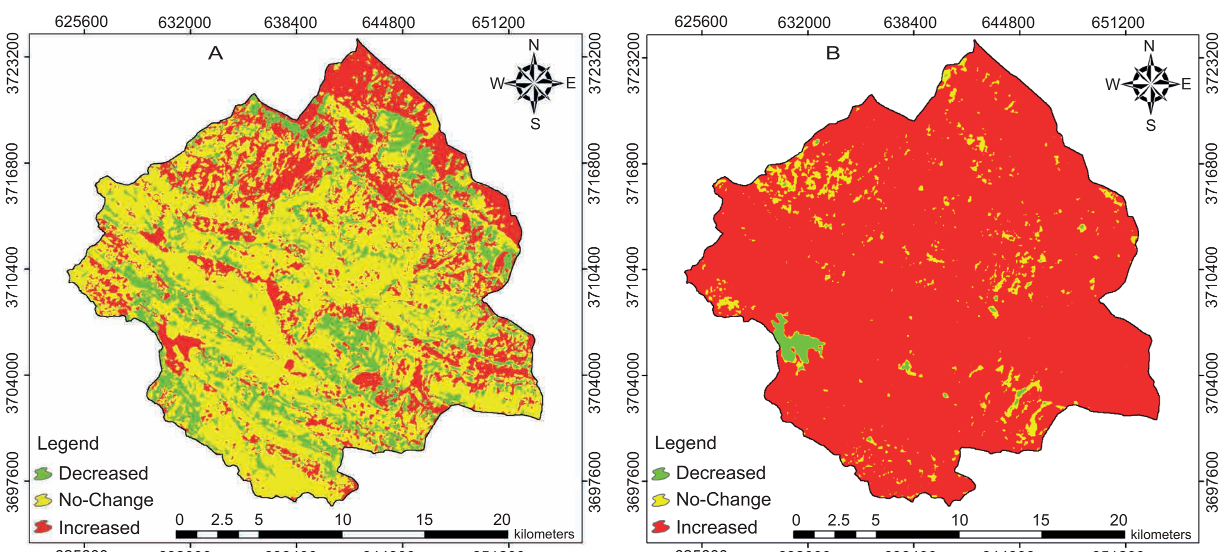

Fig. 6. Change detection map (1990-2018). (a) Land use. (b) LST.

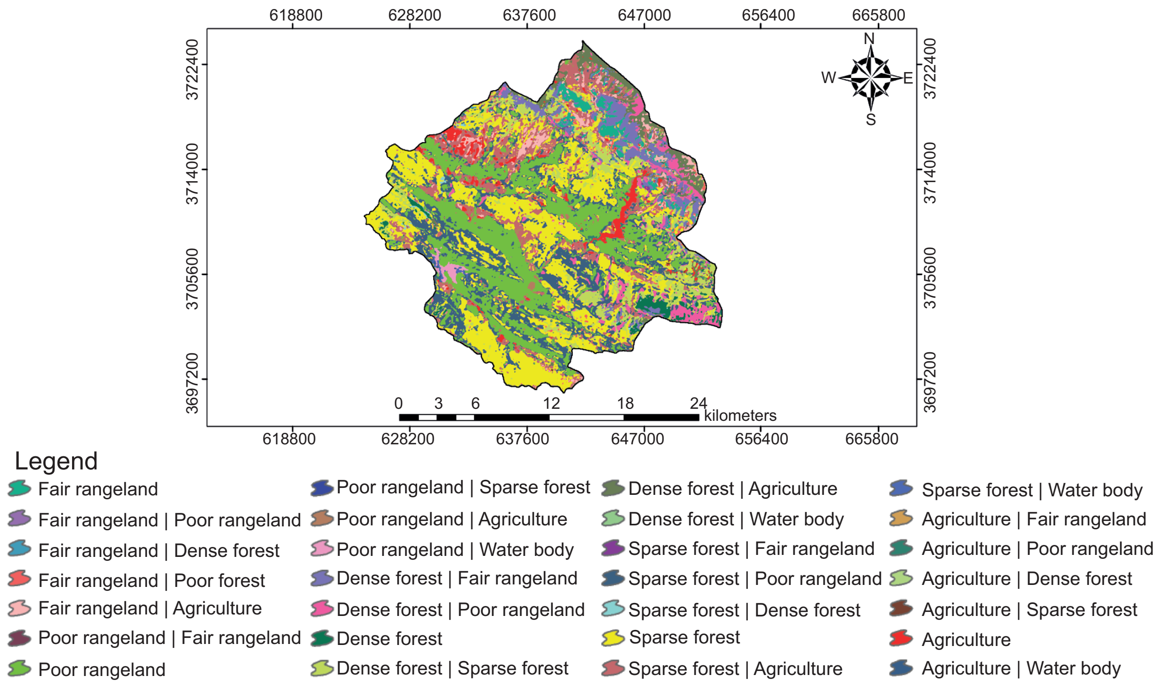

Fig. 7. Land use change map (1990 to 2018). In the map legend, each color indicates how the land use has changed over time. Some colors show two land uses, meaning that the area has changed from one land use to another. Some colors show only one land use, indicating no change in the land use.

Table IV: Results of land use and LST changes.

LST (ºC) Class	Min.	Max.	Mean	Std.
Fair rangeland | Agriculture	–4.6	8.4	2.9	1.4
Dense forest | Poor rangeland	–1.0	10.2	6.0	1.4
Dense forest | Fair rangeland	–0.5	9.0	5.3	1.2
Agriculture	–5.1	14.6	3.7	2.5
Poor rangeland | Agriculture	–4.7	8.9	2.9	2.0
Poor rangeland | Fair rangeland	3.0	6.4	4.4	1.1
Sparse forest | Agriculture	–4.7	9.5	3.3	1.6
Dense forest | Agriculture	–3.3	9.4	4.2	1.7
Poor rangeland	–10.6	9.5	4.1	1.6
Sparse forest | Fair rangeland	–0.4	7.4	3.3	1.3
Sparse forest | Poor rangeland	–10.2	9.9	4.9	1.5
Fair rangeland	–1.4	7.7	3.9	1.1
Dense forest | Sparse forest	–1.4	9.8	5.0	1.6
Sparse forest	–2.8	9.9	4.0	1.4
Fair rangeland | Sparse forest	–1.2	8.0	3.6	1.3
Dense forest	–0.4	9.1	4.9	1.4
Agriculture | Sparse forest	–0.8	10.4	4.6	2.4
Poor rangeland | Sparse forest	0.0	8.8	3.5	1.4
Fair rangeland | Poor rangeland	–2.0	7.8	3.3	2.2
Sparse forest | Dense forest	0.9	7.5	4.0	1.2
Fair rangeland | Dense forest	1.7	6.1	4.3	0.8
Agriculture | Poor rangeland	–9.0	14.1	4.9	2.8
Agriculture | Fair rangeland	4.3	7.5	5.8	0.8
Agriculture | Dense forest	2.7	5.2	4.4	1.0
Poor rangeland | Water body	–19.2	0.2	–10.8	3.5
Sparse forest | Water body	–16.8	6.0	–9.4	4.4
Agriculture | Water body	–17.8	–4.3	–12.4	3.0
Dense forest | Water body	–12.4	–12.3	–12.3	0.1

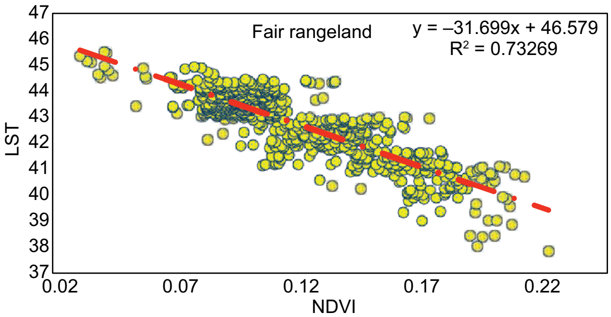

Fig. 8. Correlation chart between LST and NDVI index based on land use.

and NDVI is lower, indicating the low density of vegetation in these land uses. As shown in Figure 8, the correlation of the rangelands with the forest is lower, and their surface temperatures are higher than those of the forest.

3.7. Spatiotemporal distribution of LST

To study the spatial distribution of LST in the region, thermal images from different years were normalized by using the highest and lowest amount of surface temperature. Then, using average values and standard deviation, the normalized thermal images were classified into five temperature classes of low, medium, fairly high, high and very high limit. Figure 9 shows the thermal maps, and Figure 10 shows the area of temperature classes in the desired time periods. The results of the differences in areas between 1990 and 2018, show that the low, medium and fairly high limit classes decreased by 5, 15 and 20%, respectively, and the high and very high limit classes increased by 25 and 15%, respectively.

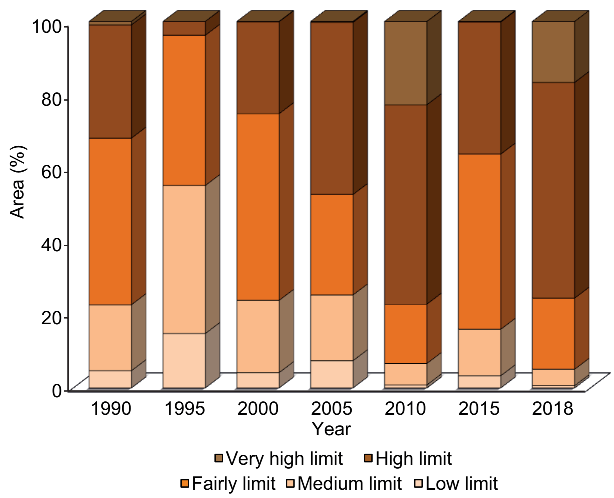

Fig. 10. Area of temperature classes in the studied period (%).

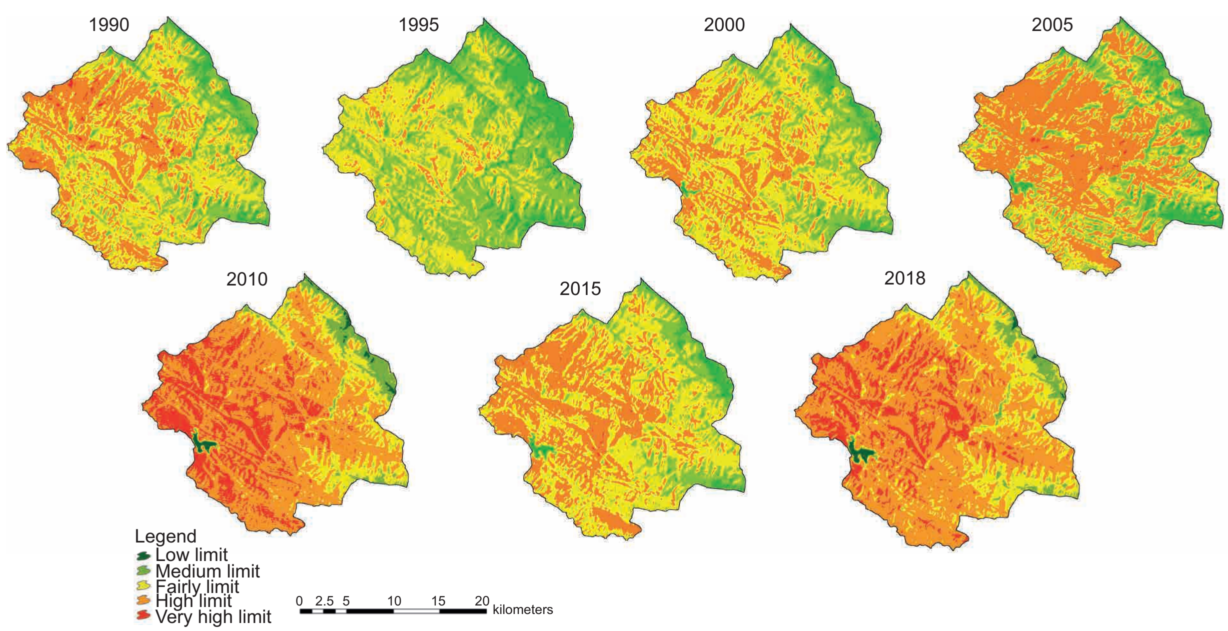

Fig. 9. LST classification maps using average values and standard deviation of thermal images (1990-2018) (in ºC).

Due to the decrease in forest area and the increase in human-induced land uses, the area of lower temperature class has decreased, and the upper temperature class has experienced a notable increase during the time analyzed. The reduced area of dense forest and the increasing trend of agricultural and rangeland land uses indicate the replacement and conversion of the region's natural coverage to lower value land uses. According to Figure 8, it can be said that the increase in LST is directly related to the increas in population density within the region and, consequently, the increas in agricultural area. The anticipated continuation of this trend provides grounds to expect a future (continued) rise in temperature (LST).

4. Discussion and conclusions

One of the important results of this research is the demonstration of the ability of fuzzy ARTMAP neural networks to classify land use types. Fuzzy classification includes methods that can provide results better suited to ground reality. In these methods, different values are calculated as the membership grade of each pixel based on land cover variation, while in definitive categorization methods each image pixel is attributed to only one class. The accuracy of the kappa coefficient for land use maps, derived from the satellite data classification by using the fuzzy ARTMAP classification for 1990, 1995, 2000, 2005, 2010, 2015, and 2018 is approximately equal to 87, 92, 90, 90, 89, 94 and 91%, respectively, which represents the high reliability of this algorithm in the classification of satellite data.

The results of the trend in land use change show that, in the period 1990-2018, most changes are related to agricultural lands and low-density (poor) rangeland, which have increased by 18.15 and 16.05%, respectively. On the other hand, land use types of dense forest and sparse forest have decreased by 20.70 and 17.04%, respectively, highlighting the destruction and change of natural and vegetated lands to cultivated lands. Another manmade land use that has many negative effects on nature is the construction of dams. From the time of construction of the Ilam dam (2005) until 2018, the water body behind the dam has increased by about 0.60%.

From LST maps, the range of surface temperature changed from 21.27 to 54.18 ºC in 1990 and from 30.07 to 56.09 ºC in 2018. Many scholars have focused on the relationship between the effects of land use change and LST. Results of Setturu et al. (2013) in the Uttara Kannada district (India), Pal and Ziaul (2017) in the English Bazar urban center of West Bengal (India), Fathizad et al. (2017) in southwest Iran, and Choudhury et al. (2019) in the Asansol-Durgapur Development show that land use changes are directly related to the increase in surface temperature. By examining the trend of temperature changes in the study area during the period 1990-2018, we observe an increase of 1.92 ºC, which is in line with the IPCC report of 2018.

The results of this study show that the LST has a high sensitivity to vegetation cover; land uses with higher vegetation density have lower surface temperatures. Hence, it can be used to detect changes in land use over time. With regard to the effects of land use changes, such as urbanization, establishment of communication roads, agricultural development and soil erosion in the study area, it can be predicted that surface temperature will increase in the future. It is evident that land use changes will result in changes in LST.

Further studies are required in this area under different seasons. Also, to achieve better results, particularly to more accurately estimate the LST, we suggest the use of image sensors with higher spatial resolution of the thermal bonding. In the future, more attention is needed to the modeling of land use changes, specifically by considering climate factors and detecting changes with different types of satellite images. This can reduce some degree of uncertainty in order to support management decisions. The results are potentially useful for various applications, including climatology, hydrology, ecology, geology, design and improvement of transport and agriculture networks.

Acknowledgments

This study is related to a project supported by Ilam University, Iran. Also, the experiments comply with the current laws of Iran. We also thank Pedro J. M. Costa, Postdoctoral Research Fellow and Invited Lecturer, Instituto D. Luiz, and Departamento de Geologia, Faculdade de Ciências, Universidade de Lisboa, Portugal, for comments that greatly improved the manuscript.

References

Agam N, Kustas WP, Anderson MC, Li F, Neale CMU. 2007. A vegetation index-based technique for spatial sharpening of thermal imagery. Remote Sensing of Environment 107: 545-558. https://doi.org/10.1016/j.rse.2006.10.006

Allison EW. 1989. Monitoring drought affected vegetation with AVHRR. Digest International Geoscience and Remote Sensing Symposium 4, 1965-1967.

Amiri R, Weng Q, Alimohammadi A, Alavipanah SK. 2009. The spatial-temporal dynamics of land surface temperatures in relation to fractional vegetation cover and land use/cover in the Tabriz urban area, Iran. Remote Sensing of Environment 113: 2606-2617. https://doi.org/10.1016/j.rse.2009.07.021

Artis DA, Carnahan WH. 1982. Survey of emissivity variability in thermography of urban areas. Remote Sensing of Environment 12: 313-329. https://doi.org/10.1016/0034-4257(82)90043-8

Baihua F, Isabela B. 2015. Riparian vegetation NDVI dynamics and its relationship with climate, surface water and groundwater. Journal of Arid Environments 113: 59-68. https://doi.org/10.1016/j.jaridenv.2014.09.010

Brovkin V, Boysen L, Arora VK, Boisier JP, Cadule P, Chini L, Claussen M, Friedlingstein P, Gayler V, Van Den Hurk BJJM, Hurtt GC, Jones CD, Kato E, Noblet-Ducoudré N, Pacifico F, Pongratz J, Weiss M. 2013. Effect of anthropogenic land-use and land-cover changes on climate and land carbon storage in CMIP5 projections for the twenty-first century. Journal of Climate 26: 6859-6881. https://doi.org/10.1175/JCLI-D-12-00623.1

Carpenter GA, Grossberg S, Reynolds JH. 1991. ARTMAP: Supervised real-time learning and classification of nonstationary data by a self-organizing neural network. Neural Networks 4: 565-588. https://doi.org/10.1016/0893-6080(91)90012-T

Chavez PS. 1988. An improved dark-object subtraction technique for atmospheric scattering correction of multispectral data. Remote Sensing of Environment 24, 459-479. https://doi.org/10.1016/0034-4257(88)90019-3

Chavez PS, MacKinnon DJ. 1994. Automatic detection of vegetation changes in the southwestern United States using remotely sensed images. Photogrammetric Engineering and Remote Sensing 60: 571-583.

Choudhury D, Das K, Das A. 2019. Assessment of land use land cover changes and its impact on variations of land surface temperature in Asansol-Durgapur Development Region. The Egyptian Journal of Remote Sensing and Space Science 22: 203-218. https://doi.org/10.1016/j.ejrs.2018.05.004

Connors JP, Galletti CS, Chow WTL. 2013. Landscape configuration and urban heat island effects: Assessing the relationship between landscape characteristics and land surface temperature in Phoenix, Arizona. Landscape Ecology 28: 271-283. https://doi.org/10.1007/s10980-012-9833-1

Deng Y, Wang S, Bai X, Tian Y, Wu L, Xiao J, Chen F, Qian Q. 2018. Relationship among land surface temperature and LUCC, NDVI in typical karst area. Scientific Reports 8: 641. https://doi.org/10.1038/s41598-017-19088-x

Du Y, Teillet PM, Cihlar J. 2002. Radiometric normalization of multitemporal high-resolution satellite images with quality control for land cover change detection. Remote Sensing of Environment 82: 123-134. https://doi.org/10.1016/S0034-4257(02)00029-9

Fathizad H, Tazeh M, Kalantari S, Shojaei S. 2017. The investigation of spatiotemporal variations of land surface temperature based on land use changes using NDVI in southwest of Iran. Journal of African Earth Sciences 137: 249-256. https://doi.org/10.1016/j.jafrearsci.2017.06.007

Feddema JJ, Oleson KW, Bonan GB, Mearns LO, Buja LE, Meehl GA, Washington WM. 2005. The importance of land-cover change in simulating future climates. Science 310: 1674-1678. https://doi.org/10.1126/science.1118160

Feizizadeh B, Blaschke T, Nazmfar H, Akbari E, Kohbanani HR. 2012. Land surface temperature relationship to land use/land cover from satellite imagery in Maraqeh County, Iran. Journal of Environmental Planning and Management 56: 1290-1315. https://doi.org/10.1080/09640568.2012.717888

Feng JM, Wang YL, Ma ZG, Liu YH. 2012. Simulating the regional impacts of urbanization and anthropogenic heat release on climate across China. Journal of Climate 25: 7187-7203. https://doi.org/10.1175/JCLI-D-11-00333.1

Halder S, Saha SK, Dirmeyer PA, Chase TN, Goswami BN. 2016. Investigating the impact of land-use land-cover change on Indian summer monsoon daily rainfall and temperature during 1951-2005 using a regional climate model. Hydrology and Earth System Sciences 20: 1765-1784. https://doi.org/10.5194/hess-20-1765-2016

Hao X, Li W, Deng H. 2016. The oasis effect and summer temperature rise in arid regions-case study in Tarim Basin. Scientific Reports 6: 35418. https://doi.org/10.1038/srep35418

Hasanlou M, Mostofi N. 2015. Investigating urban heat island estimation and relation between various land cover indices in Tehran City using Landsat 8 imagery. In: 1st International Electronic Conference on Remote Sensing.

Herb WR, Janke B, Mohseni O, Stefan HG. 2008. Ground surface temperature simulation for different land covers. Journal of Hydrology 356: 327-343. https://doi.org/10.1016/j.jhydrol.2008.04.020

Hou GL, Zhang HY, Wang YQ, Qiao ZH, Zhang ZX. 2010. Retrieval and spatial distribution of land surface temperature in the middle part of Jilin province based on MODIS data. Scientia Geographica Sinica 30: 421-427. https://doi.org/10.13249/j.cnki.sgs.2010.03.421

Inamdar AK, French A, Hook S, Vaughan G, Luckett W. 2008. Land surface temperature retrieval a high spatial and temporal resolution over the southwestern United States. Journal of Geophysical Research: Atmospheres 113: D07107. https://doi.org/10.1029/2007JD009048

Isaya Ndossi M, Avdan U. 2016. Application of open source coding technologies in the production of land surface temperature (LST) maps from Landsat: A PyQGIS plugin. Remote Sensing 88: 413. https://doi.org/10.3390/rs8050413

Jiménez-Muñoz JC, Sobrino JA. 2010. A single-channel algorithm for land-surface temperature retrieval from ASTER data. IEEE Geoscience and Remote Sensing Letters 7: 176-179. https://doi.org/10.1109/LGRS.2009.2029534

Kustas WP, Norman JM, Anderson MC, French AN. 2003. Estimating subpixel surface temperatures and energy fluxes from the vegetation index-radiometric temperatures relationship. Remote Sensing of Environment 85: 429-440. https://doi.org/10.1016/S0034-4257(03)00036-1

Latif MS. 2014. Land surface temperature retrieval of Landsat-8 data using split window algorithm – A Case study of Ranchi District. International Journal of Engineering Development and Research 2: 3840-3849.

Li S, Jiang GM. 2018. Land surface temperature retrieval from Landsat-8 data with the generalized split-window algorithm. IEEE Access 6: 18149-18162. https://doi.org/10.1109/ACCESS.2018.2818741

Lillesand T, Kiefer RW, Chipman J. 2015. Remote sensing and image interpretation. John Wiley & Sons, 736 pp.

Lu D, Mausel P, Brondizio E, Moran E. 2004. Change detection techniques. International Journal of Remote Sensing 25: 2365-2407. https://doi.org/10.1080/0143116031000139863

Luyssaert S, Jammet M, Stoy PC, Estel S, Pongratz J, Ceschia E, Churkina G, Don A, Erb K, Ferlicoq M, Gielen B, Grunwald T, Houghton RA, Klumpp K, Knohl A, Kolb T, Kuemmerle T, Laurila T, Lohila A, Loustau D, McGrath MJ, Meyfroidt P, Moors EJ, Naudts K, Novick K, Otto J, Pilegaard K, Pio CA, Rambal S, Rebmann C, Ryder J, Suyker AE, Varlagin A, Wattenbach M, Dolman AJ. 2014. Land management and land-cover change have impacts of similar magnitude on surface temperature. Nature Climate Change 4: 389-393. https://doi.org/10.1038/nclimate2196

Mahmood R, Pielke RA, Hubbard KG, Niyogi D, Dirmeyer PA, McAlpine C, Carleton AM, Hale R, Gameda S, Beltrán-Przekurat A, Baker B, McNider R, Legates DR, Shepherd M, Du J, Blanken PD, Frauenfeld OW, Nair U, Fall S. 2014. Land cover changes and their biogeophysical effects on climate. International Journal of Climatology 34; 929-953. https://doi.org/10.1002/joc.3736

Mesgari S. 2002. Investigation of the trend of forest area change using GIS and RS, Tehran. Research Project, Faculty of Engineering, K.N. Toosi University of Technology, Tehran, Iran.

Mirabolfathi M. 2013. Outbreak of charcoal disease on *Quercus* spp. and *Zelkova carpinifolia* trees in forests of Zagros and Alborz mountains in Iran. Iranian Journal of Plant Pathology 49: 257-263.

Pal S, Ziaul Sk. 2017. Detection of land use and land cover change and land surface temperature in English Bazar urban center. The Egyptian Journal of Remote Sensing and Space Sciences 20: 125-145. https://doi.org/10.1016/j.ejrs.2016.11.003

Qian C, Deyong Y, Matei G, Zhe H, Jianguo W. 2015. Impacts of land use and land cover change on regional climate: a case study in the agro-pastoral transitional zone of China. Environmental Research Letters 10: 124025. https://doi.org/10.1088/1748-9326/10/12/124025

Reutter HF, Olesen S, Fischer H. 1994. Distribution of the brightness temperature of land surfaces determined from AVHRR data. International Journal of Remote Sensing 15: 95-104. https://doi.org/10.1080/01431169408954053

Ripley BD. 1977. Modelling spatial patterns. Journal of the Royal Statistical Society: Series B (Methodological) 39: 172-192. https://doi.org/10.1111/j.2517-6161.1977.tb01615.x

Richards JA. 2013. Remote sensing digital image analysis. An introduction. 5th ed. Springer, 516 pp. https://doi.org/10.1007/978-3-642-30062-2

Rozenstein O, Qin Z, Derimian Y, Karnieli A. 2014. Derivation of land surface temperature for Landsat-8 TIRS using a split window algorithm. Sensors 14: 5768-5780. https://doi.org/10.3390/s140405768

Setturu B, Rajan KS, Ramachandra TV. 2013. Land surface temperature responses to land use land cover dynamics. Geoinformatics & Geostatistics: An Overview 1: 4. https://doi.org/10.4172/2327-4581.1000112

Snyder WC. 1998. Classification based emissivity for land surface temperature measurement from pace. International Journal of Remote Sensing 19: 2753-2774. https://doi.org/10.1080/014311698214497

Srivastava PK, Majumdar TJ, Bhattacharya AK. 2009. Surface temperature estimation in Singhbhum shear zone of India using Landsat-7 ETM + thermal infrared data. Advances in Space Research 43: 1563-1574. https://doi.org/10.1016/j.asr.2009.01.023

Tariq A, Shu H. 2020. CA-Markov chain analysis of seasonal land surface temperature and land use land cover change using optical multi-temporal satellite data of Faisalabad, Pakistan. Remote Sensing 12: 3402. https://doi.org/10.3390/rs12203402

Tariq A, Riaz I, Ahmad Z, Yang B, Amin M, Kausar R, Andleeb S, Farooqi MA, Rafiq M. 2020. Land surface temperature relation with normalized satellite indices for the estimation of spatio-temporal trends in temperature among various land use land cover classes of an arid Potohar region using Landsat data. Environmental Earth Sciences 79: 40. https://doi.org/10.1007/s12665-019-8766-2

Tomlinson CJ, Chapman L, Thrones JE, Baker C. 2011. Remote sensing land surface temperature for meteorology and climatology: A review. Meteorological Applications 18: 296-306. https://doi.org/10.1002/met.287

Waters W, Allen R, Masahiro T, Trezza R, Bastiaanssen W. 2002. SEBAL. Surface energy balance algorithms for land. Version 1.0. NASA EOSDIS/Raytheon Company/Idaho, Department of Water Resources, 97 pp.

Wei L, Jean-Daniel MS, Thomas WG. 2015. A comparison of the economic benefits of urban green spaces estimated with NDVI and with high-resolution land cover data. Landscape and Urban Planning 133: 105-117. https://doi.org/10.1016/j.landurbplan.2014.09.013

Weng Q, Lu D, Schubring J. 2004. Estimation of land surface temperature-vegetation abundance relationship for urban heat island studies. Remote Sensing of Environment 89: 467-483. https://doi.org/10.1016/j.rse.2003.11.005

Xu W, Gu S, Zhao X, Xiao J, Tang Y, Fang J, Zhang J, Jiang S. 2011. High positive correlation between soil temperature and NDVI from 1982 to 2006 in alpine meadow of the Three-River Source Region on the Qinghai-Tibetan Plateau. International Journal of Applied Earth Observation and Geoinformation 13: 528-535. https://doi.org/10.1016/j.jag.2011.02.001

Ziaul Sk, Pal S. 2018a. Anthropogenic heat flux in English Bazar Town and its surroundings in West Bengal, India. Remote Sensing Applications: Society and Environment 11: 151-160. https://doi.org/10.1016/j.rsase.2018.06.003

Ziaul Sk, Pal S. 2018b. Analyzing control of respiratory particulate matter on land surface temperature in local climatic zones of English Bazar Municipality and surroundings. Urban Climate 24: 34-50. https://doi.org/10.1016/j.uclim.2018.01.006

Atmósfera 35(4), 719-735 (2022)
https://doi.org/10.20937/ATM.52963

CONTENTS

Assessment of bioclimatic sensitive spatial planning in a Turkish city, Eskisehir

Süleyman TOY[1]*, Savaş ÇAĞLAK[2] and Aslıhan ESRINGÜ[3]

[1]*Department of City and Regional Planning, Faculty of Architecture and Design, Atatürk University, 25254 Yakutiye/Erzurum, Turkey.*
[2]*Graduate School of Social Sciences, Department of Geography, Mayıs University, 55270 Atakum/Samsun, Turkey.*
[3]*Department of Landscape Architecture, Faculty of Architecture and Design, Atatürk University, 25254 Yakutiye/Erzurum, Turkey.*
*Corresponding author; email: suleyman.toy@atauni.edu.tr

Received: August 14, 2020; accepted: March 4, 2021

RESUMEN

La ciudad de Eskişehir está ubicada en la región de Anatolia central, Turquía, donde prevalecen rigurosas condiciones climáticas continentales (i.e., inviernos fríos y veranos calientes). En años recientes, la calidad y cantidad de los estudios relativos a confort bioclimático han aumentado, tanto globalmente como en Turquía. Las condiciones externas de confort bioclimático se encuentran entre los indicadores de calidad de vida en ambientes urbanos, junto con otras características físicas, sociales y económicas como la calidad del aire, el PIB y la posibilidad de realizar actividades sociales. Los valores que representan condiciones de confort bioclimático se han utilizado en lugar de los valores medios individuales de algunos elementos climáticos para establecer el grado de habitabilidad de una ciudad. El objetivo del presente estudio es determinar: 1) condiciones horarias de confort bioclimático en el centro de la ciudad de Eskişehir en días de calor sofocante, tomando en cuenta valores de confort bioclimático, calculados a partir de una base de datos de 12 años de zonas rurales, urbanas y suburbanas, con un índice de temperatura fisiológica equivalente y el software RayMan para determinar los flujos de radiación solar en individuos durante los cinco meses más calurosos del año; 2) la distribución espacial de estos valores en intervalos de 10 días utilizando sistemas de información geográfica y mapas de bits, tomando en cuenta la elevación y los usos del suelo; y 3) qué diseño urbano y principios de planificación pueden adoptarse para enfrentar condiciones de confort climático adversas desencadenadas por el efecto de la isla urbana de calor. Los resultados del estudio indican que las peores condiciones de confort corresponden a áreas urbanas y las mejores a zonas rurales. Se toman en cuenta nuevos principios de diseño urbano sensibles a aspectos bioclimáticos para crear áreas más confortables desde la perspectiva bioclimática (es decir, sitios con más viento y menos humedad, en los que se aproveche la dirección prevalente del viento y se evite el estrés por exceso de calor).

ABSTRACT

The city of Eskişehir is located in the Central Anatolia Region of Turkey, where harsh continental climatic characteristics are prevalent (i.e., cold winters and hot summers). In recent years, quality and quantity of studies on bioclimatic comfort have increased both all over the world and in Turkey. Outdoor bioclimatic comfort conditions are counted amongst the indicators of human quality of life in urban environments, together with other physical, social and economic features such as air quality, GDP, and possibilities of social activities. The calculated values representing bioclimatic comfort conditions have been used instead of individual mean values of some climatic elements, in order to provide an insight of the liveability of a city. The aim of the present research study is to determine: (1) hourly bioclimatic comfort conditions in the Eskişehir city center during sultry summer days, considering bioclimatic comfort values calculated according to 12-year data from urban, sub-urban and rural areas using the physiological equivalent temperature (PET) index and RayMan software for the calculation of solar radiation fluxes on individuals in the hottest five months of the year; (2) the spatial distribution of these comfort values in decades (10-day intervals) using Geographic Information Systems and raster maps, taking into consideration elevation and land use; and (3) which urban design and planning principles could be adopted to deal with adverse thermal comfort conditions triggered by the urban heat island (UHI) effect. The results of the study indicate that the poorest comfort conditions are provided in urban areas, while rural areas are more advantageous in terms of comfort conditions. New bioclimatic-sensitive urban design principles are taken into consideration to create more comfortable areas from the bioclimatic perspective (i.e., windier and less humid sites open to the prevalent wind direction and out of heat stress).

Keywords: Bioclimatic comfort, urban climate, spatial planning principles, PET, RayMan, Eskişehir.

1. Introduction

Prevailing climatic conditions at a certain point on the Earth shape anthropological activities, including all socioeconomic, cultural, architectural and manufacturing activities, as well as mental and psychological wellbeing. Humans live in convenience with climatic conditions by adjusting all their habits to them and establishing settlements where suitable climatic conditions are prevalent. Following the Industrial Revolution, the sudden migration of population masses to the newly and distorted developing, unhealthy industrial cities caused rapid deteriorations and disorders in every aspect of human life, including economic, social, legal and urban development. Depending on the spatial expansion of cities, natural areas were transformed into structured areas dominated by buildings, and asphalt and concrete surfaces. Such changes, together with other air polluting anthropogenic factors like industrial manufacturing, corrupted the environmental conditions of cities by differentiating climate characteristics. A paradigmatic example is the first industrial city, London, where the first urban-rural climatic differences appeared, as explained by Luke Howard in his book *The climate of London* published in 1820 (apud. Landsberg, 1981). Although ancient people are reported to have perceived different characteristics of urban climate as understood from the descriptions of Vitruvius (75-26 BC) in Roman times (Fukuoka, 1997), there has been a growing interest in urban climatology studies since the beginning of the 20th century (Landsberg, 1981).

The ISO standard 7730 (ISO, 2005) defines thermal comfort as the state of mind that expresses satisfaction with the surrounding environment. Uncomfortable atmospheric conditions for humans such as prevalent extreme temperatures (heat/cold waves) may cause serious or even fatal health problems (chronic disorders, fatigue, headaches, mortality, etc.), decreases in work efficiency, and mental and psychological crises (Nastos and Matzarakis, 2011; Błażejczyk et al., 2018; Aboubakri et al., 2020). The concept bioclimatic comfort refers to optimum climatic conditions in which people are not warned against climate elements and feel comfortable (Toy, 2010). It can be stated that situations in which the human nervous system is not stimulated to balance body temperature, are accepted to be the conditions in which people are not thermally disturbed, that is, comfortable (Höppe, 1999; Laschewski and Jendritzky, 2002).

As reported in several previous studies (Unger, 1999; Robaa, 2003; Toy and Yılmaz, 2010; Çalışkan and Türkoğlu, 2014; Demircan and Toy, 2019), both bioclimatic comfort features and climatic conditions show differences between urbanized areas and their rural counterparts depending on some physical factors like city size (Oke, 1973), population and topography. Therefore, bioclimatic comfort conditions need to be investigated considering not only climatic elements but also the thermal characteristics of human body such as workload, clothing, psychological factors, etc.

Urban areas produce climatic changes due to their modified surface characteristics compared to rural and semi-rural areas. As the urban surfaces embrace varying artificial structures like buildings, asphalt-concrete roads, roofs, green areas and other elements, they reflect different thermal properties. Such characteristics also determine the general urban microclimate. Therefore, urban climates show differences between cities depending on their urban morphology (e.g., urban canyon, green infrastructure).

In the literature, urban thermal comfort conditions are evaluated generally associated with urban heat islands (UHIs) and their intensity from various parts of the world (Unger [1999] in Hungary; Robaa [2003] in Egypt; Demircan and Toy [2019] in Turkey, etc.). Such results are in similar ranges with those found in previous studies, e.g., in the hot and continental climate city of Szeged, Hungary, where the difference in the urban-rural physiological equivalent temperature (PET) index was found to be 2.9 ºC (Gulyas et al., 2010). In the same country, Hungary, in the city of Budapest, the mean yearly PET difference between urban and rural settings was determined to be 3.0 ºC (Kovacs and Nemeth, 2012). Blazejczyk et al. (2016) found a 4-5 ºC mean difference in the Universal Thermal Climate Index (UTCI) in Warsaw, Poland, between a densely built city part and an area covered with low-density buildings and higher vegetation. In a study in Turkey, the mean urban-rural PET difference in the city of Ankara was 2.2 ºC during the summer (Çalışkan and Türkoğlu, 2014). In Şanlıurfa, one of the hottest cities in Turkey, the yearly mean PET difference was found to be 2.1 ºC between urban and rural areas (Toy et al., 2018). Toy and Yılmaz (2010) found urban-rural comfortable range differences for the thermohygrometric index (THI) and the predicted mean vote (PMV) of 2.2 and 0.7%, respectively, in a small sized and unindustrialized city, Erzincan, Turkey,.

In urban environments, surfaces with increased heat storage capacity have adverse effects on human bioclimatic comfort conditions, recreation possibilities and human well-being by causing heat stress on individuals, especially during summer (Balık and Yüksel, 2014). However, recreational activities to be performed in livable urban environments with favorable bioclimatic comfort conditions have social, psychological and economic advantages in developing countries like Turkey (Toy and Yılmaz, 2009).

Tools that use spatial weather data in urban environment and that can assist decision makers in developing plans and strategies to minimize the negative impacts of urbanization on human thermal comfort have been developed and used to produce several useful products like maps for urban climate, thermal comfort conditions, air pollution, modeling and simulation maps (e.g., Envi-Met [Bruse, 2004] and RayMan [Matzarakis et al., 2007]). Spatial urban meteorological data obtained from real-time monitoring systems or modeled data based on the mentioned tools can help determine the spatial distribution of unfavorable conditions related to urban climate from a bioclimatic perspective, such as uncomfortable zones and areas prone to the UHI. Results of studies that use these methods and tools help authorities in planning the correct measures to cope with them (Yılmaz, 2013; Paramita and Matzarakis, 2019).

Cities, especially in developing countries like Turkey, face a rapid and deteriorating urbanization process in which natural land surfaces are turned into impervious ones. This undesired process produces urban areas with weak livability due to unfavorable and uncomfortable bioclimatic conditions. As mentioned above, all bioclimatic planning and modeling in urban environments have valuable results regarding more livable cities. As a developing country, Turkey has experienced a long-lasting urbanization process since the beginning of heavy industrialization attempts in the 1950s centered in large cities. This growth caused rural migration to urban settings as in other countries. The study area of this article, Eskişehir, started its industrialization and urbanization process in the 1930s, earlier than other Turkish cities. Public investments in Eskişehir aimed to develop manufacturing and railway industries (Gümüş, 2004), which in turn produced a rapid, unplanned and distorted urbanization process (Toy et al., 2019).

In the scope of this study, the bioclimatic comfort conditions of Eskişehir's city center are analyzed considering the warm period of the year (from May to the end of September) in order to determine the comfortable and uncomfortable zones and periods using PET, a widely accepted thermal comfort index (VDI, 1998; Höppe, 1999; Matzarakis et al., 1999), and the RayMan calculation model (Matzarakis et al., 2007). The obtained PET values were mapped with the software package ArcGIS10.1 to show areas reflecting unfavorable bioclimatic comfort conditions, which allows to intervene and determine measures from the urban planning and geographical perspectives.

2. Materials and methods

The study area is the city of Eskişehir, located on a plain (760-800 masl) in the Upper Sakarya subregion of Central Anatolia, Turkey (39º 49'-39º 43' N, 30º 24'-30º 43' E). The city is surrounded by the Sündiken mountains and high plateaus to the north. It is divided by the Porsuk stream, a branch of Sakarya river flowing from north to the south (Fig. 1).

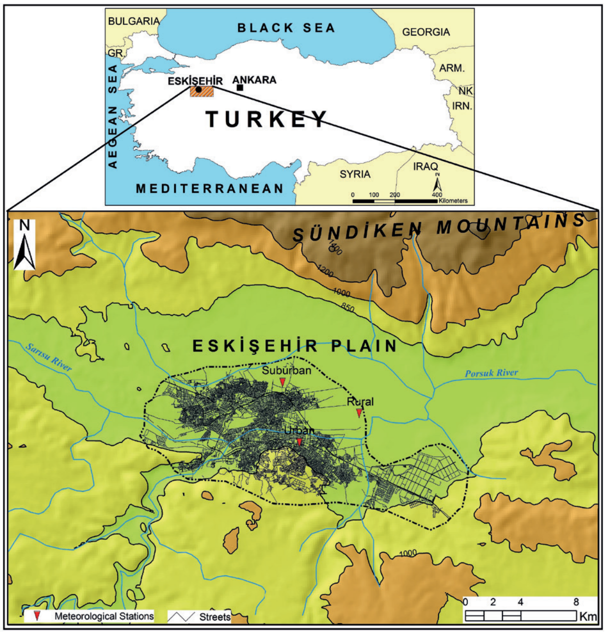

Fig. 1. Location of the study area.

The city center is comprised of two central districts (neighborhoods), Tepebaşı and Odunpazarı. Several industrial facilities, such as sugar, aircraft and automotive factories, as well as universities, are established in the city center. Since Eskişehir is located in an important road network junction, it has experienced a rapid industrialization and has received significant migration from its surroundings.

Continental climatic characteristics are prevalent in the city, with hot summers and dry, cold, snowy winters. The annual average temperature is 10.6 ºC (with extreme minimum of 27.8 ºC in January and extreme maximum of 40.6 ºC in July). Annual rainfall is 307.2 mm and relative humidity is 65%. The average annual wind speed is 3.1 m s^{-1} and the prevalent wind direction is SW (Table I).

Hourly and daily meteorological data were obtained over a 12-year observation period (2007-2018) to precisely evaluate bioclimatic comfort values, from three meteorology stations located in (1) the Eskişehir Regional Meteorology Administration, representing a densely structured urban area (U), (2) Anadolu University campus, representing a suburban area (SU), and (3) Eskişehir airport, representing an open rural area (R). Table II presents the features of the meteorological measurement stations.

Twelve-years hourly data of 153 days, covering the summer period, were used in this study. Meteorological data used were air temperature (Ta [ºC]), relative humidity (RH [%]), wind velocity (Wv [m/s]), and cloudiness (octas; x 10^{-1}).

In this study, the worldwide PET index (VDI, 1998; Höppe, 1999; Matzarakis et al., 1999) and the RayMan radiation model (Matzarakis et al., 2007), were used to calculate bioclimatic comfort values. PET considers not only the combined effects of climatic parameters on individuals but also factors related directly to human body, like physical activity, clothes and physical features like age, weight and length as coefficients. In this respect, human bioclimatic comfort conditions were calculated considering coefficients according to a 35 year-old man with a height of 175 cm and a weight of 75 kg under a clothing insulation of 0.9 clo and activity load of 80 W (Matzarakis and Mayer, 1996; Matzarakis et al., 1999).

Bioclimatic comfort intervals given in Table III were used in order to divide the calculated PET values into categories according to the predetermined thermal sensation and stress levels. Distribution of the calculated hourly PET values was determined considering nine ranges from very cold through comfortable to very hot in all temporal and spatial analyses in the area.

Spatial distribution of the calculated hourly PET values was dtermined using the 10-day averages and categories mentioned above with ArcGIS 10.1 software. Elevation data and land use characteristics (e.g., open green spaces, impervious surfaces, roofs which show different radiation properties) of the study area were included in the spatial analysis in the software. PET, elevation and land use data were overlapped in raster form. Points where data representing U, SU and R surface characteristics were obtained. U represents densely structured neighborhoods with 5-6 story buildings, while SU is a university campus

Table I. Long-term means of some climatic parameters (1975-2018).

Eskişehir	Jan	Feb	Mar	Apr	May	June	July	Aug	Sep	Oct	Nov	Dec	Mean
Mean temperature (°C)	0.5	0.7	4.6	9.7	14.7	18.9	21.8	21.5	16.7	11.7	5.7	1.4	10.6
Mean maximum temperature (°C)	3.7	6.0	11.3	16.6	21.8	26.0	29.1	29.2	25.0	19.8	12.4	5.5	17.2
Mean minimum temperature (°C)	–4.2	–4.0	–1.4	2.9	6.9	10.4	13.1	13.1	8.4	4.6	0.2	–2.2	4.0
Mean sunshine duration (h)	2.4	3.5	5.2	6.2	8.4	10.2	11.1	10.4	8.4	6.1	4.2	2.1	6.4
Mean number of rainy days	11.6	11.6	11.2	11.3	9.5	6.0	3.8	3.3	4.4	8.1	9.3	12.4	8.5
Mean monthly rainfall (kg m^{-2})	27.9	23.5	26.1	42.0	37.4	20.7	13.4	9.4	16.3	26.8	29.6	34.1	307.2 (Total)
Extremely high temperature (°C)	18.2	20.5	28.1	30.8	33.3	36.4	40.6	39	36.4	33.0	25.4	21.4	30.3
Extremely low temperature (°C)	–27.8	–22..4	–12.0	–10.4	–2.2	0.5	5.0	5.4	–2.0	–6.8	–12.2	–19.2	–8.7
Mean wind speed (m s^{-1})	3.0	3.2	3.3	3.1	3.3	3.7	3.4	2.8	2.4	2.7	2.7	3.1	3.1
Prevalent wind direction	WSW	S	WSW	SW	NNW	WNW	W	NW	W	W	ESE	SW	SW
Mean relative humidity (%)	77	73	66	63	62	57	53	55	60	66	71	78	65.0

Source: Turkish State Meteorological Service.

Table II. Meteorological stations used in this study.

Represented area	Location	Altitude (masl)	Surface
U	39º 45’ 56.2” E, 30º 33’ 00.7” N	801	Densely structured
SU	39º 48’ 29.9” E, 30º 31’ 55.2” N	786	Loosely structured
R	39º 46’ 51.6” E, 30º 34’ 46.9” N	787	Not structured

in loosely structured open space and R is an airport base with very few buildings near the measurement point (Fig. 2).

3. Results

Distribution of hourly and daily mean, maximum, minimum and extreme PET values during the whole study period (153 days) according to time of the day and areas (i.e., U, SU and R) is given in Table IV and Figure 3. It can be seen from the table that 12-year mean PET values are 21.0 ºC (35.0 to 10.6 ºC), 19.6 ºC (32.4 to 9.0 ºC) and 18.6 ºC (32.0 to 7.3 ºC) in U, SU and R, respectively. There is a 1.4, 2.4 and 1.0 ºC mean PET difference between U and SU, U and R, and SU and R, respectively. Mean maximum PET

Table III. Human thermal sensation and stress ranges of PET (Matzarakis et al. 1999; Höppe, 1999).

PET (ºC)	Thermal sensation	Level of thermal stress
< 4	Very cold	Extreme cold stress
4.1-8	Cold	Strong cold stress
8.1-13	Cool	Moderate cold stress
13.1-18	Slightly cool	Slight cold stress
18.1-23	**Neutral (comfortable)**	**No thermal stress**
23.1-29	Slightly warm	Slight heat stress
29.1-35	Warm	Moderate heat stress
35.1-41	Hot	Strong heat stress
> 41	Very hot	Extreme heat stress

PET: physiological equivalent temperature.

Fig. 2. Surface characteristics of the measurement points.

Table IV. Distribution of hourly mean PET values over the whole study period.

PET (ºC)	Hours	0	1	2	3	4	5	6	7	8	9	10	11	12	13	14	15	16	17	18	19	20	21	22	23
Locations	U	11.5[c]	11.2[c]	10.8[c]	10.6[c]	10.6[c]	13.1[d]	19.1[e]	24.9[f]	29.1[g]	31.9[g]	33.6[g]	34.1[g]	34.6[g]	35.0[g]	33.6[g]	30.8[g]	26.9[f]	21.2[e]	16.0[d]	14.7[d]	13.8[d]	12.9[c]	12.3[c]	11.8[c]
	SU	8.5[c]	8.1[c]	7.5[b]	7.3[b]	8.6[c]	11.8[c]	18.1[e]	23.9[f]	28.2[f]	30.5[g]	31.7[g]	31.9[g]	32.0[g]	31.8[g]	30.1[g]	27.2[f]	23.3[f]	18.4[e]	13.9[d]	12.4[c]	11.4[c]	10.6[c]	9.8[c]	9.2[c]
	R	9.6[c]	9.2[c]	9.0[c]	9.8[c]	11.6[c]	16.0[d]	21.5[e]	26.1[f]	29.4[g]	31.2[g]	31.9[g]	32.3[g]	32.4[g]	32.0[g]	30.5[g]	27.1[f]	22.8[e]	17.1[d]	14.2[d]	13.0[c]	12.0[c]	11.2[c]	10.4[c]	10.0[c]

	U			SU			R			U-SU			U-R			SU-R		
Hourly	H	M	L	H	M	L	H	M	L	H	M	L	H	M	L	H	M	L
Mean	35.0[g]	21.0[e]	10.6[c]	32.4[g]	19.6[e]	9.0[c]	32.0[g]	18.6[e]	7.3[b]	2.6	1.4	1.6	3.0	2.4	3.3	0.4	1.0	1.7
Max.	52.5[a]	33.5[g]	18.2[e]	50.3[a]	34.1[g]	17.6[d]	47.8[a]	30.5[g]	17.2[d]	2.2	–0.6	0.6	4.7	3.0	1.0	2.5	3.6	0.4
Min.	15.7[d]	6.5[b]	0.2[a]	13.2[d]	4.4[b]	–3.5[a]	11.1	3.5[a]	–3.9[a]	2.5	2.1	3.7	4.6	3.0	4.1	2.1	0.9	0.4

[a]Extreme cold stress, strong heat stress, extreme heat stress (< 4 °C; 35.1-41 °C; > 41 °C); [b]strong cold stress (4.1-8 °C); [c]moderate cold stress (8.1-13 °C); [d]light cold stress (13.1-18 °C); [e]no thermal stress (18.1-23 °C); [f]slight heat stress (23.1-29 °C); [g]moderate heat stress (29.1-35 °C).
U: urban; SU: suburban; R: rural; H: highest; M: mean; L: lowest.

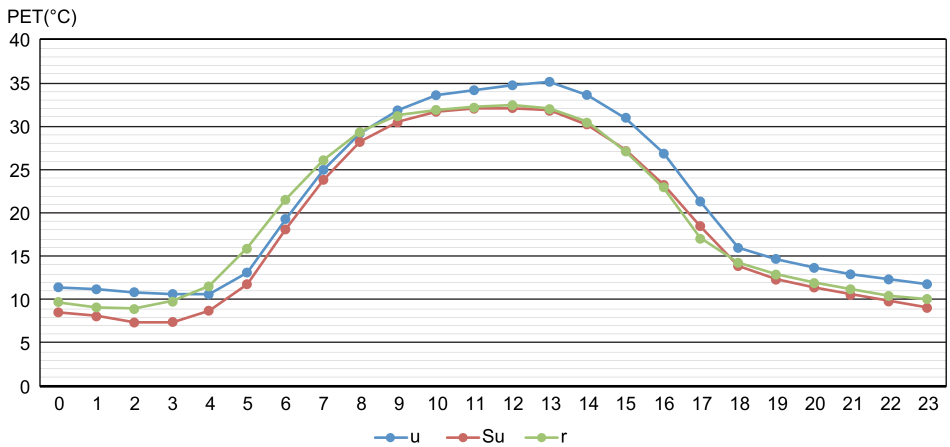

Fig. 3. Hourly trend of PET values throughout the day.

values are 33.5 ºC (52.5 to 18.2 ºC) 34.1 ºC (50.3 to 17.6 ºC) and 30.5 ºC (47.8 to 17.2 ºC), while mean minimum PET values are 6.5 ºC (15.7 to 0.2 ºC), 4.4 ºC (13.2 to –3.5 ºC) and 3.5 ºC (11.1 to –3.9 ºC) in U, SU and R, respectively, over the whole study period. There is a –0.6, 3.0 and 3.6 ºC maximum PET difference and a 2.1, 3.0 and 0.9 ºC minimum PET difference between U and SU, U and R, and SU and R, respectively.

In all areas, the comfortable time interval is 1 h in the morning at 6.00 LT and 1 h in the evening at 17:00 LT in U and SU, and at 16:00 LT in R. Moderate and slight cold stress is prevalent from 18:00 LT (17.00 LT in rural areas) to 5.00 LT. R is less exposed to heat stress (1 h less than other areas). The largest heat stress is seen in U, but the severity of heat stress is 2 h less in SU than U.

The largest difference in mean PET values is seen between U and R, as expected. Between areas, differences in mean PET values are smaller than those in the averages of maximum and minimum PET values. In terms of maximum PET values, SU represents warmer characteristics than U; however, in mean and minimum PET values U is the warmest area, which is consistent with the results of previous studies.

It is clearly understood from Figure 3 that U shows the highest PET values during the early morning (09:00-03:00 LT), as R shows a rapid temperature increase after sunrise, while SU reflects a similar trend in the afternoon.

Table V shows the hourly distribution of comfort ranges throughout the day in the evaluated period. It is seen that the area where the largest number of comfortable hours is seen is U with 431 h (of 3672 h in the hot period; 11.7%), the smallest number of comfortable hours is seen in R with 356 h (9.7%), while comfortable hours in SU amount to 10.8%. U has 0.9% more comfortable hours than SU and 2% more than R, while SU has 1.1% more comfortable hours than R (TableV).

Figure 4 shows the hourly distribution of PET values in U over the whole study period. It is seen that cold and cool ranges (cold stress) are perceived from 19:00 to 04:00 LT (10 h) and between 09:00 and 16:00 LT (8 h) warm and hot ranges (heat stress) are dominant. The comfortable range spans only between 05:00 and 08:00 LT and 17:00 and 18:00 LT (6 h).

Figure 5 shows the hourly distribution of PET values in the SU over the whole study period. Cool and cold ranges (cold stress) are dominant between 19:00 and 05:00 LT (11 h), while warm and hot ranges (heat stress) are seen between 10:00 and 15:00 LT (6 h) and comfortable conditions prevail between 06:00 and 09:00 and 16:00 and 18:00 LT (7 h).

Figure 6 shows the hourly distribution of PET values in the rural area throughout the study period. Cool and cold ranges (cold stress) are seen between 18:00 and 04:00 LT (11 h) while warm and hot ranges (heat stress) are seen between 10:00 and 14:00 LT (4 h) and comfortable conditions are prevalent between 05:00 and 10:00 and 15:00 and 17:00 LT (9 h). Daily PET values were mapped at 10-day intervals to detect their spatial distribution in the city center according to the stations. It can be seen in this figure that slightly

Table V. Distribution of comfort ranges in hours and percentage.

Comfort Ranges	< 4		4.1-8.0		8.1-13.0		13.1-18.0		**18.1-23.0**		23.1-29.0		29.1-35.0		35.1-41.0		> 41.0	
	Very cold		Cold		Cool		Slightly cool		**Comfortable**		Slightly warm		Warm		Hot		Very hot	
	A	B	A	B	A	B	A	B	**A**	**B**	A	B	A	B	A	B	A	B
U	63	1.7	239	6.9	760	20.7	763	20.8	**431**	**11.7**	422	11.5	463	12.6	386	10.5	145	3.9
SU	117	3.2	344	9.4	828	22.5	682	18.6	**396**	**10.8**	446	12.1	450	12.3	275	7.5	134	3.6
R	176	4.8	466	12.7	848	23.1	588	16	**356**	**9.7**	429	11.7	426	11.6	292	8	91	2.5

	Cold stress total (h; %)					Heat stress total (h; %)			
U	1825		49.7			1416		38,5	
SU	1971		53.7			1305		35.5	
R	2078		56.6			1238		33.8	
U-SU	–1.5	–2.9	–1.8	2.2	**0.9**	–0.6	0.3	3	0.3
U-R	–3.1	–6.2	–2.4	4.8	**2**	–0.2	1	2.5	1.4
SU-R	–1.6	–3.3	–0.6	2.6	**1.1**	0.4	0.7	–0.5	1.1

A: total hours; B: percentage of hours.

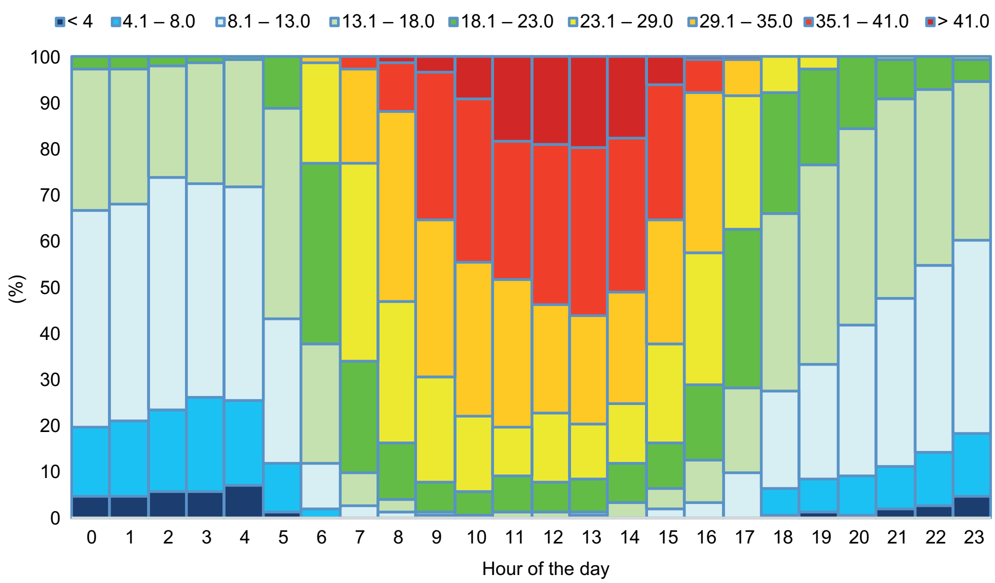

Fig. 4. Hourly distribution of PET values in U over the study period.

cool conditions are perceived in the whole study area when the spatial distribution of average daily PET values from day 130 to 150 day are considered. On day 160, 55.8% of the study area is in comfortable range, 44.2% is under the effect of slightly cool conditions, comfortable conditions are observed in the urban area. On day 170, 11.3% of the study area is in comfortable range and 88.7% is under the effect of slightly cool range. Comfortable conditions are determined to be prevalent in the areas covered by dense buildings and narrow streets in the city. This is because in the first and last months of the study period during nighttime and some hours of daytime, air temperature is lower in suburban and rural areas

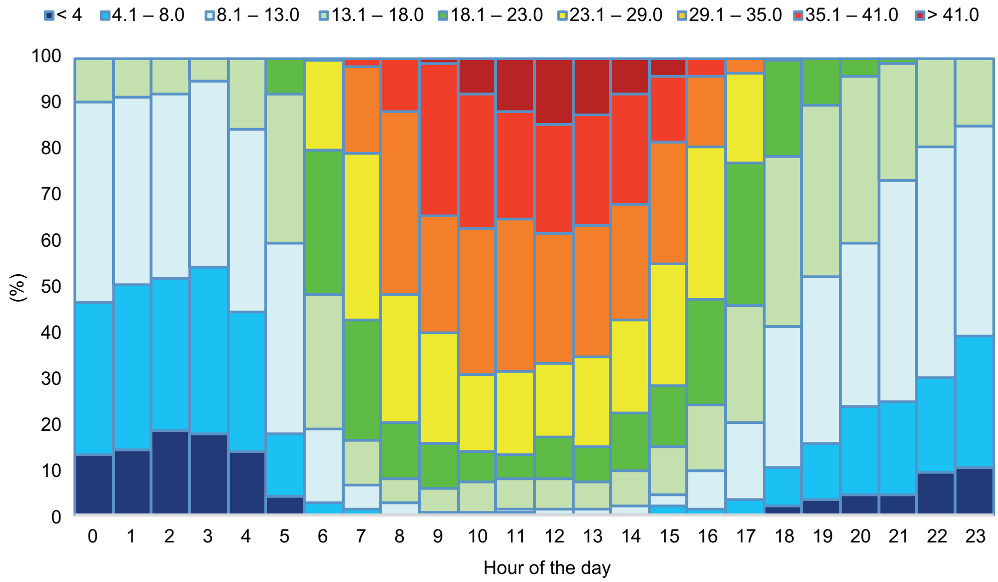

Fig. 5. Hourly distribution of PET values in SU over the study period.

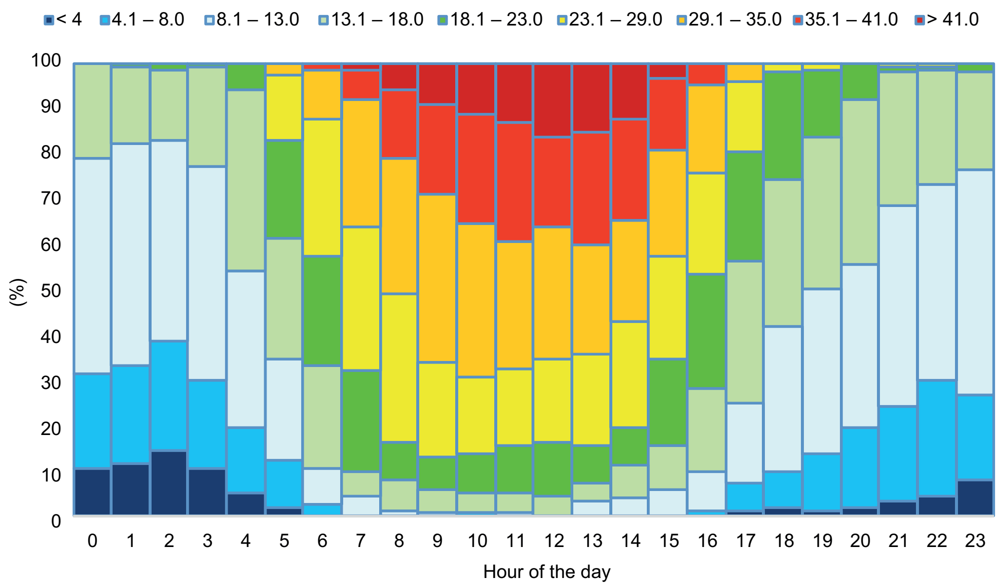

Fig. 6. Hourly distribution of PET values in R over the study period.

but higher in urban areas due to the UHI effect, which causes longer hours of calculated comfortable range. On the day 180, while slightly warm conditions (heat stress) are seen in densely built urban areas (3.5%), comfortable conditions are prevalent in the vast majority of the area (96.5%). Slightly warm conditions were determined in urban areas (32.8% of the whole study area) on day 190. Comfortable conditions were determined in 67.2% of the study area, covering rural and suburban areas. On day 200, a slightly warm stress was determined in the majority of urban and suburban areas and (60.6% of the study area). Comfortable conditions were perceived in rural areas and (39.4% of the study area). On days 210 and 220, a slightly warm stress was detected in the whole area. On day 230, a slightly warm stress was observed in the urban area, which accounts for 57.6% of the whole area. Comfortable conditions were experienced in the remaining 42.4% of the study area, corresponding to rural environments. On day 240, comfortable conditions were perceived throughout the whole area and on day 250 comfortable conditions were observed in urban and suburban areas. Comfortable conditions were detected in 61.7% of the area on day 250, while a slight cool stress was detected in the remaining 38.3% (rural settings). On day 260, a slight warm stress was experienced in the urban area (24.5% of the whole study area). Comfortable conditions were observed in 75.5% of the study area (suburban and rural). While the urban and suburban areas were comfortable on day 270, a slight cool stress was determined in the rural area (Fig. 7).

Figure 8 exhibits the spatial distribution of mean daily maximum PET values. It is seen that slightly warm stress was experienced across the study area on day 130 while comfortable conditions were prevalent in 70.9% of the area and slight warm stress in the rest. While a slightly warm stress was observed in the urban area, comfortable conditions were found in suburban and rural areas. It can be inferred from this result that due to the effect of urban morphology and surface, the urban area gets warmer earlier than the rest and remains calmer (less windy), which reflects on bioclimatic comfort values. On day 150, a slightly warm range is prevalent in the whole area, while a warm range is prevalent on day 160. On day 170, 62.2% of the area experienced warm stress and 37.8% was under the effect of slightly warm stress. On day 170, warm

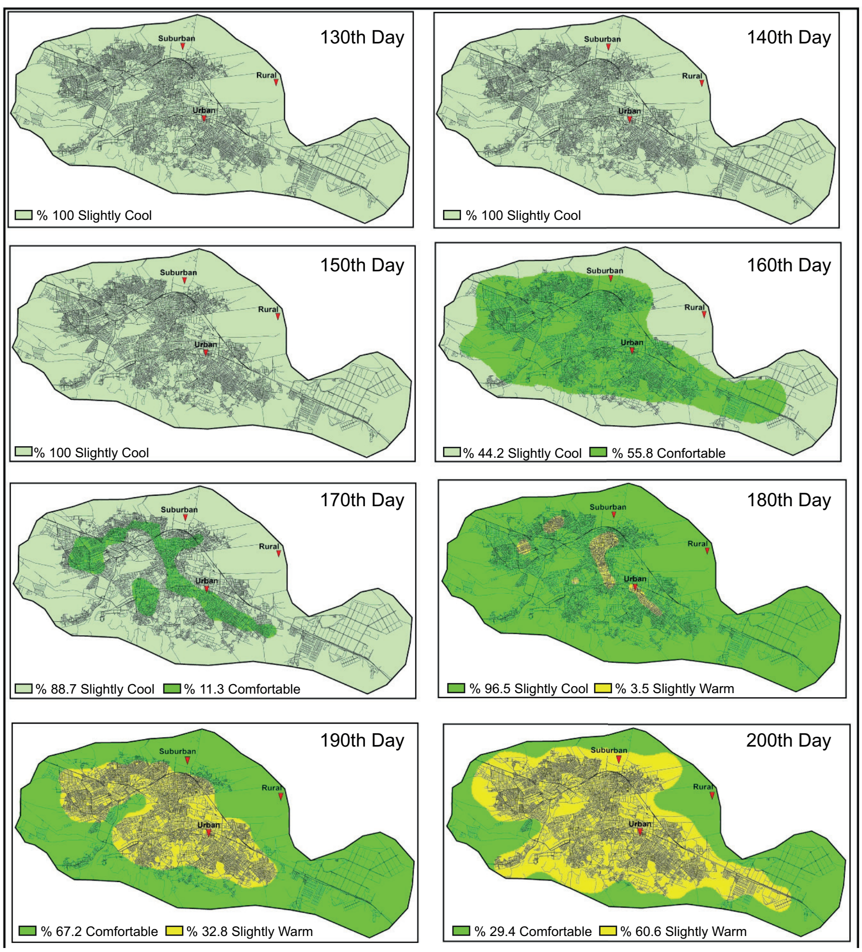

Fig. 7. Spatial distribution of daily mean PET values.

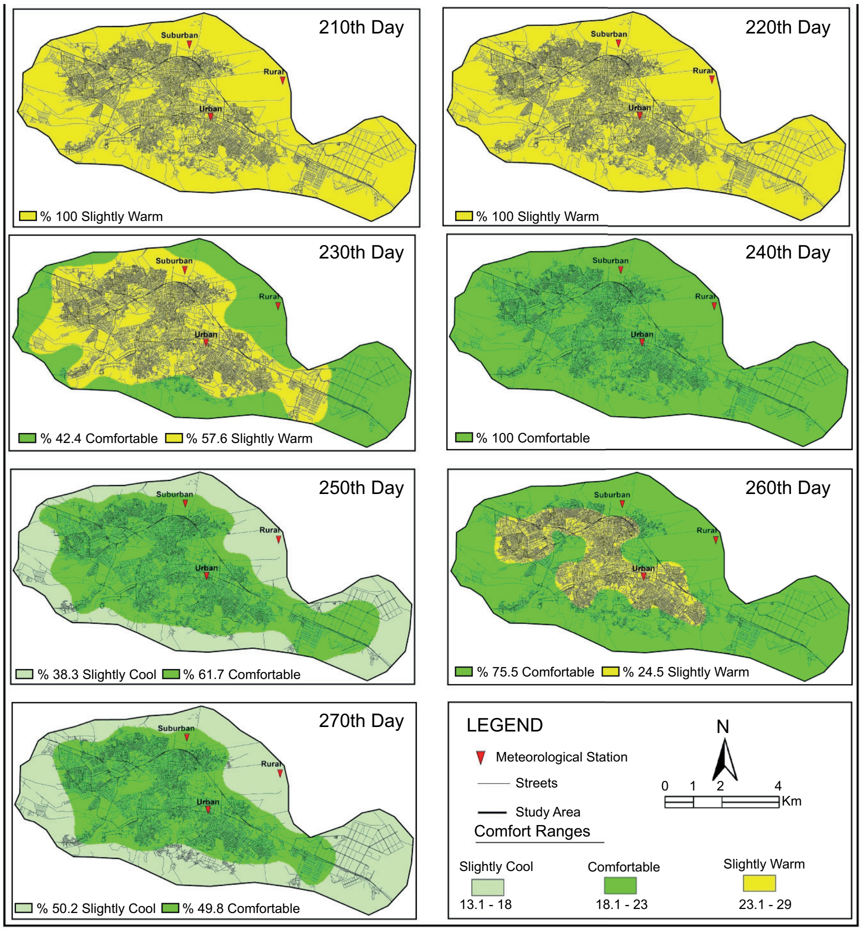

Fig. 7. Spatial distribution of daily mean PET values.

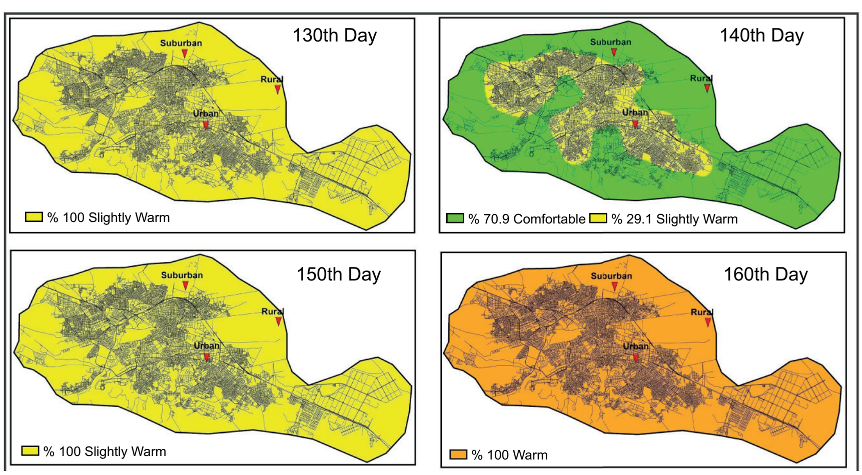

Fig. 8. Spatial distribution of daily mean maximum PET values.

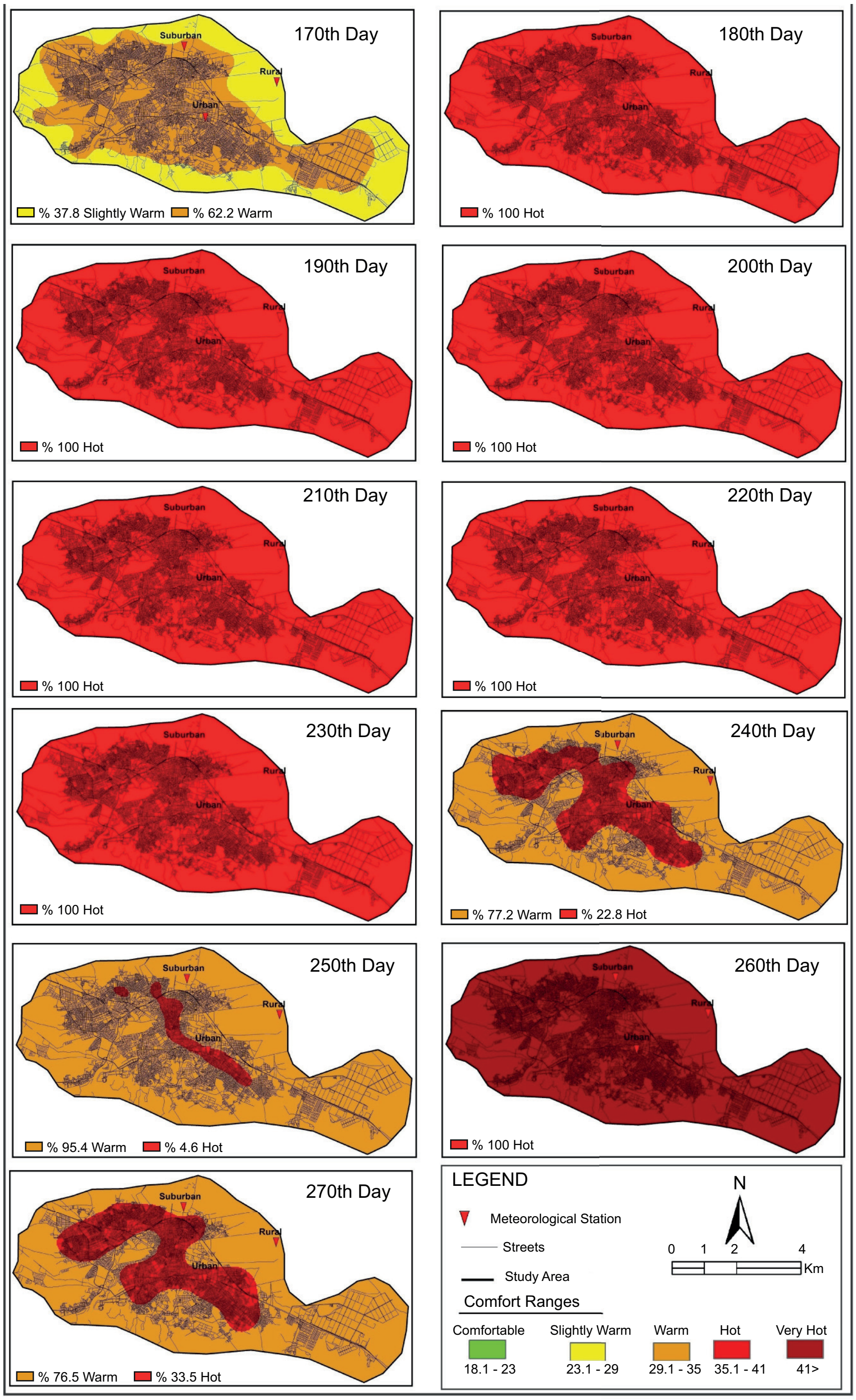

Fig. 8. Spatial distribution of daily mean maximum PET values.

stress was observed in urban and suburban areas, while slightly warm stress was observed in the rural area. From day 180 to 230, hot stress was observed throughout the study area. On day 240, 22.8% of the area consisting of dense urban areas experienced hot stress. In areas covering rural and suburban areas (77.2%), a warm stress was observed. On day 250, warm stress was determined in 95.4% of the area, and hot stress in dense built areas (4.6%). On day 260, heat stress was experienced in the whole area. On day 270, 33.5% of the area revealed hot stress and 76.5% warm stress. Hot stress was determined in densely built areas and warm stress in suburban and rural areas. PET values calculated for urban, suburban and rural areas fell into different comfort ranges on days 160, 170, 180, 190, 200, 230, 250, 260 and 270. The density of the built surface (ratio of empty spaces), urban texture (type and height of buildings and orientation and width of streets) and the characteristics of surface covers are expected to be the effective features on the spatial differences of PET values. Compared to rural areas, urban PET values fall into the next warmer comfort range on all days mentioned above while PET values for suburban are sometimes in the same range than urban and rural. As stated by Grimmond (2007), this condition of urban areas is related to their larger surface due to 3-D geometry of buildings, causing greater rate of solar radiation absorption, higher heat storage capacity of surface materials, smaller rate of heat loss through air movement (canyon geometry), larger impervious surface areas, lower evapotranspiration, and higher additional energy supply from combustion of fossil fuels and electricity.

Figure 9 shows the spatial distribution of mean daily minimum PET values. It is seen that on day 130, the rural area (48.1% of the study area) was under very cold stress, urban and suburban areas (50.7%) were under cold stress, and a portion of the urban area (1.2%) was under the effect of a cool range. On day 140, 43.1% of the area was under the effect of very

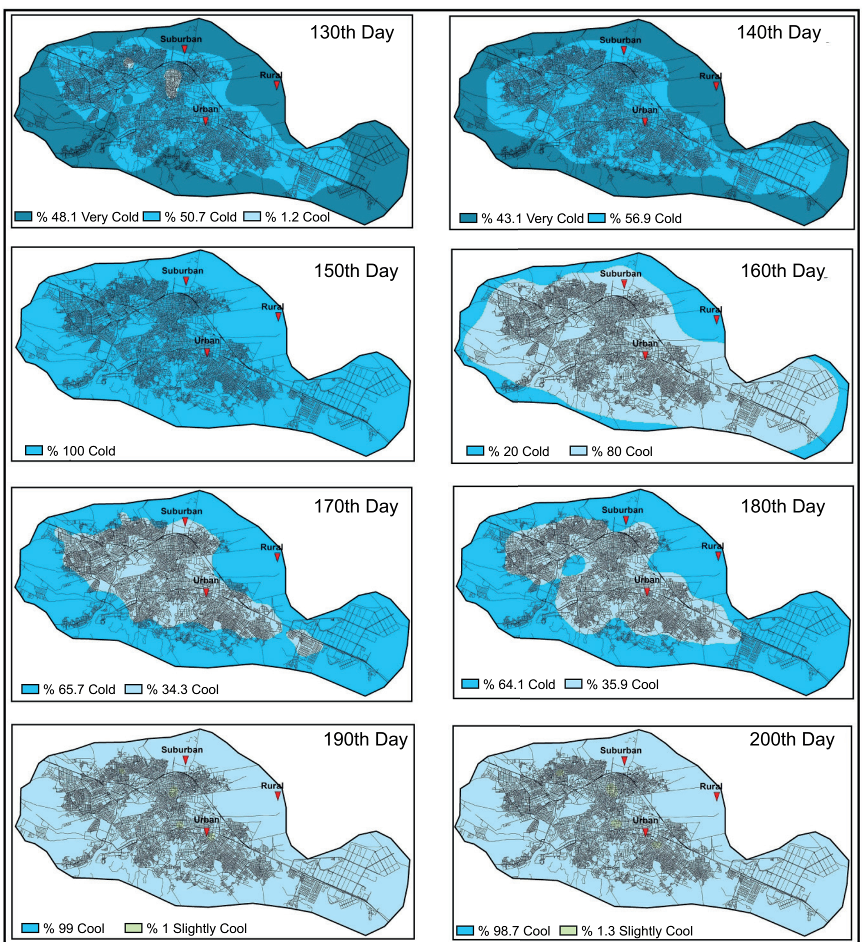

Fig. 9. Spatial distribution of daily average minimum PET values.

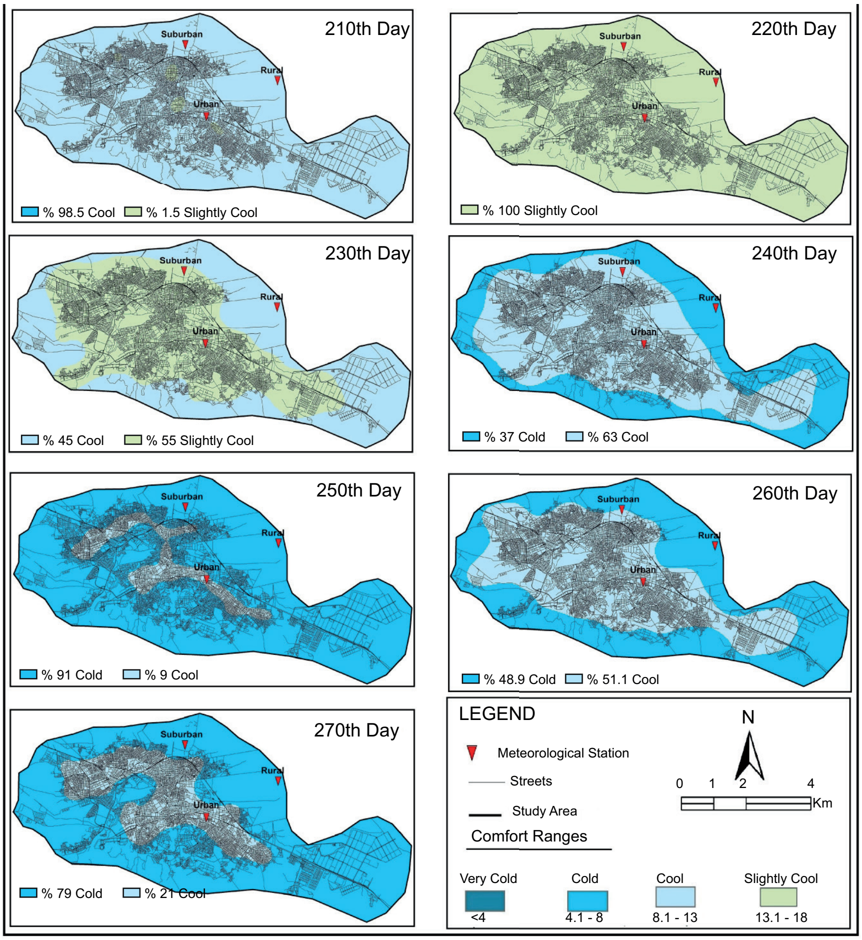

Fig. 9. Spatial distribution of daily average minimum PET values.

cold stress and 56.9% under cold stress. Very cold stress was observed in rural areas and cold stress was observed in urban and suburban areas. On day 150, cold stress was determined throughout the study area. On day 160, 20 and 80% of the study area experienced cold stress and cool, respectively, and on day 170, 65.7% of the area (rural) was under the effect of cold and 34.3% (suburban and urban) experienced a cool range. On day 180, a cool range was observed in urban areas (35.9% of the study area), and cold stress was felt in suburban and rural areas (64.1%). From day 190 to 210, the vast majority of the study area experienced cool and slightly cool ranges in dense building areas. On day 190, the slightly cool area corresponded to 1% of the study area, whilst this percentage was 1.3% on day 200 and 1.5% on day 210. On day 220, a slightly cool range was experienced in the study area. On day 230, 55% of the study area (urban and suburban) faced a slightly cool range, while 45% (rural) experienced a cool range. On day 240, 37% of the study area is under the effect of a cold range and 63% is under a cool range, while on day 250, 91.0% of the area is under a cold range and 9.0% under a cool range. On day 260, 48.9% of the area was under a cold stress and 51.1% faced a cool range, while on day 270, 79% of the area was under a cold stress and in 21% the cool range was dominant. From day 240 to 270, rural areas were under a cold stress. Suburban areas were under the effect of a cool range on day 240 and a cool range was observed on other days in urban areas.

Regarding the spatial distribution of mean PET values, the whole study area was under the same range on days 130, 140, and 150 (slightly cool), on days 210 and 220 (slightly warm), and on day 250 (comfortable). PET values were higher in urban areas on day 170 (comfortable), and days 180, 190 and 260 (slightly warm). As for urban and suburban areas, PET values were higher (comfortable) on days 160, 250, and 260, as well as on days 200 and 230 (slightly warm) in urban and suburban areas. As for the distribution of the average daily maximum PET values, the whole study area was under the same range on days 130, 150 (slightly warm) and 160 (warm), from days 180 to 230 (hot), and on day 260 (very hot). Day 140 was slightly warm and on days 240, 250 and 270 hot ranges were prevalent in urban areas, while on day 170 a warm range was prevalent in urban and suburban areas. Mean maximum daily PET values were prevalent in the area throughout the period showing warm ranges. With respect to the distribution of daily mean minimum PET values, on days 150 (cold) and 220 day (slightly cool), the whole study area was under the effect of the same PET range. On days 130, 250 days (cool) and 190, 200, 210 (slightly cool), urban areas showed the highest PET values in densely built areas with narrow streets. The lowest mean minimum PET values in urban areas were prevalent on days 180 and 270 (cool), 140 (cold), 160, 170, 240 and 260 (cool), and 230 (slightly cool) in urban and suburban areas.

4. Discussion and conclusions

Anthropogenic factors, mainly industrialization and concurrent urbanization cause cities to have unique climatic characteristics. In densely structured and industrial cities, both altered land use types and industrial and traffic combustion impact atmospheric features and thus climatic elements of the cities. Surface covers in urban areas, such as impervious surface of roads and roofs have different radiative, thermal and hydraulic properties than bare rock, soil, vegetation and water, their pre-existing counterparts; this causes urban environment to get warmer at a considerably higher rate by storing a larger amount of solar radiation and heat, and losing a smaller rate of energy.

From this point of view, every city should be analyzed on a micro scale basis and suggestions should be developed based on this type of evaluation. Turkey offers diversity in climatic characteristics even in short distances, mainly due to different topographic features. This study is significant in the literature since it deals with a middle size Turkish city, Eskişehir, in the Anatolia Region, where continental climatic features isolated from marine effects are prevalent. The city was industrialized and rapidly urbanized in the past, but over the last 2-3 decades industrial plants have been removed and some favorable urban development attempts have been made to increase the livability of the city center. The study conducted a detailed bioclimatic comfort analysis to determine the effect of a structured city center on thermal conditions by comparing it with suburban and rural counterparts. The results reveal that PET values in the city of Eskişehir are higher in urban areas than those determined in suburban and rural settings. Based on the mean PET values of 153 summer days, PET differences of 1.4, 2.4C and 1.0 ºC were found between urban and suburban, urban and rural, and suburban and rural areas, respectively. As can be seen from the mean differences, urban areas still maintain its impact on thermal conditions, even though the city lost the majority of industrial facilities. This effect is directly related to the UHI effect, which includes the impact of surface characteristics, traffic load and other heat sources. The differences are within the ranges found in literature.

This study shows that the city center is warmer than its surroundings regarding hourly maximum and minimum PET values and also spatial distributions. The suburban area shows some advantages over urban and rural areas; however, it indicates a changing bioclimatic condition closer to that prevalent in suburban areas. This study also highlights how extreme conditions affect the spatial distribution of bioclimatic features, which give clues to decision makers on a spatial basis to deal with the negative impacts caused by unplanned spatial developments. From this point of view, the study clearly shows the UHI effect in urban areas over the whole period. Land-use change is seen to be especially impactful in the study area regarding the bioclimatic characteristics, in addition to traffic density and manufacturing activities. The city has experienced a planned physical development process over the last years in order to increase the vegetation cover and water surface by reorganizing a riverbank and designing green infrastructure. However, even under such conditions, in the torrid summer period these efforts do not seem to be efficient for obtaining comfortable conditions in the city center.

More severe measures should be taken considering spatial planning and design principles to moderate the thermal effects during the summer and to increase the length of the comfortable period. Taking into account the prevalent wind direction to expand the cooling effect of water surface (already in use) to wider areas, restricting impervious surfaces, encouraging the use of public transport (already in use), and increasing the rate of green areas per capita, should be among the suggestions for the city center. The most important conclusion from the study may be that even if industrial structures have been removed from a city, it should have efficient urban systems ranging from green structures to water surfaces, public transport to motor-vehicle roads, to mitigate the effects of UHI-related human thermal discomfort.

References

Aboubakri O, Khanjani N, Jahani Y, Bakhtiari B. 2020. Thermal comfort and mortality in a dry region of Iran, Kerman; A 12-year time series analysis. Theoretical and Applied Climatology 139: 403-413. https://doi.org/10.1007/s00704-019-02977-8

Balık H, Yüksel ÜD. 2014. Integration of climate data to planning process. Turkish Journal of Scientific Reviews 7: 01-06.

Blazejczyk K, Kuchcik M, Dudek W, Krecisz B, Blazejczyk A, Milewski P, Szmyd J, Palczynski C. 2016. Urban heat island and bioclimatic comfort in Warsaw. In: Counteracting urban heat island effects in a global climate change scenario (Musco F., Ed.). Springer, Cham, 305-321.

Błażejczyk K, Baranowski J, Blazejczyk A. 2018. Climate related diseases. Current regional variability and projections to the year 2100. Quaestiones Geographicae 37: 23-36. https://doi.org/10.2478/quageo-2018-0003

Bruse M. 2004. ENVI-met. Available at: http://www.envimet.com (accessed on: March 7, 2021).

Çalışkan O, Türkoğlu N. 2014. The trends and effects of urbanization on thermal comfort conditions in Ankara. Journal of Geographical Sciences 12: 119-131.

Demircan N, Toy S. 2019. Checking three – year differences in some climatic elements between urban and rural areas after a twelve – year period considering some effective parameters and solutions. Fresenius Environmental Bulletin 28: 718-725.

Fukuoka Y. 1997. Biometeorological studies on urban climate. International Journal of Biometeorology 40: 54-57. https://doi.org/10.1007/BF02439412

Grimmond S. 2007. Urbanization and global environmental change: Local effects of urban warming. The Geographical Journal 173: 83-88. https://doi.org/10.1111/j.1475-4959.2007.232_3.x

Gulyás Á, Matzarakis A, Unger J. 2010. Comparison of the urban-rural comfort sensation in a city with warm continental climate. Proceedings of BIOMET 7 473-479.

Gümüş N. 2004. Urban development and urban typology in Eskişehir. I. International Symposium on Eskişehir Throughout History at Eskişehir-Türkiye: 153-164.

Höppe P. 1999. The physiological equivalent temperature – A universal index for the biometeorological assessment of the thermal environment. International Journal of Biometeorology 43: 71-75. https://doi.org/10.1007/s004840050118

ISO. 2005. ISO 7730 2005. Ergonomics of the thermal environment. Analytical determination and interpretation of thermal comfort using calculation of the PMV and PPD indices and local thermal comfort criteria. Available at: https://www.iso.org/obp/ui/#iso:std:iso:7730:ed-3:v1:en:sec:4 (accessed on February 26, 2021).

Kovacs A, Nemeth A. 2012. Tendencies and differences in human thermal comfort in distinct urban areas in Budapest, Hungary. Acta Climatologica et Chorologica Universitatis Szegediensis 4: 115-124.

Landsberg HE. 1981. The urban climate. 1st ed. International Geophysics Series, vol. 28. Academic Press, London, 275 pp.

Laschewski G, Jendritzky G. 2002. Effects of the thermal environment on human health: An investigation of 30 years of daily mortality data from SW Germany. Climate Research 21: 91-103. https//doi.org/10.3354/cr021091

Matzarakis A, Mayer H. 1996. Another kind of environmental stress: Thermal stress. WHO Newsletters, 18: 7-10.

Matzarakis A, Mayer H, Iziomon MG. 1999. Applications of a Universal Thermal Index: Physiological Equivalent Temperature. International Journal of Biometeorology 43: 76-84. https://doi.org/10.1007/s004840050119

Matzarakis A, Rutz F, Mayer H. 2007. Modelling radiation fluxes in simple and complex environments –

Application of the RayMan model. International Journal of Biometeorology 51: 323-334. https://doi.org/10.1007/s00484-006-0061-8

Nastos TP, Matzarakis A. 2011. The effect of air temperature and human thermal indices on mortality in Athens, Greece. Theoretical and Applied Climatology 108: 591-599. https://doi.org/10.1007/s00704-011-0555-0

Oke TR. 1973. City size and the urban heat island. Atmospheric Environment 7: 769-779. https://doi.org/10.1016/0004-6981(73)90140-6

Paramita B, Matzarakis A. 2019. Urban morphology aspects on microclimate in a hot and humid climate. Geographica Pannonica 23: 398-410. https://doi.org/10.5937/gp23-24260

Robaa SM. 2003. Urban-suburban/rural differences over Greater Cairo, Egypt. Atmósfera 16: 157-171.

Toy S. 2010. Evaluation of recreational areas in east Anatolia region for bioclimatic comfort values. Ph.D. thesis. Atatürk University, Turkey.

Toy S, Yılmaz S. 2009. Bioclimatic comfort in landscape design and its importance for living areas. Journal of the Faculty of Agriculture 40: 133-139. Available at: https://dergipark.org.tr/tr/pub/ataunizfd/issue/2929/40540 (accessed on March 7, 2021).

Toy S, Yılmaz S. 2010. Evaluation of urban-rural bioclimatic comfort differences over a ten-year period in the sample of Erzincan city reconstructed after a heavy earthquake. Atmósfera 23: 387-402.

Toy S, Aytaç AS, Kantor N. 2018. Human biometeorological analysis of the thermal conditions of hot Turkish city of Şanliurfa. Theoretical and Applied Climatology 131: 611-623. https://doi.org/10.1007/s00704-016-1995-3

Toy S, Kayıp DB, Çağlak S. 2019. A (bio)climate sensitive urban design example in the city of Eskişehir. Gümüşhane University Journal of Science and Technology Institute 9: 353-361.

Unger J. 1999. Comparisons of urban and rural bioclimatological conditions in the case of a Central-European city. International Journal of Biometeorology 43: 139-144. https://doi.org/10.1007/s004840050129

VDI. 1998. VDI 3787. Part I: Environmental Meteorology, Methods for The Human-Biometeorological Evaluation of Climate and Air Quality for The Urban and Regional Planning at Regional Level. Part I: Climate. Verein Deutscher Ingenieure/DIN-Handbuch Reinhaltung der Luft, Band 1b, Düsseldorf, 29 pp.

Yılmaz E. 2013. Heat island in Ankara city. Ph.D. thesis. Ankara University, Turkey.

Atmósfera 35(4), 737-753 (2022)
https://doi.org/10.20937/ATM.53024

CONTENTS

Regional extreme rainfall estimation in the Middle Black Sea Region, Turkey

Kadri YUREKLI[1]*, Melih ENGINSU[2] and Muberra ERDOGAN[1]

[1]*University of Gaziosmanpasa, Agriculture Faculty, Department of Biosystem Engineering, Tokat, Turkey.*
[2]*Black Sea Agricultural Research Institute, Samsun, Turkey.*
*Corresponding author; email: kadriyurekli@yahoo.com

Received: December 23, 2020; accepted: April 6, 2021

RESUMEN

Las probabilidades de ocurrencia de fuertes lluvias provocadas por inundaciones tienen un papel esencial en el diseño de estructuras relacionadas con el agua y la gestión de recursos hídricos. En muchos casos, los datos para el análisis no están disponibles o son insuficientes para un diseño confiable de dichas estructuras. Con frecuencia se prefiere el análisis de la frecuencia regional con el fin de obtener información para el diseño en sitios donde la disponibilidad de datos es particularmente inadecuada. El presente estudio implementó procedimientos de momentos L para series de precipitación anual máxima de 70 estaciones de medición en la región del Mar Negro medio (MBSR, por sus siglas en inglés), Turquía, para estimar los cuantiles regionales de precipitación. El primer intento de regionalización consistió en evaluar toda el área como una sola región homogénea. Las subregiones se definieron inicialmente con el algoritmo de agrupación en clústeres debido a la presencia de sitios discordantes desde la perspectiva de una región homogénea. De acuerdo con los resultados de las medidas de discordancia y heterogeneidad, se logró la clasificación más adecuada con seis conglomerados (subregiones). Las subregiones cumplen con la condición de homogeneidad como "aceptablemente homogéneas". Se decidió que las distribuciones GEV y GLO en cinco subregiones, la distribución GNO en cuatro subregiones y la distribución PE3 en tres subregiones eran aceptables como distribuciones de frecuencia regional. En comparación, la distribución GPA no es candidata en ninguna de las seis subregiones.

ABSTRACT

The occurrence probabilities of heavy rainfall that cause flood events have an essential role in designing water-related structures and water resource management. In many cases, data for analysis are either not available or are insufficient for reliable design of water-related structures. Regional frequency analysis is usually preferred to provide design information in sites with especially inadequate data available. Our study applied L-moment procedures to annual maximum rainfall series from 70 gauging stations in the Middle Black Sea Region (MBSR) of Turkey to estimate regional rainfall quantiles. The first attempt for regionalization aimed to evaluate the entire area as an homogeneous region. The sub-regions were initially defined with the ward's clustering algorithm due to the presence of discordant sites under a presumption of a single homogeneous region. In compliance with the results of the discordancy and heterogeneity measures, the most promising classification was achieved with six clusters (sub-regions) that satisfied the homogeneity condition as "acceptably homogeneous". It was decided that the GEV and GLO distributions in five sub-regions, the GNO distribution in four sub-regions, and the PE3 distribution in three sub-regions, were acceptable as regional frequency distributions. In comparison, GPA was not a candidate distribution in any of the six sub-regions.

Keywords: maximum rainfall, L-moment, discordancy, heterogeneity measure, index-storm.

1. Introduction

In the context of climate variability, the increasing attention to global warming emerging under the influence of anthropogenic activities has been associated with the consequences of its impacts, which ravage the natural structure of the ecosystem. The IPCC (2007) underlined that the proportional increase of greenhouse gases in the atmosphere would change the conventional climate structure in most parts of the world. It also reported (IPCC, 2013) that heavy rainfall events increased quantitatively towards the end of the 20th century. Hirabayashi and Kanae (2009) reported that more than 300 million people could be affected by even minor floods in 2060-2070. Considering only European countries, economic losses from floods in the next century are expected to rise from € 6.5 billions to € 18 billions (Cetin and Tezer, 2013). Concerning probable extreme precipitation in the future, Giorgi (2006) pointed out that the Mediterranean basin, in which Turkey is located, is among the most vulnerable regions that could be affected by climate change. Previous studies dealing with climate variability in Turkey indicate a remarkable alteration in the characteristics of precipitation (e.g., Turkes and Erlat, 2003; Turkes et al., 2009; Unal et al., 2012; Yurekli, 2015). Regarding precipitation, the most obvious impact of global warming on the world has appeared as floods and droughts, which are the most common and costly natural disasters. Among the probable natural catastrophes in Turkey, floods have caused most deaths and economic losses after earthquakes (Ozcan, 2008). During the period 1948-2015, flood events in Turkey affected 1 778 520 persons and resulted in 1350 fatalities. The economic loss associated with this natural disaster was estimated at USD 2.195 billion (Enginsu, 2015). Ozcan (2006) stated that floods commonly take place in the Black Sea, Marmara, and the Mediterranean regions in Turkey; even the Black Sea region has been exposed to flood events more frequently. Under this study, the Middle Black Sea region experienced 116 flood events in the period from 1956 to 2012, 80 of which occurred in the summer season. These floods caused 29 casualties, 4290 ha of cultivated land damaged, and 8051 homes and working places exposed to undesirable conditions. Seemingly, there has been a substantial increase in the number of floods during the last 15 years in the region (Enginsu, 2015).

Estimation of the magnitude and frequency of heavy rainfall causing floods is of great importance to understand their characteristic behaviour, in order to make decisions on water-related structures (Abolverdi and Khalili, 2010; Shahzadi et al., 2013). A frequent problem regarding the management and planning of water resources for reliable design is to estimate the probable magnitude of extreme rainfall or streamflow events due to the absence of adequate data concerning these events (Yurekli et al., 2009). In this sense, hydrologists have focused for several decades on the reliable analysis of available extreme data in their research (e.g. Kumar et al., 2003; Saf, 2009; Malekinezhad and Garizi, 2014; Ngongondo et al., 2011). The probabilistic characteristic of hydro-meteorologic variables is pivotal in designing water-related structures (Svensson and Rakhecha, 1998). Providing more reliable information about extreme events is crucially important to the management and planning of water resources within a regional context. The accuracy in the design of hydraulic structures is influenced mainly by the adopted frequency analysis approach and the quality and quantity of data used in the analysis.

The availability and quality of hydro-meteorological data is still a severe problem for hydrologists in many parts of the world (Easterling et al., 2000; Haddad et al., 2011; Hussain and Pasha, 2009). In cases where hydro-meteorological data is absent or insufficient in terms of quantity and quality, the regionalization method, referred to as regional frequency analysis, has been frequently used to assess extreme events (Lim and Lye, 2003; Zakaria et al., 2012). This approach consists of identifying the region, finding the sites compatible with each other in a region, applying an homogeneity test for the supposed region, and designating the regional statistical distribution (Sveinsson et al., 2002; Durrans and Kirkby, 2004). The method of L-moments has been widely used in the regionalization of hydrologic data, although there are different approaches for regionalization. Due to their several advantages over conventional moments (Sankarasubramanian and Srinivasan, 1999; Gubareva and Garstman, 2010), the procedure of L-moments has been adopted progressively in hydrologic studies by many researchers since the introduction of the approach (Abolverdi and Khalili, 2010; Modarres, 2010; Zakaria and Shabri, 2013; Anilan et al., 2015;

Mosaffaie, 2015; Sarmadi and Shokoohi, 2015; Yin et al., 2015; Serra et al., 2016).

Even though several efforts have been made to perform regional frequency analysis (RFA) of heavy rainfalls on some parts of Turkey (e.g., Anli, 2009; Anli et al., 2009; Yurekli et al., 2009) during the last decades, no comprehensive studies in the Middle Black Sea Region (MBSR) in which destructive flood events have taken place in the last 15 years have been conducted in the context of RFA for extreme rainfalls. In the studies conducted by Yurekli et al. (2009) and Anli et al. (2009), the L-moments approach was applied to the annual maximum rainfall series of the Cekerek basin and Trabzon Province, respectively, whereas Anli (2009) performed this analysis on both the annual maximum and the partial-duration rainfall series for Ankara province. Seçkin and Topcu (2016) investigated the regional distribution behaviour of the annual maximum rainfalls belonging to 53 precipitation stations in Turkey using the L-moments method. It has been decided that the whole study area could be considered as a homogeneous region based on the heterogeneity test and the generalized logistic distribution has been determined as the most suitable distribution for the region. Ghiaei et al. (2018) carried out a regionalization procedure based on L-moments on the annual maximum rainfall datasets with various durations from seven rainfall stations over the Eastern Black Sea Basin in Turkey. The generalized logistic (GLO) and generalized extreme value (GEV) distributions were determined for short-term (5 to 30 min) and long-term datasets (1 to 24 h) to estimate regional quantiles.

The specific objectives of the present study are: (a) to compute L-moments and its ratios; (b) to check the reliability of the data for the RFA; (c) to form groups of sites that satisfy the homogeneity condition; (d) to choose a regional frequency distribution; (e) to obtain L-moment ratio diagrams to select a candidate regional frequency distribution as an alternative way, and (f) to estimate quantiles based on the best fit distribution for the formed homogeneous region.

2. Materials and methods

2.1 Study area and data

Turkey consists of seven geographic regions, one of which is the Black Sea Region, which comprises three sub-sections, namely the Western Black Sea, Eastern Black Sea and Middle Black Sea. The MBSR lies between 39º-43º N and 34º-38º E (Fig. 1), with an elevation ranging from 2 m (Fatsa county) to 1287 m (Akkus county). The study area covers roughly 43 684 km^2, approximately 5.6% of Turkey's land area (Enginsu, 2015). The MBS has significant plains: Carşamba and Bafra in the coastal area and Niksar, Erbaa, Tasova and Suluova in the inland area. Kizilirmak and Yesilirmak rivers are the main water resources in the MBSR, which is geographically located in both river basins. The MBSR is under the influence of two different climate characteristics: a temperate oceanic climate affecting the coastal area and a continental climate reigning in the inland area. Precipitation amounts show a significant increase from the interior area towards the coastal zone. Annual rainfall varies from 600 to 800 mm in the coastal part, and decreases to 450 mm towards the inland. Heavy rainfall occurs in the coastal areas during autumn, whereas in inland areas it occurs during the spring (Sozer et al., 1990). Most floods in the period 2000-2012 were experienced across the coastal area (Enginsu, 2015). Kosarev et al. (2007) emphasized that large-scale atmospheric systems positioned over Eurasia and the North Atlantic have mainly become influential in the formation of the climate characteristics of the Black Sea.

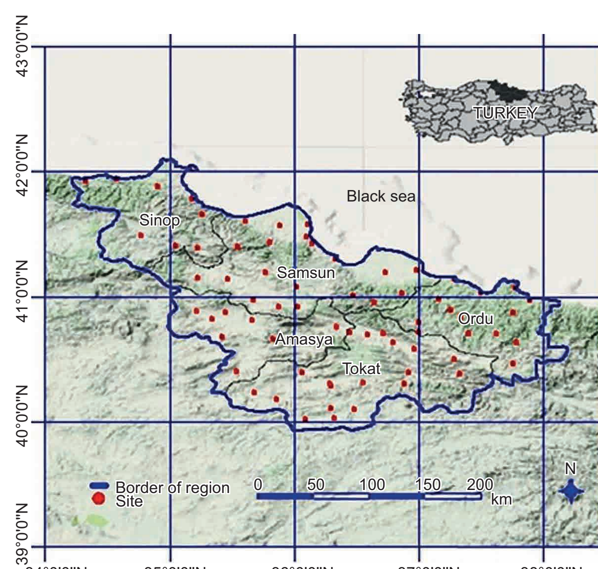

Fig. 1. Geographical location of the stations on the study area.

In the current study, daily rainfall data of 70 recording gauge stations compiled by the Turkish State Meteorological Service and General Directorate of State Hydraulic Works was used. Figure 1 shows the geographical location of the mentioned gauge stations in the study area and preliminary data associated with the sites are given in Table I. However, some recording gauge stations in the MBSR were discarded for a more reliable analysis due to very short record length and questionable data quality. Rainfall datasets belonging to the sites up to 2013 were used for regional frequency analysis in the study, but not every site had an observation length until 2013. There are two methods to choose the maximum rainfall series

Table I. Geographic characteristics of the stations in the study area.

Row	Sample size	Station name	Elevation (m)	Latitude (ºN)	Longitude (ºE)
1	38	Vezirkopru	377	41.13	35.45
2	20	Alicik	700	40.80	35.31
3	79	Amasya	412	40.65	35.85
4	20	Dogantepe	520	40.60	35.61
5	31	Aydinca	675	40.56	36.15
6	25	Goynucek	530	40.40	35.53
7	39	Gumushacikoy	770	40.88	35.23
8	32	Havza	750	40.96	35.68
9	26	Kavak	741	41.09	36.05
10	47	Ladik	950	40.91	35.91
11	83	Merzifon	755	40.88	35.48
12	39	Suluova	490	40.83	35.65
13	24	Bespinar	721	41.00	35.00
14	53	Mazlumoglu	870	40.54	36.03
15	18	Çakiralan	950	41.00	35.00
16	81	Tokat	608	40.31	36.56
17	60	Turhal	500	40.40	36.10
18	53	Zile	700	40.30	35.90
19	50	Almus	830	40.25	36.56
20	47	Artova	1200	40.05	36.31
21	27	Akkus	1287	40.79	37.01
22	26	Bereketli	1125	40.51	37.30
23	27	Camlibel	1100	40.08	36.48
24	25	Doganyurt	530	40.68	36.71
25	62	Niksar	350	40.60	36.96
26	20	Pazar	540	40.28	36.30
27	30	Resadiye	450	40.16	37.38
28	38	Resadiye / Zile	790	40.13	35.42
29	31	Hacipazari	220	40.43	36.29
30	25	Yolbasi	1050	40.41	37.01
31	31	Ekinli	1070	40.02	36.20
32	30	Sulusaray	950	40.00	36.10
33	44	Tasova	200	40.76	36.33
34	47	Erbaa	230	40.70	36.60
35	12	Camiçi	1250	40.61	37.01
36	50	Dokmetepe	635	40.18	36.20
37	19	Boztepe	750	40.18	35.88
38	27	Turkeli	127	41.94	34.33
39	39	Ayancik	630	41.83	34.77

Table I. Geographic characteristics of the stations in the study area.

Row	Sample size	Station name	Elevation (m)	Latitude (ºN)	Longitude (ºE)
40	25	Erfelek	190	41.87	34.89
41	26	Taflan	150	41.00	36.00
42	24	Duragan	287	41.43	35.05
43	28	Cerçiler	700	41.00	35.00
44	26	Dikmen	385	41.66	35.27
45	21	Kolay	70	41.00	35.00
46	81	Sinop	32	42.02	35.15
47	50	Engiz	25	41.29	36.06
48	29	Gerze	86	41.81	35.17
49	65	Bafra	103	41.55	35.92
50	16	Alacam	7	41.63	35.63
51	48	Boyabat	350	41.46	34.78
52	54	Unye	16	41.14	37.29
53	26	Fatsa	2	41.04	37.48
54	24	Hasanugurlu	120	41.01	36.37
55	84	Samsun	15	41.28	36.33
56	56	Çarşamba	35	41.20	36.73
57	50	Kizilot	10	41.18	36.46
58	34	Terme	10	41.12	37.00
59	26	Duzdag	800	41.01	36.47
60	10	Tekkiraz	550	40.59	37.09
61	23	Kumru	735	40.85	37.24
62	49	Gelemenagri	4	41.40	35.55
63	33	Golkoy	1158	40.69	37.64
64	22	Korgan	725	40.00	37.00
65	24	Topcam	550	40.00	37.00
66	24	Aybasti	632	40.67	37.37
67	35	Mesudiye	1191	40.46	37.77
68	80	Ordu	5	40.98	37.88
69	13	Perşembe	190	40.98	37.70
70	20	Ulubey	190	40.87	37.75

(Anli, 2009). The preferred method is based on selecting the maximum rainfall value of each year. In contrast, the other method (peak-over threshold, POT) is based on choosing all data greater than the considered threshold in a specific period. The overall approach, including selecting the annual maximum rainfall (hereafter referred to as AMR), has been preferred in the current study. The AMR value for daily rainfalls of the corresponding year for every gauge station was obtained.

2.2 L-moments approach

Recently, the L-moments method, popularized by Hosking (1990), has been adopted progressively in frequency analysis of hydro-meteorological variables due to its significant advantages over conventional product moments. Especially, they are relatively insensitive to the presence of outliers in a given series and they have no limits regarding sample sizes. Moreover, they define the structure of any statistical distribution more successfully and estimate the distribution parameters, particularly for hydro-meteorological data in circumstances where individual record lengths at gauging locations are relatively short, and compared with maximum likelihood estimates, they are commonly more tractable about computation. There is no need to transform the available data. On the other hand, compared to product moments, their estimators are almost unbiased, even in small samples, and are near normally distributed (Hosking, 1990; Park et al., 2001; Gubareva and Gartsman, 2010). The properties listed above make them preferable over product moments in frequency analysis of mostly roughly skewed hydro-meteorological data. L-moments are calculated based on probability-weighted moments (PWMs) characterized by Greenwood et al. (1979). A formal definition of the PWMs is provided here:

$$\beta_r = E\left\{X\left[F(X)^r\right]\right\} \tag{1}$$

where $F(x)$ is the cumulative distribution function (cdf) of a random variable X; X(F) is the inverse cfd related to X at F probability level, and r is the rth moment. In Hosking and Wallis (1997), L-moments are defined with regard to the PWMs as:

$$\lambda_{r+1} = \sum_{k=0}^{r} (p^*_{r,k}\beta_k) \tag{2}$$

$$p^*_{r,k} = -1^{r-k}\binom{k}{r}\binom{r+k}{k} \tag{3}$$

In Eq. (2), λ_{r+1} represents the $(r + 1)$th L-moment.

For a given sample $x_1, x_2 \ldots, x_n$, let $x_{1,n} \leq x_{2,n} \leq \cdots \leq x_{n,n}$ represent the order statistics of this series. Analogous to that of Eq. (2), the first four sample L-moments symbolized as l_1, l_2, l_3, l_4 are:

$$\begin{aligned} &l_1 = b_0,\ l_2 = 2b_1 - b_0 \quad l_3 = 6b_2 - 6b_{1+}b_0 \\ &l_4 = 20b_3 - 30b_{2+}12b_1 - b_0 \end{aligned} \tag{4}$$

In the Eq. (4,) b_r (r = 0, 1 and 2…) is the sample probability weighted moments. Then, sample L-moments ratios, which are t(L-CV), t_3(L-CS), and t_4 (L-CK) are defined as

$$t = l_2 / l_1,\ \ t_3 = l_3 / l_2,\ \ t_4 = l_4 / l_2 \tag{5}$$

L-CV, L-CS, and L-CK parameters are coefficients of variation, skewness and kurtosis, respectively.

2.3 Discordancy measure

Based on L-moments, a discordancy measure (D_i) is considered to screen for erroneous data and to check whether or not data are appropriate for achieving the RFA. A station is classified as discordant when its probabilistic behaviour is not like other stations of the region. D_i is calculated based on a vector u_i $[t^i, t^i_3, t^i_4]^T$, including sample L-moment ratios (L-CV, L-CS, and L-CK) of a site i (Hosking and Wallis, 1997). The discordancy measure is as follows:

$$D_i = 3^{-1} N\left(u_i - \bar{u}\right)^T S^{-1}\left(u_i - \bar{u}\right) \tag{6}$$

$$S = \sum_{i=1}^{N}\left(u_i - \bar{u}\right)\left(u_i - \bar{u}\right)^T \tag{7}$$

N is the number of sites within the pooling group, and S is a matrix of cross-products. If any site i with $Di > 3$, the site is discordant (Hosking and Wallis, 1993; Rao and Hamed, 2000).

2.4 Regional homogeneity analysis

The heterogeneity (H) test proposed by Hosking and Wallis (1997) is based on the comparison of the between-site variation in the sample L-moments for a tentatively selected region, which has no discordant stations. Therefore, this test estimates the homogeneity degree in a group of sites. Three heterogeneity measures, named H_1, H_2, and H_3 are obtained by considering dispersion measures: L-CV, L-CS and L-CK. These H statistics depend on the 500 homogeneous regions simulated by population parameters equivalent to the regional average of L-moment ratios of the formed region sites (Hosking and Wallis, 1997; Tallaksen et al., 2004). Heterogeneity test statistics (H_i, for i = 1,2 and 3) can be calculated by:

$$H_1 = \frac{V - \mu_v}{\sigma_v},\ \ H_2 = \frac{V_2 - \mu_{v2}}{\sigma_{v2}},\ \ H_3 = \frac{V_3 - \mu_{v3}}{\sigma_{v3}} \tag{8}$$

The values of V, V_2 and V_3 in Eq. (8) are estimated as:

$$V = \left\{\sum_{i=1}^{N} \frac{n_i\left(t^i - t^R\right)^2}{\sum_{i=1}^{N} n_i}\right\}^{\frac{1}{2}} \tag{9}$$

$$V_2 = \sum_{i=1}^{N} n_i \left\{\left(t^i - t^R\right)^2 + \left(t^i_{3-}t^R_3\right)^2\right\}^{1/2}\left[\sum_{i=1}^{N} n_i\right]^{-1} \tag{10}$$

$$V_3 = \sum_{i=1}^{N} n_i \left\{\left(t^i_{3-}t^R_3\right)^2 + \left(t^i_{4-}t^R_4\right)^2\right\}^{1/2}\left[\sum_{i=1}^{N} n_i\right]^{-1} \tag{11}$$

where n_i is the record length at site i, and t, t_3, and t_4 are sample L-moments ratios; t^R, t_3^R and t_4^R are the regional average of sample L-moments ratios, respectively; μ_v and σ_v are the mean and standard deviation of the V values estimated based on N_{sim}, which represents the simulation data achieved by Monte Carlo simulation. The H-statistic value indicates that the formed region is acceptably homogeneous if $H < 1$, possibly heterogeneous if $1 \leq H < 2$, and definitely heterogeneous if $H \geq 2$.

2.5 Determination of the regional frequency distributions

After statistically confirming the group of sites as a homogeneous region, the best fit distribution to the homogeneous region is chosen by the goodness-of-fit-test (Z^{DIST}), suggested by Hosking and Wallis (1997). This test is carried out based on the difference between the L-*CK* of the candidate distribution and the average L-*CK* of a homogeneous region under study. This test is given as:

$$Z^{DIST} = \left(t_4^{DIST} - t_4^R + \beta_4\right) / \sigma_4 \tag{12}$$

where *DIST* represents a candidate probability distribution; t_4^{DIST} is the L-*CK* value dealing with the simulation for the corresponding distribution; t_4^R is the regional average of the at site L-*CKs*; β_4 is the bias associated with the regional average of the at site L-*CK*s, and σ_4 is the standard deviation belonging to the L-*CK* values based on the simulation data sets. The bias and standard deviation of regional average sample L-*CK* are calculated as follows:

$$\beta_4 = N_{sim}^{-1} \sum_{m=1}^{N_{sim}} \left(t_4^{[m]} - t_4^R\right) \tag{13}$$

$$\sigma_4 = \left\{ \left(N_{sim} - 1\right)^{-1} \sum_{m=1}^{N_{sim}} \left(t_4^{[m]} - t_4^R\right)^2 - N_{sim}^{-1} \beta_4^2 \right\}^{1/2} \tag{14}$$

where N_{sim} is the number of the simulated regions with N sites, and $t_4^{[m]}$ is the L-*CK* for the *mth* simulated region. To simulate 500 regions, close to the formed region, the four-parameter Kappa distribution is recommended to estimate β_4 and σ_4. As highlighted by Hosking and Wallis (1997), the four-parameter Kappa distribution for simulation is preferred due to its capability for representing many distributions. According to their simulation analysis, the 500 value for N_{sim} is generally sufficient. The parameters dealing with the Kappa distribution were estimated by using the regional average L-moment ratios. $|Z^{DIST}| \leq 1.64$ should be for a regional candidate distribution, but the numerically smallest distribution dealing with the $|Z^{DIST}|$ is taken as the best-fit distribution for the formed homogeneous region.

2.6 Prediction of regional quantiles

The well-known index-flood and index-storm approach in either streamflow or rainfall analysis, first introduced by Dalrymple (1960), has been widely used in regional quantile estimates dealing with environmental data. This procedure is based on the assumption that the sites forming a homogeneous region have an identical statistical distribution apart from index streamflow or rainfall value (a site-specific scaling factor) (Hosking and Wallis, 1997). Due to the use of rainfall data as material in our study, the work of Dalrymple (1960) will be hereafter referred to as the index-storm method. Mathematically, the quantile estimates at site i for a region with N sites are calculated by

$$Q_i\left(F\right) = \mu_i q\left(F\right) \tag{15}$$

where μ_i is the index rainfall (a site-specific scaling factor) value for site i; F is the non-exceedance probability, and q is dimensionless distribution function (growth curve).

3. Results and discussion

Before applying the L-moments algorithm to the at-site data sets (AMR, otherwise known as block maxima) from rainfall gauging stations in the MBSR, low-order L-moments and its ratios for each site were calculated (Table II). As the first step for regionalization, the consistency among sites in the initially formed region is checked. The test on discordancy in the study was performed with a discordancy measure to assess whether or not there is inter-site consistency. In this sense, the prevalent attempt in RFA is that the whole study area (MBSR) is initially accepted as a homogeneous region. As seen from Table I, the topographic status of all rainfall gauging stations in the MBSR seems to be an obstacle for the evaluation of the entire area as an homogeneous region. Nevertheless, the above-described L-moments methodology was applied to at-site data sets under a presumption of a single homogeneous region. The results of the discordancy test dealing with a single

Table II. Summary statistics of the sites in the MBSR.

Site	ℓ_1	L-CV	L-CS	L-CK	D_i
Vezirkopru	39.25	0.1709	0.2717	0.2563	0.35
Alicik	29.70	0.1719	0.2076	0.1142	0.31
Amasya	32.56	0.1693	0.1833	0.1547	0.08
Dogantepe	30.49	0.2025	0.2805	0.2280	0.08
Aydinca	36.17	0.1484	0.1799	0.0483	1.20
Goynucek	35.60	0.1426	0.2880	0.1885	1.04
Gumushacikoy	32.50	0.1904	0.1704	0.1190	0.25
Havza	35.30	0.1480	0.1600	0.0660	0.79
Kavak	36.49	0.1122	0.1214	0.1394	0.90
Ladik	48.16	0.1871	0.3251	0.2470	0.38
Merzifon	27.91	0.1791	0.1854	0.1524	0.07
Suluova	30.70	0.1958	0.2827	0.1923	0.12
Bespinar	36.58	0.1671	0.2366	0.2694	0.54
Mazlumoglu	39.86	0.1767	0.1323	0.2394	1.18
Çakiralan	33.81	0.1210	-0.0105	0.0316	1.67
Tokat	29.96	0.1688	0.1762	0.1973	0.21
Turhal	33.98	0.1583	0.2103	0.1948	0.17
Zile	32.50	0.1719	0.2478	0.2560	0.34
Almus	33.47	0.1839	0.2911	0.2275	0.18
Artova	29.06	0.1423	0.0981	0.1163	0.53
Akkus	54.11	0.2091	0.2524	0.1798	0.09
Bereketli	32.10	0.1615	0.2502	0.0022	3.15*
Camlibel	24.97	0.1650	0.2056	0.3596	2.55
Doganyurt	39.24	0.1361	0.1183	0.0890	0.61
Niksar	33.34	0.1612	0.1835	0.1929	0.18
Pazar	28.53	0.1799	0.2904	0.3552	1.49
Resadiye	29.62	0.1435	0.1429	0.1200	0.37
Resadiye / Zile	31.92	0.1702	0.3559	0.2424	1.02
Hacipazari	35.10	0.2232	0.3072	0.2041	0.25
Yolbasi	51.78	0.1722	0.2045	0.0643	0.91
Ekinli	31.33	0.1351	0.1622	0.2643	1.31
Sulusaray	28.81	0.1554	0.2583	0.2469	0.50
Tasova	33.16	0.2313	0.4264	0.3307	1.13
Erbaa	33.98	0.1758	0.3045	0.2417	0.37
Camiçi	39.89	0.1589	0.4046	0.2496	2.21
Dokmetepe	31.65	0.1586	0.2352	0.2665	0.60
Boztepe	36.83	0.1717	0.0825	–0.0204	1.81
Turkeli	52.47	0.2059	0.2802	0.2819	0.42
Ayancik	62.00	0.1551	0.0647	0.0992	0.80
Erfelek	56.10	0.1531	0.1409	0.1591	0.30
Taflan	55.28	0.1705	0.1746	0.1600	0.10
Duragan	30.91	0.1578	0.1009	0.0640	0.67
Cerçiler	37.55	0.1728	0.2864	0.2336	0.29
Dikmen	46.71	0.1116	0.2160	0.1412	1.44
Kolay	52.00	0.2110	0.2935	0.1709	0.29
Sinop	49.91	0.2530	0.3146	0.2368	0.66
Engiz	53.90	0.2489	0.3965	0.3085	0.91
Gerze	49.76	0.2007	0.2197	0.1213	0.30
Bafra	52.38	0.1848	0.1070	0.0892	0.67

ℓ_1: first sample L-moment (mean); D_i: discordancy.
*Discordant site.

Table II. Summary statistics of the sites in the MBSR.

Site	ℓ_1	L-CV	L-CS	L-CK	D_i
Alacam	52.18	0.2593	0.0125	0.0729	5.20*
Boyabat	36.59	0.2574	0.3815	0.1707	1.49
Unye	84.35	0.2660	0.3295	0.1624	1.30
Fatsa	98.11	0.3545	0.4520	0.2591	4.38*
Hasanugurlu	66.47	0.3307	0.4253	0.2706	3.16*
Samsun	55.14	0.2251	0.3381	0.2696	0.38
Çarşamba	63.13	0.1935	0.1424	0.1754	0.54
Kizilot	63.73	0.2364	0.3701	0.2949	0.65
Terme	65.61	0.2095	0.2596	0.2784	0.51
Duzdag	104.35	0.1910	0.1775	0.2020	0.31
Tekkiraz	71.91	0.2046	0.0681	0.2022	2.48
Kumru	53.80	0.2036	0.4561	0.4585	3.22*
Gelemenagri	60.96	0.3152	0.4306	0.3296	2.67
Golkoy	57.67	0.1764	0.1424	0.0629	0.64
Korgan	46.83	0.1509	0.2263	0.2093	0.33
Topcam	42.10	0.1808	0.2835	0.1475	0.54
Aybasti	49.69	0.1673	0.1437	0.0464	0.84
Mesudiye	33.19	0.2080	0.3099	0.1551	0.57
Ordu	69.25	0.2002	0.3115	0.2341	0.19
Perşembe	75.51	0.1451	–0.0601	0.1299	3.42*
Ulubey	73.89	0.2566	0.2663	0.1145	1.39

ℓ_1: first sample L-moment (mean); D_i: discordancy.
*Discordant site.

homogeneous region covering 70 rainfall stations are given in Table II. According to the discordancy measure (D_i) results for each site, there is discordancy for six sites, namely Bereketli, Alacam, Fatsa, Hasanugurlu, Persembe, and Kumru. D values for these sites are bigger than the critical value (D_{critic} = 3.0 for ≥ 15 sites in the region). The test statistic values of heterogeneity measures (H), namely H_1, H_2, and H_3, were estimated as 5.84, 1.80, and 1.06, respectively. About these test values, the region covering 70 sites should be classified as definitely heterogeneous for H_1, and possibly heterogeneous for H_2 and H_3 in terms of homogeneity, respectively. The L-moments procedure was reapplied to the region formed by the remaining sites after removing discordant sites to eliminate their undesirable impact on homogeneity. The second effort produced similar results. The heterogeneity test results for the region with 64 sites indicated that it was definitely heterogeneous for H_1, possibly heterogeneous for H_2, and acceptably homogeneous for H_3. In comparison, four sites (Camici, Camlibel, Tekkiraz, and Gelemenagri) were discordant with the rest of the group. Hosking and Wallis (1997) highlight that the H_1 statistic has much better discriminative capability than H_2 and H_3 to distinguish homogeneity and heterogeneity. The values of H_2 and H_3 are rarely greater than two even in unpleasantly heterogeneous regions. Therefore, the H_1 statistic was considered when deciding on the homogeneity of a given region in the study. However, the results of the other two heterogeneity measures were also presented in this study.

Based on the results of the first and second attempts on regionalization, the idea of evaluating the entire MBSR as a homogeneous region was disapproved. Similarly, the scatter diagrams of L-moment ratios (the L-CV vs. L-CS and L-CS vs. L-CK) also show that the initial proposal for regionalization is not suitable owing to quite high variability in L-moment ratios of the participating sites (Fig. 2). Then, the judgment from the assumption of one homogeneous region emphasizes that the MBSR should be divided into sub-regions until the homogeneity requirement is satisfied for each sub-region. For this purpose, the

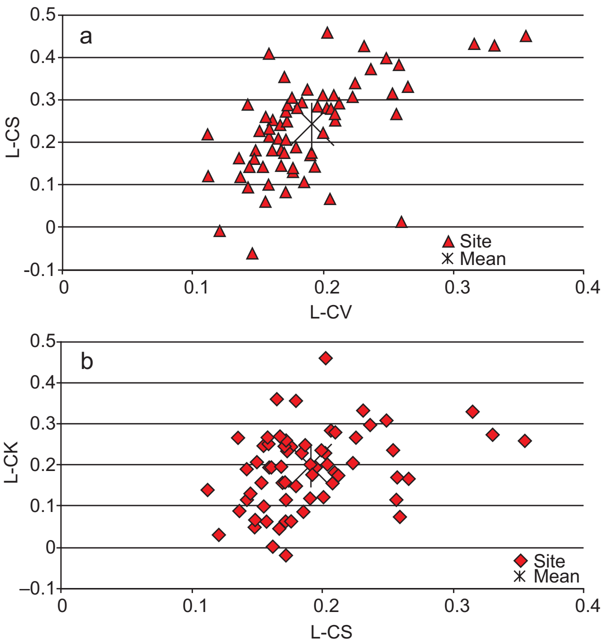

Fig. 2. Position of L-moment ratios with respect to each other for 70 sites. (a) L-CV vs. L-CS; (b) L-CS vs. L-CK.

sub-regions were initially defined with the Ward's clustering algorithm, which has been proposed by Hosking and Wallis (1997). The variables of elevation and latitude/longitude location associated with each site were used as a clustering variable in a preliminary determination of sub-regions. The results indicated that there were cases of two or more probable clusters. The inter-site consistency and homogeneity for each probable cluster (group) were checked by the discordancy measure and heterogeneity test. However, most sub-regions from the clustering method could not fulfil the requirement of inter-site consistency and homogeneity in the relevant region. Therefore, the at-site L-moment ratios were also considered together with the clustering approach in forming a homogeneous group. Moreover, the test results of groups ranging from two up to five were not satisfactory in terms of discordancy and homogeneity, except that of six groups. The most promising classification with a clustering approach was achieved by the Ward's method with six clusters. Three of these sub-regions (regions 1, 2, and 5) covered 15, 22, and 11 sites, respectively (Table III). Figure 3 illustrates the final formation of sub-regions in the studied area. Inter-site consistency in the six sub-regions was proved with discordancy measure whose critical values (D_{critic} = 3.0 for regions I and II, 1.92 for regions III and IV, 2.63 for region V, and 2.14 for region VI) were greater than the D value calculated for each site in the sub-regions. After reaching the judgment concerning the presence of inter-site consistency among sites forming each sub-region, the next step is to evaluate the homogeneity of a given sub-region in which the sites are assumed to have identical frequency distribution. In this study the homogeneity test was performed by applying heterogeneity measure (H_1) to each sub-region (Table IV). The H_2 and H_3 heterogeneity test results are also given in the Table IV. As can be seen from the table, all sub-regions have satisfied the homogeneity condition; in other words, six sub-regions were designated as acceptably homogeneous regarding the H_1 measure.

The final step in RFA is to estimate an appropriate regional frequency distribution for the data of homogeneous sub-regions identified in the previous section. In our study, three-parameter distributions such as the Generalized Logistic (GLO), Generalized Extreme Values (GEV), Generalized Normal (GNO), Pearson Type III (PE3), and Generalized Pareto (GPA) distributions were considered as candidate distributions for sub-regions. Among them, those representing the regional data were determined according to the Z^{DIST} statistic. It was decided that the distributions providing the basic assumption ($|Z^{DIST}| \leq 1.64$) dealing with this statistic could be used to make quantile estimates for the relevant region. The fitted regional distributions are given in Table V, where it can be seen that only the SR-II sub-region has a single regional distribution, while in the rest more regional distributions are selected for quantitative estimation. However, when many distributions were determined to be suitable for regional data in a specific region, the one with the smallest Z-statistic was selected as the most suitable. In this context, GEV for regions SR-I and SR-III, GLO for regions SR-II and SR-V were shosen as the most appropriate distributions. On the other hand, both GEV and GNO had the same and smallest Z-statistic value for SR-IV. The SR-VI region reached the smallest Z-statistic value in the GNO distribution. These results emphasize that GEV and GLO perform very well in fitting to the AMR data in the MBSR, so their test results are found to be acceptable in five sub-regions. The GNO distribution

Table III. Homogeneous sub-regions (SR) and results of discordancy for the sites.

SR-I		SR-II		SR-III	
Site	D_i	Site	D_i	Site	D_i
Vezirkopru	0.64	Tokat	0.31	Turkeli	1.22
Alicik	0.38	Turhal	0.08	Ayancik	1.00
Amasya	0.06	Zile	0.13	Erfelek	0.72
Dogantepe	0.71	Almus	0.15	Taflan	0.10
Aydinca	1.21	Artova	0.82	Duragan	1.62
Goynucek	1.69	Akkus	1.22	Cerciler	0.68
Gumushacikoy	1.04	Bereketli	2.33	Dikmen	1.67
Havza	0.68	Camlibel	1.67		
Kavak	1.77	Doganyurt	0.85		
Ladik	0.77	Niksar	0.16		
Merzifon	0.25	Pazar	0.87		
Suluova	0.60	Resadiye	0.50		
Bespinar	0.97	Resadiye/Zile	1.01		
Mazlumoglu	2.02	Hacipazari	1.78		
Cakiralan	2.21	Yolbasi	0.70		
		Ekinli	1.18		
		Sulusaray	0.33		
		Tasova	2.35		
		Erbaa	0.22		
		Camici	2.80		
		Dokmetepe	0.30		
		Boztepe	2.24		
SR-IV		**SR-V**		**SR-VI**	
Site	D_i	Site	D_i	Site	D_i
Kolay	0.28	Unye	1.59	Golkoy	0.55
Sinop	0.39	Fatsa	1.20	Korgan	0.92
Engiz	1.34	Hasanugurlu	0.73	Topcam	0.40
Gerze	0.44	Samsun	0.39	Aybasti	1.02
Bafra	1.01	Carsamba	0.68	Mesudiye	0.28
Alacam	1.85	Kizilot	0.29	Ordu	0.90
Boyabat	1.69	Terme	0.19	Persembe	2.11
		Duzdag	0.51	Ulubey	1.81
		Tekkiraz	2.18		
		Kumru	2.36		
		Gelemagri	0.88		

has the second-best performance after that of GEV and GLO due to its adequacy in four sub-regions. In comparison, PE3 is acceptable three sub-regions and GPA is not a candidate distribution in any of the six sub-regions. In many studies on frequency analysis of hydro-meteorological datasets (e.g., Coles, 2001; Katz et al., 2002; Ribatet et al. 2007; Aghakouchak and Nasrollahi, 2010; Obeysekera and Park, 2013; Li et al. 2015; Aziz et al., 2020) it is highlighted that AMR and POT data sequences are compatible with the GEV and GPA distributions, respectively.

Another attempt on distribution selection for a homogeneous region is a graphical approach (L-moment ratio diagram) which provides a quick visual assessment and compares the sample L-moment ratios with their theoretical counterpart (Peel et al.,

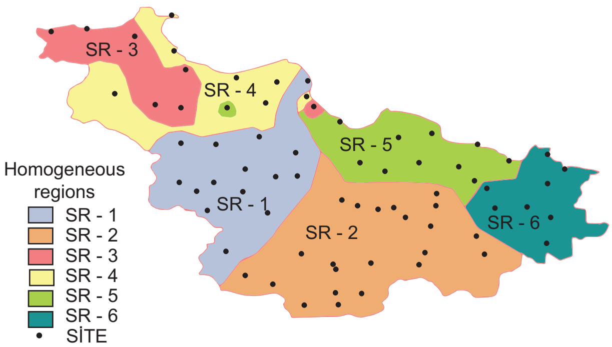

Fig. 3. Final distribution of sub-regions in the study area.

2001). L-moment ratio diagrams (Fig. 4) drawn for each sub-region present similar results to the findings based on the Z^{DIST} statistic. The points denoted by regional average values of L-CV and L-CS on the diagrams were acceptably close to the theoretical curves of distributions fitted to the data in Table V. The proximity to the curve of the candidate distributions included in the current study highlights a probable suitable regional distribution.

The estimation of regional rainfall amounts was accomplished by using the index-storm method given in Eq. (12). By taking the mean annual rainfall of the sub-region as index rainfall for that purpose, the regional rainfall amounts at return periods of 1, 2, 5, 10, 20, 50, and 100 years were obtained based on the corresponding values of growth factors (Table VI). As shown in Table VI, there is no significant difference among the regional AMR values estimated in the -regions where the multiple regional distributions are appropriate, except for the 1-yr return period. According to these results, the distributions found to be acceptable for the sub-regions can be used in the RFA. The choice should be the regional distribution with the minimum $|Z^{DIST}|$, especially for the return periods that lead to differences between estimates.

4. Conclusions

Floods are frequently experienced in the Black Sea region of Turkey. Numerous flood events have taken place in the study area (the MBSR) during the last 70 years. It is imperative to estimate possible future rainfall amounts to avoid floods and minimize their

Table IV. Heterogeneity test results for the six sub-regions.

Heterogeneity measures	SR-I	SR-II	SR-III	SR-IV	SR-V	SR-VI
H1	0.17	–0.46	0.70	0.69	0.94	0.57
H2	–0.73	–0.99	–0.04	2.52*	0.22	0.78
H3	–0.47	–0.48	–0.41	2.06*	–0.34	0.49

*According to H_2 and H_3, the sub- region is definitely heterogeneous.

Table V. Test results based on goodness of fit Z^{DIST} statistic for the six sub-regions.

Homogeneous regions	Candidate distributions				
	GEV	GLO	GNO	GPA	PE3
SR-I	**–0.44**	**1.64**	**–0.94**	–5.21	–1.98
SR-II	–2.02	**–0.15**	–2.73	–6.51	–4.04
SR-III	**–0.36**	**0.96**	**–0.53**	–3.25	**–1.00**
SR-IV	**0.30**	**1.34**	**–0.30**	–2.36	**–1.36**
SR-V	**–1.58**	**–0.86**	–2.28	–3.64	–3.48
SR-VI	**0.72**	1.84	**0.25**	–2.00	**–0.59**

Characters in bold show a suitable regional distribution.

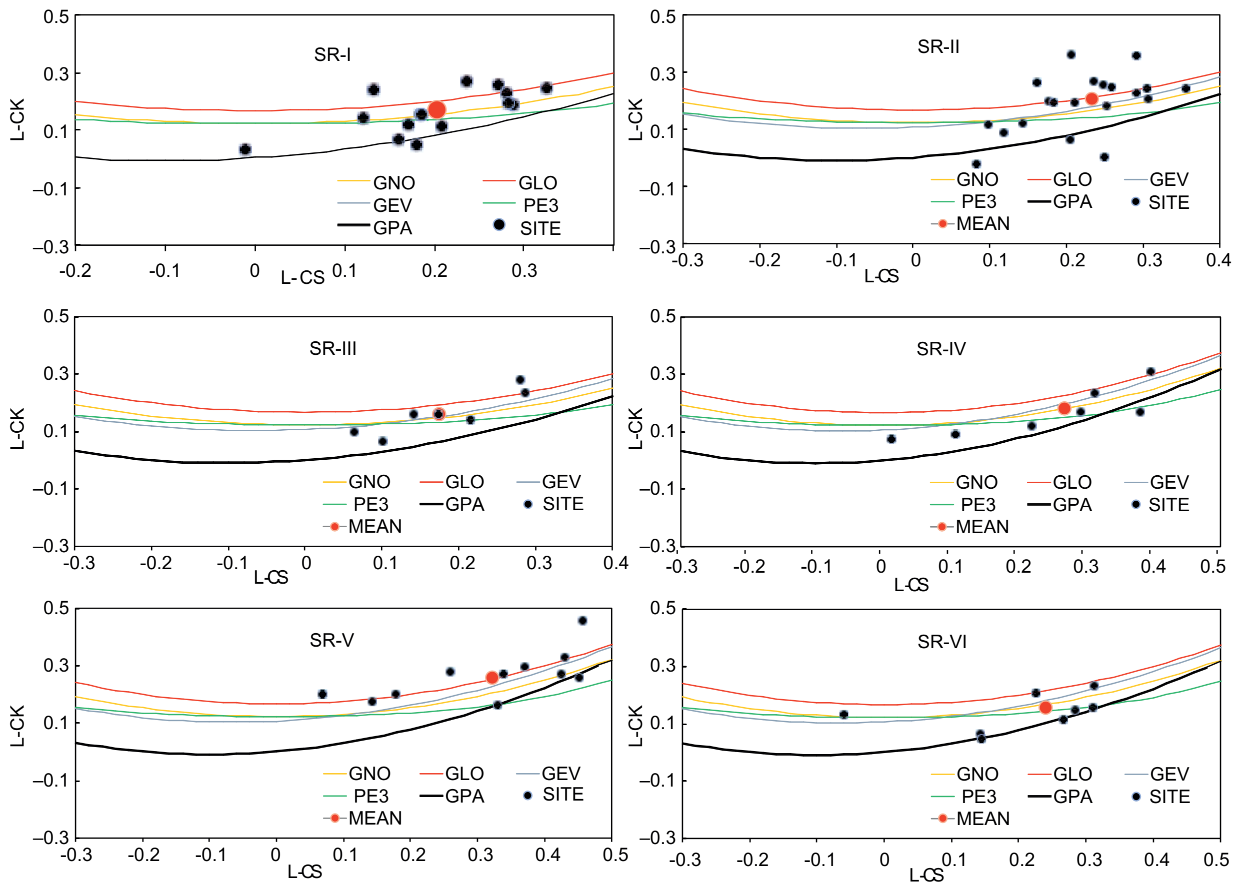

Fig. 4. L-moment ratio diagrams of L-CS vs. L-CK associated with SR-I, SR-II, SR-III, SR-IV, SR-V, SR-VI sub-rainfall homogeneous regions.

damages. The amounts in question are also predicted by frequency analysis. The current study was aimed to cope with regional frequency analysis of AMR data sequences by applying the L-moment regionalization procedure. The main conclusions are as follows:

- After initially calculating low-order L-moments and their ratios for 70 sites, the existence of discordant stations to conclude whether or not there is inter-site consistency was checked with discordancy measure for the entire study area in terms of the possibility of forming a single homogeneous region. Six of the 70 sites had discordancy. Additionally, the results associated with the test statistics of three heterogeneity measures ($H1$, $H2$, and $H3$) pointed out that the whole MBSR should be classified as definitely heterogeneous for $H1$ and possibly heterogeneous for $H2$ and $H3$. These results prove that the region could not be considered as a single homogeneous region. When the MBSR was divided into six sub-regions, each sub-region satisfied the homogeneity test.
- After weighing the inter-site consistency and homogeneity for six sub-regions, the candidate three-parameter distributions were selected based on the goodness of fit Z^{DIST} statistic. The GEV and GLO distributions in five sub-regions, the GNO distribution in four sub-regions, and the PE3 distribution in three sub-regions were found to be acceptable for regional frequency distribution. In comparison, GPA was not a candidate distribution in any of the six sub-regions.
- L-moment ratio diagrams, which are a graphical

Table VI. Annual rainfall amounts estimated from suitable regional distributions.

Region	Distribution	T (years)	1	2	5	10	20	50	100
		F	0.999	0.500	0.200	0.100	0.050	0.020	0.010
SR-I	GEV	q(F)	2.782	0.939	0.743	0.663	0.604	0.546	0.510
		Q(F)	96.9	32.7	25.9	23.1	21.0	19.0	17.8
	GLO	q(F)	3.336	0.944	0.753	0.663	0.593	0.518	0.471
		Q(F)	116.2	32.9	26.2	23.1	20.7	18.0	16.4
	GNO	q(F)	2.709	0.939	0.740	0.661	0.606	0.554	0.523
		Q(F)	94.4	32.7	25.8	23.0	21.1	19.3	18.2
SR-II	GLO	q(F)	3.600	0.937	0.753	0.67	0.606	0.54	0.499
		Q(F)	120.5	31.4	25.2	22.4	20.3	18.1	16.7
SR-III	GEV	q(F)	2.505	0.95	0.756	0.674	0.613	0.553	0.515
		Q(F)	124.4	47.2	37.5	33.5	30.4	27.5	25.6
	GLO	q(F)	3.011	0.954	0.766	0.675	0.602	0.523	0.472
		Q(F)	149.5	47.4	38.0	33.5	29.9	26.0	23.4
	GNO	q(F)	2.487	0.95	0.753	0.672	0.614	0.558	0.524
		Q(F)	123.5	47.2	37.4	33.4	30.5	27.7	26.0
	PE3	q(F)	2.366	0.949	0.749	0.67	0.618	0.57	0.544
		Q(F)	117.5	47.1	37.2	33.3	30.7	28.3	27.0
SR-IV	GEV	q(F)	4.219	0.894	0.656	0.563	0.498	0.434	0.397
		Q(F)	207.8	44.0	32.3	27.7	24.5	21.4	19.6
	GLO	q(F)	5.015	0.901	0.664	0.562	0.485	0.407	0.361
		Q(F)	247.0	44.4	32.7	27.7	23.9	20.0	17.8
	GNO	q(F)	3.872	0.891	0.65	0.562	0.504	0.452	0.423
		Q(F)	190.7	43.9	32.0	27.7	24.8	22.3	20.8
	PE3	q(F)	3.396	0.886	0.638	0.56	0.517	0.486	0.472
		Q(F)	167.3	43.6	31.4	27.6	25.5	23.9	23.2
SR-V	GEV	q(F)	5.304	0.869	0.639	0.554	0.496	0.44	0.407
		Q(F)	364.2	59.7	43.9	38.0	34.1	30.2	28.0
	GLO	q(F)	6.156	0.876	0.645	0.551	0.484	0.418	0.381
		Q(F)	422.8	60.2	44.3	37.8	33.2	28.7	26.2
SR-VI	GEV	q(F)	3.343	0.921	0.714	0.632	0.573	0.516	0.481
		Q(F)	190.4	52.5	40.7	36.0	32.6	29.4	27.4
	GNO	q(F)	3.156	0.919	0.71	0.631	0.577	0.528	0.5
		Q(F)	179.8	52.3	40.4	35.9	32.9	30.1	28.5
	PE3	q(F)	2.858	0.916	0.701	0.629	0.585	0.551	0.536
		Q(F)	162.8	52.2	39.9	35.8	33.3	31.4	30.5

Q(F): Regional rainfall amounts estimated by the index-storm method [$\mu_i\, q(F)$]; q(F): corresponding value of growth factors at different return periods based on the non-exceedance probability; μ_i: index rainfall for site *i* (regional index rainfall is used for regional quantile estimation); F: probability; T: return period (1/F).

approach to the selection of regional frequency distribution, presented similar results to the findings from the Z^{DIST} statistic.

- The estimation of regional rainfall amounts was performed with the index-storm method. There was no significant difference among the regional AMR values estimated for the sub-regions where the multiple regional distributions are appropriate, except for the 1-yr return period. Nevertheless, the regional distribution with the minimum $|Z^{DIST}|$ should be considered in the regional rainfall quantile estimate, especially for the return periods that lead to differences between estimates.

References

Abolverdi J, Khalili D. 2010. Development of regional rainfall annual maxima for southeastern Iran by L-moments. Water Resources Management 24: 2501-2526. https://doi.org/10.1007/s11269-009-9565-4

Aghakouchak A, Nasrollahi N. 2010. Semi-parametric and parametric inference of extreme value models for rainfall data. Water Resources Management 24: 1229-1249. https://doi.org/10.1007/s11269-009-9493-3

Anilan T, Satilmis U, Kankal M, Yuksek O. 2015. Application of artificial neural networks and regression analysis to L-moments based regional frequency analysis in the Eastern Black Sea Basin, Turkey. KSCE Journal of Civil Engineering 20: 2082-2092. https://doi.org/10.1007/s12205-015-0143-4

Anli AS. 2009. Regional frequency analysis of rainfall data in Ankara province via L-moment methods. Ph.D. thesis. University of Ankara.

Anli AS, Apaydın H, Öztürk F. 2009. Regional frequency analysis of the annual maximum precipitation observed in Trabzon province. Journal of Agricultural Sciences (Turkey) 15: 240-248.

Aziz R, Yucel I, Yozgatligil C. 2020. Non-stationarity impacts on frequency analysis of yearly and seasonal extreme temperature in Turkey. Atmospheric Research 238: 104875. https://doi.org/10.1016/j.atmosres.2020.104875

Çetin NI, Tezer A. 2013. ABD, Avrupa Birliği ve Türkiye'de sel risk yönetiminin karşılaştırılması. 3. Ulusal Taşkın Sempozyumu 29-30 Nisan, İstanbul.

Coles S. 2001. An introduction to statistical modelling of extreme values. Springer, Heidelberg and New York.

Dalrymple T. 1960. Flood frequency methods. Water Supply Paper 1543-A:11-51. U.S. Geological Survey.

Durrans SR, Kirby JT. 2004. Regionalization of extreme precipitation estimates for the Alabama rainfall atlas. Journal of Hydrology 295: 101-107. https://doi.org/10.1016/j.jhydrol.2004.02.021

Easterling DR, Evans JL, Groisman PY. 2000. Observed variability and trends in extreme climate events: A brief review. Bulletin of the American Meteorological Society 81: 417-425. https://doi.org/10.1175/1520-0477(2000)081<0417:OVATIE>2.3.CO;2

Enginsu M. 2015. Regional frequency analysis of daily maximum rainfalls on Middle Black Sea region caused flood. M.Sc. thesis. University of Gaziosmanpasa, Tokat.

Ghiaei F, Kankal M, Anilan T, Yuksek O. 2018. Regional intensity-duration-frequency analysis in the Eastern Black Sea Basin, Turkey, by using L-moments and regression analysis. Theoretical and Applied Climatology 131: 245-257. https://doi.org/10.1007/s00704-016-1953-0

Giorgi F. 2006. Climate change hot-spots. Geophysical Research Letters 33: L08707. https://doi.org/10.1029/2006GL025734

Greenwood JA, Landwehr JM, Matalas NC, Wallis JR. 1979. Probability weighted moments: Definition and relation to parameters of several distributions expressible in inverse form. Water Resources Research 15: 1049-1054. https://doi.org/10.1029/WR015i005p01049

Gubareva TS, Gartsman BI. 2010. Estimating distribution parameters of extreme hydrometeorological characteristics by L-Moment method. Water Resources 37: 437-445. https://doi.org/10.1134/S0097807810040020

Haddad K, Rahman A, Green J. 2011. Design rainfall estimation in Australia: A case study using L-moments and generalized least squares regression. Stochastic Environmental Research and Risk Assessment 25: 815-825. https://doi.org/10.1007/s00477-010-0443-7

Hirabayashi Y, Kanae S. 2009. First estimate of the future global population at risk of flooding. Hydrological Research Letters 3: 6-9. https://doi.org/10.3178/hrl.3.6

Hosking JRM. 1990. L-moments: Analysis and estimation of distributions using linear combinations of order statistics. Journal of the Royal Statistical Society: Series B (Methodological) 52: 105-124. https://doi.org/10.1111/j.2517-6161.1990.tb01775.x

Hosking JRM, Wallis JR. 1997. Regional frequency analysis: An approach based on L-moments. Cambridge University Press, United Kingdom.

Hosking JRM, Wallis JR. 1993. Some statistics useful in regional frequency analysis. Water Resources Research 29: 271-281. https://doi.org/10.1029/92WR01980

Hussain Z, Pasha GR. 2009. Regional flood frequency analysis of the seven sites of Punjab, Pakistan, using L-moments. Water Resources Management 23: 1917-1933. https://doi.org/10.1007/s11269-008-9360-7

IPCC. 2007. Climate Change 2007: Synthesis Report, contribution of working groups I, II and III to the fourth assessment report of the Intergovernmental Panel on Climate Change. Cambridge University Press, Cambridge.

IPCC. 2013. Climate Change 2013: The physical science basis, contribution of working group I to the fifth assessment report of the Intergovernmental Panel on Climate Change. Cambridge University Press, Cambridge. https://boris.unibe.ch/id/eprint/71452

Katz RW, Parlang MB, Naveau P. 2002. Statistics of extremes in hydrology. Advances in Water Resources 25: 1287-1304. https://doi.org/10.1016/S0309-1708(02)00056-8

Kosarev AN, Arkhipkin VS, Surkova GV. 2007. Hydrometeorological conditions. In: The Black Sea Environment. The handbook of environmental chemistry (Kostianoy AG, Kosarev AN, Eds.). Springer, Berlin, Heidelberg. https://doi.org/10.1007/698_5_086

Kumar R, Chatterjee C, Kumar S, Lohani AK. 2003. Development of regional flood frequency relationships using L-moments for Middle Ganga Plains Subzone 1(f) of India. Water Resources Management 17: 243-257. https://doi.org/10.1023/A:1024770124523

Li LC, Zhang LP, Xia J, Gippel CJ, Wang RC, Zeng SD. 2015. Implications of modelled climate and land cover changes on runoff in the middle route of the south to north water transfer project in China. Water Resources Management 29: 2563-2579. https://doi.org/10.1007/s11269-015-0957-3

Lim YH, Voeller DL. 2009. Regional flood estimations in Red River using l-moment-based index-flood and bulletin 17b procedures. Journal of Hydrologic Engineering 14: 1002-1016. https://doi.org/10.1061/(ASCE)HE.1943-5584.0000102

Malekinezhad H, Garizi AZ. 2014 Regional frequency analysis of daily rainfall extremes using L-moments approach. Atmósfera 27: 411-427. https://doi.org/10.1016/S0187-6236(14)70039-6

Modarres R. 2010. Regional dry spells frequency analysis by L-moment and multivariate analysis. Water Resources Management 24: 2365-2380. https://doi.org/10.1007/s11269-009-9556-5

Mosaffaie J. 2015. Comparison of two methods of regional flood frequency analysis by using L-moments. Water Resources 42: 313-321. https://doi.org/10.1134/S0097807815030112

Ngongondo CS, Xu CY, Tallaksen LM, Alemaw B, Chirwa T. 2011. Regional frequency analysis of rainfall extremes in Southern Malawi using the index rainfall and L-moments approaches. Stochastic Environmental Research and Risk Assessment 25: 939-955. https://doi.org/10.1007/s00477-011-0480-x

Obeysekera J, Park J. 2013. Scenario-based projections of extreme sea levels. Journal of Coastal Research 29: 1-7. https://doi.org/10.2112/JCOASTRES-D-12-00127.1

Ozcan E. 2006. Floods and Turkey. Gazi Egitim Fakultesi Dergisi 26: 35-50 (in Turkish).

Ozcan O. 2008. Evaluation of flood risk analysis in Sakarya river subbasin by using remote sensing and GIS. M.Sc. thesis. Technical University of Istanbul.

Park JS, Jung HS, Kim RS, Oh JH. 2001. Modelling summer extreme rainfall over the Korean Peninsula using Wakeby distribution. International Journal of Climatology 21: 1371-1384. https://doi.org/10.1002/joc.701

Peel MC, Wang QJ, Vogel RM, McMahon TA. 2001. The utility of L-moment ratio diagrams for selecting a regional probability distribution. Hydrological Sciences Journal 46: 147-155. https://doi.org/10.1080/02626660109492806

Rao AR, Hamed KH. 2000. Flood frequency analysis. CRC Press, Boca Raton, FL.

Ribatet M, Sauquet E, Grésillon JM, Ouarda TBMJ. 2007. A regional Bayesian POT model for flood frequency analysis. Stochastic Environmental Research and Risk Assessment 21: 327-339. https://doi.org/10.1007/s00477-006-0068-z

Saf B. 2009. Regional flood frequency analysis using l-moments for the West Mediterranean region of Turkey. Water Resources Management 23: 531-551. https://doi.org/10.1007/s11269-008-9287-z

Sankarasubramanian A, Srinivasan K. 1999. Investigation and comparison of sampling properties of L-moments and conventional moments. Journal of Hydrology 218: 13-34. https://doi.org/10.1016/S0022-1694(99)00018-9

Sarmadi F, Shokoohi A. 2015. Regionalizing precipitation in Iran using GPCC gridded data via multivariate analysis and L-moment methods. Theoretical and Applied Climatology 122: 121-128. https://doi.org/10.1007/s00704-014-1292-y

Seçkin N, Topçu E. 2016. Regional frequency analysis of annual peak rainfall of Adana and the vicinity. Journal of the Faculty of Engineering and Architecture of Gazi University 31: 1049-1062. https://doi.org/10.17341/gazimmfd.278460

Serra C, Lana X, Burgueño A, Martínez MD. 2016. Partial duration series distributions of the European dry spell lengths for the second half of the twentieth century. Theoretical and Applied Climatology 123: 63-81. https://doi.org/10.1007/s00704-014-1337-2

Shahzadi A, Akhter AS, Saf B. 2013. Regional frequency analysis of annual maximum rainfall in monsoon region of Pakistan using l-moments. Pakistan Journal of Statistics and Operation Research 1: 111-136. https://doi.org/10.18187/pjsor.v9i1.461

Sozer AN, Isik S, Mutluer M. 1990. Agean region geography. Lecture note. Ege University, Izmir, 126 pp.

Sveinsson OGB, Salas JD, Boes DC. 2002. Regional frequency analysis of extreme precipitation in northeastern Colorado and Fort Collins flood of 1997.

Journal of Hydrologic Engineering 7: 49-63. https://doi.org/10.1061/(ASCE)1084-0699(2002)7:1(49)

Svensson C, Rakhecha PR. 1998. Estimation of probable maximum precipitation for dams in the Hongru River catchment, China. Theoretical and Applied Climatology 59: 79-91. https://doi.org/10.1007/s007040050014

Tallaksen LM, Van Lanen HAJ, Eds. 2004. Hydrological drought: Processes and estimation methods for streamflow and groundwater. Elsevier, Amsterdam, 579 pp. (Developments in Water Science, 48).

Turkes M, Erlat E. 2003. Precipitation changes and variability in Turkey linked to the North Atlantic Oscillation during the period 1930-2000. International Journal of Climatology 23: 1771-1796. https://doi.org/10.1002/joc.962

Turkes M, Koc T, Sarıs F. 2009. Spatiotemporal variability of precipitation total series over Turkey. International Journal of Climatology 29: 1056-1074. https://doi.org/10.1002/joc.1768

Unal YS, Deniz A, Toros H, Incecik S. 2012. Temporal and spatial patterns of precipitation variability for annual, wet, and dry seasons in Turkey. International Journal of Climatology 32: 392-405. https://doi.org/10.1002/joc.2274

Yin Y, Chen H, Xu CY, Xu W, Chen C, Sun S. 2015. Spatio-temporal characteristics of the extreme precipitation by L-moment-based index-flood method in the Yangtze River Delta region, China. Theoretical and Applied Climatology 124: 1005-1022. https://doi.org/10.1007/s00704-015-1478-y

Yurekli K, Modarres R, Ozturk F. 2009. Regional daily maximum rainfall estimation for Cekerek Watershed by L-moments. Meteorological Applications 16: 435-444. https://doi.org/10.1002/met.139

Yurekli K. 2015. Impact of climate variability on precipitation in the upper Euphrates-Tigris rivers basin of southeast Turkey. Atmospheric Research 154: 25-38. https://doi.org/10.1016/j.atmosres.2014.11.002

Zakaria ZA, Shabri A, Ahmad UN. 2012. Regional frequency analysis of extreme rainfalls in the west coast of Peninsular Malaysia using partial L-moments. Water Resources Management 26: 4417-4433. https://doi.org/10.1007/s11269-012-0152-8

Zakaria ZA, Shabri A. 2013. Regional frequency analysis of extreme rainfalls using partial L-moments method. Theoretical and Applied Climatology 113: 83-94. https://doi.org/10.1007/s00704-012-0763-2

Atmósfera 35(4), 755-779 (2022)
https://doi.org/10.20937/ATM.52962

Economic disparities in pollution-related mortality in three municipalities of the Metropolitan Area of the Valley of Mexico

Alejandro ISLAS-CAMARGO[1]*, Alok K. BOHARA[2] and J. Mario HERRERA RAMOS[3]

[1] *Departamento de Estadística, Instituto Tecnológico Autónomo de México, Río Hondo 1, Col. Progreso Tizapán, 01080 Ciudad de México, México.*
[2] *Department of Economics and RWJF Center for Health Policy, University of New Mexico, 1915 Roma Ave., Albuquerque, NM 87131, United States of America.*
[3] *Facultad Latino Americana de Ciencias Sociales, Carretera Picacho Ajusco 377, Col. Héroes de Padierna, 14200 Ciudad de México, México.*
*Corresponding author; email: aislas@itam.mx

Received: August 13, 2020; accepted: February 8, 2021

RESUMEN

En este artículo evaluamos empíricamente el efecto de la contaminación del aire y la variación de la temperatura sobre los riesgos de salud de la población en tres municipios de la Zona Metropolitana del Valle de México (ZMVM). Con base en la teoría de la justicia ambiental nos preguntamos si en estos municipios de la ZMVM la asociación entre la concentración de PM_{10} y la mortalidad depende de las disparidades socioeconómicas de la población. En esta investigación diferimos de lo que habitualmente se ha hecho en otros estudios que establecen la relación entre la concentración de PM_{10} y la mortalidad al usar un modelo de espacio de estados, en lugar del modelo de regresión de Poisson. El modelo de espacio de estados permite estimar el tamaño de la población en riesgo no observada, su tasa de riesgo, la esperanza de vida de los individuos de esa población y el efecto de los cambios en las condiciones ambientales sobre la esperanza de vida. Nuestros resultados muestran una tasa de riesgo más baja en el municipio de mayor nivel socioeconómico comparada con la tasa más alta del municipio con menor nivel socioeconómico. La menor tasa de riesgo del municipio con mayor nivel socioeconómico incrementa la esperanza de vida y la probabilidad de que sus habitantes permanezcan más tiempo en la población en riesgo, aumentando de esta forma el tamaño de dicha población, en comparación con el municipio de menor nivel socioeconómico, cuyos habitantes muestran menor esperanza de vida. Entonces, entre más pequeña sea la población en riesgo, más enfermos estarán sus habitantes y, por tanto, menor será el impacto sobre la mortalidad en el largo plazo. Nuestro estudio examina cómo se comportan las disparidades de salud a nivel regional y podría proporcionar información para proponer iniciativas de políticas de salud pública, con el fin de mejorar las condiciones de vida entre las diferentes comunidades.

ABSTRACT

This study explored the nature of health risks in the population of three municipalities within the Metropolitan Area of the Valley of Mexico (MAVM) by means of an empirical analysis of health effects associated with air pollution and temperature variation. Based on the environmental justice theory, we asked whether, in unequal socioeconomic municipalities of the MAVM, the association between PM_{10} concentrations and mortality depends on socioeconomic disparities. We differ from previous studies that have established a relationship between PM_{10} and mortality based on a state-space model instead of the Poisson regression model. The state-space model allows estimating the size of the unobserved at-risk population, its hazard rate, the life expectancy of individuals in that population, and the effect of changes in environmental conditions on that life expectancy. Our results show a lower hazard rate in a wealthy municipality, as compared to a higher hazard rate in a poor one. The lower hazard rate of the wealthy municipality extends life expectancy and enhances the likelihood of inhabitants staying long-lasting within the population at risk, thus increasing the size of that population, as compared to the population at risk in the poor municipality, whose members show a lower life expectancy. Thus, the smaller the at-risk population, the sicker its average member and the smaller the impact on long-term mortality. Our study examines how regional health disparities could provide information for public health policy initiatives which might improve living conditions among different communities.

Keywords: mortality displacement, Poisson model, state-space model, environmental justice, health disparities.

1. Introduction

There is ample evidence on the relationship between ambient Particulate Matter (PM) concentration and mortality, morbidity, and other health-related effects. According to a study made by the World Health Organization (WHO) in 2014 (WHO, 2017), 92% of the world population was living in places that did not meet the WHO's air quality standards, and in 2012 air pollution caused 3.7 million premature deaths around the world[1]. In relation to the health effects of PM, the Technical Report of the European Regional Office of WHO (2013) concludes that there has been increasing evidence on the short and long-term consequences of PM exposure on health, mortality, and morbidity.

Many studies interpret the association between PM concentration and mortality as the response in a cluster of people with fragile health, for example, individuals with chronic cardiac or respiratory diseases and the elderly (US-EPA, 1996), which suggests that this association reflects the shortening of life expectancy by a few days. This represents, essentially, the mortality displacement effect, and it is the dominant interpretation of the strong and systematic association between air pollutants and mortality.

We think that the severity of environmental problems requires a new approach to environmental public policy and stress the need to quantify the shortening of life expectancy implied by the evidence relating air pollution to mortality. To achieve this objective, we applied the Murray and Nelson (2000) model, which allows us to plot the number of individuals in the at-risk population over time using the mortality data observed, as well as to estimate the hazard rate and life expectancies among the at-risk population. Just like them, we believe that understanding the dynamics of the at-risk population will improve our understanding of the relationship between pollution and health.

In this study, we explore whether socioeconomic differences across municipalities of the Metropolitan Area of the Valley of Mexico (MAVM) have an effect on the health risks associated with air pollution within the framework of environmental justice. According to Schlosberg (2013), environmental justice in general addresses inequality in the distribution of negative effects of environmental damage, and therefore some population groups are at higher environmental risk than others due to their unequal socioeconomic and locational characteristics. In these terms, environmental justice is just one of the many faces of social inequality. In our work, we adopt the traditional concept of environmental justice, namely, the association of a geographically localized relation between socially disadvantaged populations and environmental pollution.

There are different conceptions of environmental justice. According to Menton et al. (2020), the most widely accepted considers the following four dimensions: (1) distributional justice, that is, the fair distribution of environmental costs and benefits, the allocation of material goods or the distribution of social standing; (2) recognitional justice, recognition of, and respect for, the difference; (3) procedural justice, the fair and equitable institutional processes of a State, and (4) the capability approach, the recognition that justice takes into consideration the distribution of goods but also, and more importantly, the way those goods enhance the capacities of each person to lead a life worth living.

In this paper we study the relation between air pollution and the unequal socioeconomic characteristics of the population that live in three different municipalities in the MZVM. We are interested in

---

[1]In its Air quality guidelines, the WHO (2006) reported that air pollution was responsible for over two million premature deaths worldwide.

studying the association of those unequal conditions on the life shortening effects of air pollution upon the most vulnerable population who live in conditions of social inequality. Within the environmental justice framework, there is a very new and interesting approach to the study of the joint effects of inequality and air pollution on heath. This new line of research is less interested in the direct and indirect effects of income inequality on health due to air pollution. Particularly, in one of the first studies within this approach Hill et al. (2019) ask if a specific localized population (in this case that of USA states) is especially vulnerable to similar levels of air pollution (Hill et al., 2019). They argue that income inequality has a multiplier effect based on the following three theoretical principles:

1. Power: income inequality tends to concentrate economic and political power and as a consequence, the design of environmental policy in favor of the status quo
2. Proximity: income inequality tends to spatially segregate the socially vulnerable population in certain parts of the city or the territory.
3. Psychology: multiplier effect of psychological factors associated with social disadvantage in general and income inequality in particular generate a diversity of stressful situations that increase the cumulative burden of chronic stress and life events or the so-called allostatic load (Guidi et al., 2021).

The authors find that air pollution has a negative effect on life expectancy in those USA states with higher income inequality as measured by the income share of the top 10%.

A more recent study by Jorgenson et al. (2021) within the above-mentioned approach following Hill et al. (2019) asks if the effect of air pollution as measured by the concentration of $PM_{2.5}$ on life expectancy is greater in nations with higher levels of income inequality. Jorgenson et al (2021) tend to confirm their hypothesis.

Therefore, understanding exposure variations among subpopulations is important for risk management and environmental justice. Environmental health policy must seek not only to reduce population average risk but also to ensure that specific subpopulations are not unduly burdened relative to the overall population. Policymakers concerned about environmental justice argue that communities who are segregated in neighborhoods with high levels of poverty and material deprivation are also disproportionately exposed to a physical environment that adversely affects their health and well-being. They have also noted that groups with low socioeconomic status become concentrated, centralized, and isolated in abandoned inner-city cores where employment opportunities are few and where communities are clustered around industrial sites, undesirable land use, and transportation corridors that pose a significant health hazard (Pulido et al., 1996).

In terms of social and economic inequality, it has been documented the importance of economic and political power and their negative effects on environmental justice and thus on life expectancy (Romero et al., 2013; Hill et al., 2019). This is particularly true in urban areas where economic and political elites concentrate and live, in parts of the cities equipped with the best urban infrastructure, the higher density of green areas and open spaces, and, in general, with a higher supply of urban amenities including those related with a higher quality of life. As Romero et al. (2013) argued, intra-urban differences in temperature are related to affluence, and as poorer municipalities tend to be more densely settled and have a smaller proportion of green spaces, they are exposed to higher levels of air pollution. Furthermore, some studies have found that poorer neighborhoods are exposed to higher levels of air pollution and that the less financial, human, natural or social resources or assets people have, the more vulnerable they are to the various hazards they face (Moser and Satterthwaite, 2010).

The study of environmental justice is particularly important for MAVM due to several reasons. First, there is no explicit recognition of environmental justice in any of the different laws, local and federal, related to the environment[2]. Consequently, the design of environmental public policies does not consider the possibility of differences in environmental risks

[2]Article 15, fraction XII of the Ley General de Equilibrio Ecológico y Protección al Ambiente (General Law of Ecological Equilibrium and Protection; LGEEPA) recognizes the right of every person to enjoy an adequate environment

according to the socioeconomic conditions of the population[3].

Second, like all Mexican urban areas the MAVM has two important characteristics for the study of pollution-related mortality from the environmental justice point of view:

It is deeply segregated both socially and spatially and this phenomenon has been increasing throughout the years (Monkkonen, 2012; Sánchez, 2012a, b; Rubalcava and Schteingart, 2012). There is also evidence that there is spatial segregation according to the distribution of green areas in Mexico City (González, 2020). Furthermore, urban segregation has positive effects on socioeconomic inequalities (Reardon and Bischof, 2011).

According to the Consejo Nacional de Evaluación de la Política de Desarrollo Social (National Council for Evaluation of Social Development Policy; CONEVAL), about 34.4% of the MAVM population is living in poverty conditions and elder people are even more segregated (Garrocho y Campos, 2016).

Third, there is evidence that in Mexico there is a systematic relation between social inequalities in health, including health care, and socioeconomic inequalities (Barraza-Lloréns et al., 2013). Therefore, we think that it is important to consider this fact given the close relationship between environmental justice and health inequality (Brulle and Pellow, 2005; Wakefield and Baxter, 2010).

Fourth, there are a few studies for the MAVM that explore whether socioeconomic differences have an effect on the relationship between health risks and pollution. Romero et al. (2013), for example, analyzed the origin of health risk among the inhabitants of Bogotá, Mexico City, and Santiago. These authors concluded that "[W]hile proponents of the environmental justice perspective may expect that spatial differences in environmental hazards overlap with socioeconomic characteristics of human settlement, our results suggest that the association between levels of air pollution and social vulnerabilities do not always hold within the study cities." Their findings also suggest a kind of "boomerang effect", i.e., a situation that affects both rich and poor people. Even though we agree that pollution affects rich as well as poor inhabitants, our proposal shows some evidence in favor of environmental justice.

Finally, we think that environmental justice, both as analytical framework and as a principle to design and evaluate environmental policies, provides the right perspective to face some of the most urgent environmental problems that Mexican local governments need to solve. The environmental justice approach allows considering the different factors that affect environmental problems: an environmental policy must be a health, social, urban, and transport policy as well.

Accordingly, we hypothesize that the association between PM concentration and mortality in unequal socioeconomic municipalities of the MAVM depends on socioeconomic differentiation. To test this hypothesis, we selected three municipalities of the MAVM, with high, middle, and low-income levels. From a public health viewpoint, the arguments for taking a municipality approach to examining the relationship between socioeconomic status, environment, and health disparities are twofold. First, the theory suggests that it is appropriate to assess environmental health disparities at the territorial level because economic trends, transport planning, and industrial clusters tend to be regional in nature. In fact, zoning, facility location, and urban planning decisions tend to be local (Morrelo-Froch et al., 2002). Second, studies examining how health disparities play out regionally could provide information to propose public health policy initiatives that improve living

that favours his or her development, health and wellbeing. Nonetheless, we argue that this universal guarantee of the human right to a healthy environment does not mean that a government has an environmental justice perspective when designing and implementing environmental policies. The constitutional recognition of a human right does not by itself implies that social and economic inequalities would not hamper its enjoyment by a person or group of persons.

[3]In the USA, the Environmental Protection Agency established in 1993 the Office of Environmental Justice. According to this office, environmental justice is "…the fair treatment and meaningful involvement of all people regardless of race, colour, national origin, or income with respect to the development, implementation and enforcement of environmental laws, regulations and policies" (US-EPA, 2018). For a different point of view see Ramírez et al. (2015).

conditions among diverse communities, particularly for those communities whose illnesses relate to poor environmental conditions.

To our knowledge, our work is the first study for the MAVM case that estimates and plots the unobserved at-risk population as well as its hazard rate and life expectancy using the Kalman filter. As a result, it was possible for us to show inconsistency with the displacement hypothesis for the high-income municipality. We provide evidence of an impact not only to the at-risk population but also to the generally healthy individuals exposed to high levels of air pollution for a sufficient amount of time to develop chronic conditions and enter the at-risk population. We found that low socioeconomic municipalities tend to have high vulnerability to air pollution, that is, a given exposure level may cause greater than average health reduction for these groups. The socioeconomic disparities between municipalities partially explain why we observe a lower hazard rate with high variability in the wealthy municipality as compared to the higher hazard rate with low variability in the poor one. The lower hazard rate of the wealthy municipality extends life span and allows people to stay longer in the at-risk group, thus increasing the size of that population, as compared to the at-risk population in the poor municipality, whose individuals have a lower life expectancy.

We organized the paper into four additional sections besides this introduction. Section 2 describes the climatic, atmospheric, and socioeconomic conditions of our selected municipalities and highlights the high disparities among them. It also describes and characterizes the data applied to explore health risks. Section 3 presents the model we used to estimate the relationship between PM concentration and mortality. We propose a state-space model that allows us to estimate the number of individuals of the population at risk, the life span of individuals in that group, as well as the effect of changes in air quality over the life span. The empirical analysis is carried out in section 4, while section 5 presents some discussion and concluding remarks.

2. Study area and data

2.1 Municipalities

The MAVM, with a population of nearly 21 million people, expands over three states (Mexico City and the states of Mexico and Hidalgo). It comprises the 16 municipalities of Mexico City, 59 municipalities of the state of Mexico, and one municipality of the state of Hidalgo. In 2010, according to CONEVAL (2014), almost 35% of the total population was in poverty conditions.

The MAVM is located in an elevated basin surrounded by mountains on the east, south, and west, with a narrow gap to the south-southwest and a broad opening to the north. Pollutants are trapped within the basin by mountains and term inversions, which are frequent during winter. In addition, the high altitude makes combustion sources less efficient. The tropical latitude (19º 25' N) and the high altitude (2240 masl) make sunlight less intensive than in lower elevation, higher latitude cities (Molina and Molina, 2004). The MAVM's climate is generally dry, but thunderstorms are frequent and intensive from June through October. Winter is slightly cooler than summer. Since specific humidity, temperature, and wind speed acted as cleaners of PM for the atmosphere, the safest period for the MAVM in terms of PM emissions is precisely from June through October.

We used diverse criteria in the selection of the three municipalities to evaluate if health risks related to air pollution are socioeconomically differentiated. In order to examine health risks, we needed to gather, validate, and analyze data on air pollution, local temperature, and socioeconomic vulnerability. Álvaro Obregón, Iztapalapa, and Naucalpan de Juárez were those municipalities having the complete data set to carry out our study.

With a population of 1 815 768 inhabitants, according to data from the 2010 census, Iztapalapa is the most populous municipality both in the MAVM and the whole country. Over 92% of Iztapalapa's territory is urban, whil 43.8 and 45% of Álvaro Obregón's, and Naucalpan's territory, respectively, was urban. Regarding industrial land use, 3.0, 3.2, and 0.7% of the territory of Iztapalapa, Naucalpan de Juárez, and Álvaro Obregón, respectively, is used for industrial activities.

Being the most populous municipality, Iztapalapa has very demanding transportation requirements. Almost all means of transportation in this municipality operate through various roadways on both public and private vehicles. The most important road in Mexico City goes through this area. Every day, a total of about

80 000 vehicles moves through this route, making it the second busiest in the MAVM. According to the 2017 origin-destiny survey (INEGI, 2017), Iztapalapa was the origin of 971 765 daily trips and the destiny of 970 135 daily trips.

The most relevant economic activities in Iztapalapa are manufacturing and commerce. The three largest sectors of retail sales are street markets, flea markets, and street vendors who flagrantly violate sanitation and environmental laws. Food processing, tobacco products, metals, machinery, surgical equipment, paper and printing, and textiles are also included.

Naucalpan de Juárez is a municipality in the state of Mexico, northwest of Mexico City, which according to the 2010 census had a total population of 833 779 inhabitants. Its subsoil is highly polluted, mainly because of the Bordo Poniente landfill and the sagging of the subsoil due to the overpumping of groundwater and the jettison of untreated wastewater. Furthermore, other small businesses (e.g., brick making operations, public restrooms, and restaurants) blatantly infringe sanitation and environmental laws and increase the pollution in the municipality. Nevertheless, vehicles are the origin of 70% of the air pollution; in 2017, they were the origin of 442 063 daily trips and the destiny of 447 799 daily trips (INEGI, 2017).

The most stringent environmental regulations promoted by a growing middle class have been enacted and enforced, which has caused the relocation of several highly polluting industries to the north and west of the MAVM. Industries that have left Naucalpan de Juárez include the metal, cement, and glass industries, as well as others using a large quantity of energy. About 20% of the manufacturing facilities have closed their doors and six industrial parks are empty.

Álvaro Obregón encompasses a large portion of the southwest area of Mexico City. According to the 2010 census, it had a total population of 727 034 inhabitants. The municipality occupies 7720 ha, of which is 66.1% urban land and 38% is considered protected land. Services—including financial services—make up the largest segment of the municipality economy, accounting for 75.6% of gross domestic product and employing about 76.14% of the workforce. This municipality is an important economic center and in 2017 it was the origin of 552 720 daily trips and the destiny of 555 629 daily trips (INEGI, 2017).

Table I shows that, while variations in the average daily temperature in any of these municipalities are not high, variations in daily average pollution are. For example, the daily average level of PM_{10}[4] range between 6.88 and 115.32 $\mu m\ m^{-3}$ in Álvaro Obregón, while for Iztapalapa the daily average level ranges between 7.00 and 268.00 $\mu m\ m^{-3}$. Large differences in pollution emissions will imply different hazard exposures to those municipalities. According to impact studies about urban vulnerability, the risks of adverse health impacts depend on two different factors. The first one is related to the origin of the hazard for urban populations, while the second is related to the socioeconomic conditions influencing the exposure, the sensitivity and the responsiveness to risk, as well as its effects on health, all of which may reflect inequalities in the access to services and well-being systems. Therefore, it is important to explain the current environmental and socioeconomic situation of these municipalities.

Table I characterizes the three municipalities according to their levels of socioeconomic segregation using data from the 2000 and 2010 censuses as well as from the 2005 population and housing count. The first set of socioeconomic variables in Table I measures poverty characteristics and shows differences in average per capita income between municipalities. The annual per capita income in the wealthiest municipality is 1.25 times the one of the poorest municipalities. There is, however, important variability between households within each municipality and between municipalities. The GINI coefficient, which measures income distribution, suggests that there is greater inequality in the two wealthiest municipalities, reflecting the more heterogeneous composition of the neighborhoods.

[4]Particles with aerodynamic diameter less than 10 μm. PM_{10} are composed of fugitive dust from roadways, construction, bared land, organic and black carbon, and combustion and industrial processes. They have been linked to asthma, lung cancer, cardiovascular harm and a higher probability of premature mortality.

Table I. Environmental and socioeconomic features of the study municipalities.

	Álvaro Obregón			Naucalpan de Juárez			Iztapalapa		
	Min.	Mean	Max.	Min.	Mean	Max.	Min.	Mean	Max.
PM_{10} (daily average in μg m^{-3})	6.88	38.79	115.32	6.33	45.14	137.27	7.00	54.36	268.00
Daily average temperature (ºC)	5.80	16.30	23.94	5.44	16.24	25.82	7.00	16.70	25.00
Non-accidental mortality	1.00	9.28	25.00	1.00	9.91	24.00	5.00	20.00	47.00
Cardiovascular and respiratory mortality	0.00	2.56	11.00	0.00	2.53	10.00	0.00	5.06	21.00
	Years								
	2000	2005	2010	2000	2005	2010	2000	2005	2010
Population	687,020	706,567	727,034	858,711	821,442	833,779	1,773,343	1,820,88	1,815,786
Poverty									
Annual per capita income (PPP USD)	14,816	13,651	20,177	13,583	14,171	20,112	10,078	10,481	16,126
PWNM2S	43.07	33.24	23.64	47.11	38.72	28.02	50.29	38.82	36.04
Gini coefficient	na	na	0.442	na	na	0.454	na	na	0.409
Dwelling									
% all home appliances	17.18	na	29.78	16.01	na	25.85	8.22	na	22.36
% home ownership	73.63	na	65.52	67.77	na	59.75	75.78	na	66.95
Socio-demographics									
PRM18BD	131.82	178.77	210.50	112.87	153.70	163.38	83.52	117.73	138.71
% people where the head-household is indigenous	2.58	1.69	1.83	4.93	4.35	5.63	3.94	2.95	3.88
Gender and household composition									
% female labor force	39.16		41.93	35.15		37.23	35.01		38.44
% female-headed household	23.61	26.93	29.38	20.00	23.20	24.87	22.27	26.09	29.00
Average person per household	4.15	3.87	3.68	4.18	3.94	3.82	4.33	4.09	3.91
Percentage of households with more than seven members	5.89	4.40	3.46	5.45	4.10	3.45	6.81	5.39	4.31
Employment									
% unemployment	1.76	na	4.43	1.37	na	4.51	1.66	na	5.05
% informally employed	na	na	26.13	na	na	24.06	na	na	28.03
Health									
% population without public healthcare	47.12	40.57	30.03	44.79	43.56	41.60	51.31	50.51	38.30
Infant mortality rate (per thousand)	19.27	12.66	11.65	19.85	10.12	15.65	20.39	15.81	12.42

na: not available; PWNM2S: percentage of workers with at most two minimum salaries; PRM18BD : population rate under 18 years of age with at least bachelor degree (is a measure of the number of person in a municipality with at least bachelor degree per a 1000 individuals per year).
Data source: the 2000 and 2010 census, as well as the 2005 population and housing count, for levels of socioeconomic segregation; air pollution and weather data were obtained from the Red Automática de Monitoreo Atmosférico (Mexico City's Automatic Air Quality Monitoring Network). Daily numbers of deaths were obtained from the National Center of Health Statistics.

In terms of the demographic composition within neighborhoods, Table I shows that the population rate over 18 years, with at least a bachelor's degree, decreases as the proportion of poor households increases. Further, there is evidence that racial dynamics are at play. Largely this may reflect the low income of indigenous residents (in terms of the number of minimum wages[5]), but their high concentration in a few neighborhoods is highly suggestive of at least some elements of ethnic segregation.

Female labor force participation increases along with segregation in agreement with multiple studies that suggest that poor urban households have increased their labor supply in order to compensate for decreasing real income since the 1980s. However, in contrast to the case of the USA, the average percentage of female-headed households is the same in wealthy and poor households. This is in agreement with studies showing that in Mexico, low-income single mothers tend to move in with other family members, forming extended families to cope with scarcity and family demands. Studies show that women in these conditions seldom declare they are the household head, regardless of their monetary contribution.

Turning to employment patterns, Table I shows a consistent link between socioeconomic segregation and character of employment: the more segregated a municipality, the higher the percentage of informal employment workers. Thus, people living in areas with higher concentrations of poor households are likely to hold jobs that do not provide health insurance or pension contributions and, therefore, they have a lower level of health, as indicated by the infant mortality rate. In general, these trends show the anticipated pattern of greater levels of precarious employment in the poorest municipalities. However, unemployment does not rise with poverty; it remains at close levels across municipalities. This is not surprising in Mexico, where joblessness is more common among educated workers because low-income workers cannot afford to remain unemployed. Hence, poor quality employment rather than unemployment could be a more accurate indicator of labor disadvantage.

Housing conditions differ across neighborhoods. While in the wealthy municipality, 17.18% of houses have all home appliances (computer, radio, television, blender, telephone, fridge, hot water heater, own car), only 8.22% of houses in the poor municipality do. Homeownership is high across the three municipalities; this tendency reflects the high proportion of self-constructed units that characterize Mexican municipalities, as is the case in most developing countries.

2.2 Data

We used daily time series of air pollution, weather, and mortality data for Iztapalapa, Álvaro Obregón, and Naucalpan de Juárez for the period 2001-2010. Figure 1 shows that temperature, PM_{10}, and death counts seem to be dominated by annual seasonal patterns, with PM_{10} and the daily number of deaths highest in winter. Air pollution and weather data were obtained from the monitoring system of air pollutants in Mexico City's Red Automática de Monitoreo Atmosférico (Automatic Air Quality Monitoring Network; RAMA), which currently has 47 stations located all over Mexico City's Metropolitan Area. The station runs 24 h during the 365 days of the year. Separated samples of PM, based on a measurement of particles with aerodynamic diameter less than or equal to 10 μm (PM_{10}) per cubic meter and temperature, were obtained for each municipality. The hourly measures were collapsed over the 24-h period to obtain a mean value for PM_{10} and ambient temperature[6]. Daily numbers of deaths were obtained from the National Center of Health Statistics for the same time period. Deaths due to accidental and other external causes according to the International

---

[5]We use the minimum wage (which is equal to 80.04 Mexican pesos, roughly USD 4.30 as of December 2018) as the base figure from which to calculate numerous other payments such as fines or benefits.

[6]For this paper, we had access to a relatively rich panel data set that is available for the MAVM. Data are available not only for particulate PM_{10}, but also for sulfur dioxide (SO_2), carbon monoxide (CO), and ozone (O_3). It is generally agreed that these are high quality data, and, as Davis (2008) has pointed out, "these measures are widely used in scientific publications".

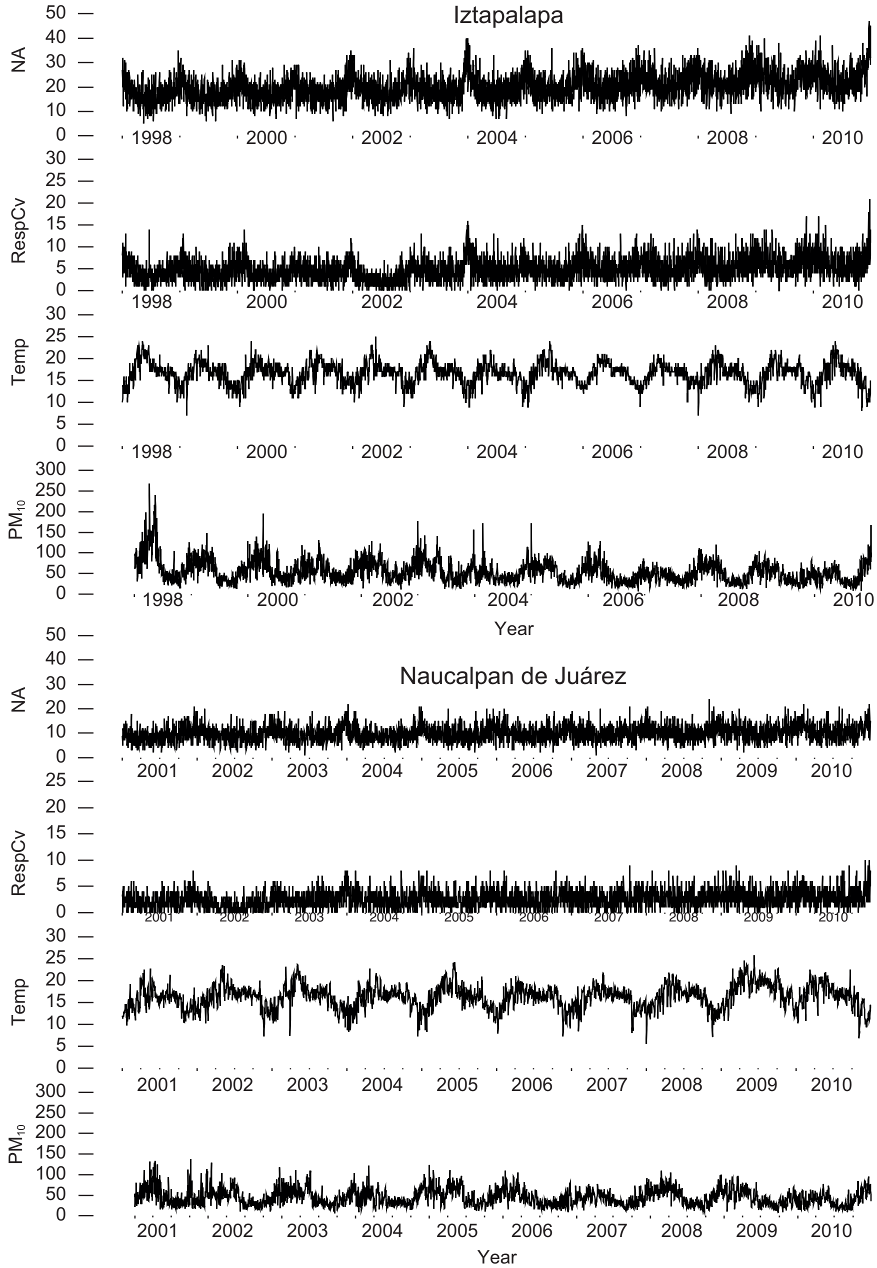

Fig. 1. Daily time series of non-accidental mortality (NA), cardiovascular and respiratory diseases (RespCV), temperature (Temp), and levels of particulate matter with an aerodynamic diameter less than 10 μm for Naucalpan de Juárez and Álvaro Obregón during the period 2001-2010, and for Iztapalapa during the period 1988-2010.

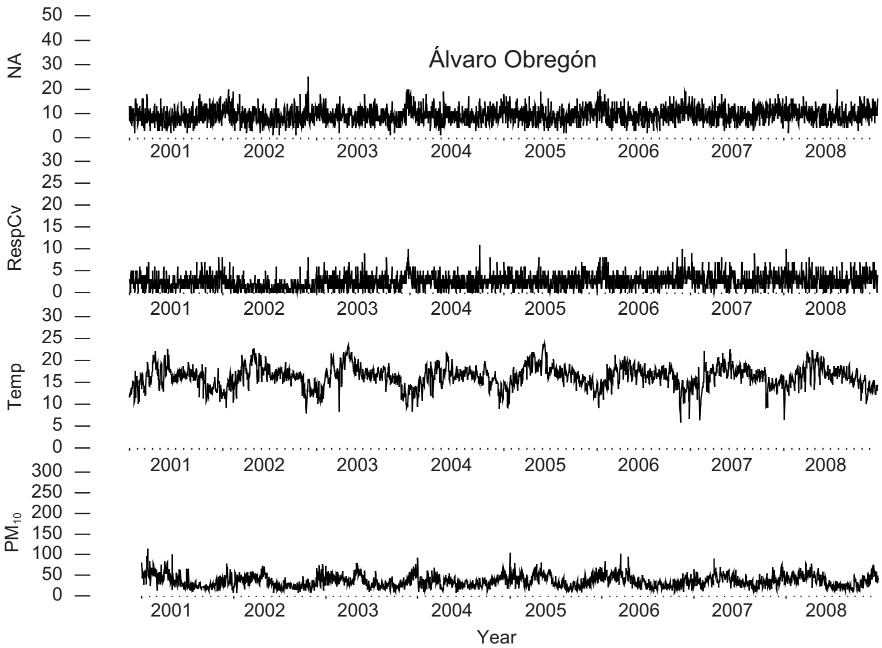

Fig. 1. Daily time series of non-accidental mortality (NA), cardiovascular and respiratory diseases (RespCV), temperature (Temp), and levels of particulate matter with an aerodynamic diameter less than 1μm for Naucalpan de Juárez and Álvaro Obregón during the period 2001-2010, and for Iztapalapa during the period 1988-2010.

Classification of Disease 10th revision (ICD-10) were excluded. We also separated deaths into those that are likely to be related to pollution levels and those related to other causes. Therefore, separate counts were also computed for deaths related to diseases of the respiratory system (ICD-10, causes J) and deaths related to diseases of the circulatory system (ICD-10, causes I).

3. Model and estimation strategy

Murray and Nelson (2000) propose a state-space model that allows, through the observed mortality data, to estimate and study the dynamics of the at-risk population usually unobserved. Without a doubt, knowing the size and dynamics of the population at risk will increase our understanding of the relationship between pollution and individuals' health of the at-risk population. Thus, one of our aims was to plot the at-risk population of these municipalities over time using their observed mortality data. Following Murray and Nelson (2000), we assumed that part of the population of these municipalities is at risk, subject to a risk rate that varies with atmospheric conditions including total suspended particles and temperature. New entrants will eventually replace the at-risk population that dies. This at-risk population, the new entrants, as well as the hazard rate are not noticed but can be estimated by applying the Kalman filter to the daily atmospheric conditions and mortality counts. By means of the Kalman filter, it is possible to estimate the hazard rate over time, its relationship to atmospheric variables, and the trajectory of the unobserved at-risk population. Murray and Nelson (2000) claim that it is also possible in the state-space framework, to address the following questions: What is the size of the population at risk? What is the life expectancy of individuals within that population? What is the effect of changes in air quality over that life expectancy?

Contrary to the Poisson regression model widely used in this kind of analysis (e.g., Peng and Dominici, 2008), in the case of the state-space model the effect of an at-risk factor such as PM_{10} on mortality is indirect. As shown in the following lines, it is proportional to the size of the at-risk population that is not observed. If the at-risk population has been reduced by recent mortality due to an increase in the hazard rate, then the effects of a new increment on the hazard rate will be mitigated, since the at-risk population is temporarily smaller. In fact, it is this reap effect which allows us to estimate the unobserved at-risk population by the Kalman filter. If a higher hazard rate persists, then the mortality count will fall back towards its previous level, since mortality is limited, in the long run, to the rate of new arrivals. However, the life expectancy of individuals in the at-risk population will fall, and this alternative approach offers estimations of this effect.

At the core of the Murray and Nelson (2000) model, there is an unobserved at-risk population from which all no-traumatic deaths are assumed to happen. This at-risk population is the group of individuals whose health is threatened due to various reasons, even in the absence of environmental hazards. The model assumes that the at-risk population decreases its size due to deaths and replenishes it with the arrival of new members. The model focuses on people whose health is frail and that eventually die. These authors define the at-risk population on a given day as its value on the previous day, plus new entrants, minus deaths. A first-order difference equation accounts for daily changes in the at-risk population in the following way:

$$P_t = P_{t-1} + N_t - D_t \tag{1}$$

where P_t is the unobserved at-risk population, N_t is the number of new arrivals, and D_t is the observed number of deaths, all of them on day t. Each member of the at-risk population faces a probability of death that is a function of the environmental conditions, including ambient air quality. Daily deaths are represented by the following equation:

$$D_t = \left(\gamma' x_t\right) P_{t-1} + e_t \tag{2}$$

Environmental x_t hazards are expressed in a hazard function $\gamma' x_t$ that models the amount of risk that is reduced or increased daily by environmental and seasonal factors. The hazard function is the daily probability of death, and we assume that it is a linear combination of atmospheric variables, including an intercept term. We do not know what the correct hazard function is, as it is in the Poisson regression model. To do this, an exploration is required about various hazard functions, which will be known as models. Deaths are also allowed to occur at random, as captured by the random error term .

As we mentioned above, both short- and long-term exposure to PM have been linked to adverse health effects, including the following: (*i*) increased number of hospital admissions and/or emergency department visits (Dockery and Pope, 1994; Rodopoulou et al., 2014); (*ii*) negative respiratory symptomatology (Pope et al., 1995; Wu et al., 2016), and (*iii*) increased aggravation of chronic diseases in cardiovascular and respiratory system (Schlesinger, 2007; Belen et al., 2014). Therefore, as in Murray and Nelson (2000), our baseline model uses the following hazard function:

$$\gamma' x_t = \gamma_0 + \gamma_1 PM_{10} \tag{3}$$

In this model, γ_0 is the constant probability of death in the absence of environmental effects, and γ_1 is the marginal effect of PM_{10} on mortality.

On the other hand, temperature has been considered as a potential risk factor that could lead to a series of adverse health outcomes (Zhang et al., 2015; Chen et al., 2017) and as a control for the effect of seasonality variation in atmospheric conditions on the health status. Moreover, there is a U-shaped relationship between temperature and mortality, with mortality being lowest at moderate temperatures and highest at extremely low and high temperatures (Kan et al., 2003). Therefore, since the correct hazard function is unknown, this requires an exploration of various plausible hazard functions. As in Murray and Nelson (2000), we explored some hazard functions by including ambient temperature to control for seasonality, and since the mortality-temperature relationship is non-linear, we also investigated the quadratic and interactive function of temperature with PM, as shown below.

In the basic model of Murray and Nelson (2000), where the time series of mortality analyzed was stationary, new members of the at-risk population were assumed to enter randomly with a constant mean N

equal to the mean daily deaths, plus Gaussian errors. Given the high variability in the population growth rate on most of the MAVM municipalities, the time series of mortality counts that we analyzed are of a non-stationary nature. Therefore, we departed from Murray and Nelson at this point, assuming that the new members of the at-risk population are included as follows[7]:

$$N_t = N_{t-1} + \eta_t \tag{4}$$

Since the at-risk population P_t and the new entrants N_t are unobserved, the parameter of this dynamic model cannot be estimated by means of conventional methods. However, the unobserved components can be estimated by using the state-space technique. Casting the model in this form, makes it possible to use the Kalman filter for parameter estimation. The representation considers Eq. (2) as a measurement equation, that is:

$$D_t = \begin{bmatrix} 0 & \gamma' x_t & 0 \end{bmatrix} \begin{bmatrix} P_t \\ P_{t-1} \\ N_t \end{bmatrix} + e_t$$

Then, we write Eqs. (1) and (4) as the following state equation:

$$\begin{bmatrix} P_t \\ P_{t-1} \\ N_t \end{bmatrix} = \begin{bmatrix} 1 & 0 & 1 \\ 1 & 0 & 0 \\ 0 & 0 & 1 \end{bmatrix} \begin{bmatrix} P_{t-1} \\ P_{t-2} \\ N_{t-1} \end{bmatrix} - \begin{bmatrix} D_t \\ 0 \\ 0 \end{bmatrix} + \begin{bmatrix} 0 \\ 0 \\ 1 \end{bmatrix} \eta_t$$

If we assume that the error terms are normally distributed, then we can estimate the parameters of the model employing a maximum likelihood technique. For instance, the parameters estimate in the above system can be obtained by starting with an initial guess for the state vector and its covariance matrix. Given the initially estimated parameters, the Kalman filter recursively generates the prediction equation. Ultimately, the filter generates estimates of the unobserved components $\hat{P}_t$ and $\hat{N}_t$, as well as $\hat{\gamma}$, $\hat{\sigma_e}$, and $\hat{\sigma_\eta}$. To calculate the mean life expectancy of subjects in the at-risk population, the reciprocal of the estimated mean hazard rate is used; besides, the daily average at-risk population deaths are the ratio of the average mortality to the daily average at risk-population.

4. Empirical results

Using Kalman filters, we estimated the observation and state equation by maximum likelihood. Tables II to VII report the estimates and asymptotic standard errors of the five baseline settings of the risk function including various combinations of PM_{10} and average temperature (Avtem*)*, the square of temperature, and the multiplicative interaction of PM_{10} with Avtem*.* A constant term is included in each one of the risk functions. Model 1 uses only PM_{10}. Model 2 adds Avtem to Model 1. Model 3 adds the square of *Avtem* allowing for hazard rate that increases at both extremes of temperature. Model 4 is included for comparison purposes and uses only the Avtem variable. Finally, Model 5 allows the effect of PM_{10} and Avtem, so they depend on the value of each other by adding the Avtem*PM_{10}, an interaction variable. Estimates are produced using the Kalman smoother, which uses all information available in the sample, thus providing a better in-sample fit, as compared with the basic Kalman filter, which only uses information available at time *t*.

As for the analysis of each of the municipalities, Tables II and III show that when comparing the log-likelihood of Model 5 with that of Model 4, which does not include information about the levels of PM_{10}, the likelihood ratio test suggests that, for non-accidental and cardiovascular-respiratory mortality causes, PM_{10} is highly significant in both populations. We can also observe that, when comparing Model 5 with Model 1, which does not include information about the level of Avtem, the likelihood ratio test suggests that Avtem is also highly significant in both populations. We also note that the interaction variable Avtem*PM_{10} is not significant in Model 5 when the log-likelihood is compared with

[7]Lipfert and Murray (2012) extend the Murray and Nelson (2000) model by allowing environmental factors to affect new entries as well as deaths, using separated hazard functions, something we are considering for a future research work.

Table II. Parameter estimates for Iztapalapa state-space models (standard errors in parentheses). Non-accidental mortality counts.

Parameter	Model 1	Model 2	Model 3	Model 4	Model 5
γ_0	0.0517673* (0.013920)	0.0711946* (0.015207)	0.0731026* (0.014924)	0.0813666* (0.016433)	0.0698405* (0.015839)
PM_{10}	0.0000428* (0.000015)	0.0000489* (0.000018)	0.0000471* (0.000017)		0.0000861 (0.000062)
Avtem		0.0006401** (0.000298)	0.0000330 (0.001020)	0.0001982 (0.001200)	–0.0000038 (0.000876)
Avtem^2			0.0000182 (0.000029)	0.0000209 (0.000035)	0.0000231 (0.000024)
PM_{10} *Avtem					–0.0000025 (0.000004)
σ_e	0.2863* (0.0527)	0.2585* (0.0354)	0.2597* (0.0358)	0.2583* (0.0301)	0.2612* (0.0375)
σ_η	19.5635* (0.4636)	19.0177* (0.4941)	19.0651* (0.5205)	18.9513* (0.4971)	19.1061* (0.5242)
AVERISPO	372	238	247	222	256
MLE (days)	15-19	10-12	10-13	10-12	11-13
DAVERISPD	5.3%	8.4%	8.0%	9%	7.8%
ln(L)	–14060.123	–14055.217	–14055.064	–14059.057	–14054.914

Model selection test: likelihood ratio test
Model 5 vs. Model 4: 8.28** Model 5 vs. Model 1: 10.41** Model 5 vs. Model 3: 0.30

Avtem: average temperature; AVERISPO: average at risk-population; MLE: mean life expectancy; DAVERISPD: daily average at-risk population deaths.
Significant at *1, **5 and ***10%.

that of Model 3; the likelihood ratio test suggests that Model 3 is preferable to Model 5. Thus, for Iztapalapa, we considered Model 3 as a reasonable baseline specification in both non-accidental and cardiovascular-respiratory deaths.

For non-accidental and cardiovascular-respiratory deaths, the hazard functions of Model 3 imply that both extremes of temperature are detrimental and that PM_{10} is also detrimental to the effect of rising temperature. At the average level of PM_{10} observed in the sample, the effect of an increase in temperature from the minimum (7 ºC) to the maximum (25 ºC) value is an increase in the hazard rate from 0.076 to 0.087 for non-accidental deaths, while for the cardiovascular-respiratory deaths the increment goes from 0.077 to 0.153. On the other hand, at the maximum temperature of 25 ºC, the effect of an increase of PM_{10} from the minimum (7 µg m^{-3}) to the maximum (268 µg m^{-3}) value observed in the sample is an increase in the hazard rate from 0.085 to 0.097 for non-accidental mortality, while for cardiovascular-respiratory deaths, the increase goes from 0.150 to 0.165. Consistent with previous studies (Samet et al., 2000a, b), the effects of an increase on the risk function are highest for cardiovascular and respiratory mortality than for non-accidental deaths.

Figures 2 and 3 plot the Kalman filter estimates of at-risk populations along with the estimated hazards

Table III. Parameter estimates for Iztapalapa state-space models (standard errors in parentheses). Cardiovascular and respiratory mortality counts.

Parameter	Model 1	Model 2	Model 3	Model 4	Model 5
γ_0	0.0390000* (0.014156)	0.0478247* (0.014572)	0.0572752* (0.020528)	0.052562* (0.020113)	0.035773* (0.012902)
PM_{10}	0.0000599* (0.000022)	0.0000675** (0.000027)	0.000056** (0.000026)		0.0001829* (0.000067)
Avtem		0.0005804 (0.000373)	0.001874*** (0.001052)	0.002018 (0.001489)	–0.001452* (0.000524)
Avtem^2			0.000074*** (0.000042)	0.000091 (0.000049)	0.000069* (0.000026)
PM_{10} *Avtem					–0.000009 (0.000003)
σ_e	0.0493* (0.0105)	0.0464* (0.0075)	0.0477* (0.0100)	0.0465* (0.0075)	0.05285** (0.0145)
σ_η	5.0243* (0.1235)	4.9317* (0.1332)	4.9768* (0.1364)	4.9195* (0.1315)	5.0583* (0.1191)
AVERISPO	119	83	101	78	153
MLE (days)	18-25	12-18	6-13	12-16	25-34
DAVERISPD	5.8%	8.4%	6.9%	8.9%	4.5%
ln(L)	–10779.983	–10777.679	–10774.915	–10779.770	–10773.693

Model selection test: likelihood ratio test
Model 5 vs. Model 4: 12.15* Model 5 vs. Model 1: 12.58* Model 5 vs. Model 3: 2.44

Avtem: average temperature; AVERISPO: average at risk-population; MLE: mean life expectancy; DAVERISPD: daily average at-risk population deaths.
Significant at *1, **5 and ***10%.

rates in Model 3. The estimated at-risk population average is 247 for non-accidental deaths, but 144 for cardiovascular-respiratory deaths, and varies seasonally, with the daily number of deaths increasing to reach the highest level in winter. Since average mortality is 20 and seven deaths per day, this implies that about 8 and 6.9% of the at-risk population die on average per day due to non-accidental causes and cardiovascular-respiratory diseases, respectively. Hazard rates fluctuate seasonally as periods of high emission of PM_{10} and temperature extremes gather a severe harvest, followed by less lethal conditions. Historically, data suggest that the highest PM_{10} concentration occurs in the MAVM during late winter and early spring. We observed that, in the case of non-accidental deaths, the estimated at-risk population series moves higher with time, from an average of 216 at the beginning of the period to around 287 in the final years, while it moves from an average of 83 to around 123 in the same period for cardiovascular-respiratory deaths. There is a corresponding and offsetting decline in the hazard rate, moving downwards from an average of about 0.082 to 0.081 for non-accidental deaths, while it moves downwards from 0.113 to 0.112 for cardiovascular-respiratory deaths in the same period. This decline in hazard rates is driven by a reduction of about 65 to 47 μg m^{-3} in PM_{10} average emissions during the early and later years, respectively, and suggests that air control strategies implemented by the government since 1990 contributed to maintaining PM_{10} under a 24-h

Table IV. Parameter estimates for Naucalpan de Juárez state-space models (standard errors in parentheses). Non-accidental mortality counts.

Parameter	Model 1	Model 2	Model 3	Model 4	Model 5
γ_0	0.0344581** (0.013759)	0.0424385* (0.000042)	0.0475469* (0.015814)	0.0497855* (0.014354)	0.0400705* (0.014322)
PM_{10}	0.000036*** (0.000019)	0.0000422*** (0.000023)	0.0000355*** (0.000021)		0.0001398** (0.00008)
Avtem		0.0002985 (0.000213)	–0.0008906 (0.000771)	–0.0010178 (0.000732)	–0.0007899 (0.000843)
Avtem^2			0.0000375 (0.000026)	0.0000437*** (0.000024)	0.0000445* (0.000027)
PM_{10} *Avtem					0.0000070* (0.000004)
σ_e	0.0547* (0.0140)	0.0525* (0.0111)	0.0528* (0.0117)	0.0536* (0.0118)	0.0522* (0.01179)
σ_η	9.7460* (0.2626)	9.6217* (0.2482)	9.6520* (0.2537)	9.6602* (0.2549)	9.6887* (0.2589)
AVERISPO	274	201	221	219	245
MLE (days)	25-32	19-22	19-23	19-23	21-27
DAVERISPD	3.6%	4.9%	4.5%	4.5%	4.0%
ln(L)	–9466.406	–9464.690	–9463.463	–9465.930	–9461.233

Model selection test: likelihood ratio test
Model 5 vs. Model 4: 9.39* Model 5 vs. Model 1: 10.34** Model 5 vs. Model 3: 4.46**

Avtem: average temperature; AVERISPO: average at risk-population; MLE: mean life expectancy; DAVERISPD: daily average at-risk population deaths.
Significant at *1, **5 and ***10%.

maximum limit and resulted in a decreasing trend during this period. The effect of this air control strategies on reducing PM_{10} emissions were also observed in the other two municipalities, as shown below.

As pointed out by Murray and Nelson (2000), while an increase in risk factors cannot increase mortality, in the long run life expectancy is the inverse of the hazard rate, so hazard causing agents will shorten it. The hazard rates observed over the sample period go from 0.075 to 0.096 for non-accidental deaths, while they go from 0.075 to 0.157 for cardiovascular-respiratory deaths. Therefore, we have a life expectancy ranging from 10 to 13 days for the group of non-accidental death population, while life expectancy ranges from 6 to 13 days for the frail cardiovascular-respiratory death population.

Analogous to the Iztapalapa's selection model, we have that, for Naucalpan de Juárez, the likelihood ratio test suggests that Model 5 is preferable for non-accidental deaths, while Model 3 is preferable for cardiovascular-respiratory deaths.

At the average level of PM_{10} observed in the sample, the effect of an increase in temperature from the minimum (5.44 ºC) to the maximum (25.82 ºC) value observed in the sample, is an increase in the Naucalpan de Juárez's hazard rate from 0.045 to 0.063 for non-accidental deaths, and from 0.042 to 0.05 for cardiovascular-respiratory deaths. On the

Table V. Parameter estimates for Naucalpan de Juárez state-space models (standard errors in parentheses). Cardiovascular and respiratory mortality counts.

Parameter	Model 1	Model 2	Model 3	Model 4	Model 5
γ_0	0.0309206** (0.015591)	0.0352771* (0.011758)	0.0464546* (0.017443)	0.0481114* (0.018152)	0.0418381** (0.018547)
PM_{10}	0.0000232** (0.000012)	0.0000203*** (0.000015)	0.0000158 (0.000015)		0.0001117*** (0.000861)
Avtem		0.0003810*** (0.000279)	–0.0012113*** (0.000981)	–0.0012816 (0.001335)	–0.0011105 (0.001294)
Avtem^2			0.0000521*** (0.000030)	0.0000557*** (0.000043)	0.0000588 (0.000046)
PM_{10} *Avtem					–0.0000063 (0.000008)
σ_e	0.0096* (0.0028)	0.0093* (0.0020)	0.0093* (0.0022)	0.0092* (0.0021)	0.0092* (0.0020)
σ_η	2.4501* (0.0687)	2.4255* (.0525)	2.4263* (0.0643)	2.4250* (0.0643)	2.4293* (0.0649)
AVERISPO	79	59	60	59	63
MLE (days)	29-32	21-26	19-25	19-25	20-27
DAVERISPD	2.5%	3.3%	3.3%	3.3%	3.1%
ln(L)	–6928.885	–6926.768	–6925.972	–6928.885	–6925.684

Model selection test: likelihood ratio test
Model 5 vs. Model 4: 6.40** Model 5 vs. Model 1: 6.56** Model 5 vs. Model 3: 0.57

Avtem: average temperature; AVERISPO: average at risk-population; MLE: mean life expectancy; DAVERISPD: daily average at-risk population deaths.
Significant at *1, **5 and ***10%.

other hand, at the maximum temperature of 25.82 ºC, the effect of an increase in PM_{10} from the minimum (6.33 µg m^{-3}) to the maximum (137 µg m^{-3}) found in the sample is to raise the hazard rate from 0.051 to 0.093 for non-accidental deaths, while for cardiovascular-respiratory deaths, the increment goes from 0.050 to 0.052.

Figures 4 and 5 plot the Kalman filter estimates of the at-risk populations along with the estimated hazards rates in Models 5 and 3, respectively. The estimated at-risk population average is 245 for non-accidental deaths, while the average is 60 for cardiovascular-respiratory deaths, and, as in the case of Iztapalapa, it varies seasonally with the daily number of deaths, being the highest in winter. Since average mortality is 9.91 and 2.53 per day, this implies that about 4.0 and 3.3% of the at-risk population dies on average per day in the non-accidental and cardiovascular-respiratory populations, respectively. As in Iztapalapa, the hazard rates fluctuate seasonally as periods of high emissions of PM_{10} and of extreme temperature gather a grim harvest, followed by less lethal conditions. We observe that the estimated at-risk population series does move higher with time, from an average of 232, in the first years, to around 263 in the final

Table VI. Parameter estimates for Álvaro Obregón state-space models (standard errors in parentheses). Non-accidental mortality counts.

Parameter	Model 1	Model 2	Model 3	Model 4	Model 5
γ_0	0.0014023* (0.000359)	0.0071729 (0.005121)	0.0071047** (0.002813)	0.0022783* (0.016433)	0.0071041* (0.001885)
PM_{10}	0.0000019** (0.0000008)	0.0000163*** (0.000009)	0.0000093* (0.000003)		0.0000188* (0.000006)
Avtem		–0.0001000** (0.000042)	–0.0002715** (0.000134)	–0.0000928* (0.000032)	–0.0002405* (0.000039)
Avtem^2			0.0000066 (0.000004)	0.0000025** (0.000001)	0.0000077* (0.000001)
PM_{10} *Avtem					0.0000005* (0.0000002)
σ_e	3.4531* (0.0624)	0.0315* (0.0009)	0.1124* (0.0026)	2.1569* (0.0047)	0.1089* (0.0634)
σ_η	9.1451* (0.2511)	9.2280* (0.2687)	9.15710* (0.2483)	9.1676* (0.2369)	9.1528* (0.2361)
AVERISPO	6275	1501	1913	6371	1858
MLE (days)	625-714	128-185	166-227	55-714	158-217
DAVERISPD	0.14%	0.59%	0.47%	0.14%	0.48%
ln(L)	–7429.322	–7423.335	–7422.738	–7425.923	–7419.444

Model selection test: likelihood ratio test
Model 5 vs. Model 4:12.95* Model 5 vs. Model 1: 19.75* Model 5 vs. Model 3: 6.58***

Avtem: average temperature; AVERISPO: average at risk-population; MLE: mean life expectancy; DAVERISPD: daily average at-risk population deaths.
Significant at *1, **5 and ***10%.

years for non-accidental deaths, while it moves from an average of 60 to around 70 in the same period for cardiovascular-respiratory deaths. There is a corresponding and offsetting decline in the hazard rate, moving downwards from an average of about 0.040 to 0.039 for non-accidental deaths, while it moves downwards from 0.041 to 0.040 for cardio-vascular-respiratory deaths in the same period. This decline in hazard rates is driven by a reduction of PM_{10} emissions of about 47.16 to 43.90 μg m^{-3} during the early and later years, respectively.

The hazard rates observed during the period considered in the sample go from 0.037 to 0.046, for non-accidental deaths, and from 0.039 to 0.051 for cardiovascular-respiratory deaths. Therefore, we have a life expectancy ranging from 21 to 27 days for non-accidental deaths, while life expectancy ranges from 19 to 25 day, for cardiovascular-respiratory deaths.

We observed that having a small at-risk population in Iztapalapa and Naucalpan de Juárez led to a clear mortality displacement, as the number of deaths fell below the average seasonal pattern after a high-risk event and did not return to the normal level until November. We also observed that the at-risk population was exhausted at the end of winter (the end of the risk period) and was mostly replenished by the middle of autumn (the end of the safest period).

Table VII. Parameter estimates for Álvaro Obregón state-space models (standard errors in parentheses). Cardiovascular-respiratory mortality counts.

Parameter	Model 1	Model 2	Model 3	Model 4	Model 5
γ_0	0.0022922* (0.000502)	0.0019600* (0.000621)	0.0066468* (0.002375)	0.0124210* (0.003084)	0.0087584* (0.003251)
PM_{10}	0.0000065* (0.000001)	0.0000061** (0.000002)	0.0000123* (0.000004)		0.0000105 (0.000022)
Avtem		–0.0000413* (0.000013)	–0.0003802** (0.000174)	–0.0007212* (0.000238)	–0.0004931** (0.001294)
$Avtem^2$			0.0000093*** (0.000005)	0.0000200* (0.000007)	0.0000116 (0.000046)
PM_{10} *Avtem					0.0000039*** (0.000001)
σ_e	0.1590* (0.0040)	0.1258* (0.0029)	0.0293* (0.0004)	0.0260* (0.0003)	0.0183* (0.00007)
σ_η	2.5630* (0.0678)	2.5735* (0.0643)	2.5627* (0.0702)	2.5521* (0.0671)	2.5604* (0.0687)
AVERISPO	1007	1681	739	419	565
MLE (days)	333-434	476-833	193-334	112-164	149-263
DAVERISPD	0.19%	0.11%	0.27%	0.47%	0.35%
ln(L)	–5563.340	–5554.896	–5553.908	–5558.009	–5552.023

Model selection test: Likelihood ratio test
Model 5 vs. Model 11.9** Model 5 vs. Model 1: 22.63* Model 5 vs. Model 3: 3.77***

Avtem: average temperature; AVERISPO: average at risk-population; MLE: mean life expectancy; DAVERISPD: daily average at-risk population deaths.
Significant at *1, **5 and ***10%.

Finally, in a way that is similar to the case of Iztapalapa and Naucalpan de Juárez, based on the likelihood ratio test results, Model 5 was regarded as a reasonable baseline specification in both non-accidental and cardiovascular-respiratory deaths for Álvaro Obregón.

As in the case of the previous two municipalities, we explored how PM_{10} and temperatures affect Álvaro Obregón's hazard rate. Our results show that at the average level of PM_{10} observed in the sample, the effect of an increase in temperature from the minimum (5.80 ºC) to the maximum (23.94 ºC) value corresponds to an increase in the hazard rate from 0.0068 to 0.0069 for non-accidental deaths, while for cardiovascular-respiratory deaths the increase is from 0.0075 to 0.0076. On the other hand, at the maximum temperature level of 23.94 ºC, the effect of an increase of PM_{10} from the minimum (6.88 µg m^{-3}) to the maximum (115.32 µg m^{-3}) observed value in the sample consists in raising the hazard rate from 0.0059 to 0.0093 for non-accidental deaths, while for cardiovascular-respiratory deaths the increase is from 0.0043 to 0.0155.

Figures 6 and 7 plot the Kalman filter estimates of the at-risk populations along with the estimated hazards rates in Model 5. We observe a lower hazard rate with high variability, as compared with that of Iztapalapa, which is higher with low variability.

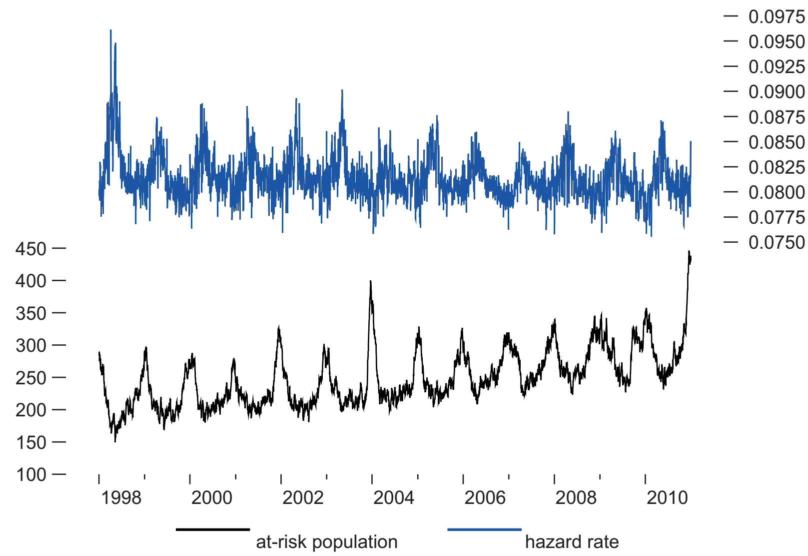

Fig. 2. Iztapalapa's estimated at-risk population and hazard rate from Model 3. Non-accidental mortality counts.

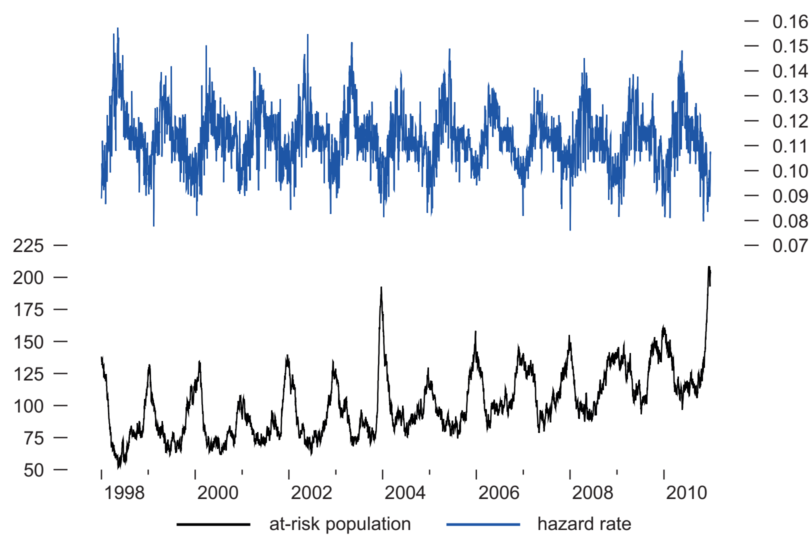

Fig. 3. Iztapalapa's estimated at-risk population and hazard rate from Model 3. Cardiovascular-respiratory mortality counts.

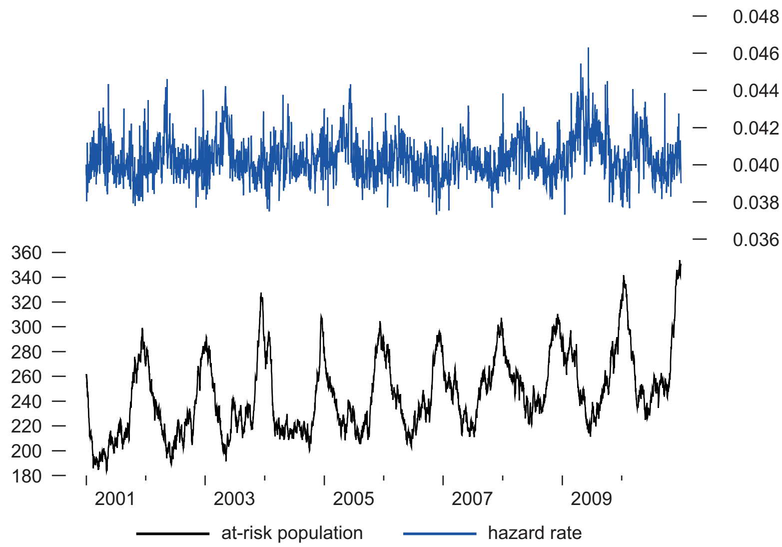

Fig. 4. Naucalpan de Juárez' estimated at-risk population and hazard rate from Model 5. Non-accidental mortality counts.

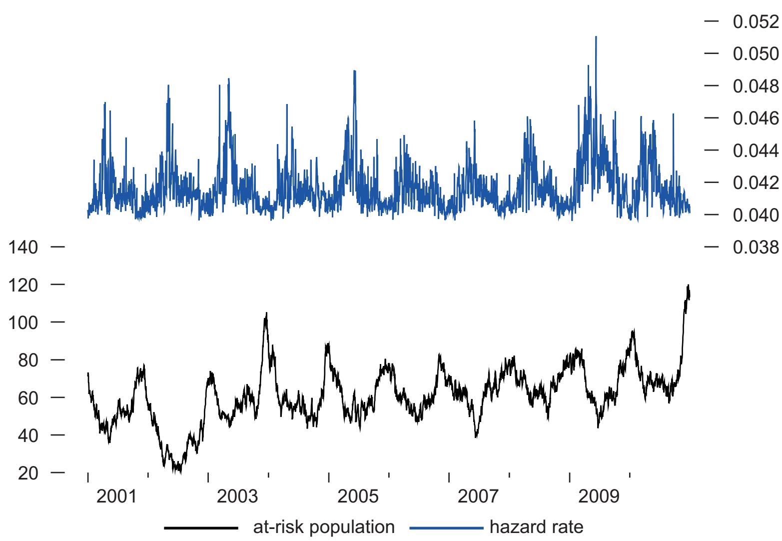

Fig. 5. Naucalpan de Juárez' estimated at risk population and hazard rate from Model 3. Cardiovascular-respiratory mortality counts.

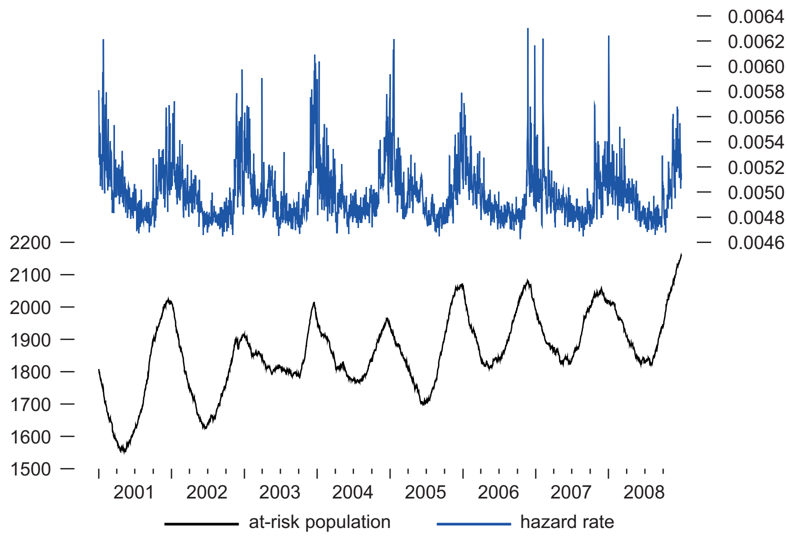

Fig. 6. Álvaro Obregón's estimated at risk population and hazard rate from Model 5. Non-accidental mortality counts.

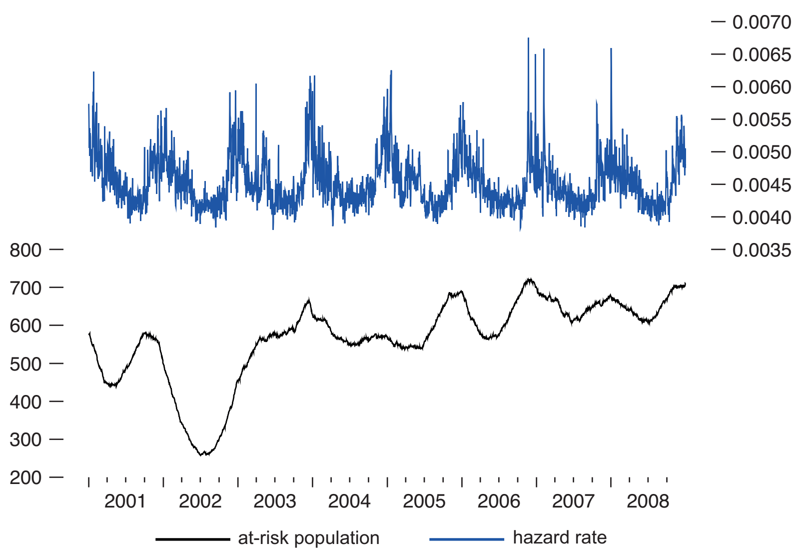

Fig. 7. Álvaro Obregón's estimated at risk population and hazard rate from Model 5. Cardiovascular-respiratory mortality counts.

A lower percentage of hazard lengthens life expectancy and allows individuals to remain longer in the at-risk population, thus making that population greater than the one in Iztapalapa and Naucalpan de Juárez. The estimated at-risk population average for non-accidental deceases is 1850, while the one for cardiovascular-respiratory deaths is 565 and varies seasonally; since average mortality is, respectively, 9.28 and 2.56 per day, this implies that, on average per day, about 0.48 and 0.35% of the at-risk population constitutes a case of either non-accidental or cardiovascular-respiratory death, respectively. The hazard rates fluctuate seasonally, according to the periods of high temperature. As in the other two cases, we noticed that the estimated at-risk population series does move higher with time, from an average of 1788 in the early years to around 1933 in the later years, for non-accidental deaths, and from an average of 473 to around 644 during the same period for cardiovascular-respiratory deaths. There is a corresponding and offsetting decline in the hazard rate, which moves downwards from an average of about 0.0050 in the early years to 0.0049 in the later years for non-accidental deaths, and from 0.0045 in the early years to 0.0044 in the later years for cardiovascular-respiratory deaths. This decline in the hazard rates is driven by a reduction of PM_{10} emissions of about 35.93 μg m^{-3} to 35.68 μg m^{-3} during the early and later years, respectively.

The hazard rates noticed over the sample period go from 0.0046 to 0.0063, in the case of non-accidental deaths, and from 0.0038 to 0.0067 in the case of cardiovascular-respiratory deaths. Therefore, life expectancy ranges from 158 to 217 days in the case of non-accidental deaths, and from 149 to 263 days in the case of cardiovascular-respiratory deaths.

The seasonal pattern in the at-risk population with a low hazard rate is interesting. We observed that, for a large at-risk population, the number of fatalities remained slightly below average for about two years. This longer-term impact on deaths is reflected in the mean life expectancy per high-risk event of 13 and 27 days for the small at-risk population of Iztapalapa and Naucalpan de Juárez, respectively, while the large at-risk population of Álvaro Obregón showed a mean life expectancy of 217 days.

5. Conclusions

The results of the analysis suggest that the main determinants of environmental health risk should be taken into consideration when assessing risk and vulnerability in urban populations. Our findings suggest that health risks related to air pollution are socioeconomically differentiated across the municipalities. Our estimates show evidence that various aspects of social inequality contribute to the greater burden of environmental hazard exposure and health risk for a municipality with low socioeconomic status. Social inequality, such as residential segregation, may affect the options of communities to address environmental and health problems. For example, poverty may affect the likelihood of having health insurance. Low education reduces knowledge and life skills that allow people to gain more ready access to information and resources to promote health (Link and Phelan, 1995). High population density may influence transportation demand, as expressed through average daily vehicle-kilometers traveled in private motor vehicles per capita; in turn, changes in transportation demand influence total vehicle emissions (vehicles for the transportation of passengers) to which population is exposed.

These socioeconomic disparities between municipalities partially explain why we observed a lower hazard rate in Álvaro Obregón, a wealthy area, as compared to the higher hazard rate observed in Iztapalapa, a poor area. In Álvaro Obregón—an area that showed a lower hazard rate—a higher life expectancy was observed, which allowsindividuals to stay longer in the at-risk population, thereby making that population larger than the at-risk population of Iztapalapa, whose inhabitants have a lower life expectancy. This is because the state-space model proposed applied the assumption that all fatalities must first be susceptible, so the smaller the at-risk population, the greater the individual probability of death. Therefore, the smaller the size of the population at risk, the sicker its average member will be, and hence the smaller the impact over long-term mortality. These findings are consistent with what would be normally predicted in texts about environmental justice.

As we already know, a proportion of these deaths occurs in susceptible people who would probably have died in the immediate future; however, a substantial number of them could have been prevented.

Implementation of health policies should blunt some of the adverse impacts of air pollution on the pool of very frail people. We strongly believe that such health policies need to be addressed from the perspective of environmental justice.

Acknowledgments

A. Islas-Camargo thanks the financial support provided by Asociación Mexicana de Cultura to carry out this work and acknowledges support from the Consejo Nacional de Ciencia y Tecnología (CONACYT) of Mexico through a sabbatical scholarship. This work was done whilst A. Islas Camargo was visiting the Department of Economics, Nepal Study Center, and the RWJF Center for Health Policy at the University of New Mexico, USA.

References

Barraza-Lloréns M, Panopoulou G, Díaz BY. 2013. Income-related inequalities and inequities in health and health care utilization in Mexico, 2000-2006. Revista Panamericana de Salud Pública 33: 122–130. https://doi.org/10.1590/s1020-49892013000200007

Belen R, Stafoggia M, Rasschou-Nielsen O, Andersen ZJ, Xun WW, Katsouyanni K, et al. 2014. Long-term exposure to air pollution and cardiovascular mortality: An analysis of 22 European cohorts. Epidemiology 25: 368-378. https://doi.org/10.1097/EDE.0000000000000076

Brulle RJ, Pellow DN 2005. Environmental justice: Human health environmental inequalities. Annual Review of Public Health 27: 103-124. https://doi.org/10.1146/annurev.publhealth.27.021405.102124

Chen F, Fan Z, Qiao Z, Cui Y, Zhang M, Zhao X, Li X. 2017. Does temperature modify the effect of PM_{10} on mortality? A systematic review and meta-analysis. Environmental Pollution 224: 326-335. https://doi.org/10.1016/j.envpol.2017.02.012

CONEVAL. 2014. Pobreza urbana y de las zonas metropolitanas de México. Consejo Nacional de Evaluacion de la Politica de Desarrollo Social. Available at: http://www.coneval.org.mx/Informes/Pobreza/Pobreza%20urbana/Pobreza_urbana_y_de_las_zonas_metropolitanas_en_Mexico.pdf (accessed on May 11, 2017).

Davis LW. 2008. The effect of driving restrictions on air quality in Mexico City. Journal of Political Economy 116: 38-81. https://doi.org/10.1086/529398

Dockery DW, Pope CA. 1994. Acute respiratory effects of particulate air pollution. Annual Review of Public Health 15: 107-132. https://doi.org/10.1146/annurev.pu.15.050194.000543

Garrocho C, Campos J. 2016. Segregación socioespacial de la población mayor en la Ciudad de México, 2000-2010. En: La situación demográfica de México 2105. Consejo Nacional de Población, México, 167-195.

Guidi J, Lucente M, Sonino N, Fava GA. 2021. Allostatic load and its impact on health: A systematic review. Psychotherapy and Psychosomatics 90: 11-27. https://doi.org/10.1159/000510696

González GG. 2020. Áreas verdes, segregación urbana y calidad de vida en la Ciudad de México: un estudio desde el hábitat urbano. Master thesis. Facultad Latinoamericana de Ciencias Sociales, Mexico.

Hill TD, Jorgenson AD, Ore P, Balistreri KS, Clark B. 2019. Air quality and life expectancy in the United States: An analysis of the moderating effect of income inequality. SSM-Population Health 7: 100346. https://doi.org/10.1016/j.ssmph.2018.100346

INEGI. 2017. Encuesta origen destino en hogares de la Zona Metropolitana del Valle de México 2017. Instituto Nacional de Estadística y Geografía, Mexico. Available at: http://www.beta.inegi.org.mx/proyectos/enchogares/especiales/eod/2017/ (accessed on June 2018).

Jorgenson AD, Thombs RP, Clark B, Givens JF, Hill TD, Huang X, Kelly OM, Fitzgerald JB. 2021. Inequality amplifies the negative association between life expectancy and air pollution: A cross-national longitudinal study. Science of the Total Environment 758: 143705. https://doi.org/10.1016/j.scitotenv.2020.143705

Kan H, Jia J, Chen B. 2003. Temperature and daily mortality in Shanghai: A time-series study. Biomedical and Environmental Sciences 16: 133-139.

Link BG, Phelan JC. 1995. Social conditions as fundamental causes of disease. Journal of Health and Social Behavior. 35: 80-94. https://doi.org/10.13016/rpln-eiwa

Lipfert FW, Murray CJ. 2012. Air pollution and daily mortality: A new approach to an old problem. Atmospheric Environment 55: 467-474. https://doi.org/10.1016/j.atmosenv.2012.03.013

Menton M, Larrea C, Latorre S, MartínezAlier J, Peck M, Temper L, Walter M. 2020. Environmental justice and the SDGs: From synergies to gaps and contradictions. Sustainability Science 15: 1621-1636. https://doi.org/10.1007/s11625-020-00789-8

Molina LT, Molina MJ. 2004. Improving air quality in megacities: Mexico City case study. Annals of the New York Academy of Sciences **1023**: 142-158. https://doi.org/10.1196/annals.1319.006

Monkkonen P. 2012. La segregación residencial en el México urbano: niveles y patrones. EURE (Santiago) 38: 125-146. https://doi.org/10.4067/S0250-71612012000200005

Morello-Frosch R, Pastor M, Porras C, Sadd J. 2002. Environmental justice and regional inequality in southern California: Implications for future research. Environmental Health Perspectives 110 (Suppl 2): 149-154. https://doi.org/10.1289/ehp.02110s2149

Moser C, Satterthwaite D. 2010. Toward pro-adaptation to climate change in the urban centers of low and middle-income countries. In: Social dimensions of climate change: Equity and vulnerability in a warming world (Mobin R, Norton A, Eds.). International Bank for Reconstruction and Development, Washington DC, 231-258.

Murray CJ, Nelson CR. 2000. State-space modeling of the relationship between air quality and mortality. Journal of the Air & Waste Management Association 50: 1075-1080. https://doi.org/10.1080/10473289.2000.10464158

Peng D, Dominici F. 2008. Statistical methods for environmental epidemiology with R. A case study in air pollution and health. Springer, New York, 151 pp.

Pope CA, Dockery DW, Schwartz J. 1995. Review of epidemiology evidence of health effects of particulate air pollution. Inhalation Toxicology 7: 1-18. https://doi.org/10.3109/08958379509014267

Pulido L, Sidawi S, Vos R. 1996. An archeology of environmental racism in Los Angeles. Urban Geography 17: 419-439. https://doi.org/10.2747/0272-3638.17.5.419

Ramírez GS, Mendoza MG, Servín CC. 2015. Justicia ambiental. Entre la utopía y la realidad social. Culturales 3: 225-250.

Reardon S, Bischoff K. 2011. Income inequality and income segregation. American Journal of Sociology 116: 1092-1153. https://doi.org/10.1086/657114

Rodopoulou S, Chalbot MC, Samoli E, Dubois D, Fillipo BD, Kavouras IG. 2014. Air pollution and hospital emergency room and admissions for cardiovascular and respiratory diseases in Doña Ana County, New Mexico. Environmental Research 129: 39-46. https://doi.org/10.1016/j.envres.2013.12.006

Romero LP, Qin H, Borbor CM. 2013. Exploration of health risks related to air pollution and temperature in three Latin American cities. Social Science & Medicine 83: 110-118. https://doi.org/10.1016/j.socscimed.2013.01.009

Rubalcava RM, Schteingart M. 2012. Ciudades divididas. Desigualdad y segregación social en México. El Colegio de México, 214 pp.

Samet JM, Dominici F, Zeger S L, Schwatz D, Dockery DW. 2000a. The National Morbidity, Mortality, and Air Pollution Study. Part I: Methods and methodologic issues. Health Effects Institute, Cambridge MA, 5-14.

Samet JM, Zeger SL, Dominici F, Curriero F, Coursac I, Dockery DW, Schwartz J, Zanobetti A. 2000b. The National Morbidity, Mortality, and Air Pollution Study. Part II: Morbidity and mortality from air pollution in the United States. Health Effects Institute, Cambridge MA, 5-70.

Sánchez PL. 2012a. ¿Viviendo cada vez más separados? Un análisis multigrupo de la segregación residencial en la Ciudad de México, 1990-2005. Estudios Demográficos y Urbanos 27: 57-93. https://doi.org/10.24201/edu.v27i1.1405

Sánchez PL. 2012b. Cambios en la segregación residencial socioeconómica en México. Realidad, datos y espacio. Revista Internacional de Estadística y Geografía 3: 98-115.

Schlesinger RB. 2007. The health impact of common inorganic components of fine particulate matter ($PM_{2.5}$) in ambient air: A critical review. Inhalation Toxicology 19: 811-832. https://doi.org/10.1080/08958370701402382

Schlosberg D. 2013. Theorizing environmental justice: expanding sphere of a discourse. Environmental Politics 22: 37-55. https://doi.org/10.1080/09644016.2013.755387

US-EPA 1996. Review of the National Ambient Air Quality Standards for Particulate Matter: Policy assessment of scientific and technical information. Publication No. EPA-452\R-96-013. Office of Air Quality Planning and Standards, US Environmental Protection Agency, Research Triangle Park, NC.

US-EPA. 2018. Environmental justice. US Environmental Protection Agency. Available at: https://www.epa.gov/environmentaljustice (accessed on August 24, 2018).

Wakefield S, Baxter J. 2010. Linking health inequality environmental justice: Articulating a precautionary framework for research and action. Environmental Justice 3: 95-102. https://doi.org/10.1089/env.2009.0044

WHO. 2006. Air Quality Guidelines for particulate matter, ozone, nitrogen dioxide and sulfur dioxide. Global update 2005. Summary of risk assessment. World Health Organization. Available at: http://www.euro.who.int/__data/assets/pdf_file/0005/78638/E90038.pdf?ua=1 (accessed on May 11, 2017).

WHO. 2013. Review of evidence on health aspects of air pollution—REVIHAAP Project. Technical Report. World Health Organization, Regional Office for Europe, Copenhagen, Denmark.

WHO. 2017. Seven million premature deaths annually linked to air pollution. World Health Organization. Available at: http://www.who.int/mediacentre/news/releases/2014/air-pollution/en/ (accessed on May 11, 2017).

Wu S, Ni Y, Li H, Pan L, Yang D, Bacarrelli AA, Deng F, Chen Y, Shima M, Guo X. 2106. Short-term exposure to high ambient air pollution increases airway inflammation and respiratory symptoms in chronic obstructive pulmonary disease patients in Beijing, China. Environment International 94: 76-823. https://doi.org/10.1016/j.envint.2016.05.004

Zhang Y, He M, Wu S, Zhu Y, Wang S, Shima M, Tamura K, Ma L. 2015. Short-term effects of fine particulate matter and temperature on lung function among healthy college students in Wuhan, China. International Journal of Environmental Research and Public Health 12: 7777-7793. https://doi.org/10.3390/ijerph120707777

Atmósfera 35(4), 781-802 (2022)
https://doi.org/10.20937/ATM.52987

CONTENTS

Characterization of particulate matter in the iron ore mining region of Itabira, Minas Gerais, Brazil

Ana Carolina VASQUES FREITAS[1]*, Rose-Marie BELARDI[1] and Henrique de Melo JORGE BARBOSA[2]

[1] *Federal University of Itajubá (UNIFEI), Rua Irmã Ivone Drumond nº 200, Bairro Distrito Industrial II, Itabira, MG, Brazil, 35903-087.*
[2] *University of São Paulo (USP), Physics Institute, Rua do Matão nº 1371, Cidade Universitária, São Paulo, SP, Brazil, 05508-090.*
*Corresponding author; email: ana.freitas@unifei.edu.br

Received: October 4, 2020; accepted: March 24, 2021

RESUMEN

En el territorio de Itabira se encuentra el mayor complejo de minería a cielo abierto del mundo, ubicado cerca de las zonas residenciales de la ciudad. La red de monitoreo de la calidad del aire instalada en la ciudad es la principal fuente de datos de emisión de material particulado (PM, por sus siglas en inglés). Sin embargo, estas estaciones de calidad del aire sólo cubren las áreas cercanas a las minas y no miden el material particulado fino ($PM_{2.5}$). Así, se llevó a cabo una primera campaña de campo para caracterizar el material particulado en la ciudad y comparar los datos de alto volumen de las estaciones de calidad del aire con los datos del muestreador de aire dicotómico. Los resultados del análisis de conglomerados de trayectorias mostraron un transporte de aerosoles de largo alcance durante los días de muestreo desde las direcciones noreste (84% de las trayectorias), este-sureste (12%) y sur-suroeste (3%). En cuanto a las condiciones meteorológicas durante los días de muestreo, se observaron correlaciones negativas entre el material particulado grueso (PM_{10}) de la mayoría de las estaciones de calidad del aire y todos los parámetros meteorológicos (excepto la temperatura). Los resultados de los análisis de fluorescencia de rayos X y componentes principales mostraron que los principales oligoelementos en los modos grueso ($PM_{2.5\text{-}10}$) y fino ($PM_{2.5}$) son hierro y azufre, asociados con emisiones de actividades mineras, transporte masivo de aire de las actividades regionales de la industria siderúrgica, emisiones de vehículos, quema de biomasa local y regional, y emisiones biogénicas naturales. Este trabajo es la primera evaluación de la distribución de fuentes realizada en la ciudad. Las comparaciones con otros estudios, para algunas grandes áreas metropolitanas, mostraron que Itabira tiene contribuciones comparables de azufre, hierro y otros elementos como cobre, selenio, cromo, níquel, vanadio y plomo.

ABSTRACT

Itabira has in its territory the largest complex of opencast mining in the world, located close to residential areas of the city. The air quality monitoring network installed in the city is the main source of particulate matter (PM) emission data. However, these air quality stations only cover the areas near the mines and do not measure fine particulate matter ($PM_{2.5}$). Thus, a first field campaign was carried out to characterize PM in the city and to compare high volume data from air quality stations with the dichotomous air sampler data. Results of trajectories' cluster analysis showed a long-range transport of aerosols during the sampling days from northeast (84% of the trajectories), east-southeast (12%), and south-southwest (3%) directions. Regarding the meteorological conditions during the sampling days, negative correlations were seen between coarse particulate matter (PM_{10}) from mostly air quality stations and all meteorological parameters (but temperature). Results of the X-ray fluorescence and principal component analyses showed that the main trace elements in the coarse ($PM_{2.5\text{-}10}$) and fine modes ($PM_{2.5}$) are iron and sulfur, associated with emissions from mining activities, air mass transport from regional iron and steelmaking industry activities, vehicle emissions, local and regional biomass burning, and natural biogenic emissions. This work is the first assessment of source apportionment done in the city. Comparisons with other studies, for some large metropolitan areas, showed that Itabira has comparable contributions of sulfur, iron and elements such as copper, selenium, chromium, nickel, vanadium and lead.

Keywords: black carbon, trace elements, mining city, air mass trajectories, meteorological conditions.

1. Introduction

Mining operations, whether small or large, are inherently disruptive to the environment (Makweba and Ndonde, 1996). Opencast mining creates much more air quality deterioration regarding dust and gaseous pollutants in and around the mining complexes than underground mining (Ghose and Majee, 2001). Major sources of atmospheric emissions from opencast mining activity include land clearing, removal of overburden, vehicular movement on the haul roads, excavation, and loading and unloading of ore materials (Singh and Perwez, 2015).

The extraction of iron ore through open pit mining is the main economic activity of Itabira, a countryside city in the Minas Gerais state, Brazil. Founded in Itabira in 1942, the company Vale is currently the world's largest producer of iron ore. Its annual production record was of 348.8 million tons in 2016 (Figueiredo et al., 2016).

Reserves in the Itabira district are classified as "reasonably assured ore," or ore that, except in localities where underground exploration made necessary greater extrapolation in depth, lies within 50 m of the surface, and as "inferred ore," or ore that lies within 250 m of the other ore (Dorr and Barbosa, 1963). For that reason, Vale has installed the largest complex of opencast mining in the world in Itabira, with an annual production of roughly 46 million tons of iron ore (about 15% of the total ore produced by Vale) (Tubino et al., 2011). The complex, unfortunately, is located close to residential areas of the city. The large emission of particulate matter (PM) into the atmosphere, inherent to mining activity, has generated significant levels of pollution, mainly affecting the communities that live around the mining areas (Braga et al., 2007; Devlin and Tubino, 2012; Wasylycia-Leis et al., 2014; Alves and Freitas, 2021).

Pollutants released from ground level and elevated sources (smokestacks) are immediately subject to atmospheric processes, with dispersion in ever-increasing volumes of air by both vertical and horizontal transport. The atmospheric dynamics and turbulence, and physical laws that govern them, may facilitate or constrain transport and dispersal (Godish, 2003).

Thus, the emission of atmospheric pollutants by fixed and mobile sources, local and remote, natural and anthropogenic, added to the orographic characteristics and the typical meteorological conditions of each region, form a set of factors that influence the concentration and dispersion of those pollutants (Pérez et al., 2020).

An air quality monitoring network was installed in Itabira and is managed by Vale, due to the normative deliberation of the Municipal Environmental Council, which imposed that the company would have to display and operate this network. Also, the results of the air quality monitoring have to be presented at monthly meetings in the Council.

This air quality monitoring network is the only source of PM emission data in Itabira; however, this data is not available in real time to the public. Besides, it only covers areas near the mines and does not measure fine particulate matter ($PM_{2.5}$), defined as those particles less than 2.5 µm in aerodynamic diameter, that are the most harmful to health, compared to the coarser particles (Braga et al., 2007). Thus, a first field campaign was carried out in the city in the spring of 2016, where PM was collected on filters allowing analysis of mass concentration, black carbon content, and elemental composition.

Here we use this data to characterize the composition of PM, reveal other potential sources besides mining activities, and produce a validation against data obtained from the air quality monitoring network managed by Vale.

Principal component analysis (PCA) is used to infer the source apportionment. As long-range sources also have an impact on urban air quality, cluster analysis is also employed to identify the main air mass transport pathways based on 48 h back-trajectories calculated with the NOAA Hybrid Single-Particle Lagrangian Integrated Trajectory (HYSPLIT) model

(Draxler et al., 2012). Sampling and analysis methods are detailed in section 2. Results are discussed in section 3, and our final conclusions are presented in section 4.

2. Materials and methods

2.1 Study area

Itabira has an estimated population of 120 904 inhabitants occupying an area of 1 253 704 km² (IBGE, 2020). It is located at 19º 37'08" S and 43º 13' 37" W, about 100 km northeast of Belo Horizonte, the capital of the Minas Gerais state, Brazil (Fig.1). The Itabira iron district is located in the northeastern corner of the iron quadrangle of Minas Gerais. The district is the world's leading center of iron-ore production (Dorr and Barbosa, 1963; Dixon, 1979). The geologic structure of the Itabira mining complex consists of a 14-km long, NE-trending range with three main synclines at both extremes (Conceição and Cauê) and middle (Minas do Meio) sections (MDO, 2020; see Fig. 2a for location).

Itabira is also only about 100 km away from the headquarters of one of the largest flat steel complexes in Latin America and the leader of the Brazilian flat steel market, producing 9.5 million tons of steel per year (Usiminas, 2020).

The regional topography is rugged (20%) and mountainous (70%) (Sobreiro et al., 2001). The altitude of the municipality is between 530 and 1638 m (Fig. 2a). The annual rainfall is about 1471 mm yr^{-1}, with the wet period in November to February and the dry period in June to August, and the annual average temperature is 20.4 ºC (Sobreiro et al., 2001).

Two hydrographic basins are enclosed in the region, the Rio do Peixe basin to the south and the Rio Tanque basin to the north, both belonging to the Rio Doce basin. The watersheds divide is formed by the Serra do Itabiruçu, which extends from southwest to northeast, representing the more outstanding topographical feature, sustained by the alignment of the iron formation, with original maximum heights close to 1400 m (Sobreiro et al., 2001).

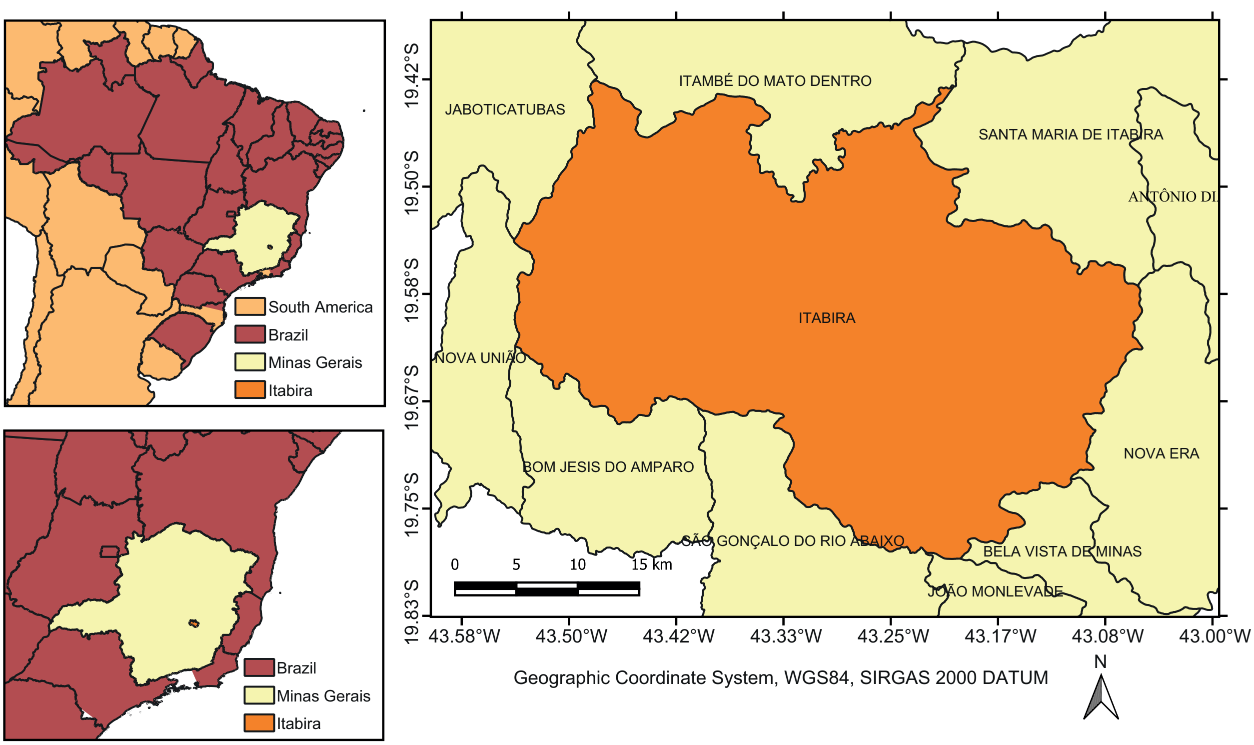

Fig. 1. Location of Itabira, Minas Gerais, Brazil. Data sources (right panel): Tapiquén (2015), IBGE (2018).

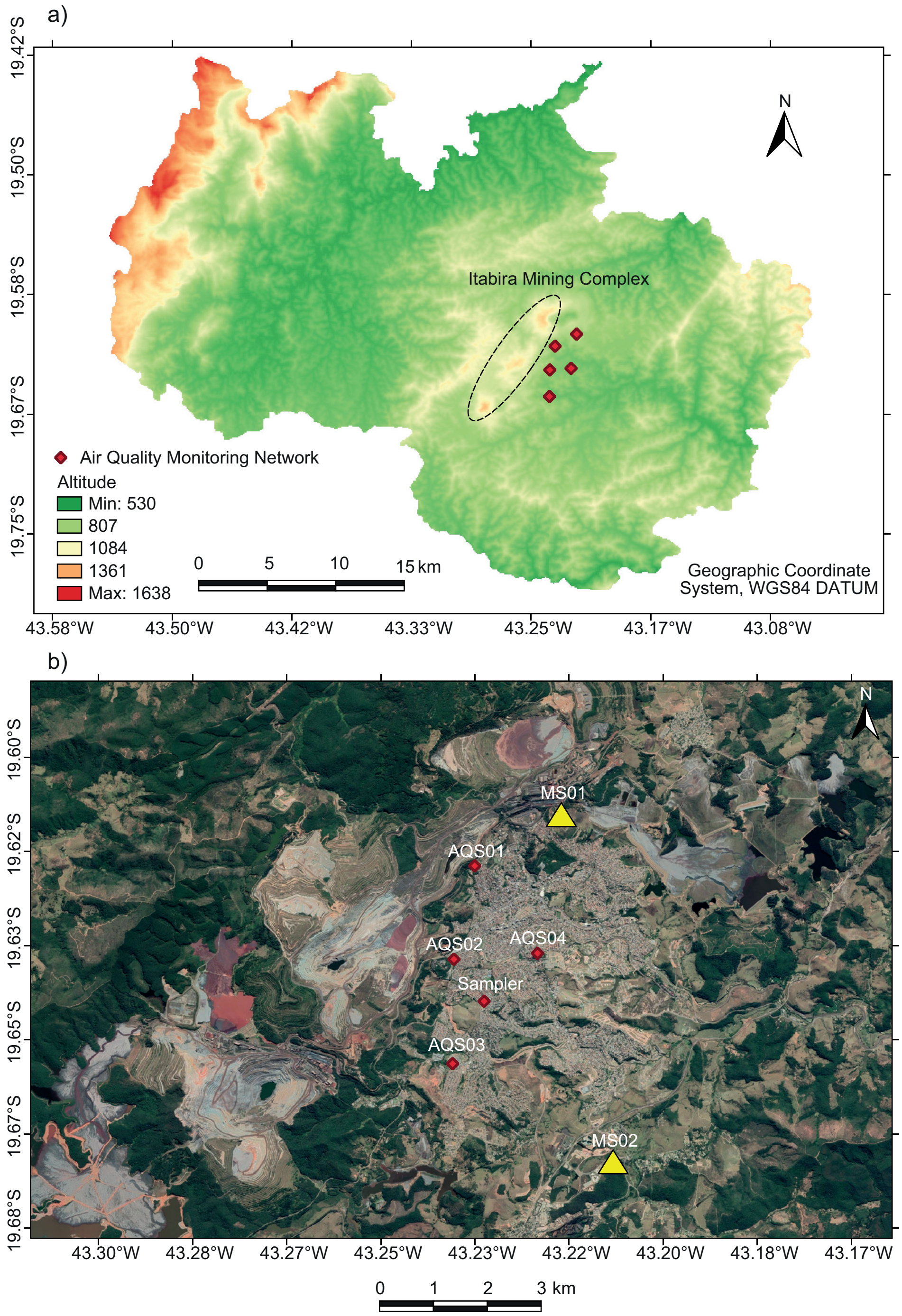

Fig. 2. (a) Topography (altitude in meters) of Itabira municipality and locations of mining complex and air quality monitoring network in the city (AQ01-AQS04 and MS01). (b) Detailed location of the sampler, the four AQS (AQS01-AQS04) and the two meteorological stations (MS01 and MS02) in urban area. Data sources: (a) Miranda (2005); (b) Google Earth.

2.2 Air quality monitoring network

The city of Itabira has a network of automatic air quality stations (AQS) operated by Vale, composed of four stations (identified here as AQS01, AQS02, AQS03 and AQS04; see Fig. 2a, b for location) providing a continuous monitoring, with hourly means of total suspend particles (TSP) and coarse particulate matter (PM_{10}, defined as particles lesser than 10 µm in aerodynamic diameter) during 24 h a day. TSP are very coarse particles (30 µm and above) that settle very close to the point of emission.

The monitoring network uses Rupprecht & Patashnick Tapered Element Oscillating Microbalance (TEOM) Series 1400a samplers. These real-time monitors were included in the list of U.S. Environmental Protection Agency (EPA) approved PM_{10} samplers in 1990 (US-EPA, 1990) and designated as Federal Equivalent Method (FEM) samplers according to Federal regulation 40 CFR Part 53 (US-EPA, 1999).

The Rupprecht & Patashnick Series 1400a monitor consists of three main components: a sample inlet; the TEOM sensor unit, containing the microbalance and filter chamber; and the control unit to monitor and record sampling flow rate data, filter mass measurements, and ambient temperature and barometric pressure measurements (Wanjura et al., 2008).

According to the operating manual (Thermo Scientific, 2004) of this monitor, the ambient sample stream first passes through the PM-10 inlet at a flow rate of 16.7 L min^{-1}, allowing particles smaller than 10 µm diameter to pass through. At the exit of the PM-10 inlet, the 16.7 L min^{-1} flow is isokinetically split into a 3 L min^{-1} sample stream that is sent to the instrument's mass transducer and a 13.7 L min^{-1} exhaust stream. Inside the mass transducer, this sample air stream passes through a filter made of Teflon-coated borosilicate glass fiber, which is weighed every 2 s. The difference between the filter's current weight and the filter's initial weight gives the total mass of the collected PM. These instantaneous readings of total mass are then smoothed exponentially to reduce noise. Next, the mass rate is calculated by taking the change in the smoothed total mass between the current reading and the immediately preceding one. This mass rate is also smoothed exponentially to reduce noise. Finally, the mass concentration is computed by dividing the mass rate by the flow rate (corrected to EPA standard temperature and pressure). It is worth to highlight that the internal temperatures in the instrument are controlled to minimize the effects of changing ambient conditions.

The Rupprecht & Patashnick Series 1400a monitor also measure TSP concentration using size-selective inlets (Wanjura et al., 2008). However, here we analyze only PM_{10} concentrations obtained from AQS instruments, because TSP cannot be directly related to health impacts (WHO, 2000; Patra et al., 2016).

Hourly and monthly data from the AQS and the meteorological station of the monitoring network (identified here as MS01; see Fig. 2b for location), which measures wind speed and direction, temperature, relative humidity, pressure, solar radiation and rainfall, have been used in the analyses during the sampling days. These data are provided by the Itabira Municipality Environment Secretary under request.

In addition, the hourly data of wind speed and direction from the meteorological station of the Federal University of Itajubá (identified here as MS02; see Fig. 2b for location) have been also used for comparison purposes in the analyses of wind and pollution roses, since the altitude of MS01 is 919 m, whereas for MS02 is 645 m. All wind measurements are performed at 10 m above ground level (agl). The altitudes of AQS01 to AQS04 are 769, 727, 643, and 808 m, respectively.

2.3 PM sampling and analysis

The field campaign was carried out in Itabira city continuously for 37 days, from October 8 to November 14, 2016. Inhalable PM ($PM_{2.5}$ and $PM_{2.5\text{-}10}$) were sampled using a dichotomous sampler (Andersen Instruments) with a standard averaged flow rate of 16.7 L min^{-1}, which corresponds to 1 m^3 h^{-1}. The air stream passes through two 47 mm diameter nucleopore polycarbonate filters and is separated into two different sizes fractions. Coarse particles (> 2.5 particle diameter [dp] < 10 µm) are collected in an 8.0 µm pore size filter while fine particles (dp < 2.5 µm) are collected in 0.4 µm pore size filters, as described by Castanho and Artaxo (2001).

Mass concentrations of fine and coarse polycarbonate filters were analyzed by gravimetry with a Mettler Toledo electronic microbalance (Model

XP6) with ±1 µg sensitivity in a controlled atmosphere room (20 ºC, 40% relative humidity, with fluctuations less than 10% of these set points). The filters were equilibrated in this room for 24 h before weighing and electrostatic charges were controlled using radioactive sources, as described by Castanho and Artaxo (2001). Each filter was weighted twice, prior to and after the sampling, and the average was calculated. The difference between pre- and post-weighting represents the mass of PM deposited during the sampling period. This result is corrected for any mass change observed in the blank filters, which are weighted and handled similarly. This procedure was performed for both fine and coarse filters, resulting in mass concentrations of the fine and coarse particulate matter ($PM_{2.5}$ and $PM_{2.5\text{-}10}$) during the sampling period.

It is worth to highlight that the Rupprecht & Patashnick Series 1400a monitors used in the monitoring network of Itabira correct the mass concentration to EPA standard temperature and pressure and this correction was not applied for the mass concentration obtained with the sampler.

During the campaign, the equipment inlets were located about 3 m agl. Filters were changed every two days or before if the flow rate reached less than 16.7 L min^{-1}. The location of the sampler was relatively close to the city center and of AQS02 and AQS04, at an elevation of 810 m (Fig. 2b).

The concentration of black carbon (BC) in the fine and coarse fractions was determined using a M43D Smokestain reflectometer (Difusion Systems). BC mass present in the samples was calculated from reflectance measurements, as described in Loureiro et al. (1994). X-ray fluorescence spectroscopy was performed with an Epsilon 5 equipment of PANalytical to determine the elemental composition and concentration of the atmospheric particulates contained in the filters. The measurement was repeated three times for each sample, in both fine and coarse modes, and the mean value was considered for each trace element. The energy dispersive X-ray equipment was calibrated using NIST standards, as described by Arana et al. (2014). The analyses of gravimetry, BC concentration and the X-ray fluorescence were performed in the Laboratory of Atmospheric Physics, Sao Paulo University Institute of Physics.

2.4 Air mass trajectories and long-range transport of pollutants

To verify if there is a contribution from sources outside the city, the HYSPLIT model (Draxler et al., 2012) was used to calculate air-mass trajectories arriving at the sampling site. Meteorological data obtained from the global data assimilation system (GDAS) at a 0.25 × 0.25º resolution grid was used, and back trajectories for each campaign's day were simulated for 48 h starting at 100 m agl.

Then, a cluster analysis was performed on the simulated trajectories to identify the preferential direction of the air masses. This method consists of grouping air masses trajectories with similar transport patterns (speed and direction) and representing their mean trajectory. The method minimizes the intra-cluster differences among trajectories while maximizing the inter-cluster differences (Su et al., 2015).

According to Draxler et al. (2012), at first each trajectory is defined to be a cluster (i.e., there are N trajectories and N clusters). For the first iteration, for every combination of trajectory pairs, the cluster spatial variance (*SPVAR*; Eq. 1) is calculated. *SPVAR* is the sum of the squared distances between the endpoints of the cluster's component trajectories and the mean of the trajectories in that cluster. Then, the total spatial variance (*TSV*; Eq. 2), i.e., the sum of all *SPVAR*, is calculated. The pair of clusters combined are the ones with the lowest increase in *TSV*. After the first iteration, the number of clusters is N-1.

$$SPVAR = \sum (\text{all trajectories in cluster}) \left[\sum (\text{all trajectory endpoints}) \{D*D\}\right] \tag{1}$$

$$TSV = \sum (\text{all } SPVAR) \tag{2}$$

where D is the distance between a trajectory endpoint and the corresponding cluster-mean endpoint.

The iterations continue until the last two clusters are combined, resulting in N trajectories in one cluster. In the first few clustering iterations, the *TSV* increases rapidly, then it increases slowly, generally at constant rate, for much of the clustering, but at some point, it again increases rapidly, indicating that the clusters being combined are not similar and, thus, this sudden change in *TSV* can be used as a tool to identify the optimum number of clusters (Yang et al., 2019).

3. Results and discussions

3.1 PM concentration and meteorological conditions

Figure 2b shows the location of the sampler relative to the four AQS. It is also possible to see the mining areas around the city. Figure 3a, b illustrates the prevailing wind direction and its velocity during the period of sampling for MS01 and MS02. For both meteorological stations it is possible to verify that winds blow primarily from the northeast towards the southwest with speeds varying mostly between 2.1 to 5.7 m s^{-1}. The wind speed in MS02 is greater

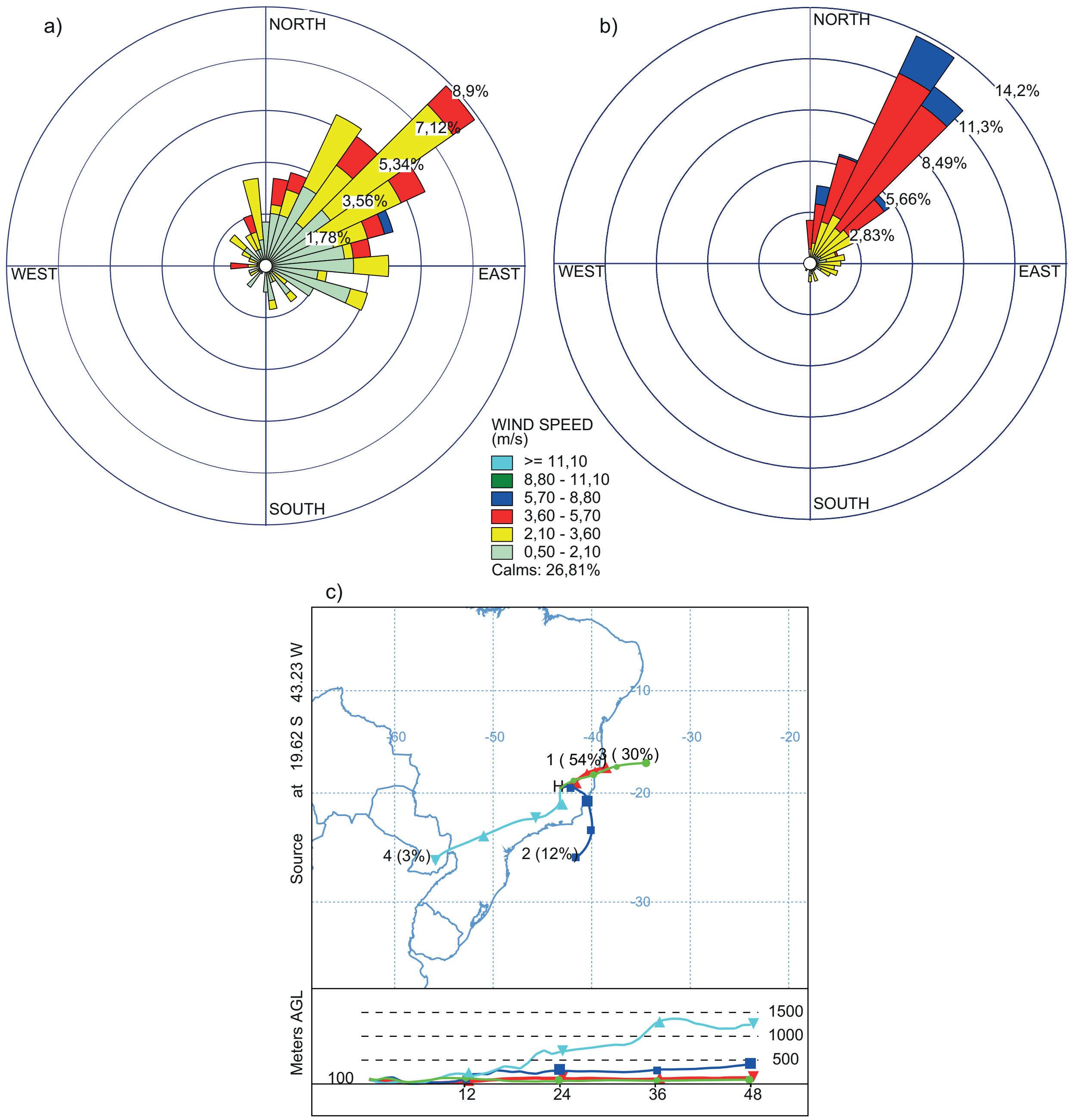

Fig. 3. Wind rose for (a) MS01 and (b) MS02. (c) NOAA HYSPLIT backward trajectory cluster analysis for the sampling days.

than MS01 due to the differences of altitude (Fig. 3a, b). As Itabira is a mining town, the urban area of the municipality was formed near the mining complex. It would be expected that downwind receptors are far more likely to be affected by air pollution. Thus, the sampler was located exactly in the typical downwind direction (Figs. 2 and 3).

As of this writing, the city of Itabira has two industrial districts, dedicated to non-metallic mineral transformation and food products, metallurgical, mechanical and wood industries, which are located in the south direction. Thus, most of the city lies upwind of the industrial zone, and hence is largely protected from local industrial emissions, but not from mining emissions to the NE, as we already mentioned.

Figure 3c shows there is also a long-range transport of aerosols from the northeast (84% of the trajectories), east-southeast (12%) and south-southwest (3%) directions. This cluster analysis was also performed using GDAS data with 1 × 1º resolution, as Su et al. (2015) found that different GDAS resolutions in areas with complicated topography could lead to differences between back trajectories due to differences in vertical motion calculation. However, the results here were similar, with east and northeast directions appearing as the main long-range transport routes of pollutants, agreeing with the prevailing wind direction (Fig. 3a , b). Thus, on east and northeast wind days, most of the city is exposed to cross-border pollution.

Figure 4a, b show the diurnal variations of PM_{10} for January 1, 2014 to November 30, 2018 and the annual variations from January 1, 2014 to September 30, 2020, respectively, for all AQS. This period was selected according to data availability. Regarding the diurnal variations (Fig. 4a), it is possible to verify an increase in PM_{10} concentrations during the nocturnal period due to less favorable conditions for particle dispersion caused by the inversion temperature and lower planetary boundary layer. Lower concentrations are seen from 09:30 to 15:30 LT when atmospheric dispersion is greater due to a more unstable atmosphere that promotes transport and mixing of air. The annual variations (Fig. 4b) are characterized by an increase in PM_{10} concentrations from a minimum in March to a peak in September. From November to March, when the precipitation is significative, PM_{10} concentrations are the lowest.

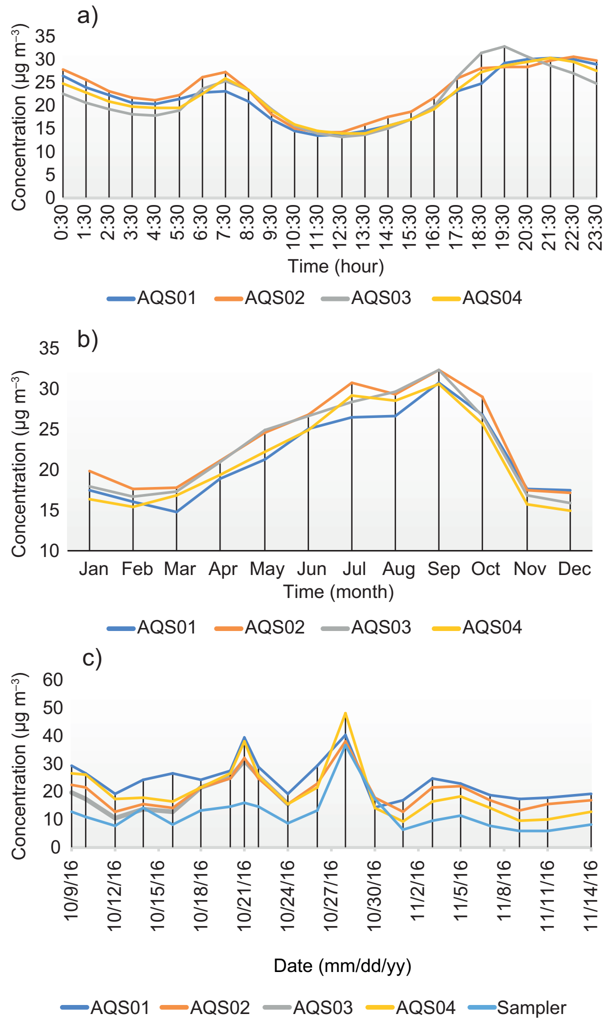

Fig. 4. (a) Diurnal and (b) annual variations of PM_{10} ($\mu g\ m^{-3}$) for the four AQS from January 1, 2014 to November 30, 2018 (diurnal) and form January 1, 2014 to September 30, 2020 (annual). (c) Sampler and automatic air quality stations concentrations ($\mu g\ m^{-3}$) of coarse particulate matter ($PM_{2.5\text{-}10}$ and PM_{10}, respectively) for the sampling days.

Figure 4c shows the concentration of PM_{10} obtained from all AQS and from the sampler ($PM_{2.5\text{-}10}$). The time scale of the plot corresponds to the filter change days. For this comparison, hourly data of the four AQS were averaged considering the days and the approximated hour of beginning and ending of filter change. From October 24, 2016 onwards, the AQS03 has been disabled. The correlation between the average concentration of the four AQS and the concentration of the sampler is 0.84 (significant at

95% level). As expected, concentration values obtained through the sampler are lower than obtained for all AQS as it refers to the $PM_{2.5-10}$ fraction.

The concentration was the highest on October 28, 2016 for all AQS and the sampler (Fig. 4c). This day was characterized by no rainfall occurrence and a change in the wind direction relative to the five preceding days (NE and ENE to SSE). The anomaly for this day (value of the wind direction in this particular day minus the monthly mean) was equal to +77.9º. The five preceding days were characterized by negative anomalies. In the SSE direction there is an open pit mining in the municipality of Bela Vista de Minas (distant about 50 km from Itabira), which in this particular day could have collaborated to an increase in coarse PM.

PM_{10} concentrations stay below the Brazilian Legal Patterns stated by the Brazilian National Environmental Council (CONAMA) Resolution number 3 (daily mean of 150 μg m^{-3}). This is the same standard considered by the EPA (2020). However, the World Health Organization (WHO) and the European Union air quality guidelines for 24-h average is 50 μg m^{-3}, not to be exceeded more than 35 times a calendar year (European Parliament, 2008; WHO, 2008). Recently, in 2018, Brazilian federal air quality standards were changed to CONAMA Resolution number 491, which revoked and replaced CONAMA Resolution number 3, with the goal to reach the same standard of WHO (50 μg m^{-3} for PM_{10}), but no deadline was defined for it to be accomplished.

The days before the start of data collection campaign in 2016 were rainy. During the sampling period, the rainfall occurred on October 24 (0.5 mm), November 11 (17 mm) and November 14 (41 mm). Light rain occurred on days between November 1 to 7. In addition, October 12 was a holiday, and as during the weekends, concentrations are lower. According to Gour et al. (2013), Dinoi et al. (2020) and Yousefian et al. (2020), concentrations of atmospheric particles are lower during weekends and holidays because pollution is related to the weekly cycle of human activities. This happens in Itabira as mining operations are also altered during weekends, with reduction in some activities.

Table I shows the descriptive statistics for the AQS and the sampler during the beginning and end of campaign days. It is possible to note that AQS01, the nearest station to the mine, presents the greatest PM_{10} mean and maximum values.

Figure 5a shows the daily concentrations of PM for coarse ($PM_{2.5-10}$) and fine ($PM_{2.5}$) modes obtained from the sampler. The $PM_{2.5}$ concentration

Table I. Descriptive statistics for air quality and meteorological parameters from the four AQS (considering the hourly data) and the sampler during the begin and end of campaign days.

Parameters	Mean	SD	MV (%)	Maximum	Minimum
PM_{10} (AQS01) (μg m^{-3})	23.3	13.7	2.1	148.2	2.2
PM_{10} (AQS02) (μg m^{-3})	19.2	10.2	0.9	86.0	3.0
PM_{10} (AQS03) (μg m^{-3})	18.3	9.0	57.2	47.8	0.7
PM_{10} (AQS04) (μg m^{-3})	18.1	10.6	2.7	115.4	0.7
$PM_{2.5-10}$ (sampler) (μg m^{-3})	12.2	6.8	0	36.7	5.8
$PM_{2.5}$ (sampler) (μg m^{-3})	7.0	2.9	0	15.3	3.0
$BC_{2.5}$ (sampler) (μg m^{-3})	1.0	0.4	0	2.2	0.4
$BC_{2.5-10}$ (sampler)	0.2	0.05	0	0.3	0.08
Pressure (mbar)	955.4	15.7	36.9	1058.8	880.5
Solar radiation (W m^{-2})	189.5	266.9	17.7	919.1	0
Wind Velocity (m s^{-1})	3.6	1.44	39.2	7.7	0.4
Wind direction (º)	114.6	97.9	1.0	359.6	0
Rainfall (mm)	0.1	0.9	1.0	17	0
Temperature (ºC)	23.1	4.0	39.3	35.3	14.8
Relative humidity (%)	68.1	17.3	35.0	99.9	28.1

SD: standard deviation; MV: missing values.

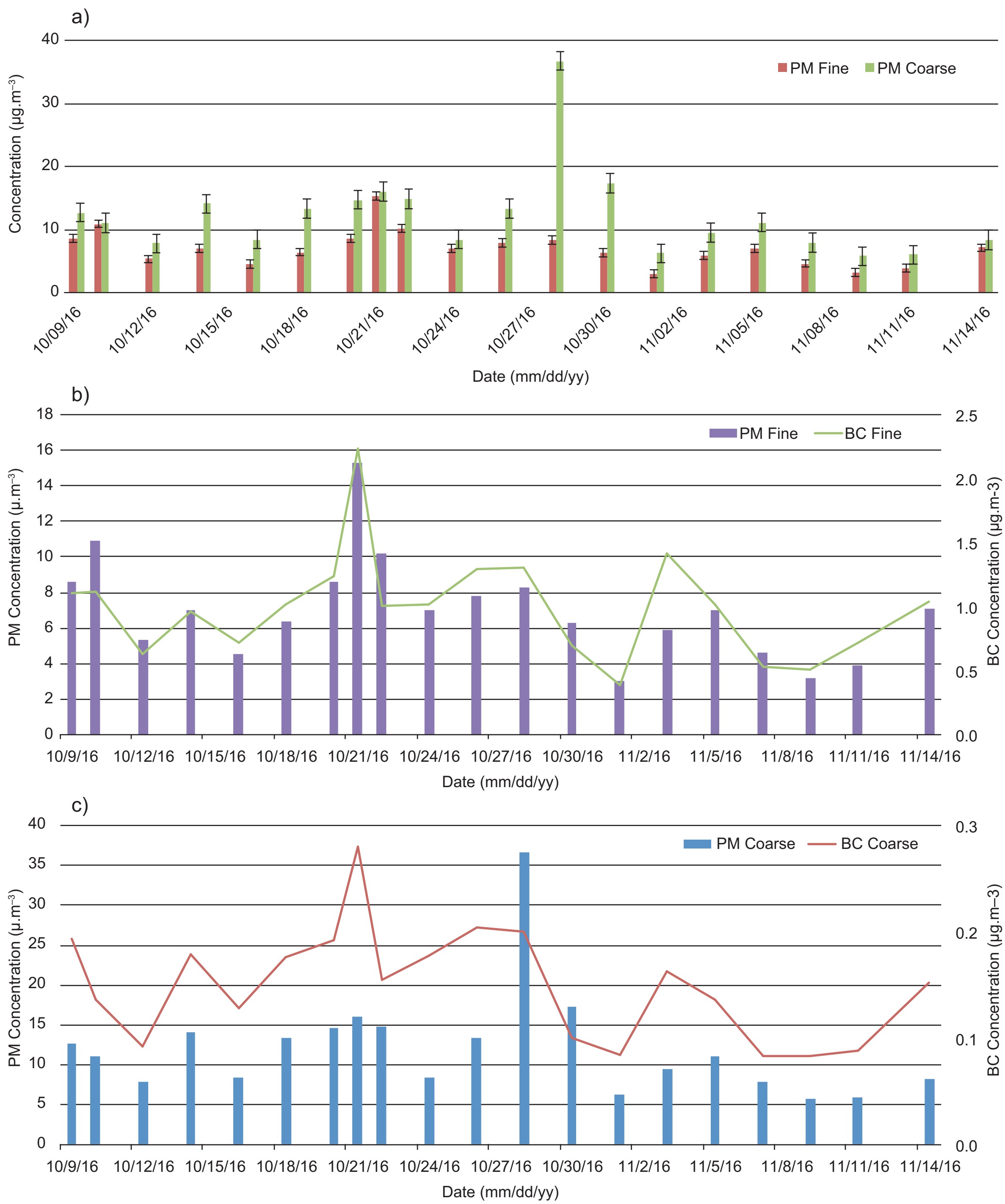

Fig. 5. Sampler concentrations (μg m^{-3}) of (a) particulate matter for fine ($PM_{2.5}$) and coarse ($PM_{2.5\text{-}10}$) modes with error bars, which represent the uncertainty of each measurement. (b) $PM_{2.5}$ and fine mode of black carbon. (c) $PM_{2.5\text{-}10}$ and coarse mode of black carbon for the sampling days.

was highest on October 21, whereas for $PM_{2.5-10}$ it was highest on October 28 (Fig. 5a). The average of $PM_{2.5}/PM_{2.5-10}$ ratio is 0.57 (Table I), a value quite similar to what was found by Soluri et al. (2007) for annual mean in Rio de Janeiro, the second largest Brazilian city. On October 28 this ratio was lower and equal to 0.2 (Fig. 5a) because of the significant contribution of coarse particles in this particular day, mentioned earlier. The correlation between the two modes is 0.45 (significant at a 95% level).

According to Xu et al. (2017), fine and coarse particles are generally produced by different sources: $PM_{2.5-10}$ is mainly produced from natural processing, such as re-suspension of local soil, as well as from anthropogenic sources like road dust, whereas $PM_{2.5}$ is largely comprised of primary and secondary anthropogenic combustion products. The authors verified that the daily average $PM_{2.5}/PM_{10}$ ratio vary significantly day by day, e.g., minimum values of the ratio in one day can occur during traffic hours in consequence of re-suspended coarse road dust. Moreover, fine particles have smaller settling velocities compared with their coarse counterparts (Kumar et al., 2018), hence they have a longer atmospheric residence time and their dispersion pattern will be different from the coarse ones (Patra et al., 2016).

The concentrations of fine BC and $PM_{2.5}$ present a similar pattern, but this cannot be verified for the coarse mode of BC and $PM_{2.5-10}$ (Fig. 5a, b). The correlation between fine BC and $PM_{2.5}$ is 0.86 (significant at the 95% level), whereas between coarse BC and $PM_{2.5-10}$ it is 0.25 (not significant). The fine and coarse BC mean concentrations are 1.0 ± 0.4 μg m^{-3} and 0.2 ± 0.05 μg m^{-3}, respectively (Table I) and represent 14 and 2% in the $PM_{2.5}$ and $PM_{2.5-10}$, respectively. Castanho and Artaxo (2001) found for São Paulo city a fine BC mean concentration ranging from 7.6 to 4.1 μg m^{-3} in winter and summertime, respectively, representing 21 ± 4% in winter and 28 ± 10% in summer of $PM_{2.5}$. De Miranda et al. (2012) found, for urban areas of São Paulo, Rio de Janeiro, Belo Horizonte, Curitiba, Porto Alegre and Recife cities, fine BC mean concentrations of 10.6 ± 6.4, 3.4 ± 2.5, 4.5 ± 3.3, 4.4 ± 4.0, 3.9 ± 4.3 and 1.9 ± 1.1 μg m^{-3} for a one-year or longer period. Also, according to the authors, the percentage contribution of BC was lowest in Rio de Janeiro (20 ± 7%) probably because diesel-powered (heavy-duty) vehicles represent a smaller proportion of the total vehicle fleet in this city than in others evaluated.

Figure 6 depicts the correlation between hourly data of meteorological parameters obtained from MS01 and particulates from all AQS. It is worth to highlight that some meteorological variables present a large number of missing values, especially pressure, wind velocity, temperature and relative humidity. Thus, the pairwise correlation was used here, and the sampler data was not considered, since the number of pairs for the sampling days mean would be very small.

Wind direction shows weak and negative correlations with PM_{10} for all AQS, except for AQS03 (positive correlation) (Fig. 6). Atmospheric pressure has a significant (at a 95% level) negative correlation with PM_{10} (–0.66) from AQS03, the farthest station from the mines.

Rainfall and relative humidity have a significant negative correlation with PM_{10} for all AQS, except for AQS03 (not significant for rainfall). The lower the relative humidity, the higher the concentration of particulates in the atmosphere. Low air humidity is related to a lower chance of rainfall (positive correlation; Fig. 6) and is, therefore, associated with dry air, which favors high concentrations of air pollutants. The mean relative humidity for the sampling period is 68 ± 17%, with a minimum of 28% and a maximum of 99.9% (Table I).

Wind velocity has significant negative correlations with PM_{10} for all AQS (Fig. 6). Particles can travel for greater distances at higher wind speeds, contributing to pollutants dispersion. The mean wind velocity for the sampling period is 3.6 ± 1.4 m s^{-1} (Table I). Significant and positive correlations are seen between temperature and PM_{10} for all AQS, except for AQS01 (negative correlation), the closest station from the mines. High temperature causes lifting of soil particles into the atmosphere (Latha and Highwood, 2006), which can reach the more distant AQS from the mines, increasing the concentration they measure. The mean temperature for the sampling period is 23.1 ± 4 ºC, with a minimum of 14.8 ºC and a maximum of 35.3 ºC (Table I).

Solar radiation is an important factor for the concentration of particulates, since high values of radiation increase the lower troposphere instability, favoring convective activity. Although temperature has a positive correlation with solar radiation,

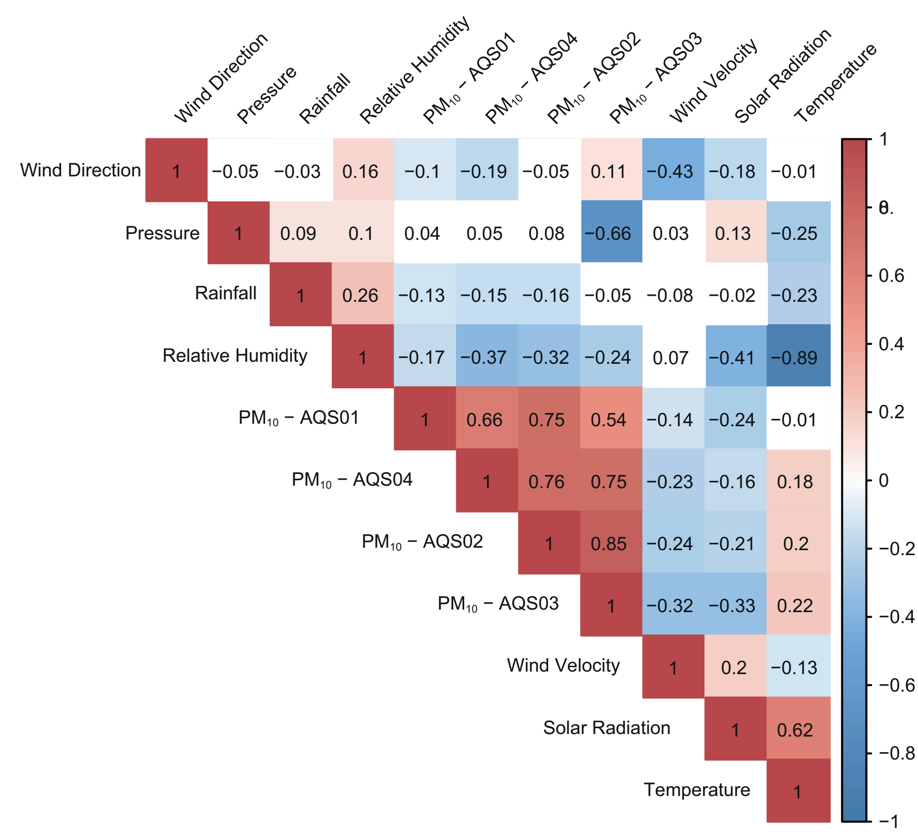

Fig. 6. Pearson correlation coefficient between the meteorological parameters and particles from air quality stations for the sampling days. Shaded colors represent significant values at the 95% level (p-value < 0.05).

significant negative correlations are seen between solar radiation and PM_{10} for all AQS (Fig. 6), the opposite being found for temperature. It is worth to highlight that this variable presents the greater percentage of missing values (Table I). Mean solar radiation during the sampled period is 189.5 W m^{-2} and its standard deviation is high (266.9 W m^{-2}) due to daily cycle (Table I). The lowest correlations for PM_{10} are of AQS01 with AQS04 and AQS03 (Fig. 6).

3.2 PM Elemental analysis

Different sources contribute to coarse and fine particles. In general, diesel vehicles emit a larger number of fine particles per vehicle. In addition, a significant contribution to fine PM mass comes from secondary aerosols (inorganics such as ammonium sulfate and ammonium nitrate, but also secondary organic aerosols), which are formed in the atmosphere through chemical/physical processes (WHO, 2006).

Table II presents the results of the X-ray fluorescence analysis for the main trace elements present in fine ($PM_{2.5}$) and coarse ($PM_{2.5\text{-}10}$) modes, respectively. The mean concentration for the 37 days of sampling was calculated for each element in both modes, as well as the standard deviation and mean relative distribution (calculated by dividing the total sample concentration by the trace element concentration and multiplying by 100). It can be noted that sulfur (S) has the highest concentration in the fine mode (representing 32.2% relative to the total trace element load). Iron (Fe) has also a significant presence in the fine mode of PM (15.9%), compared to the other elements, such as potassium (K) (13.6 %), silicon (Si) (11.3%), sodium (Na) (10.6%), aluminum (Al) (8.8%), and calcium (Ca) (3.8%). De Miranda et al. (2012) analyzed the mean concentrations of trace elements in the fine mode for urban areas of six great cities (see table 7 in their paper). They found

Table II. Mean concentration (MC), standard deviation (SD) of MC, mean relative distribution (RD) and missing values percentage (MV) of trace elements (TE) in the fine ($PM_{2.5}$) and coarse ($PM_{2.5\text{-}10}$) modes.

Trace element	Fine mode				Coarse mode			
	MC (ng m^{-3})	SD (ng m^{-3})	RD (%)	MV (%)	MC (ng m^{-3})	SD (ng m^{-3})	RD (%)	MV (%)
Na	110.2	44.9	10.6	0.0	162.2	76.7	5.6	0.0
Mg	12.0	5.6	0.6	45.0	98.6	37.2	3.3	0.0
Al	95.2	44.8	8.8	0.0	505.6	208.2	17.2	0.0
Si	122.0	50.7	11.3	0.0	605.1	226.6	20.8	0.0
P	9.2	3.8	0.8	0.0	11.8	15.6	0.5	0.0
S	349.8	137.9	32.2	0.0	86.3	28.4	3.1	0.0
Cl	2.0	0.8	0.2	15.0	234.9	223.6	7.6	0.0
K	150.9	75.6	13.6	0.0	105.0	30.7	3.7	0.0
Ca	39.4	12.3	3.8	0.0	291.9	94.8	10.3	0.0
Ti	6.5	2.8	0.6	0.0	34.4	13.3	1.2	0.0
V	0.4	0.1	0.01	70.0	0.8	0.2	0.01	40.0
Cr	1.0	0.4	0.1	10.0	2.1	0.9	0.07	0.0
Mn	3.9	2.1	0.4	0.0	16.0	9.2	0.6	0.0
Fe	171.7	71.9	15.9	0.0	746.9	305.7	25.7	0.0
Ni	0.5	0.2	0.04	5.0	0.4	0.2	0.01	15.0
Cu	0.8	0.4	0.07	5.0	1.3	0.4	0.04	5.0
Zn	4.3	2.9	0.4	0.0	6.0	1.8	0.2	0.0
As	0.1	0.0	0.01	5.0	0.1	0.0	0.004	5.0
Se	0.7	0.3	0.02	60.0	0.6	0.3	0.01	45.0
Br	2.3	0.8	0.2	0.0	0.6	0.3	0.01	55.0
Rb	0.9	0.7	0.02	70.0	0.6	0.2	0.003	80.0
Sr	1.2	0.2	0.01	85.0	3.3	1.7	0.06	45.0
Cd	3.0	—	0.01	95.0	1.6	0.1	0.004	90.0
Sb	3.2	0.6	0.06	75.0	4.6	1.6	0.02	85.0
Pb	2.2	1.3	0.2	10.0	0.6	0.3	0.01	75.0

in summer (October to March) high concentrations of S and minerals (Al, Si, Ca, and Fe) in the fine mode, derived from fuel combustion and soil resuspension, respectively. The concentration of S found here (349.8 ± 137.9 ng m^{-3}) is higher than what they found for Belo Horizonte (331.5 ± 195.0 ng m^{-3}) and Recife (228.6 ± 104.5 ng m^{-3}). In addition, in fine mode Fe presented a higher concentration (171.7 ± 71.9 ng m^{-3}) in Itabira than in all the six cities analyzed by the above-mentioned authors (see Table III for comparison).

In the coarse fraction, some elements appeared in a higher concentration, compared to the fine fraction, such as Fe (25.7%), Si (20.8%), Al (17.2%), Ca (10.3%), titanium (Ti) (1.2%), magnesium (Mg) (3.3%), and chlorine (Cl) (7.6%) (Table II).

Principal components factor analysis with varimax rotation was conducted with IBM SPSS statistics software to identify the possible sources of PM. Although this method is qualitative, the great advantage is that there is no need for a priori knowledge of emission inventories (Chio et al., 2004), since Itabira city does not have any yet. All elements with missing data (see Table II) were dropped from the analysis, maintaining only the common trace elements to both modes. The missing values are due to very low concentrations of the elements, some of them below the detection limit of the instrument. Three and four principal components with eigenvalues greater than 1.0 were extracted with 83.9 and 93.2% cumulative variance for coarse and fine particles, respectively.

Figure 7 shows the main factor loadings for the coarse ($PM_{2.5\text{-}10}$) and fine ($PM_{2.5}$) modes of PM. The first factor has 54.7% (coarse mode) and 48.6% (fine mode) of total variance and shows high loadings of Fe > Si > Mn > Al > Ti in coarse mode and Al > Si

Table III. Comparison of the trace elements concentration and their standard deviation in fine mode ($PM_{2.5}$) sampled at Itabira, with other six cities in Brazil and one city in China ($ng\ m^{-3}$).

Trace element	This study	De Miranda et al. (2012)						Zhou et al. (2014)
	Itabira	Sao Paulo	Rio de Janeiro	Belo Horizonte	Porto Alegre	Curitiba	Recife	Ji'nan (China)
Al	95.2 ± 44.8	33.2 ± 28.4	32.9 ± 41.2	43.9 ± 55.8	28.3 ± 24.3	48.4 ± 81.9	55.4 ± 83.3	670.0 ± 460.0
Si	122.0 ± 50.7	76.6 ± 49.9	77.9 ± 63.0	162.4 ± 126.5	74.8 ± 60.6	74.3 ± 74.4	139.7 ± 163.8	
P	9.2 ± 3.8	36.4 ± 147.9		9.5 ± 48.6	7.1 ± 8.2	5.4 ± 5.2	1.9 ± 1.5	
S	349.8 ± 137.9	896.6 ± 472.0	638.2 ± 398.8	331.5 ± 195.0	389.0 ± 348.4	384.0 ± 260.3	228.6 ± 104.5	
Cl	2.0 ± 0.8	33.5 ± 49.5	18.8 ± 54.6	11.1 ± 34.8	54.5 ± 80.5	41.8 ± 189.9	58.8 ± 64.6	
K	150.9 ± 75.6	137.6 ± 130.1	124.9 ± 281.0	141.2 ± 140.4	158.5 ± 156.7	154.6 ± 151.4	117.4 ± 77.7	
Ca	39.4 ± 12.3	52.7 ± 26.6	31.9 ± 23.7	98.5 ± 72.5	35.8 ± 22.5	37.0 ± 35.0	53.5 ± 29.9	
Ti	6.5 ± 2.8	5.7 ± 3.2	4.4 ± 3.5	4.4 ± 4.1	3.7 ± 2.7	4.0 ± 3.8	4.0 ± 5.2	50.0 ± 20.0
V	0.4 ± 0.1	1.3 ± 0.9	4.9 ± 2.9	1.5 ± 0.8	0.9 ± 0.5	0.7 ± 0.6	0.4 ± 0.3	
Cr	1.0 ± 0.4	1.0 ± 1.0	1.8 ± 0.7	0.7 ± 0.9	1.3 ± 0.7	0.7 ± 0.6	0.4 ± 0.4	10.0 ± 10.0
Mn	3.9 ± 2.1	6.6 ± 21.2	3.7 ± 1.9	25.2 ± 60.5	2.8 ± 2.8	2.1 ± 4.4	1.3 ± 1.3	110.0 ± 70
Fe	171.7 ± 71.9	128.3 ± 57.2	56.3 ± 26.4	107.9 ± 80.6	60.2 ± 44.9	57.3 ± 31.7	50.7 ± 46.7	2,410.0 ± 1,190.0
Ni	0.5 ± 0.2	0.9 ± 1.5	3.6 ± 1.5	0.8 ± 0.5	0.7 ± 0.2	0.4 ± 0.5	0.3 ± 0.3	10.0 ± 10.0
Cu	0.8 ± 0.4	8.1 ± 13.8	7.7 ± 4.8	4.1 ± 6.4	1.9 ± 1.8	2.6 ± 4.2	0.9 ± 0.9	40.0 ± 30.0
Zn	4.3 ± 2.9	53.6 ± 41.1	18.1 ± 15.9	12.6 ± 12.3	12.4 ± 18.9	9.0 ± 10.6	8.9 ± 10.9	440.0 ± 270.0
Se	0.7 ± 0.3	3.3 ± 3.6		0.4 ± 0.5	0.8 ± 0.3	0.4 ± 0.6	1.1 ± 1.1	
Br	2.3 ± 0.8	2.8 ± 2.7	4.5 ± 2.1	2.5 ± 1.8	2.4 ± 1.3	2.0 ± 1.5	2.9 ± 1.5	
Pb	2.2 ± 1.3	15.4 ± 12.6	9.5 ± 7.1	3.0 ± 4.8	3.2 ± 3.1	7.9 ± 15.8	2.1 ± 1.9	200.0 ± 100.0
As	0.1 ± 0.0							60.0 ± 70.0

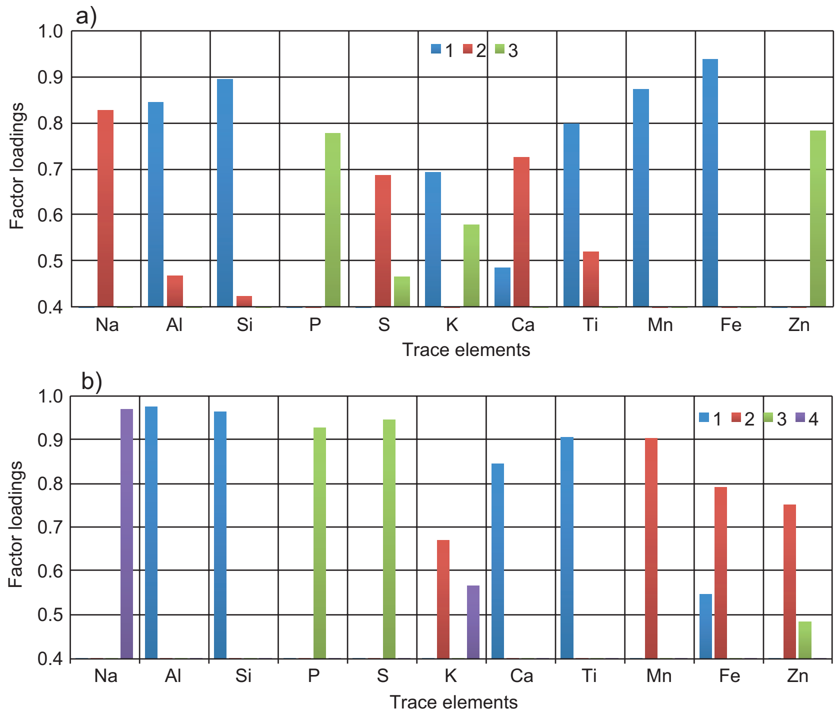

Fig. 7. Main factor loadings (values above 0.4) from principal components factor analysis with varimax rotation for (a) coarse ($PM_{2.5-10}$) and (b) fine ($PM_{2.5}$) modes of particulate matter. Factor 1: mining activities; factor 2: mining operations/iron and steelmaking industries/sea-salt; factor 3: traffic/biomass burning/biogenic; factor 4: unidentified.

> Ti > Ca > Fe in fine mode (Fig. 7a, b). There are significant correlations between these elements, especially in the coarse mode (Fig. 8a, b). As mentioned earlier, Al, Si and Fe have the greatest mean concentration in coarse mode (Table II). One of the sources of these elements is soil dust resuspension (Venter et al., 2017).

The mineralogical characterization of soils may assist in the identification of sources contributing to atmospheric aerosols (Espinosa and Miranda, 2013). Figueiredo et al. (2006), using the X-ray fluorescence technique, determined the chemical composition of the iron quadrangle soil in Minas Gerais, where Itabira is located. According to them, the elements Al, Fe, Ti, K and Si came from soil minerals kaolinite (Al2Si2O5(OH)4), gibbsite (αAl(OH)3), and goethite (αFe(OH)3).

Vega et al. (2004) found that the major component of the coarse fraction was geological material (60% of PM_{10} mass). According to Guevara (2016), soil particles generated by wind erosion processes, traffic resuspension, mining and construction operations, and agricultural land management activities are large contributors to the coarse fraction of primary PM emissions. As Itabira is a mining city, blasting, due to opencast iron ore mine activities, is very common and the mineral dust plume generated spreads for the entire city. Monjezi et al. (2009) found that in opencast mines of Iran, blasting is one of the main sources of dust generation. It should be noted that wind speed and mine geometry are important factors influencing the pollutants dispersion from mines (Patra et al., 2016). Itabira is formed by a succession of hills and valleys. The mining area consists of the mine complexes (Fig. 2a), beneficiation areas and sterile material deposits, which are located in the urban perimeter of the city. The mean wind velocity (average of hourly data for the sampling days) is very low when Fe, Si and Mn in coarse mode and Al, Si, Ti in fine mode have the highest concentrations

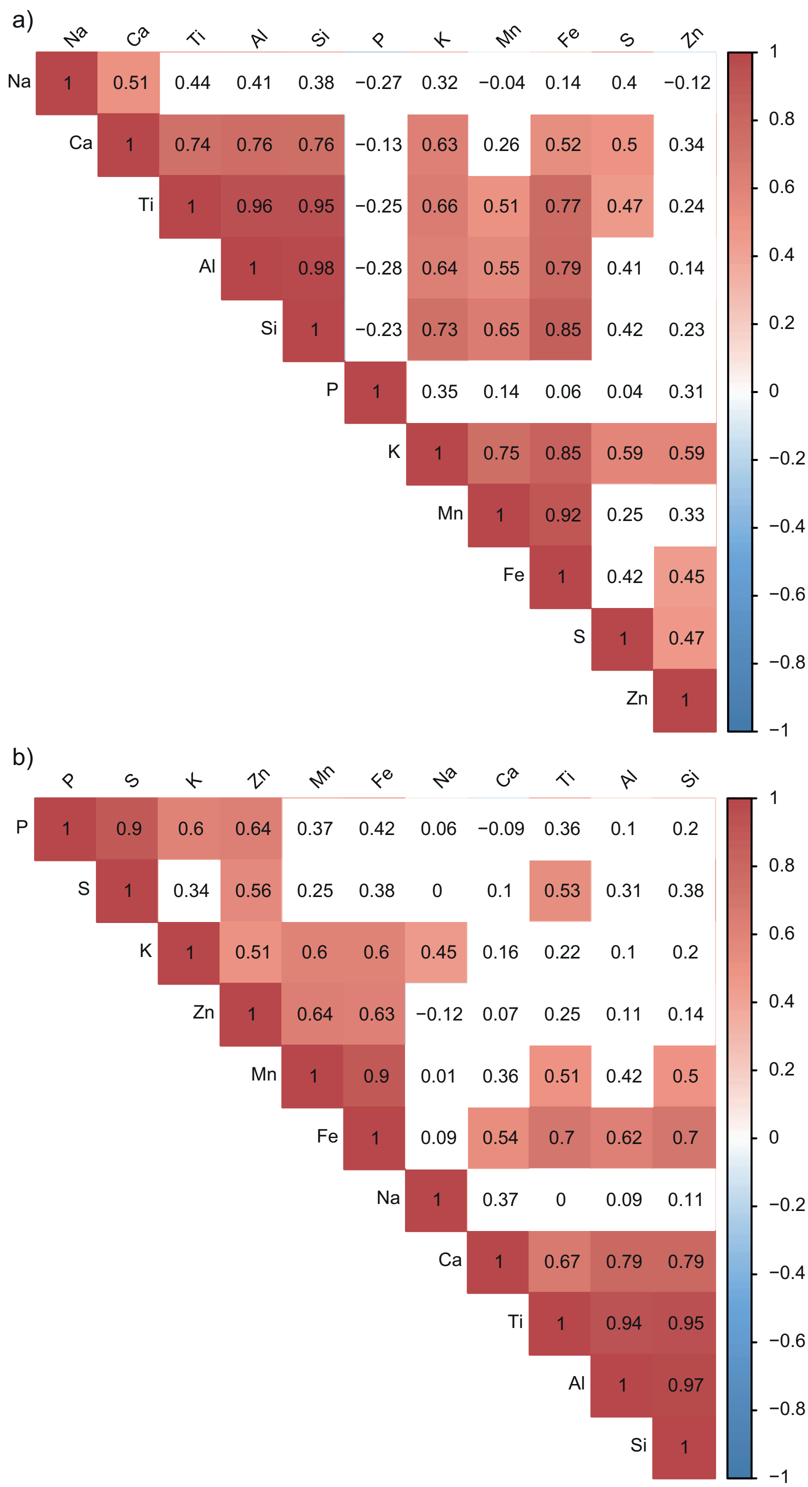

Fig. 8. Pearson correlation coefficient between the trace elements in the (a) coarse and (b) fine modes for the sampling days. Shaded colors represent significant values at the 95% level (p-value < 0.05).

(between all samples from the same element in each mode), indicating that these tracers come from a local source. Also, earlier we found a negative correlation between wind speed and PM_{10} concentration, i.e., higher wind speeds result in lower concentrations. Thus, the first factor is associated with emissions from the mining activities, consisting mainly of coarse fractions ($PM_{2.5\text{-}10}$) of the respirable particle.

The second factor contributes to 17.9 and 22% of the total variance (coarse and fine particles, respectively) and shows high loadings of Na > Ca > S in the coarse mode ($PM_{2.5\text{-}10}$) and Mn > Fe > Zn > K in the fine mode ($PM_{2.5}$) (Fig. 7a, b). There is a significant positive correlation between Na and Ca (0.5) and between Ca and S (0.5) in the coarse mode (Fig. 8a). Na, Cl and Mg are good indicators of marine influence (sea-salt tracers). Table II shows greater concentrations of these elements in the coarse mode (Ca > Cl > Na > Mg). The correlation between Mn-Fe is 0.9 and between Mn-K, Mn-Zn and Fe-Zn is 0.6 in the fine mode (Fig. 8b). These metal emissions can be associated with iron and steelmaking industry activities (Mohiuddin et al., 2014; Dai et al., 2015).

Figure 9a, b shows the pollution rose maps for the PM_{10} hourly concentration, considering the four AQS mean during the sampling days, for both meteorological stations (MS01 and MS02). It is possible to note that high concentrations of coarse particles (PM_{10}) are associated with wind's drag mainly from the east-northeast direction (seen in both meteorological stations), but also being generated locally from the north-west quadrant direction (mining complex location) seen in MS02 (Fig. 9b; a lower altitude that is associated with lower wind speed) and from the southwest-south-east quadrants direction (locations of Itabira industrial district and some other regional open pit mines). The mean wind direction varied between east and northeast when Na, Ca and S in the coarse mode, and Mn, Fe and Zn in fine mode had the highest concentrations. Earlier, we showed through back trajectories that air masses arriving in Itabira originate mainly from the Atlantic Ocean, passing through the region denominated Steel Valley, as well as other steel industries located northeast and eastward of Itabira (Fig. 2c). The Steel Valley region in Minas Gerais represents one of Brazil's most outstanding metal smelting resources (Jordão et al., 1999). Thus, the second factor is associated mainly with mining operations in the city and air mass transport from regional iron and steelmaking industry activities in the fine mode and, secondly, from long-range transport of sea salt in the coarse mode.

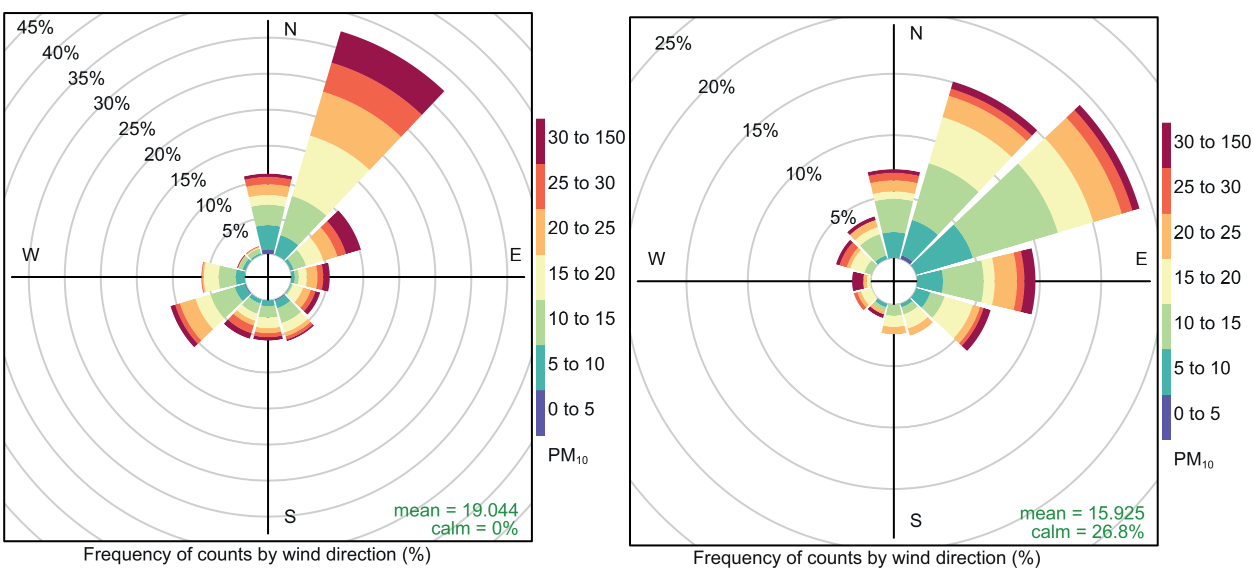

Fig. 9. Pollution rose maps for the PM_{10} ($\mu g\ m^{-3}$) hourly concentration for the four air quality stations mean during the sampling days for (a) MS01 and (b) MS02. The percentage of hourly profiles for a given wind sector is indicated for each radius.

The third factor, which accounts for 11.3 and 12.6% of the total variance for coarse ($PM_{2.5-10}$) and fine ($PM_{2.5}$) modes, respectively, show strong loadings of Zn > P > K > S in the coarse mode and S > P > Zn in the fine mode (Fig. 7a, b). As mentioned earlier, fine particles of S can be directly emitted by automotive fuel combustion. The greatest correlations in the coarse mode are between K-S (0.59) and K-Zn (0.59), and in the fine mode between P-S (0.9) and P-Zn (0.64). Arana et al. (2014) found that high concentrations of S, K, Zn and P during the dry season in Manaus are associated with a mixture of long-range transported biomass burning and natural biogenic emissions. In Itabira, burning of vegetation for land clearing and land-use change is a common practice. The mean wind velocity ranges from 2.6 to 4.4 m s^{-1} and the mean wind direction from 59.6º (east-northeast) to 130.8º (southeast) when Zn, P, K and S in the coarse mode and S, P, Zn and K in the fine mode have the highest concentrations. Thus, the third factor could be associated with vehicle emissions, local and regional biomass burning and natural biogenic emissions. Finally, a fourth factor accounts for 10% of the total variance of the fine mode, with high loadings of Na > K. Here, the wind direction varies from SW to NE and the velocity ranges from 0.4 to 3.8 m s^{-1}. Ooki et al. (2002) detected the existence of anthropogenic Na within the fine particle range in urban air and found that land-based mineral dust emissions contribute to 42% of the total sodium emissions. According to these authors, K in the urban air is thought to be derived largely from anthropogenic sources and a high correlation between the concentrations of these elements in fine mode suggests that they have the same anthropogenic source. For Itabira, this needs to be investigated, as the correlation between these elements is 0.45.

It is worth to highlight that some elements, such as copper (Cu), selenium (Se), chromium (Cr), nickel (Ni), vanadium (V), arsenic (AS), cadmium (Cd), and lead (Pb) have also been detected by X-ray fluorescence, but they were not included in factor analysis, as there was missing data in some samples (see Table II). Although none of them has exceeded the air quality standards, they deserve a lot of attention. Polidori et al. (2009) and Venter et al. (2017) stated that As, Cd, Cr, Ni, Pb and Se are considered human and animal carcinogens even in trace amounts (ATSDR, 2015). These authors also mentioned that Cu, Cr and V can contribute to oxidative DNA damage.

Itabira city has comparable contributions of Cu, Se, Cr, Ni, V and Pb with what de Miranda et al. (2012) found in summer for Recife (0.9 ± 0.9, 1.1 ± 1.1, 0.4 ± 0.4, 0.3 ± 0.3, 0.4 ± 0.3 and 2.1 ± 1.9, respectively), Porto Alegre (1.9 ± 1.8, 0.8 ± 0.3, 1.3 ± 0.7, 0.7 ± 0.2, 0.9 ± 0.5 and 3.2 ± 3.1, respectively) and Belo Horizonte (4.1 ± 6.4, 0.4 ± 0.5, 0.7 ± 0.9, 0.8 ± 0.5, 1.5 ± 0.8 and 3.0 ± 4.8, respectively), a city situated in a mining region (Table III). These are large metropolitan cities with a population of 1.56 (Recife), 1.44 (Porto Alegre) and 2.45 (Belo Horizonte) million inhabitants (de Miranda et al. 2012). Although the sampling period here was shorter, the fact that Itabira, which has an estimated population of 120 904 inhabitants (IBGE, 2020), has similar contributions of these elements (which are emitted from a variety of sources) and of S and Fe (as seen earlier), is very concerning. However, Zhou et al. (2014) measured trace metals in $PM_{2.5}$ during September 2010 at one industrial area surrounded by several iron and steel plants in Ji'nan City, eastern China and found much greater concentrations of Al, Ti, Cr, Mn, Fe, Ni, Cu, Zn, Pb and As compared to Itabira (Table III). In fact, little is known about the long-term exposure of these elements regarding their impact (or not) to the health of inhabitants of the region. Thus, further research about this topic is needed.

4. Conclusions

Itabira city, in the state of Minas Gerais, Brazil, is home to the largest complex of opencast mining in the world, which is located upwind of the city. The air quality monitoring network, installed in Itabira and managed by the Vale, the company exploiting the mines, is the main source of PM emission data in the city. Moreover, these AQS only cover areas near the mines and do not measure fine PM, which could be used to evaluate potential health effects to nearby population.

Thus, in this study we sampled atmospheric aerosols of filters, with the initial objective of characterizing PM in the city and comparing high-volume data from the AQS with a dichotomous air sampler. Mass concentrations of the fine and coarse modes of PM were analyzed by gravimetry, and X-ray fluorescence spectroscopy was performed to determine the elemental composition and concentration of atmospheric particulates. Analysis was completed by a PCA on the elemental composition, and by clustering air masses trajectories, which helped identifying potential sources besides mining activities.

The city lies upwind of the industrial zone, hence it is largely protected from local industries air pollution. However, results of the trajectories cluster analysis showed a long-range transport of aerosols during the sampling days from the northeast (84% of the trajectories), east-southeast (12%) and south-southwest (3%) directions. Thus, the prevailing wind directions correspond to the largest steel production complex region in Latin America. This was corroborated by pollution rose maps, which showed wind's drag mainly from east-northeast direction, but also with local sources of pollution (due to the lower wind speed) coming from the north-west and south-west-south-east quadrants, representing the locations of the mining complex, local industrial district and some other open pit mines in close municipalities.

Regarding the meteorological conditions during the sampling days, negative correlations were seen between PM_{10} from AQS and mostly all meteorological parameters (but temperature).

The average $PM_{2.5}/PM_{2.5\text{-}10}$ ratio obtained through the sampler was 0.57 and BC represents 14 and 2% in the fine ($PM_{2.5}$) and coarse ($PM_{2.5\text{-}10}$) modes of PM, respectively. Therefore, it can be considered a fine particulate material. These values are comparable to what was found by other authors for Rio de Janeiro city in terms of the annual mean.

The results of the X-ray fluorescence analysis showed that the main trace elements in the coarse ($PM_{2.5\text{-}10}$) and fine ($PM_{2.5}$) modes are Fe and S, respectively. The first factor obtained with PCA is associated with emissions from mining activities, contributing to 54.7 and 48.6% of the total with high loadings of Fe and Al (coarse and fine particles, respectively). The second factor contributes to 17.9 and 22% of the total variance with high loadings of Na and Mn (coarse and fine particles, respectively), and is associated, mainly, with mining operations and air mass transport from regional iron and steelmaking industry activities in fine mode and, secondly, from long-range transport of sea salt in coarse mode. The third factor accounts for 11.3 and 12.6% of the total variance with strong loadings of Zn and S (coarse and fine particles, respectively), and is associated with vehicle emissions, local and regional biomass burning and natural biogenic emissions. Finally, a fourth factor accounts for 10% of the total variance for fine mode, with high loadings of Na and K.

The sampling period of 37 days was short; however, it served well to perform a validation against data from the air quality monitoring network managed by Vale. Besides, our measurements were the first ever aerosol filter-sampling in the city. Further field campaigns are also necessary to characterize PM in all seasons of the year and at different areas of the city.

Acknowledgments
The authors thank the Physics Institute of the University of São Paulo for technical support. Special thanks to Alcides C. Ribeiro, Fábio de Oliveira Jorge and Ana Lúcia Loureiro from the Applied Physics Department for their support in program sampling. We also gratefully acknowledge the NOAA Air Resources Laboratory (ARL) for the provision of the HYSPLIT model and the data from air quality stations provided by the Itabira Environment Secretary, used in this publication. We also thank graduate students João Manoel Alonso de Souza Gambarra and William Gomes Epaminondas for operational support. Funding sources: Federal University of Itajubá (UNIFEI) supported the collection of data and preparation of the article, and H.B. acknowledges the support grants 2009/54201-1, 2013/50510-5 and 2017/17047-0, São Paulo Research Foundation (FAPESP), which supported analysis of data, providing materials, reagents, laboratory samples, computing resources and other analysis tools.

References

Alves HS, Freitas ACV. 2021. Critical air pollution events analysis in Itabira – Minas Gerais, Brazil. Research, Society and Development 10: 1-21. https://doi.org/10.33448/rsd-v10i1.10587

Arana A, Loureiro A, Barbosa HMJ, van Grieken R, Artaxo P. 2014. Optimized energy dispersive X-ray fluorescence analysis of atmospheric aerosols collected at pristine and perturbed Amazon Basin sites. X-Ray Spectrometry 43: 228-237. https://doi.org/10.1002/xrs.2544

ATSDR. 2015. Toxicological Profiles. Agency for Toxic Substances and Disease Registry. Available at: https://www.atsdr.cdc.gov/toxprofiledocs/index.html (accessed on August 28, 2020).

Braga ALF, Pereira LAA, Procópio M, de André PA, Saldiva PHN. 2007. Associação entre poluição atmosférica e doenças respiratórias e cardiovasculares na cidade de Itabira, Minas Gerais, Brasil. Cadernos de Saúde Pública 23: 570-578. https://dx.doi.org/10.1590/S0102-311X2007001600017

Castanho ADA, Artaxo P. 2001. Wintertime and summertime São Paulo aerosol source apportionment study. Atmospheric Environment 35: 4889-4902. https://doi.org/10.1016/S1352-2310(01)00357-0

Chio CP, Cheng MT, Wang CF. 2004. Source apportionment to PM in different air quality conditions for Taichung urban and coastal areas, Taiwan. Atmospheric Environment 38: 6893-6905. http://dx.doi.org/10.1016/j.atmosenv.2004.08.041

Dai QL, Bi XH, Wu JH, Zhang YF, Wang J, Xu H, Yao L, Jiao L, Feng YC. 2015. Characterization and source identification of heavy metals in ambient PM_{10} and $PM_{2.5}$ in an integrated iron and steel industry zone compared with a background site. Aerosol Air Quality Research 15: 875-887. https://doi.org/10.4209/aaqr.2014.09.0226

De Miranda RM, de Fatima MA, Fornaro A, Astolfo R, de André PA, Saldiva P. 2012. Urban air pollution: A representative survey of $PM_{2.5}$ mass concentrations in six Brazilian cities. Air Quality Atmosphere & Health 5: 63-77. https://doi.org/10.1007/s11869-010-0124-1

Devlin J, Tubino DI. 2012. Contention, participation, and mobilization in environmental assessment follow-up: The Itabira experience. Sustainability 8: 106-115. https://doi.org/10.1080/15487733.2012.11908089

Dinoi A, Conte M, Grasso FM, Contini D. 2020. Long-term characterization of submicron atmospheric particles in an urban background site in southern Italy. Atmosphere 11: 1-15. https://doi.org/10.3390/atmos11040334

Draxler RR, Stunder B, Rolph G, Stein A, Taylor A. 2012. HYSPLIT_4 User's Guide. NOAA Air Resources Laboratory, Silver Spring, Maryland, USA. Available at: https://www.arl.noaa.gov/data/web/models/hysplit4/win95/user_guide.pdf (accessed on August 28, 2020).

Dixon CJ. 1979. The iron deposits of the Itabira District - Brazil. In: Atlas of economic mineral deposits (Dixon CJ, ED.). Springer, Dordrecht, 38-39. https://doi.org/10.1007/978-94-011-6511-2_15

Dorr JVN, Barbosa AL de M. 1963. Geology and ore deposits of the Itabira District, Minas Gerais, Brazil. Report. Available at: https://pubs.usgs.gov/pp/0341c/report.pdf (accessed on August 28, 2020).

Espinosa AA, Miranda J. 2013. Elemental analysis of soils as possible resuspended dust sources in Mexico City. International Journal of Environment Research 7: 1015-1020. https://doi.org/10.22059/IJER.2013.685

European Parliament. 2008. Directive 2008/50/EC of the European Parliament and of the Council of 21 May 2008 on ambient air quality and cleaner air for Europe. Official Journal of the European Union L 152. Available at: https://eur-lex.europa.eu/legal-content/en/ALL/?uri=CELEX:32008L0050 (accessed on August 28, 2020).

Figueiredo A, Miller CA, Mascarenhas F, Gutman A, Siqueira B, Rodrigues C, Caruncho D, Szachtman M, Capanema R. 2016. Vale production in 4Q16. Report. Available at: http://www.vale.com/EN/investors/information-market/quarterly-results/QuarterlyResultsDocs/2016%204Q%20Production%20Report_i.pdf (accessed on August 28, 2020).

Figueiredo MA, Fabris JD, Varajão AFDC, Couceiro PR da C, Loutfi IS, Azevedo I de S, Garg VK. 2006. Óxidos de ferro de solos formados sobre gnaisse do Complexo Bação, Quadrilátero Ferrífero, Minas Gerais. Pesquisa Agropecuária Brasileira 41: 313-321. https://doi.org/10.1590/S0100-204X2006000200017

Ghose MK, Majee SR. 2001. Air pollution due to opencast mining and it's control in Indian context. Journal of Scientific & Industrial Research 60: 786-797.

Godish T. 2003. Air quality. 4 ed. Lewis Publishers, Boca Raton, USA.

Gour AA, Singh SK, Tyagi SK, Mandal A. 2013. Weekday/weekend differences in air quality parameters in Delhi, India. International Journal of Research in Engineering & Technology 1: 69-76.

Guevara M. 2016. Emissions of primary particulate matter. In: Airborne particulate matter: Sources, atmospheric processes and health (Harrison RM, Hester RE, Querol X, Eds.). Royal Society of Chemistry, Cambridge, 1-34. https://doi.org/10.1039/9781782626589-00001

IBGE. 2018. Malha municipal do Brasil (base digital georreferenciada). Instituto Brasileiro de Geografia e Estatística. Available at: https://geoftp.ibge.gov.br/organizacao_do_territorio/malhas_territoriais/malhas_municipais/municipio_2018/Brasil/BR/ (accessed on February 21, 2021).

IBGE. 2020. População estimada. Instituto Brasileiro de Geografia e Estatística. Available at: https://cidades.ibge.gov.br/brasil/mg/itabira/panorama (accessed on February 23, 2021).

Jordão CP, Pereira JL, Jham GN, Bellato CR. 1999. Distribution of heavy metals in environmental samples near smelters and mining areas in Brazil. Environmental Technology 20: 489-498. https://doi.org/10.1080/09593332008616844

Kumar P, Rivas I, Singh AP, Ganesh VJ, Ananya M, Frey HC. 2018. Dynamics of coarse and fine particle exposure in transport microenvironments. NPJ Climate and Atmospheric Science 1: 1-12. https://doi.org/10.1038/s41612-018-0023-y

Latha KM, Highwood EJ. 2006. Studies on particulate matter (PM_{10}) and its precursors over urban environment of Reading, UK. Journal of Quantitative Spectroscopy and Radiative Transfer 101: 367-379. https://doi.org/10.1016/j.jqsrt.2005.11.067

Loureiro AL, Ribeiro AC, Artaxo P, Yamasoe MA. 1994. Calibration of refletometer system to measure black carbon and field inter-comparison in the Amazon Basin. In: Proceedings of the 5th International Conference on Carbonaceous Particles in the Atmosphere. Berkley, California, USA.

Makweba MM, Ndonde PB. 1996. The mineral sector and the national environmental policy. In: Proceedings of the Workshop on the National Environmental Policy for Tanzania (Mwandosya MJ, Luhanga ML, Mugurusi EK, Eds.). Centre for Energy, Environment, Science, and Technology, Dar es Salaam, 73-164.

MDO. 2020. Itabira complex. Mining Data Online. Available at: https://miningdataonline.com/property/1355/Itabira-Complex.aspx (accessed on February 23, 2021).

Miranda EE de. 2005. Brasil em relevo. Embrapa Monitoramento por Satélite, Campinas, Brazil. Available at: http://www.relevobr.cnpm.embrapa.br (accessed on February 2021, 21).

Mohiuddin K, Strezov V, Nelson PF, Stelcer E, Evans T. 2014. Mass and elemental distributions of atmospheric particles nearby blast furnace and electric arc furnace operated industrial areas in Australia. Science of the Total Environment 487: 323-334. https://doi.org/10.1016/j.scitotenv.2014.04.025

Monjezi M, Shahriar K, Dehghani H, Samimi NF. 2009. Environmental impact assessment of open pit mining in Iran. Environmental Geology 58: 205-216. https://doi.org/10.1007/s00254-008-1509-4

Ooki A, Uematsu M, Miura K, Nakae S. 2002. Sources of sodium in atmospheric fine particles. Atmospheric Environment 36:4367-4374. https://doi.org/10.1016/S1352-2310(02)00341-2

Patra AK, Gautam S, Kumar P. 2016. Emissions and human health impact of particulate matter from surface mining operation – A review. Environmental Technology & Innovation 5: 233-249. https://doi.org/10.1016/j.eti.2016.04.002

Pérez IA, García MÁ, Sánchez ML, Pardo N, Fernández-Duque B. 2020. Key points in air pollution meteorology. International Journal of Environmental Research and Public Health 17: 8349. https:// doi.org/10.3390/ijerph17228349

Polidori A, Cheung KL, Arhami M, Delfino RJ, Schauer JJ, Sioutas C. 2009. Relationships between size-fractionated indoor and outdoor trace elements at four retirement communities in southern California. Atmospheric Chemistry and Physics 9: 4521-4536. https://doi.org/10.5194/acp-9-4521-2009

Singh G, Perwez A. 2015. Estimation of assimilative capacity of the airshed in iron ore mining region of Goa. Indian Journal of Science and Technology 8: 1-7. https://doi.org/10.17485/ijst/2015/v8i23/54671

Sobreiro Neto AF, Bertachini AC, Girado AC, Almeida DC. 2001. Hydrogeological model of the Itabira iron ore district. In: Proceedings of the IMWA Symposium, Belo Horizonte.

Soluri DS, Godoy, MLDP, Godoy, JM, Roldão, LA. 2007. Multi-site $PM_{2.5}$ and $PM_{2.5\text{-}10}$ aerosol source apportionment in Rio de Janeiro, Brazil. Journal of the Brazilian Chemical Society 18: 838-845. https://dx.doi.org/10.1590/S0103-50532007000400025

Su L, Yuan Z, Fung JCH, Lau AKH. 2015. A comparison of HYSPLIT backward trajectories generated from two GDAS datasets. Science of the Total Environment 506-507: 527-537. https://doi.org/10.1016/j.scitotenv.2014.11.072

Tapiquén CEP. 2015. South America shapefile. Available at: http://tapiquen-sig.jimdo.com (accessed on February 21, 2021).

Thermo Scientific. 2004. TEOM Series 1400a Ambient Particulate (PM-10) Monitor. Available at: http://www.lisa.u-pec.fr/~formenti/Tools/Manuals/TEOM-model1400-manual.pdf (accessed on February 22, 2021).

Tubino DIS, Nonita TY, Devlin JF. 2011. Vale and its corporate sustainability performance in Itabira, Brazil: Is the glass half full or half empty? Impact Assessment and Project Appraisal 29: 151-157. https://doi.org/10.3152/146155111X12913679730638

US-EPA. 1990. Automated equivalent method: EQPM-1090-079 (Federal Register 55: 43406). U.S. Environmental Protection Agency. Available at: https://www.epa.gov/system/files/documents/2021-12/designated-referene-and-equivalent-methods-12152021.pdf

US-EPA. 1999. Ambient air monitoring reference and equivalent methods (40 CFR 53). U.S. Environmental Protection Agency. Available at: https://www.ecfr.gov/current/title-40/part-53

US-EPA. 2020. National ambient air quality standards (NAAQS) for PM. Available at: https://www.epa.gov/pm-pollution/national-ambient-air-quality-standards-naaqs-pm (accessed on February 15, 2021).

Usiminas. 2020. Usiminas companies. Available at: http://ri.usiminas.com/en/usiminas/usiminas-companies/ (acessed on February 23, 2021).

Vega E, Reyes E, Ruiz H, García J, Sánchez G, Martínez-Villa G., González U, Chow JC, Watson JG. 2004. Analysis of $PM_{2.5}$ and PM_{10} in the atmosphere of Mexico City during 200-2002. Journal of Air & Waste Manage Association 54: 786-798. https://doi.org/10.1080/10473289.2004.10470952

Venter AD, van Zyl PG, Beukes JP, Josipovic M, Hendricks J, Vakkari V, Laakso L. 2017. Atmospheric trace metals measured at the regional background site (Welgegund) in South Africa. Atmospheric Chemistry and Physics 17: 4251-4263. https://doi.org/10.5194/acp-17-4251-2017

Xu G, Jiao L, Zhang B, Zhao S, Yuan M, Gu Y, Liu J, Tang X. 2017. Spatial and temporal variability of the $PM_{2.5}/PM_{10}$ ratio in Wuhan, central China. Aerosol Air Quality Research 17: 741-751. https://doi.org/10.4209/aaqr.2016.09.0406

Yang L, Mukherjee S, Pandithurai G, Waghmare1 V, Safai PD. 2019. Influence of dust and sea-salt sandwich effect on precipitation chemistry over the Western Ghats during summer monsoon. Scientific Reports 9: 1-13. https://doi.org/10.1038/s41598-019-55245-0

Yousefian F, Faridi S, Azimi F, Aghaei M, Shamsipour M, Yaghmaeian K, Hassanvand MS. 2020. Temporal variations of ambient air pollutants and meteorological influences on their concentrations in Tehran during 2012-2017. Scientific Reports 10: 1-11. https://doi.org/10.1038/s41598-019-56578-6

Wanjura JD, Shaw BW, Parnell CB, Jr, Lacey RE, Capareda SC. 2008. Comparison of continuous monitor (TEOM) and gravimetric sampler particulate matter concentrations. Transactions of the ASABE 51: 251-257. http://doi.org/10.13031/2013.24218

Wasylycia-Leis J, Fitzpatrick P, Fonseca A. 2014. Mining communities from a resilience perspective: Managing disturbance and vulnerability in Itabira, Brazil. Environmental Management 53: 481-495. https://doi.org/10.1007/s00267-014-0230-1

WHO. 2000. Particulate matter. In: Air Quality Guidelines for Europe, 186-193. Available at: https://www.euro.who.int/__data/assets/pdf_file/0019/123085/AQG2ndEd_7_3Particulate-matter.pdf (accessed on August 28, 2020).

WHO. 2006. Health risks of particulate matter from long-range transboundary air pollution. Regional Office for Europe, World Health Organization/European Centre for Environment and Health. Available at: euro.who.int/__data/assets/pdf_file/0006/78657/E88189.pdf

WHO. 2008. Air quality and health – Fact sheet nº 313. Available at: http://www.WHO.int/mediacentre/factsheets/fs313/en/ (accessed on August 28, 2020).

Zhou S, Yuan Q, Li W, Lu Y, Zhang Y, Wang W. 2014. Trace metals in atmospheric fine particles in one industrial urban city: Spatial variations, sources, and health implications. Journal of Environmental Sciences 26: 205-213. https://doi.org/10.1016/S1001-0742(13)60399-X

ISSN 0187-6236
9 770187 623606

UNIVERSIDAD NACIONAL AUTONOMA DE MEXICO

POR MI RAZA HABLARA EL ESPIRITU

Universidad Nacional
Autónoma de
México